Universidade de Aveiro Departamento de Física
2015

CLÁUDIO MIGUEL SILVA NICO

NIOBIUM OXIDES AND NIOBATES PHYSICAL PROPERTIES

PROPRIEDADES FÍSICAS DE ÓXIDOS DE NIÓBIO E DE NIOBATOS

Universidade de Aveiro Departamento de Física
2015

CLÁUDIO MIGUEL SILVA NICO

NIOBIUM OXIDES AND NIOBATES PHYSICAL PROPERTIES

PROPRIEDADES FÍSICAS DE ÓXIDOS DE NIÓBIO E DE NIOBATOS

Dissertação apresentada à Universidade de Aveiro para cumprimento dos requisitos necessários à obtenção do grau de Doutoramento em Nanociências e Nanotecnologia, realizada sob a orientação científica do Doutor Manuel Pedro Fernandes Graça, Investigador do Departamento de Física da Universidade de Aveiro, e sob a coorientação científica da Doutora Teresa Maria Fernandes Rodrigues Cabral Monteiro, Professora Associada com Agregação, do Departamento de Física da Universidade de Aveiro.

Apoio financeiro através da Bolsa de Doutoramento da FCT com a referência SFRH / BD / 68295 / 2010.

Apoio financeiro através dos projetos, QREN 05 NbO/5309, RECI/FIS-NAN/0183/2012 (FCOMP-01-0124-FEDER-027494) e UID/CTM/50025/2013.

FCT Fundação para a Ciência e a Tecnologia
MINISTÉRIO DA EDUCAÇÃO E CIÊNCIA

Dedico este trabalho ao Mundo.

o júri / the jury

presidente / president	Doutor Joaquim Arnaldo Carvalho Martins Professor Catedrático da Universidade de Aveiro
vogais / examiners committee	Doutor Henrique Leonel Gomes Professor Associado com Agregação da Faculdade de Ciências e Tecnologia da Universidade do Algarve
	Doutor Eduardo Jorge da Costa Alves Investigador Principal do Instituto Superior Técnico da Universidade de Lisboa
	Doutora Florinda Mendes da Costa Professora Associada da Universidade de Aveiro
	Doutor Rui Alberto Garção Barreira do Nascimento Igreja Professor Auxiliar da Faculdade de Ciências e Tecnologia da Universidade Nova de Lisboa
	Doutor Manuel Pedro Fernandes Graça Investigador Auxiliar da Universidade de Aveiro (Orientador)

agradecimentos / acknowledgements

Além de uma luta pelo conhecimento, foi uma luta pela motivação. Sozinho, não seria possível. As palavras de agradecimento, aos que contribuíram para este trabalho e/ou para o meu percurso, pouco se comparam ao que gostaria de lhes retribuir. Quero ainda assim deixar registadas tais palavras.

Agradeço à Universidade de Aveiro, ao Departamento de Física e ao laboratório associado I3N, que disponibilizaram as suas instalações, recursos técnicos e humanos para a realização deste trabalho.

Agradeço ao Prof. Manuel Graça e à Prof.ª Teresa Monteiro, por toda a dedicação, pelos conselhos, tempo, paciência e confiança no meu trabalho e capacidades.

Agradeço a KEMET Évora, e em particular à Mariana Matos e ao Rui Monteiro pela disponibilidade e importante contributo ao longo, e após, o projeto QREN.

Agradeço à Prof.ª Florinda Costa, ao Prof. Manuel Valente, ao Prof. Luís Rino, à Prof.ª Rosário Correia, ao Prof. Jorge Soares, ao Prof. Luís Cadillon e ao Prof. Augusto Lopes, por todos os conselhos e auxílio.

Agradeço ao Sr. Reis, Marco Peres, ao Tozé e ao Jorge Monteiro por todas as soluções, ideias, conversas, e por tudo o que me ensinaram.

Agradeço ao Sr. Ivo, Sr. Miguel e Sr. Júlio que sempre me ajudaram a resolver vários tipos de problemas.

Agradeço à Dra. Rosário Soares e Dra. Paula Brandão por muitas das medidas de XRD, disponibilidade e simpatia, assim como à Marta Ferro por toda a formação e ajuda na aquisição e interpretação de imagens de SEM.

Agradeço à minha colega Joana Rodrigues por muitas das discussões e aquisição de resultados, assim como aos meus colegas Ricardo Carvalho, José Carreira, Vânia Freitas, Nuno Santos, Nuno Ferreira e Tiago Holz, pelas mais variadas ajudas.

Quero agradecer, de forma muito especial, à minha grande colega de laboratório M.R.N. Soares pela sua preciosíssima contribuição, desde a preparação de amostras, aquisição e interpretação de resultados, orientação, conselhos e motivação. Este trabalho dificilmente existiria sem a sua ajuda.

Obrigado amigos, por o serem.

Mãe, Pai, Sofia, Tia e Avós: bem hajam pelo vosso estímulo, apoio, educação e carinho. Vocês são os maiores culpados.

Agradeço à Rosa, uma mulher admirável e que me faz acreditar, afinal, que a lua está tão perto.

palavras-chave

Nióbio, óxido, niobato, ortoniobato, condensador, polimorfos, terras-raras, propriedades elétricas, fotoluminescência, Raman, lacunas de oxigénio.

resumo

Os óxidos de nióbio têm sido apontados como uma alternativa ao tântalo na produção de condensadores eletrolíticos sólidos, com vantagens relativamente à constante dielétrica, densidade e preço. Neste trabalho, pretende-se criar uma nova família de condensadores de óxidos de nióbio, adaptando a tecnologia e linha de produção atualmente utilizada com o tântalo.

Apesar das já conhecidas potencialidades dos óxidos de nióbio, e vários tipos de niobatos, em diversas aplicações tecnológicas, o conhecimento destes sistemas óxidos é ainda manifestamente insuficiente. Assim, é apresentada uma cuidadosa revisão bibliográfica que evidencia a complexidade destes materiais, as dificuldades na identificação das suas várias fases e polimorfos, assim como na interpretação das suas propriedades.

Neste contexto, são apresentados vários estudos fundamentais em óxidos de nióbio, nomeadamente caracterização estrutural, microestrutural, ótica e elétrica, que permitem não só contribuir de uma forma importante para o conhecimento geral das propriedades físicas destes materiais, como avançar para o desenvolvimento sustentado dos condensadores eletrolíticos sólidos à base de óxidos de nióbio. Estudaram-se vários parâmetros de processamento abrindo caminho para a criação de um protótipo.

Avançou-se também para um estudo preliminar da síntese e caracterização de outros sistemas óxidos à base de nióbio, nomeadamente ortoniobatos de terras-raras ($RENbO_4$), cujo interesse tem sido manifestado relativamente às suas propriedades óticas e de condutividade protónica. Assim, amostras mono e policristalinas de $RENbO_4$ foram sintetizadas e caracterizadas estrutural, ótica e eletricamente, deixando em aberto um interessante trabalho futuro.

keywords

Niobium, oxide, niobate, orthoniobate, capacitor, polymorphs, rare-earths, electrical properties, photoluminescence, Raman, oxygen vacancies.

abstract

Niobium oxides have been pointed as an alternative to tantalum in the production of solid electrolytic capacitors, with advantages regarding the dielectric constant, density and price. In this work, it is intended to create a new family of niobium oxides based capacitors, adapting the technology and production line currently used with tantalum.

Despite the known potentialities of niobium oxides, and many types of niobates, in several technological applications, the understanding of these oxide systems is still noticeably insufficient. Hence, a careful bibliographic review is shown, which evidences the complexity of these materials, the difficulty in identifying of their different phases and polymorphs, as well as in the interpretation of their properties.

In this context, several fundamental studies on niobium oxides are presented, namely structural, microstructural, optical and electrical characterizations, which allow not only to contribute in an important way for the general knowledge of the physical properties of these materials, but also to advance to a sustained development of the niobium oxides based solid electrolytic capacitors. Several processing parameters were studied, clearing the way towards the creation of a prototype.

It was also decided to perform a preliminary study on the synthesis and characterization of other oxide systems based in niobium, namely rare-earth orthoniobates ($RENbO_4$), which interest has been related to their optical properties and protonic conductivity. Hence, single and polycrystalline samples of $RENbO_4$ were synthesized and characterized structural, optical and electrically, leaving open an interesting future work.

Index

Index i

List of Acronyms v

List of Figures vii

List of Tables xv

Preface xvi

1. Introduction 3

  1.1 Niobium and Tantalum 3

    1.1.1 A tantalizing story 3

    1.1.2 World Market 4

  1.2 A New Family of Capacitors 7

  1.3 The Niobium Oxides system 11

    1.3.1 Nb 13

    1.3.2 NbO 15

    1.3.3 NbO_2 17

    1.3.4 Nb_2O_5 19

    1.3.5 Non-Stoichiometric Niobium Oxides 30

  1.4 Niobates 38

    1.4.1 Alkali Niobates 38

    1.4.2 Columbite Niobates 40

    1.4.3 Rare-Earths Orthoniobates 44

2. Synthesis and Characterization Techniques 51

  2.1 Synthesis and processing techniques 51

    2.1.1 Solid State Reaction 51

    2.1.2 Sol-Gel Method 54

    2.1.3 Laser Floating Zone 56

  2.2 Characterization techniques 60

- 2.2.1 Differential Thermal Analysis 60
- 2.2.2 X-Ray Diffraction 61
- 2.2.3 Scanning Electron Microscopy 65
- 2.2.4 Raman Spectroscopy 68
- 2.2.5 Photoluminescence Spectroscopy 71
- 2.2.6 Electrical Measurements and Impedance Spectroscopy 77

3. Solid Electrolytic Capacitor 87
  - 3.1 Types of Capacitors 87
  - 3.2 Manufacturing 91
    - 3.2.1 Pressing 91
    - 3.2.2 Sintering 92
    - 3.2.3 Bar Welding 93
    - 3.2.4 Teflon ring (Primer) 93
    - 3.2.5 Dielectric Forming (Pre-Forming) 94
    - 3.2.6 Tempering and re-forming 95
    - 3.2.7 MnO_2 Impregnation 96
    - 3.2.8 Contacting of the Cathode 97
    - 3.2.9 Assembly 98
4. Niobium Oxides prepared by sintering NbO powders 103
  - 4.1 Experimental Procedure 103
  - 4.2 Results and Discussion 104
  - 4.3 Summary 116
5. Thermal Oxidation of NbO Anodes 121
  - 5.1 Experimental Procedure 121
  - 5.2 Results and Discussion 123
  - 5.3 Summary 129
6. Niobium Oxides based Capacitors 133
  - 6.1 Pressing and Sintering 133
  - 6.2 Anodization 139

6.3 Tempering ... 146
6.4 MnO_2 impregnation ... 153
6.5 Summary ... 158
7. Rare-Earth Orthoniobates ... 163
7.1 Synthesis ... 163
7.2 Results and Discussion ... 170
7.2.1 XRD ... 170
7.2.2 Raman ... 172
7.2.3 SEM ... 174
7.2.4 Photoluminescence spectroscopy ... 177
7.2.5 Electrical Properties ... 196
7.2.6 A note on oxygen vacancies ... 201
7.3 Summary ... 202
8. Final overview, conclusions and future work ... 207
References ... 215

List of Acronyms

Acronym	Definition
AC	Alternating Current
AFM	Atomic Force Microscopy
BMT	Barium Magnesium Tantalate
BSE	Backscattered Electrons
BZCN	Barium Zinc Cobalt Niobate
BZN	Barium Zinc Niobate
BZT	Barium Zinc Tantalate
CBMM	Companhia Brasileira de Metalurgia e Mineração
CCD	Charge-Coupled Device
CERN	Conseil Européen pour la Recherche Nucléaire
CIE	Commission Internationale de l'Éclairage
CMOS	Complementary Metal Oxide Semiconductor
CT	Charge Transfer
DC	Direct Current
DOS	Density of States
DSC	Differential Scanning Calorimetry
DTA	Differential Thermal Analysis
EDLC	Electrical Double-Layer Capacitors
EDTA	Ethylene Diamine Tetraacetic Acid
EDX	Energy-Dispersive X-Ray
EELS	Electron Energy Loss Spectroscopy
EPR	Electron Paramagnetic Resonance
ESR	Equivalent Series Resistance
FTIR	Fourier-Transform Infrared Spectroscopy
GPS	Global Positioning System
HN	Havriliak-Negami
HSLA	High Strength Low Alloys
HT	Heat Treatment
ICDD	International Centre for Diffraction Data
IR	Infrared
IUPAC	International Union of Pure and Applied Chemistry

JCPDS	Joint Committee on Powder Diffraction Standards
KNN	Potassium Sodium Niobate
LFZ	Laser Floating Zone
LHC	Large Hadron Collider
LHPG	Laser Heated Pedestal Growth
MIM	Metal Insulator Metal
MOS	Metal Oxide Semiconductor
MPB	Morphotropic Phase Boundary
PCB	Printed Circuit Board
PL	Photoluminescence
PLE	Photoluminescence Excitation
PPT	Polymorphism Phase Transition
PTFE	Polytetrafluoroethylene
PVA	Polyvinyl Alcohol
PZT	Lead Zirconium Titanate
RE	Rare-Earth
RT	Room Temperature
SCXRD	Single-Crystal X-Ray Diffraction
SE	Secondary Electrons
SEM	Scanning Electron Microscopy
SHG	Second Harmonic Generation
SMD	Surface Mounted Devices
TCO	Transparent Conductive Oxide
TEM	Transmission Electron Microscopy
TGA	Thermogravimetric Analysis
TMA	Thermomechanical Analysis
UA	University of Aveiro
USB	Universal Serial Bus
UV	Ultraviolet
XRD	X-Ray Diffraction

List of Figures

Figure 1.1 – Photographs of a Columbite (left) and a Tantalite (right), taken at the public exposition of the mineral collection of the Natural History Museum in London. 4
Figure 1.2 – Global percentages of Tantalum and Niobium end-uses in 2004 [8].......................6
Figure 1.3 - Austrian Mint Silver Niobium coins, with coloured cores obtained by anodization of niobium [13]. 6
Figure 1.4 – Price of Tantalum and Niobium in US dollars per kg from 1964 to 2007 [14]...7
Figure 1.5 - Capacitor technology average annual growth in 2002 [34]. 8
Figure 1.6 - Comparison of the heat capacity, burning rate and ignition energy between NbO, Ta and Nb capacitors [34]. 10
Figure 1.7 - Schematic illustration of the different oxidation states of Niobium. 11
Figure 1.8 - Niobium-Oxygen phase diagram [53]. 13
Figure 1.9 – Cubic crystalline structure of metallic Nb. 13
Figure 1.10 – Cubic structure of NbO. 16
Figure 1.11 - Structure of a) tetragonal and b) rutile NbO_2. 18
Figure 1.12 - Monoclinic structure of the H-Nb_2O_5 phase. 22
Figure 1.13 - Monoclinic structure of the B-Nb_2O_5 phase. 22
Figure 1.14 - Monoclinic structure of the N-Nb_2O_5 phase. 23
Figure 1.15 - Tetragonal structure of the M-Nb_2O_5 phase. 24
Figure 1.16 – Tetragonal structure of the P-Nb_2O_5 phase. 24
Figure 1.17 - Monoclinic structure of the R-Nb_2O_5 phase. 25
Figure 1.18 - Monoclinic structure of the Z-Nb_2O_5 phase. 26
Figure 1.19 - Orthorhombic structure of the T-Nb_2O_5 phase. 26
Figure 1.20 – Monoclinic structure of the $Nb_{22}O_{54}$ phase. 33
Figure 1.21 - Structure of the orthorhombic $Nb_{12}O_{29}$ phase. 34
Figure 1.22 - Structure of the monoclinic $Nb_{12}O_{29}$ phase. 34
Figure 1.23 – Typical perovskite structure of an alkali niobate. 39
Figure 1.24 – Typical orthorhombic structure of most columbite niobates. 41
Figure 1.25 - Structure of the monoclinic phase of $RENbO_4$. 44
Figure 1.26 - Structure of the tetragonal phase of $RENbO_4$. 45
Figure 2.1 – Schematic representation of common routes of the sol-gel process (inspired in a similar scheme from Brinker and Scherer [200]). 55
Figure 2.2 – Schematic representation of the Laser Floating Zone (LFZ) technique. 58

Figure 2.3 – Typical DTA experimental arrangement. 61
Figure 2.4 - Bragg's Law graphical interpretation (adapted from [213]). 62
Figure 2.5– General representation of Ewald’s sphere (adapted from [213]). 63
Figure 2.6 – Phenomena resulting of the interaction of high energy electrons with a sample (adapted from [221]). 66
Figure 2.7 - Scanning Electron Microscope scheme [222]. 67
Figure 2.8 - Simplified energy level diagram showing the transitions involved in Raman signal (Stokes and Anti-Stokes) as well as the Rayleigh dispersion, and an example of a Raman spectrum. 70
Figure 2.9 – Schematic of Raman spectrometer in a backscattering geometry. 71
Figure 2.10 - Schematic of a typical PL/PLE experimental arrangement. 73
Figure 2.11 – Configurational coordinate diagram (adapted from [226]). 75
Figure 2.12 – Schematic representation of parallel plate capacitor. 79
Figure 2.13 - Phasor Diagram of a generic electrical impedance. 81
Figure 2.14 - Two common equivalent RC circuits used in impedance spectroscopy. 82
Figure 2.15 - Representation of the real and imaginary parts of the dielectric constant of a material with contributions from different polarization mechanisms (adapted from [232]). 84
Figure 3.1 – Classification of different types of capacitor technologies (adapted from [239] and [240]). 89
Figure 3.2 – Operating voltages and capacitance ranges for different types of capacitors available in the market (adapted from [239] and [241]). 89
Figure 3.3 – Illustration of the pressing of the tantalum powders to form the capacitor anode. 92
Figure 3.4 – Illustration of the sintering process of the Ta anodes in vacuum. 92
Figure 3.5 – Illustration of Ta anodes being welded into an aluminium bar. 93
Figure 3.6 – Teflon ring incorporation around the Ta wire of the anodes. 93
Figure 3.7 – Schematic representation of the experimental apparatus of the anodization process and the time evolution of the applied voltage and current. 95
Figure 3.8 – Illustrative representation of the microstructure of a Ta anode with the formed dielectric layer of amorphous Ta_2O_5. 96
Figure 3.9 – Illustration of a dipping and pyrolysis cycle to the impregnation of MnO_2. 97
Figure 3.10 – Illustration of the conductive baths around the MnO_2, and a schematic representation of the final microstructure of the capacitors. 98
Figure 3.11 – Cross-section view of a tantalum solid electrolytic capacitor (at left) and a picture of a capacitor welded into a PCB. 99

Figure 4.1 - Differential Thermal Analysis of NbO-80K and NbO-120K powders. 105
Figure 4.2 – Photograph of some of the NbO pellets before (grey) and after heat treatment at 300 ºC (blue) and at higher temperatures (white). 105
Figure 4.3 - XRD patterns of the NbO-80K and NbO-120K sintered pellets (C - Cubic NbO; T - Orthorhombic T-Nb_2O_5; B - Monoclinic B-Nb_2O_5; H – Monoclinic H-Nb_2O_5)........ 106
Figure 4.4 – Simulated powder XRD pattern for the cubic NbO structure. 107
Figure 4.5 - Scanning Electron Micrographs for the NbO-80K and NbO-120K sintered pellets........ 108
Figure 4.6 - RT Raman spectra of NbO-80K and NbO-120K sintered pellets, obtained with the 325 nm He-Cd laser line (T, B and H polymorphs are assigned to the corresponding spectra). 109
Figure 4.7 – IR absorption spectra of the NbO 80K and 120K samples. 110
Figure 4.8 - (a) 14 K PL spectra of the 450, 700, 800 and 900 ºC sintered pellets of NbO-120K; (b) Temperature dependent PL spectra and RT absorption of the 800 ºC sample and (c) The same as in (b) for the 900 ºC sintered pellets of NbO 120K. 111
Figure 4.9 - (a) Dielectric constant and (b) dielectric loss, measured at 300 K for the NbO-80K pellets sintered at 800, 900 and 1100 ºC. 114
Figure 4.10 – (a) Dielectric constant and (b) dielectric loss, measured at 300 K for the NbO-120K pellets sintered at 800, 900 and 1100 ºC........ 114
Figure 4.11 - M´´ versus frequency, at 300 K for the pellets NbO-80K (a) and NbO-120K (b) sintered at 800, 900 and 1100 ºC. 115
Figure 4.12 - (a) Dielectric constant and (b) dielectric loss, measured at 300 K for the NbO-80K pellets sintered at 300 and 450 ºC........ 116
Figure 5.1 - In-Situ XRD and DTA analyses performed to the NbO powders. 124
Figure 5.2 – Snapshots of the anode at different times (between 0 and 24 min) of the HT with a heating rate of 20 ºC/min........ 125
Figure 5.3 – Snapshots of the anode at different times of the HT with a heating rate of 2.5 ºC/min........ 125
Figure 5.4 - Stack of representative frame fractions from the video of niobium oxide anode heated at 2.5 ºC/min (increase of temperature from left to right)........ 125
Figure 5.5 – *In-situ* Raman analysis of the NbO anode (left); Representation of the variation of the maximum intensity of the Raman peak (~690 cm^{-1}) with the HT temperature (right). 126
Figure 5.6 - SEM analysis of four NbO anodes heat treated at different temperatures, in SE mode (at left) and BSE mode (at right). 128

Figure 5.7 - Optical interference patterns of the NbO samples obtained between 340 and 500 °C. The colour coordinates calculated from the spectra are plotted in the CIE colour diagram shown in the inset. 129
Figure 6.1 – SEM pictures of the NbO 80K and 120K powders........ 133
Figure 6.2 – XRD patterns of the NbO 80K and 120K powders. 134
Figure 6.3 – XRD patterns of the sintered NbO 80K and 120K anodes........ 136
Figure 6.4 – Pressed and sintered NbO anodes welded into an aluminium bar. 136
Figure 6.5 – XRD pattern of the NbO pellets sintered in vacuum in the UA laboratory. 137
Figure 6.6 – Raman spectra (under 325 nm laser excitation) of the NbO 80K and 120K samples oxidized into NbO_2........ 138
Figure 6.7 – IR absorption spectra of the NbO 80K and 120K samples oxidized into NbO_2. 138
Figure 6.8 – Pictures of the anodized NbO anodes, showing their different colours. 139
Figure 6.9 – XRD patterns of the anodized NbO anodes. 140
Figure 6.10 – Raman spectra of the anodized NbO anodes under 325 nm laser excitation. 141
Figure 6.11 – Capacitance and Resistance, as a function of frequency, of the NbO anodized anodes........ 142
Figure 6.12 – SEM images of the anodized NbO anodes. 144
Figure 6.13 – XRD patterns of the anodes before and after the tempering process. 147
Figure 6.14 – Detail of the bands observed by the XRD patterns of the anodes tempered at 350 °C, assigned to the presence of an amorphous phase. 148
Figure 6.15 – Raman spectra, under 325 nm laser excitation, of the anodes before and after the tempering process........ 149
Figure 6.16 – Capacitance of the anodes before and after the tempering process. 150
Figure 6.17 – Resistance of the anodes before and after the tempering process. 151
Figure 6.18 – SEM images of the anodized NbO anodes after the tempering process. 152
Figure 6.19 – SEM images of inner body part of the NbO anodes after MnO_2 impregnation through a pyrolysis at 230 °C. 154
Figure 6.20 – SEM images of inner body part of the NbO anodes after MnO_2 impregnation through a pyrolysis at 270 °C. 154
Figure 6.21 – Manganese oxide particles with mushroom shape observed at the surface of the NbO anodes after a pyrolysis at 270 °C. 156
Figure 6.22 – Manganese oxide particles with mushroom shape observed at the surface of the NbO anodes after a pyrolysis at 270 °C. 157

Figure 6.23 – Manganese oxide particles a hexagonal pyramid shape, observed next to the Ta wire of the NbO anode after a pyrolysis at 270 °C. 158
Figure 7.1 – Schematic illustration of the followed Pechini route for the synthesis of the $RENbO_4$ gel. 165
Figure 7.2 – Heating profile followed during the gel drying process. 166
Figure 7.3 – XRD patterns (left) and Raman spectra under 325 nm laser excitation (right) of the $ErNbO_4$ and $SmNbO_4$ powders........ 166
Figure 7.4 – Representative SEM images of all $RENbO_4$ synthesized powders........ 168
Figure 7.5 - Photograph of $ErNbO_4$ fibre (left) and pellet (right). 169
Figure 7.6 - Photograph of $EuNbO_4$ fibre (left) and pellet (right). 169
Figure 7.7 – Photograph of $SmNbO_4$ fibre (left) and pellet (right). 169
Figure 7.8 – Representative Laue patterns acquired of all the $RENbO_4$ fibres. 170
Figure 7.9 – XRD patterns for the $RENbO_4$ pellets. 171
Figure 7.10 – Raman spectra of the $RENbO_4$ fibres (at left) and pellets (at right) acquired with a 325 nm laser as excitation source. 173
Figure 7.11 – SEM pictures of the $ErNbO_4$ fibre (on top) and pellet (on bottom). 175
Figure 7.12 – SEM pictures of the $EuNbO_4$ fibre (on top) and pellet (on bottom)........ 176
Figure 7.13 – SEM pictures of the $SmNbO_4$ fibre (on top) and pellet (on bottom)........ 177
Figure 7.14 – High resolution PL spectra of the $ErNbO_4$ pellet at 14 K, excited with a 325 nm laser. 178
Figure 7.15 - Detail of the emission lines from the $^4S_{3/2}$ to $^4I_{15/2}$ transition of the $ErNbO_4$ pellet at 14 K excited with a 325 nm laser. 179
Figure 7.16 – PL spectra of the $ErNbO_4$ pellet at different temperatures excited with a 325 nm laser; integrated intensity of different transitions, as a function of temperature, in inset........ 179
Figure 7.17 - PL spectra of the $ErNbO_4$ pellet at RT, excited with a 532 nm laser. 180
Figure 7.18 – PL spectra of the $ErNbO_4$ fibre at RT, excited with a 532 nm laser. 181
Figure 7.19 – IR PL spectra at RT of the $ErNbO_4$ pellet excited with a 488 nm laser. 181
Figure 7.20 –PL spectra at 5 K of the $ErNbO_4$ for different excitation powers of a 980 nm laser........ 182
Figure 7.21 – PL spectra at 5 K of the $ErNbO_4$ as a function of the excitation power of a 980 nm laser; in inset, the CIE diagram with the corresponding colour coordinates. 183
Figure 7.22 – Energy levels diagram of the free Er^{3+} ion and respective observed transitions observed in the $ErNbO_4$ samples, when excited with 325 nm (at left) and 532 nm (at right)........ 184

Figure 7.23 – Energy levels diagram of the free Er^{3+} ion and respective observed transitions observed in the $ErNbO_4$ samples, when excited with 488 nm (at left) and 980 nm (at right) 184
Figure 7.24 – PL spectrum of the $EuNbO_4$ fibre at RT, under 325 nm laser excitation. 185
Figure 7.25 – PLE spectra at RT of the $EuNbO_4$ fibre, monitored at the 612 nm emission. 186
Figure 7.26 – Energy level diagram of the $4f^6$ electron configuration for the Eu^{3+} free ion with the observed radiative transitions of the ions embedded in the $EuNbO_4$ crystalline hosts 187
Figure 7.27 – High resolution PL spectra of the $EuNbO_4$ fibre and pellet (separated by an onset) at 14 K, under 325 nm laser excitation. 188
Figure 7.28 – Temperature dependent PL spectra of the $EuNbO_4$ pellet under 325 nm laser excitation; integrated intensity of the $^5D_0$ bands as a function of temperature (inset) 189
Figure 7.29 – High resolution temperature dependent PL spectra of the $EuNbO_4$ fibre under 325 nm laser excitation. 190
Figure 7.30 – PL spectrum of the $SmNbO_4$ pellet at 14 K, under 325 nm laser excitation. 191
Figure 7.31 –PLE spectra at RT of the $SmNbO_4$ fibre and pellet, monitored at the 647 nm emission (colour bars refer to the electronic levels assignment in Figure 7.35). 191
Figure 7.32 – Excitation edge, at high energies, of the $SmNbO_4$ fibre and pellet, from the PLE spectra monitored at the 647 nm emission. 192
Figure 7.33 – PL spectra at RT of the $SmNbO_4$ samples excited with 480 nm from a Xe Lamp. 193
Figure 7.34 – PL spectra of the $SmNbO_4$ samples excited with a 532 nm laser at RT. 193
Figure 7.35 – Energy level diagram of the $4f^5$ electron configuration of Sm^{3+} with the observed radiative transitions observed in the $SmNbO_4$ samples. 194
Figure 7.36 – High resolution PL spectra of the emission assigned to the $^4G_{5/2}$ to $^6H_{7/2}$ transition, from the $SmNbO_4$ pellet at 14 K under 325 nm laser excitation. 194
Figure 7.37 – Temperature dependent PL spectra of the $SmNbO_4$ pellet; in inset it is shown the integrated intensity of the $^5G_{5/2}$ emissions lines for the different temperatures. 195
Figure 7.38 – Total ac conductivity of the $ErNbO_4$ pellet, measured at different frequencies, from RT to 1000 °C in air. 196
Figure 7.39 – Total ac conductivity of the $EuNbO_4$ pellet, measured at different frequencies, from RT to 1000 °C in air. 197
Figure 7.40 – Total ac conductivity of the $SmNbO_4$ pellet, measured at different frequencies, from RT to 1000 °C in air 197

Figure 7.41 – Schematic illustration of the Grotthuss mechanism for protonic conduction through oxygen vacancies (adapted from [268]). 198

Figure 7.42 – Relative dielectric constant of the $ErNbO_4$ pellet, measured at different frequencies, from RT to 1000 °C in air........ 199

Figure 7.43 – Relative dielectric constant of the $EuNbO_4$ pellet, measured at different frequencies, from RT to 1000 °C in air........ 199

Figure 7.44 – Relative dielectric constant of the $SmNbO_4$ pellet, measured at different frequencies, from RT to 1000 °C in air........ 200

Figure 7.45 – Pictures of the $ErNbO_4$ pellet before (at left) and after (at right) laser irradiation........ 201

Figure 7.46 – Pictures of the $EuNbO_4$ fibre before (at left) and after (at right) laser irradiation........ 202

List of Tables

Table 1.1 - Niobium Oxides Crystalline Phases 37

Table 6.1 – List of the pressed NbO anodes. 135

Table 6.2 – List of the anodes submitted to the anodization process and the respective forming current and voltage. 139

Table 6.3 – Average thickness of the dielectric layer of each anodized NbO anode and the calculated ratio thickness/voltage 145

Table 6.4 – List of the anodes submitted to the tempering process at different temperatures and atmospheres, and respective pictures. 146

Table 7.1 – Growth parameters of the $RENbO_4$ fibres. 164

Table 7.2 – Single-crystal XRD data of the $RENbO_4$ fibres. 171

Table 7.3 – Lattice parameters of the matched reference structure from the XRD analysis of the $RENbO_4$ pellets 172

Preface

The main focus of this work is about the physical properties niobium oxides. The interest in working with these materials is related to their many interesting properties reported in literature and was motivated by the experience of our research group in many different oxides and also by the opportunity in using the niobium oxides for the development of a new family of electrolytic capacitors. However, this metal oxide system has proved to be extremely complex, which led to the need of performing several fundamental characterization studies and a thorough bibliographic investigation.

This thesis is divided in eight chapters. In chapter 1, this work is contextualize from a technological and scientific point of view, performing an historical review on the available literature of niobium oxides and other niobates which helps to know better the characteristics of these materials, their complexities, and also justifies the course and sequence followed along this work.

In chapter 2, the materials synthesis methods and also the characterization techniques used in this work, are described with the respective theoretical background.

Chapter 3 shows the different types of capacitors that exist, and also explains in detail the manufacturing process steps of tantalum based solid electrolytic capacitor.

Chapter 4 and 5 describe several fundamental physical characterizations of niobium oxides, while chapter 6 shows a systematic work of synthesis and processing of NbO to produce the desired niobium oxides based solid electrolytic capacitors.

Apart from the niobium oxides, rare-earth orthoniobates were found to be an interesting material to study regarding their optical and electrical properties. The synthesis and a group of preliminary physical characterization of some of these materials, are presented in chapter 7.

Finally, in chapter 8, it is performed a general overview of the work, summarizing the main conclusions of each chapter, and also future work developments, related to niobium oxides and rare-earth orthoniobates, are suggested.

Chapter 1

Introduction

1. Introduction

In this first chapter, a general introduction about niobium and tantalum is made, explaining how these two elements are related with each other from an historical, economical and scientific point of view.

It will be explained how this work is contextualized in an industry-related project, which purpose was to develop a new family of solid electrolytic capacitors based on niobium oxides, as an alternative to the current tantalum-based capacitors.

Finally, it will be made a literature review and a thorough description of the niobium oxides system, but also on different niobates, with a special focus on the rare-earth orthoniobates.

1.1 Niobium and Tantalum

The history of niobium is inevitably attached to the history of tantalum. It is known today that niobium (Nb), atomic number 41, is a transition metal with the electronic configuration [Kr] $4d^4\ 5s^1$ belonging to the group 5 of the periodic table of elements, the same group of vanadium (V) and tantalum (Ta). Both elements, Nb and Ta, present a greyish bright colour, typical of their metallic form, and are mostly found together, in different ratios, in minerals such as Columbite, Tantalite, Pyrochlore and Microlite (and others).

1.1.1 A tantalizing story

Due to their similarities and because they are commonly found together in the same ores, Niobium and Tantalum were often confused with each other. In 1801, the English chemist Charles Hatchett analysed a mineral called columbite (named after *Columbia,* the Latin name for North America, where it was found), from which he reported the discovery of a new element, then named Columbium. In the following year, in 1802, the Swedish chemist Anders Ekeberg reported the discovery of a new element, from a rare mineral called yttrotantalite, named Tantalum because it did not react with acids in analogy with the Greek mythological figure Tantalus who could not drink water. A few years later, William Wollaston (an English chemist), stated that columbium and tantalum were in fact the same element, tantalum, after he analysed both minerals columbite and tantalite, illustrated in Figure 1.1. In 1844, the German chemist Heinrich Rose rediscovered the columbium, but named it Niobium [1] (from Niobe, daughter of Tantalus, since that element resembled tantalum). In the following years, other elements were reported to be found in columbites and tantalites: Pelopium in 1845 by Heinrich Rose [2], Ilmenium in 1847 by R. Hermann [3], and Dianium in 1860 by Wolfgang Franz von Kobell [4]. These new elements were in fact compounds containing different amounts of tantalum and niobium, which were finally isolated, and proved to be the only two elements, by Jean Charles de Marignac in 1866 [5,6]. Despite the official name given by IUPAC in 1950, Niobium, it is still nowadays referred as Columbium in some industries, especially in North America [7].

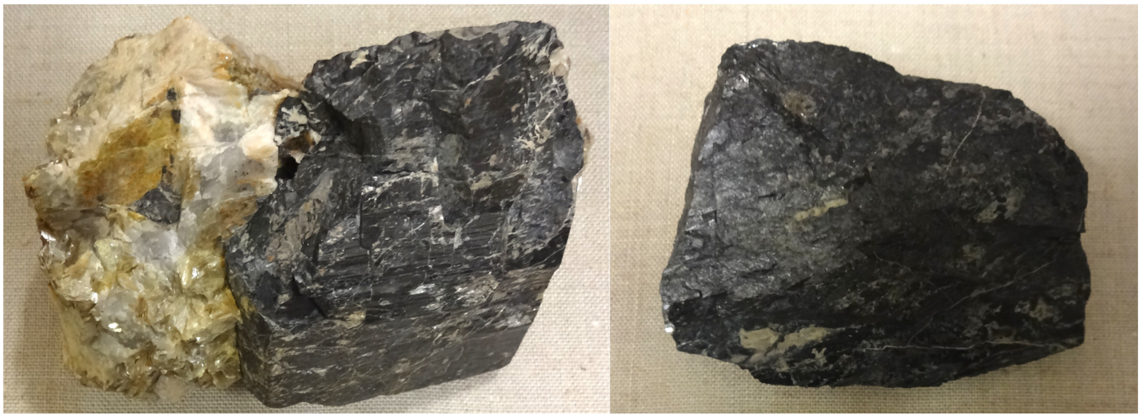

Figure 1.1 – Photographs of a Columbite (left) and a Tantalite (right), taken at the public exposition of the mineral collection of the Natural History Museum in London.

1.1.2 World Market

Most of world's niobium and tantalum is extracted from mining methods. Typically, these extraction methods can be either surface mining (*open-pit*) or sub-surface mining (*underground*), or a combination of both. There are, however, significant amounts of these metals extracted by artisanal and small scale mining [8–11], while a less significant amount (i.e. <2 % and around 14 % of niobium's and tantalum's global production respectively), is extracted as a by-product of tin smelter waste [8]. Recycling of tantalum is also an important process in the global production of this metal.

The occurrence of Nb in nature is about 20 ppm, which is considerably higher when compared with Ta which occurrence is only around 1.7 ppm. As mentioned, niobium and tantalum are usually extracted from minerals such as columbite-tantalites (coltans) and pyrochlores, with a general composition $(Fe,Mn)(Nb,Ta)_2O_6$. More specifically, Nb_2O_5

contents of 78.72 % and 75.12 % can be found in Columbite and Pyrochlore, respectively. Tantalite and Microlite (which belongs to the pyrochlores mineral group) have typical contents of 86.17 % and 83.53 % of Ta_2O_5, correspondingly [8]. The full processing route of these minerals is complex and with many different stages.

Typically, the processing of the tantalum and niobium minerals begins with the crushing and milling of the raw materials, followed by the ore beneficiation which comprises the extraction and separation by several techniques such as desliming, froth flotation, acid leaching, and gravity, magnetic and electrostatic separation. The obtained product (a slurry) is typically called the *ore concentrate* [8,9,12]. The ore concentrates, respectivelly containing around 30 % tantalum oxide and 54 % of niobium oxide, are then processed in a refinery plant where they are separated using either an acid or solvent extraction process, or (in the case of niobium) using aluminothermy reduction or an electric arc furnace to produce ferroniobium [8,9,12].

Cabot Corporation, H.C. Starck GmbH and Ningxia Nonferrous Metals Import & Export Corporation are the world's three largest processors of tantalum concentrates [9]. In 2004, 42 % of world's tantalum was used for the production of solid electrolytic capacitors, produced mainly by AVX and KEMET corporations, which are highly demanded by the electronics industry such as IBM, Sony, Dell, LG and others [8,9]. Tantalum is also very used in the production of superalloys for aviation, military and automotive industry, glass coatings, cutting tools, prosthetics, night vision goggles, global positioning systems (GPS), chemical processing equipment, oil and gas pipelines, and also in the form of different chemical products [9,10].

Niobium, on the other hand, has a much narrower range of final applications. The niobium concentrates are generally processed by the same companies that process tantalum's, but niobium is further processed by many other industries related to production of steels and other types of alloys, such as Nippon Steel or Posco. Around 89 % of world's niobium is used nowadays for the production of high strength low alloys (HSLA) and other types of alloys, which end-use can range between oil and gas pipelines, jet engines and turbine blades, vehicles and ships hulls, cutting tools or superconducting coils. A smaller percentage is used for glass coatings and camera lenses, in the form of niobium oxide, or in other technologies in the form of different compounds (lithium niobate for instance) [9,11]. Figure 1.2 graphically synthesizes the global percentage of tantalum and niobium end-uses.

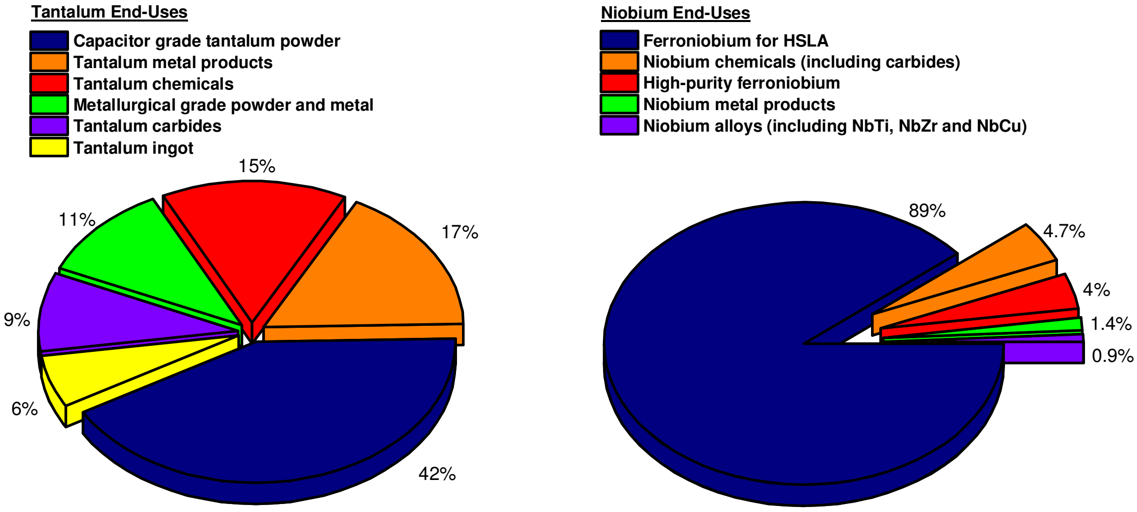

Figure 1.2 – Global percentages of Tantalum and Niobium end-uses in 2004 [8].

Niobium is also very used in jewellery and coin mintage given the ability to be coloured by anodization as illustrated by Figure 1.3.

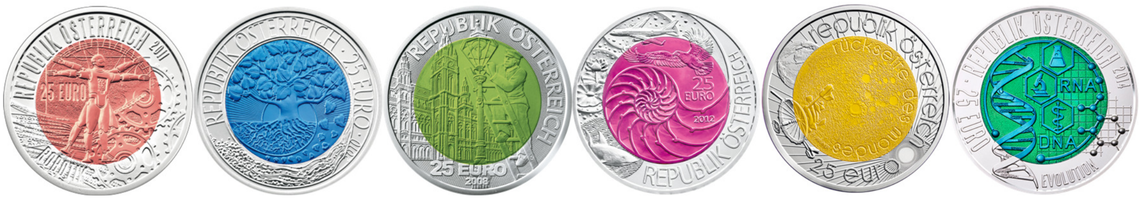

Figure 1.3 - Austrian Mint Silver Niobium coins, with coloured cores obtained by anodization of niobium [13].

The world's largest reserves of Niobium are in Brazil, with more than 90 % (Companhia Brasileira de Metalurgia e Mineração (CBMM) is the main producer), and also in Canada [8–11]. These two countries are also the world's largest producers of this metal, with Brazil producing c.a. 92 % and Canada c.a. 7 % of the global niobium demand [8–11]. However, regarding tantalum, the correspondence between the reserves and the production is not direct. The world's known reserves of tantalum are more widespread across the globe, mainly located in Brazil (~40 %), Australia (~21 %), China and Southeast Asia (~10 %), Russia and Middle East (~10 %) and Central Africa (~10 %). In 2005, around 66 % of world's tantalum was produced in Australia, while ~13 % came from Brazil and ~12 % from Africa. Since then, an increased volume of tantalum entering the market from conflict zone countries (such as Rwanda and Democratic Republic of Congo), lead to a decrease of its price, at first, which by its turn lead to the close of the most important Australian tantalum mines. In 2009, more than 60 % of the world's tantalum was coming from Africa, 22 % from Brazil, and only around 8 % from Australia [8]. Most of the developed countries have been making efforts to limit the importation of conflict tantalum, which has pushed the price of tantalum back up, though it is expected that the Australian mines might resume their production soon in the future [8]. Additionally, the fact that Nb is much more abundant than Ta might justify, in part, the substantial difference of prices between these metals, which are plotted over time in Figure 1.4. It should be noticed that these metals, unlike others, are not openly traded and the contract prices are usually kept confidential between buyer and seller, and it is therefore a very speculative market [8–11].

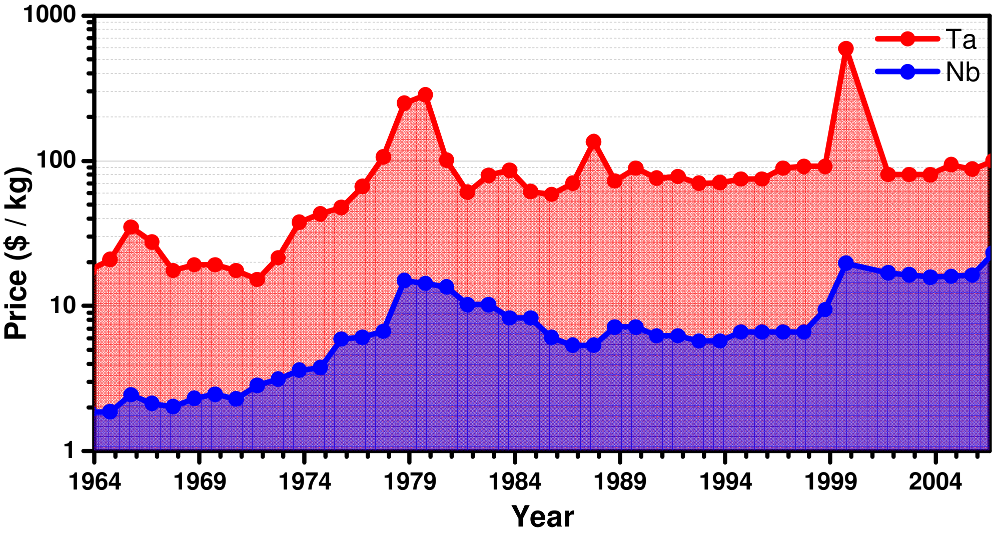

Figure 1.4 – Price of Tantalum and Niobium in US dollars per kg from 1964 to 2007 [14].

It is possible to observe that, along the years, tantalum has been almost 10× more expensive than niobium. Since tantalum is mainly used for the production of capacitors, which are basic components for computers, mobile phones, and basically everything related to digital electronics, is interesting to notice the peak of its price in the year 2000 related to the *dot-com bubble,* driven by speculation of the technological market.

1.2 A New Family of Capacitors

In this context, the interest in niobium and niobium oxides such as NbO and Nb_2O_5 has been gradually increasing due to its potential as an alternative to the use of tantalum oxide in electronic applications, specifically in capacitors [15–33]. In fact, while tantalum leaded and aluminium foil capacitors have been presenting a very small growth in the past years (considered to be a technology in decline), tantalum chips technology is considered to be at its peak, and niobium-based capacitors are considered an emergent technology as the Figure 1.5 illustrates [34].

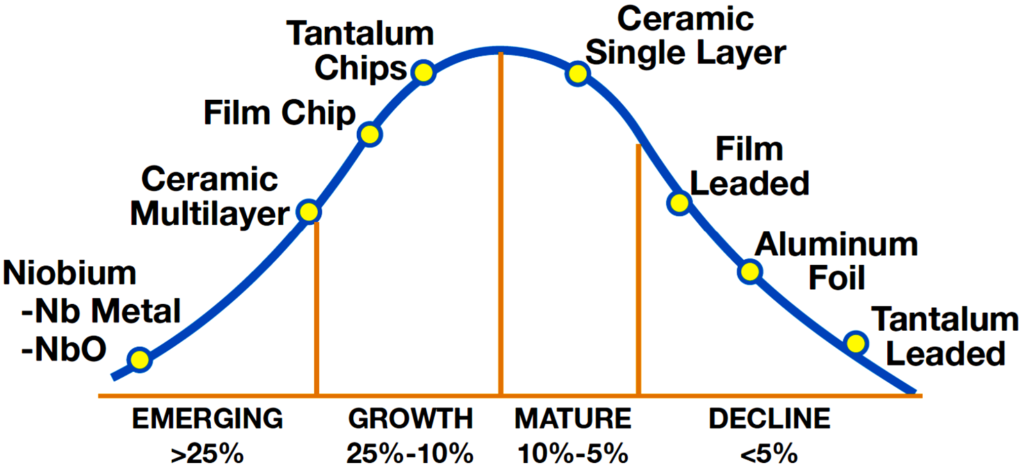

Figure 1.5 - Capacitor technology average annual growth in 2002 [34].

The current tantalum technology for the production of solid electrolytic capacitors is based on the pressing of metallic tantalum powders into a pellet, which grains are oxidized, through an anodization process, to form a thin layer of tantalum pentoxide. In this case, the metallic tantalum is the anode and the tantalum pentoxide the dielectric of the capacitor. The dielectric constant value typically reported for niobium pentoxide, quite superior to the Ta_2O_5 ($\varepsilon'_{Nb_2O_5} = 41$ vs. $\varepsilon'_{Ta_2O_5} = 27$) [31,35], and the fact that Nb and NbO are less dense than Ta ($\rho_{Nb} = 8.57$ g/cm^3 vs. $\rho_{NbO} = 7.3$ g/cm^3 vs $\rho_{Ta} = 16.7$ g/cm^3), thus with higher specific capacitance, are some of the advantages of niobium for such passive electronic device components. These facts, allied to the much lower price of niobium compared with tantalum, have been the main motivations for the industry's research and development of niobium based capacitors.

Already in 1958, a former capacitor manufacturing company called Sprague Electric Co. (founded by Robert C. Sprague, the inventor of the paper capacitor) wrote a patent for the production of solid electrolytic capacitors based on different valve metals, including niobium [15]. A few years later, in 1961, Schwartz *et al.* from Aerovox (a US capacitor manufacturing company still in operation) published a work [16] specifically regarding niobium based solid electrolytic capacitors. The authors found that such niobium capacitors compared favourably to the tantalum equivalents, but had limited operation voltages (only up to 20 V) and short lifetime. In the same year, A. Shtasel and H. T. Knight also reported a study on niobium for electrolytic capacitors, which have shown lower operating voltages and higher leakage currents compared to tantalum, but with improved performance in severe nuclear environment [17].

In 1995, a work reported a study on a conductive polymer as a cathode for high-frequency niobium capacitors, which exhibited enhanced electrical properties when compared to the typical tantalum capacitors with MnO_2 as a cathode [18]. Between 1997 and 1998, Cabot Corporation registered two patents: one claiming the production of electrolytic capacitors based on niobium [20] and other based on nitrided niobium powders [21]. Both patents refer to details about the sintering temperatures, stabilization, anodization process and methods for reducing DC leakage current. During the same period, Pozdeev [19] (affiliated with Vishay, an electronic components manufacturer) reported on the comparison between tantalum and niobium capacitors with an interesting discussion on the failure mechanisms of these components. Pozdeev pointed out that the main problems are related to the dielectric material, where oxygen diffusion leads to local oxygen deficiency thus increasing the conductivity, and also the crystallization of its amorphous phase. The author concluded that if the metallic anode is able to be protected from oxygen saturation and if the oxygen diffusion is suppressed, a stable and reliable niobium-based capacitor can be successfully produced [19].

A few years later, in 2002, Qiu *et al.* [25], from the Cabot Corporation, reported on "The Stabilization of Niobium-based solid electrolyte capacitors". Aware of the difficulties of the previous attempts, the authors tried the stabilization of the dielectric layer, i.e. to avoid oxygen migration to the anode, by two different approaches. The first one consisted on the incorporation of nitrogen in Nb powders of the anode, as previously reported [21], which the authors found to compromise the dielectric constant of the dielectric layer. The second approach consisted in using NbO (instead of Nb) as the anode, combining its metallic electrical characteristics and its ceramic physical properties of high hardness and bulk diffusion sintering behaviour, and thus reducing the oxygen gradient between the dielectric and the anode. The capacitors based on NbO showed good capacitance values, low DC leakage and good durability. Upon annealing, up to 350 ^{o}C, the variation of capacitance for NbO is also much smaller than for Nb capacitors. Furthermore, the authors have shown that the NbO capacitors were much more stable with temperature, requiring at least one order of magnitude more energy to ignite, and a lower burning rate, as Figure 1.6 illustrates [34]. This makes the NbO a promising material for capacitors working at higher temperatures (such as those applied in the automobile industry), and complying with safety regulations that require non-burning components.

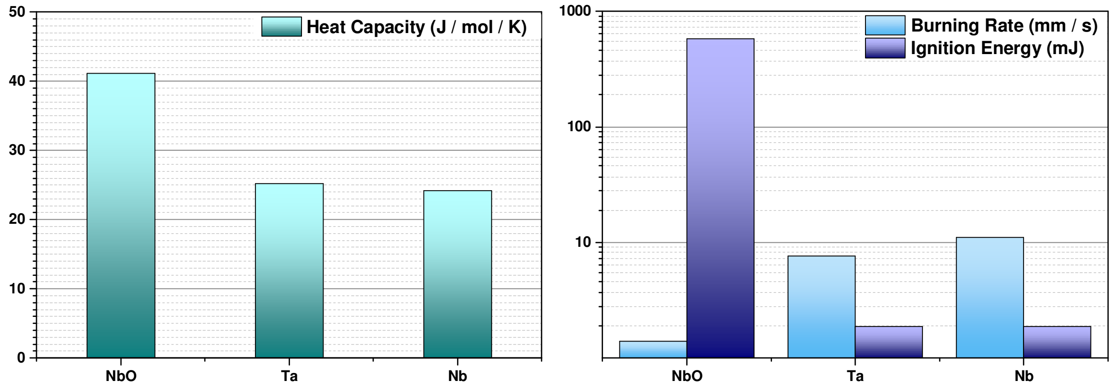

Figure 1.6 - Comparison of the heat capacity, burning rate and ignition energy between NbO, Ta and Nb capacitors [34].

Since 2002, many other works and patents have been published regarding the production of solid electrolytic capacitors based on niobium oxides [26–32]. However, this is still an active area of research because there have been difficulties in achieving a similar performance as tantalum capacitors for the same range of voltages and temperatures. In 2011, it was published a study, worth to mention in this context, on Nb_2O_5 nanostructures which were doped with Ta in order to stabilize a monoclinic structure at lower temperatures, showing improved dielectric properties and stability [33].

The two largest manufacturers of tantalum capacitors in the world are most likely AVX Corporation (a subsidiary of Kyocera) and KEMET Corporation. AVX has already entered the market with niobium-based capacitors, with the OxiCap® series, sold under the patent license from Cabot Corporation. This series is however still limited to a small range of low voltages, not actually being a true alternative to tantalum capacitors. KEMET did not yet reported any niobium based technology. Thus, from 2009 to 2012, KEMET (Évora, Portugal), whose facilities were dedicated to the production of tantalum capacitors, together with the Department of Physics of the University of Aveiro, co-promoted a project for the research and development of capacitors based on niobium oxides to be implemented in their tantalum production line. The work presented in this thesis proceeds the work developed in that project.

Summarizing, one of the main obstacles of the implementation of niobium oxides for the production of capacitors is related to growth of the dielectric, where the sintering temperature and atmosphere are determinant factors in the (in)stability of its electrical properties, strongly influencing the appearance of different phases and structures. Furthermore, these types of oxide matrices often present many stoichiometry problems with lack or excess of oxygen.

A solid electrolytic capacitor, when operating, is commonly subjected to heat produced by the electronics. This, in a niobium oxide capacitor, can easily lead to the diffusion of oxygen from the dielectric (higher oxidation state) to the anode (lower oxidation state), thus creating oxygen vacancies that strongly influence the conductivity of the material. Thus, if a conducting channel is created (originated by the oxygen defects), a high electrical current can flow from the anode to the cathode leading to the dielectric breakdown and consequent definitive damage of the capacitor. Using NbO instead of Nb, knowing that both have a metallic behaviour, for the production of the anodes, can help to overcome many of these oxygen diffusion obstacles that are common when using Nb.

Hence, the objective of this work will pass mainly by the study of the structural, electrical and also the optical properties of different phases and polymorphs of niobium oxides, prepared by different routes.

For this, different approaches will be taken. Regarding the final application as a capacitor, the study of samples prepared by industrial processes, used for tantalum capacitors, with different parameters, have been done. In parallel, fundamental studies on niobium oxides prepared in a laboratory environment and extensive characterization will be helpful to not only better understand the results and further development of the niobium capacitor prepared in industry, but also to contribute in a general way to the knowledge about these materials aiming other possible applications.

1.3 The Niobium Oxides system

In niobium-oxygen system, the niobium element can be found in four different charge states: 0, 2+, 4+ and 5+. Generally, these charge states are related to the phases of metallic Nb and to the NbO, NbO_2 and Nb_2O_5 respectively, as Figure 1.7 synthetically illustrates.

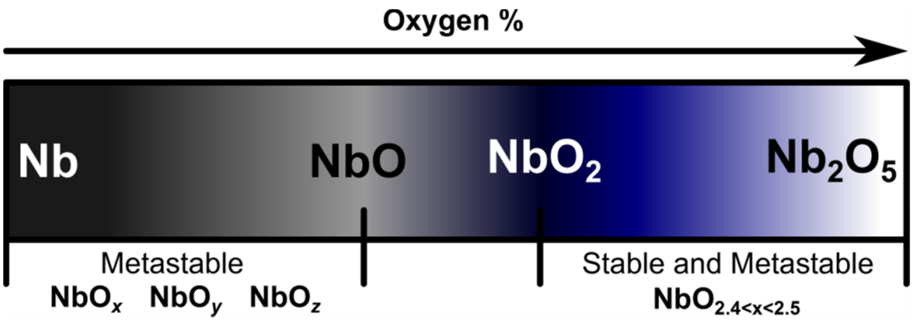

Figure 1.7 - Schematic illustration of the different oxidation states of Niobium.

The special complexity of the niobium oxides system is related to the existence of several stoichiometric and non-stoichiometric phases, some of which are have several polymorphs, some of which are metastable, and the difficulty in synthesizing a single phase, i.e. without mixture of phases or stoichiometry. Controlling, identifying and determining small variations of the stoichiometry is rather difficult in niobium oxides as the structure of these phases may be extremely similar, and also because the precise quantification of oxygen is technically a great challenge. This is probably the major drawback of this system which can present a wide range of interesting physical properties, which are highly dependent on the phase, polymorph and stoichiometry.

Although the first studies in niobium oxides are from Brauer in 1940 [36], and from other authors later in the decade of 1960 [16,37–45], there still has been no consensus in literature concerning the physical properties and the nomenclature of the different niobium oxides phases. The fact that many of the first scientific works on niobium oxides are written in German may partially justify the difficulty of the international scientific community having access to very important information regarding these materials and thus contributing for a better understanding of these materials.

David Bach makes a very good collection and review of both early and recent literature of the niobium oxides system in his PhD thesis (2009) defended at the University of Karlsruhe [46]. However, it is stressed that many doubts about the synthesis, structure and physical properties of niobium oxides still remain [46]. Bach *et al.* [46–51] used electron energy loss spectroscopy (EELS) as a high spatial resolution technique for quantitative analysis of the niobium oxygen ratio and their oxidation state, which is an extremely useful type of information, hardly obtained by any other technique, especially because the properties of niobium oxides highly depend on their stoichiometry.

One of the first works on niobium oxides, by R.P. Elliot in 1960 [52], reports the phase diagram of the niobium–oxygen system. Since then, other phase diagrams have been reported, and one of the most recent is from 1990 by Massalski [53] is illustrated in Figure 1.8. Massalski shows the existence of four thermodynamically stable phases of niobium–oxygen system (Nb, NbO, NbO_2 and Nb_2O_5) with very narrow single-phase fields and negligible deviations from the exact stoichiometry [46,53]. However, one should consider that this phase diagram is incomplete, as it fails to describe the formation of stable non-stoichiometric phases at room temperature (RT) and the formation of different polymorphs, as it will be further mentioned.

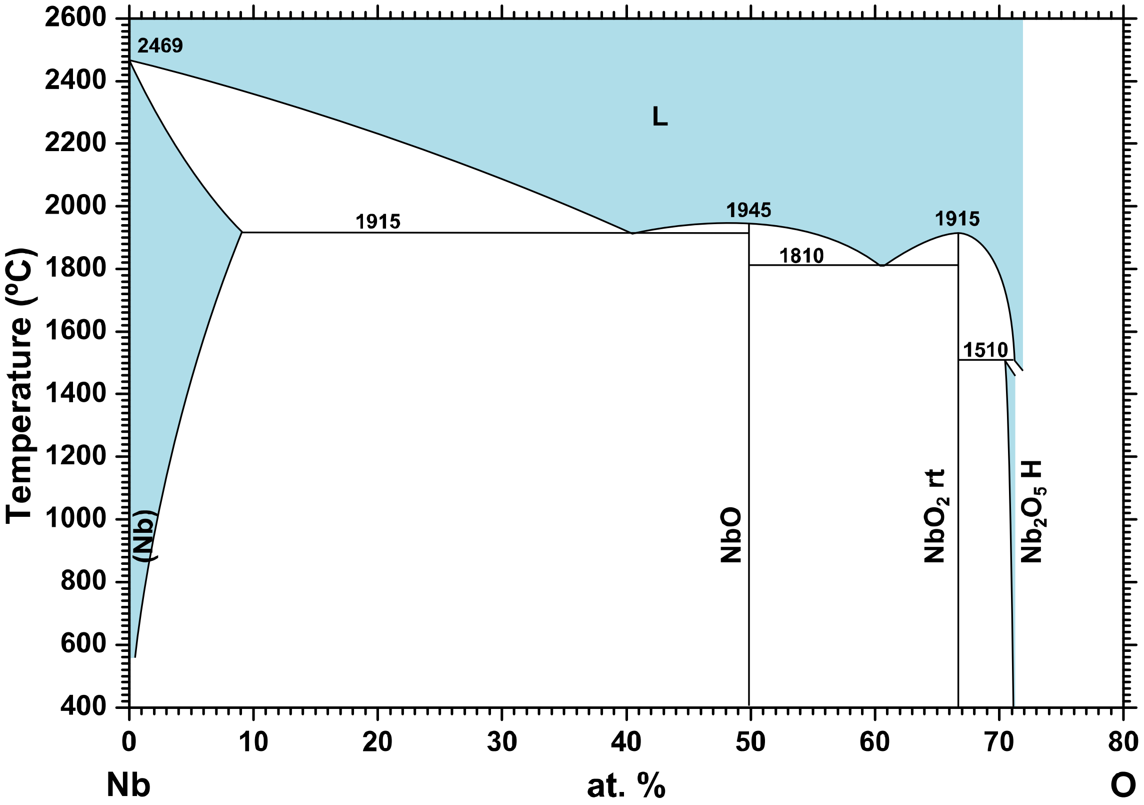

Figure 1.8 - Niobium-Oxygen phase diagram [53].

1.3.1 Nb

Niobium is a metal which crystallizes in a body-centred cubic (bcc) lattice (O_h^9 spatial group) with a density of 8.57 g/cm^3. It is a refractory metal, good thermal conductor, with a melting and boiling points at 2477 ^{o}C and 4744 ^{o}C respectively [46]. It has an electrical resistivity of c.a. 13.4 μΩ·cm at 0 ^{o}C and it is a superconductor below the critical temperature Tc ≃ 9.3 K [46].

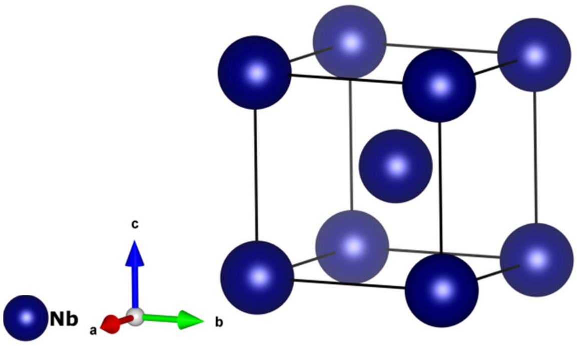

Figure 1.9 – Cubic crystalline structure of metallic Nb.

Niobium can form very stable carbides, nitrides, borides and silicides, possessing high bonding energies. Hence, niobium is used in the stabilization of stainless steels to prevent intergranular corrosion since it helps lowering the content of carbon in the steel. A small niobium amount, from 0.01 to 0.20 wt.%, is typically necessary for the prevention and retardation of austenitic grain growth which leads to higher strength and toughness. These high-strength microalloyed steels are commonly used in pipelines for oil and gas transportation, in high rise buildings construction, in tools steels and heat resisting cast steel auto parts [46]. Niobium is also commonly added to most nickel-based superalloys for application in aircraft engines, land-based turbines for power generation, chemical processing industries and other applications where a special resistance to abrasion and corrosion is required [46].

Pure niobium and niobium-based alloys have a high resistance to corrosion in several environments, which is attributed to a passivating niobium oxide film at the surface [46]. These materials also present high melting points and refractory properties, particularly the niobium-based alloys which can surpass the maximum application temperatures of nickel-based superalloys, thus being well suited for space, nuclear and aircraft applications. Furthermore, niobium-based alloys are typically characterized by low densities and relatively high ductility at RT which is an advantage for cold-working and fabrication of complex structures [46]. However, these alloys typically require a protective coating, such as a silicide, to prevent them from easily oxidizing at high temperatures. Other applications of niobium comprise the fabrication of metal insulator metal (MIM) tunnel diodes and hard tissue replacements (given its good biocompatibility) [46].

Niobium also presents type II superconductivity properties. In fact, from all the chemical elements, metallic niobium is the one with the highest critical temperature ($T_c \simeq 9.3$ K) [46]. Other niobium-based compounds, such as Nb_3Ga or $Nb_{0.75}(GeAl)_{0.25}$, are among the materials with the highest critical temperatures for superconductivity ($T_c = 20.0$ K and $T_c = 20.7$ K respectively). Hence, niobium is frequently used in the fabrication of radio-frequency superconducting cavities (for particle accelerators), production of Josephson tunnel junctions, single photon detectors or superconducting quantum interference devices (SQUIDs) used, for instance, to cover the surface of nearly perfect spheres for the Gravity Probe B mission, which purpose was to measure the space-time curvature near the Earth. However, pure metallic niobium is not suitable for superconducting magnets where high upper critical magnetic fields (B_{c2}) are required. Still, while niobium has a $B_{c2} \simeq 420$ mT (at 0 K), an alloy of NbTi can have a $B_{c2} \simeq 11$ T (at 4.2 K), and the Nb_3Sn compound a $B_{c2} \simeq 25$ T (at 4.2 K). Therefore, it is no surprise that these niobium-based materials are fundamental and used, almost exclusively, in the production of high magnetic fields, required in a series of industrial and scientific applications. One flagrant example is the LHC project, in CERN, that required hundreds of tons of Nb and NbTi alloy.

Niobium is also characterized by its high affinity and binding energy to oxygen [46]. Solubility of oxygen in the niobium matrix, where it occupies octahedral interstitial sites, increases with temperature (ranging from approximately 0.8 at.% at 500 °C and 9.0 at.% at 1915 °C) [53]. Oxygen in solution leads to an increase of the lattice parameter of metallic niobium, acts as an hardener and decreases the ductility of the metal [46]. Oxygen does also affect the electrical properties increasing the resistivity of niobium c.a. 4.1 μΩ·cm per at.% of oxygen, and decreasing the superconductivity transition temperature T_c ~0.93 K per at.% of oxygen [46]. Therefore, and also because defects at the surface may produce heat, high-purity niobium is required for superconductivity applications. It is commonly mentioned in literature the existence of a native oxide layer at the surface of niobium exposed to oxygen [46,54]. In a superconductor, the electromagnetic fields have a penetration depth of c.a. 60 nm, and therefore the existence of an oxide layer at the surface is critical. To obtain highly pure Nb surfaces, i.e. without and oxide layer, the metal is typically heated above 2000 K in ultra-high vacuum conditions [46]. The composition and thickness of such native oxide layer is not yet well clarified, but it is accepted that it depends on the processing parameters and techniques of the metal, crystallographic orientation, and ambient conditions such as oxygen partial pressure, temperature and exposure time [46]. Some authors suggest that this layer is around 5-6 nm thickness with a composition of nearly stoichiometric Nb_2O_5, while other authors report thicknesses as high as 25 nm and/or with different layers of niobium suboxides [46]. More recently (2008), Delheusy *et al.* [55] suggested a three-layer model of NbO, NbO_2 and Nb_2O_5 between the metallic niobium and the oxide surface.

1.3.2 NbO

NbO crystallizes in a face-centred cubic structure, O_h^1 space group, with 3 Nb atoms in the lattice sites 3(c) (0 ½ ½; ½ 0 ½; ½ ½ 0), and 3 O atoms in the lattice sites 3(d) (½ 0 0; 0 ½ 0; 0 0 ½;) [41], where each Nb atom is coordinated to four O atoms in a square planar array, as illustrated in Figure 1.10. Moreover, NbO crystalline structure is a very particular case since it shows 25 % ordered vacancies in both sublattices of Nb and O [46,56]. This is the highest number of point defects among all transition metal monoxides.

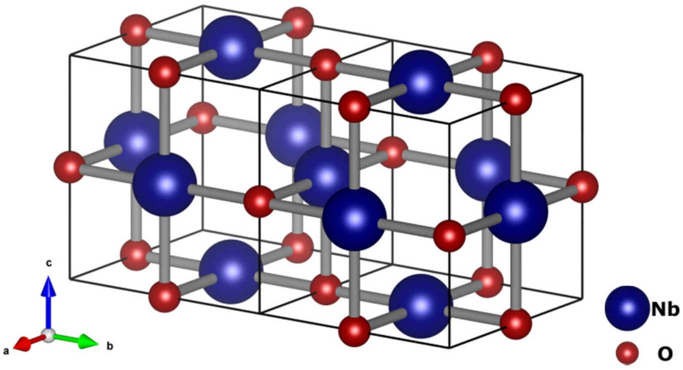

Figure 1.10 – Cubic structure of NbO.

The density of NbO is c.a. 7.3 g/cm^3 and has a melting point at $T_m \simeq 1940\ ^oC$ [46,52]. Niobium monoxide presents a typical metallic behaviour, and is widely regarded as a metal [45,46,56,57], with a resistivity of about 21 μΩ·cm at 25 ^{o}C[45,46,57], decreasing with temperature down to 1.8 μΩ·cm at 4.2 K [57]. Kurmaev *et al.* [56] performed X-Ray fluorescence measurements for different niobium oxides and compared the results of NbO to the band structure calculations of $Nb_{1.0}O_{1.0}$, founding that there were significant differences. Therefore, Kurmaev *et al.* then tried to mimic the NbO structure by performing calculations of the band structure for $Nb_{0.75}O_{0.75}$ in order to make account for the 25 % of vacancies. Given the good correspondence between these calculations and the experimental results, the authors assigned the electrical properties of NbO to the aforementioned vacancies, characteristic of this structure: "*The electronic DOS of* $Nb_{0.75}O_{0.75}$ *is characterised by the formation of additional subbands connected with vacancy states*." [56].

Below the critical temperature, $Tc \simeq 1.38$ K, NbO becomes superconductive [57]. Hulm *et al.* [57] performed electrical measurements and studied the superconductivity of different transition metal monoxides, and found that, in NbO, there is no evidence of negative temperature-coefficient behaviour of the type that was observed in TiO and VO. Furthermore, the authors verified that a small increase of the oxygen ratio (towards NbO_2) would induce a sharp increase of the resistivity. Oppositely, an increase of the niobium ratio (towards metallic Nb) would promote an increase of the critical temperature for superconductivity [57]. The authors attribute this behaviour to a mixed-phase sample with contributions of both NbO and NbO_2 (when the O % is increased), or of both Nb and NbO (when the Nb % is increased).

Niobium monoxide is not used massively in any major technological application. However, the fact that NbO has improved properties, regarding the oxygen diffusion, in comparison with Nb, makes it a suitable candidate to niobium-based solid electrolytic capacitors [25,30,46,58].

1.3.3 NbO_2

The NbO_2 has the Nb element in a 4+ charge state, presents a stoichiometry between NbO and Nb_2O_5, and has a melting point of ~1915 °C [46]. NbO_2 is typically characterized by a dark-blue colour and can be obtained by controlled oxidation of Nb or NbO, or reduction of Nb_2O_5.

Some authors [59,60] have mentioned the existence of a monoclinic crystalline structure of NbO_2, citing the work of Nobuzo Terao [61] as the reference for such phase. In addition, JCPDS card No. 19-0859 does in fact report the X-Ray powder diffraction data of a monoclinic phase of NbO_2, with lattice parameters a = 12.03 Å, b = 14.37 Å, c = 10.36 Å and β = 121.17 °, also referring to the work of Nobuzo Terao [61]. However, in the abstract of the Terao's work (which happens to be the only part accessible), he only mentions a tetragonal phase of NbO_2, among other phases of niobium oxides. It is therefore reasonable to doubt about the true existence of such monoclinic structure, since the work of Terao is the only work reporting, allegedly (as it is not mentioned in the abstract), a fundamental structural study on an NbO_2 monoclinic phase.

Actually, most of the works regarding the NbO_2 phase report a tetragonal phase [46,56,61–63]. At room temperature NbO_2 crystallizes in what can be described as a distorted tetragonal superstructure with a rutile-type sublattice, with a space group C_{4h}^6, and a density c.a. 5.9 g/cm^3 [46,62,64]. This structure, illustrated in Figure 1.11a is characterized by chains of edge-sharing NbO_6 octahedrons which are cross-linked by corner sharing [46,62] where the Nb-O distances in the octahedral are practically the same, c.a. 2.05 Å [62]. Similarly to other rutile structures, in NbO_2 the metal ions tend to pair along the fourfold [001] axis, along the edge-sharing chains, with alternated Nb-Nb distances of 2.80 and 3.20 Å [62,64]. Inherent instabilities of the NbO_6 octahedra and the structure of NbO_2 have been reported [64,65]. This phase of NbO_2 is also characterized as being an n-type semiconductor with a small band gap of 0.5 eV, and an electrical resistivity in the order of 10^4 Ω·cm [46,56,62–64].

It is also known that between 797 and 808 °C, the NbO_2 suffers a reversible second-order phase transition, together with a change of the crystal structure into a regular rutile lattice, illustrated in Figure 1.11b [62–64]. Electrically, this is characterized as being a semiconductor-metal transition, where this high temperature NbO_2 phase shows a typical metallic conductivity. It was reported that above 1100 ºC and a small, but measurable, change of the stoichiometry towards $NbO_{2.006}$, which strongly influence the electrical conductivity of the room temperature phase.

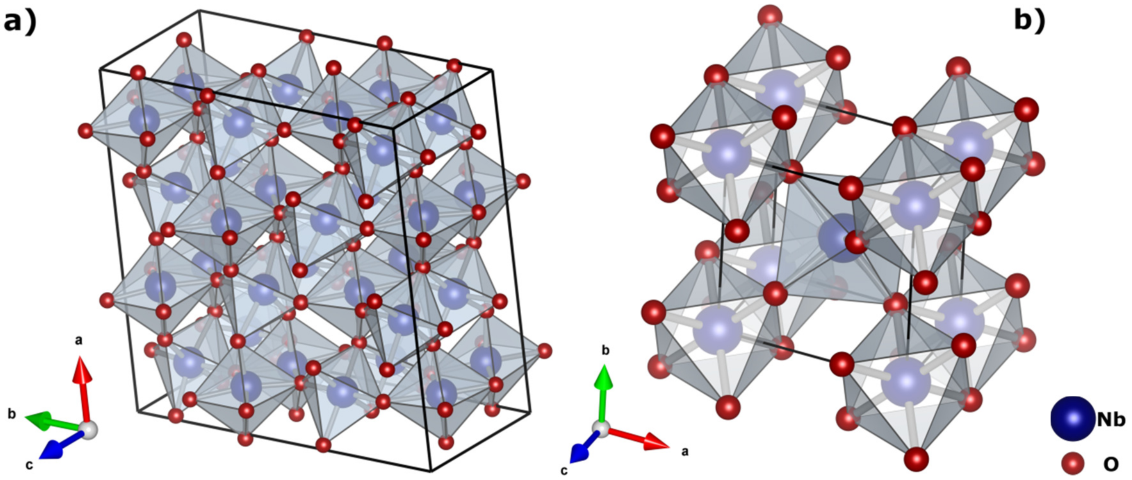

Figure 1.11 - Structure of a) tetragonal and b) rutile NbO_2.

The physical properties of NbO_2, namely the optical and dielectric properties, were not yet extensively studied. One of the few works, dated from 2004 by Zhao *et al.* [63], reports the optical and dielectric properties of nanostructured NbO_2 (in the form of nanoslices), synthesized by thermal deposition, using a metallic niobium wire in a low vacuum, deposited as a thin film on a Si substrate. In this work, the authors report for the first time the Raman spectrum of NbO_2, showing at least 12 active modes with energies of 139, 170, 247, 333, 343, 405, 436, 463, 580, 631, 699 and 815 cm^{-1} [63]. Furthermore, the photoluminescence analysis of the NbO_2 nanoslices, under 512 nm laser excitation and at room temperature, revealed two emission bands centred at 700 nm (1.77 eV) and 825 nm (1.50 eV). The origin and corresponding mechanism for the observed luminescence emissions were not clarified, but it was suggested that, in analogy with other metal dioxides, they may be attribute to intraionic Nb^{4+} d_{xy}-d_{yz} band transitions [63]. The dielectric characterization performed by Zhao *et al.*, between 1 kHz and 10 MHz, revealed interesting properties of the NbO_2 nanostructures. It was observed that the relative dielectric constant of NbO_2 remains almost constant, c.a. 10, in the measured frequency range, and with low dielectric losses (< 1%) for the same frequency range [63]. This type of dielectric characteristics on nanostructures, allied to the simplicity of fabrication, may be quite attractive for the production of MOS devices, as suggested by the authors [63].

More recently, NbO_2 has been studied regarding other technological applications, such as impedimetric biosensors using biofunctionalized Nb/NbO_2 electrodes [66,67]. Moreover, Sasaki *et al.* [68] took advantage of the good chemical stability of NbO_2 to produce highly efficient electrocatalysts of Pt/NbO_2/C nanostructures for oxygen-reduction reactions for application in proton exchange membrane fuel cells. In 2012 Lee *et al.* [67] reported the synthesis of NbO_2 nanowires by chemical vapour transport method which can further enhance the potentiality of this material for such technological applications.

1.3.4 Nb_2O_5

Niobium pentoxide (Nb_2O_5) is the most thermodynamically stable state of the niobium-oxygen system. With an charge state of 5+ in Nb_2O_5, the electronic structure of the Nb atom is [Kr]$4d^0$, which means that all the 4*d* electrons are bonded to the O 2*p*-band, thus justifying the fact that Nb_2O_5 has a much lower electrical conductivity than the other niobium oxides [46]. Nb_2O_5 can occur in the amorphous state or in one of many different crystalline polymorphs. Generally, all the Nb_2O_5 polymorphs have a white colour (in the form of powders) or transparent (in single-crystals). However, most of the physical properties of Nb_2O_5 depend on its polymorph and on the used synthesis parameters and technique [42,46,69–73].

The complexity, confusion and contradictions regarding the niobium oxides system are old and still prevail up to the present. In 1966, Schäfer *et al.* published a work entitled "The modifications of Niobium Pentoxide" [42], where it was stated that "*The abundance of observations makes it desirable to subject the available material* [niobium pentoxide] *to a critical review and classification, and thus simultaneously to create a basis for further investigations*". Already then, there were many different phases of niobium oxides with different nomenclatures, and there was, therefore, the need of clarifying, organizing and compiling all the existent information. Some of the Nb_2O_5 polymorphs were classified with a sequence of Greek letters as it is common in well-known systems. However, since there was not yet a well-established knowledge of all polymorphs, Schäfer *et al.* decided to use neutral symbols following, and extending, the same type of classification as Brauer's [36]. Thus, some polymorphs were classified based on the temperature they were obtained: TT, T, M and H (from the German Tief-Tief, Tief, Medium and Hoch, meaning low-low, low, medium and high), while other polymorphs were named after the shape of the particles B, N and R (from the German Blätter, Nadeln and Prismen, meaning leaves/plates, needles and prisms). While Schäfer *et al.* [42] were able to match some of the same polymorphs reported by different authors, there were other niobium pentoxide modifications, such as the *ε*, *I-high* and *II*, that they were not able to reproduce and study, suggesting the possibility of these phases to be metastable and/or non-stoichiometric.

From what it is possible to assess from current literature, the opinion shared in this work is that not all Nb_2O_5 polymorphs are yet well known and studied, what justifies the choice of following the nomenclature suggested and reported by Schäfer *et al.* [42], also followed by some authors. There are however other authors that misuse this nomenclature by choosing the letter according to the crystalline structure, e.g. T-, H-, O- and M-Nb_2O_5, respectively standing for Tetragonal, Hexagonal, Orthorhombic and Monoclinic structures of niobium pentoxide [74,75], which can be confusing and misleading.

The Nb_2O_5 phase can exist in an amorphous state, but it may crystallize in several kinds of polymorphs with different physical properties: T (D_{2h}^9, orthorhombic), B (C_{2h}^6, monoclinic), H (C_{2h}^1, monoclinic), N (C_{2h}^3, monoclinic), Z (C_2^1, monoclinic), R (C_{2h}^3, monoclinic), M (D_{4h}^{17}, tetragonal), P (D_4^{10}, tetragonal) and also TT (pseudohexagonal or monoclinic) [22,42,46,70]. The TT-Nb_2O_5 polymorph can be interpreted as a less developed phase of the T- polymorph, which is only stabilized by impurities, such as OH^- or Cl^-, or vacancies [47,70,76]. Among all the Nb_2O_5 polymorphs, and niobium oxides in general, the H- phase is thermodynamically the most stable. The H-Nb_2O_5 is therefore one of the most common, and probably the most studied, niobium pentoxide polymorph. A lot more of metastable Nb_2O_5 modifications were reported, but not extensively studied [42,46,77–79].

Generally, the structures of niobium pentoxides are based on NbO_6 octahedra which may be more or less distorted depending on the type of linkage between the octahedra. Most of Nb_2O_5 polymorphs structures are described by the combination of one or both of these types of links between octahedra that can happen by corner-sharing or by edge-sharing. Particularly, the structures characterized by perpendicular edge-sharing octahedra are arranged in such a way that a zigzag chain is produced. This type of chains, linked in parallel by corner-sharing, are very common as an additional constructional element in many forms of niobium pentoxide but also in related compounds [42]. Actually, the fact that there are several possible combinations of octahedral linkages that can produce an O/Nb ratio of 2.5, is pointed as the reason for the multiplicity of Nb_2O_5 structures [42]. Furthermore, the principle of crystallographic shear formed by the existence of different types of linkage regions (but preserving the cation coordination), but also the formation of point defects, can explain the possibility of variations of stoichiometry in relation to Nb_2O_5, giving rise to the formation of non-stoichiometric niobium oxide phases [42,46,80–84]. In a very recent paper, Valencia-Balvín *et al.* [70] report first-principle studies on the energetics and phase stability of the several Nb_2O_5 polymorphs under pressure, and also perform a very good and detailed description of their crystalline structures.

Additionally, the structural characteristics of the different niobium oxides can vary significantly with the synthesis technique [42,54,69,70]. This is clearly evidenced by Reznichenko *et al.* [69] who make a very complete list of numerous works in the literature with different production methods of several stable and metastable Nb_2O_5 polymorphs, their structural parameters and different designations or nomenclatures. The most reported techniques used to prepare different Nb_2O_5 polymorphs involve the oxidation of niobium oxides of lower stoichiometry, promoted by heating in air, or by heat treating other Nb_2O_5 phases. Other methods, such as heating sulphate or chloride niobic acid, anodization, chemical transport, sol-gel, special hydrothermal conditions, or high temperatures and/or pressure, are also commonly used in the production of different Nb_2O_5 polymorphs [42,46,69,71–73,76]. Generally, the temperature and starting material used in the synthesis method will be the most determinant parameters.

One interesting behaviour that is observed in the synthesis of the niobium oxides, is the "*memory of solids*", as it was referred by Schäfer *et al.* [42]. This behaviour is characterized by how the same Nb_2O_5 phase will behave differently under the same heat treatment, depending on the original preparation method, i.e. similar crystalline samples undistinguishable by X-Ray diffraction (XRD) measurements will "remember" their synthesis method by changing to different phases under the same heat treatment [42]. While this behaviour is not yet well clarified, it is suggested that it might be related to the incorporation of different impurities or specific structural defects, that are dependent on the original synthesis route [42].

The H-Nb_2O_5 phase is rather easy to be obtained. Starting from any Nb_2O_5 polymorph, or a lower stoichiometric oxide (such as NbO_2, NbO or even the metallic Nb), the H-Nb_2O_5 is obtained by a treatment at high temperatures (>1000 ^{o}C) in air [42,46]. Heating any type of niobic acid precipitates (sulphate, chloride, bromide, iodide or fluoride) at high temperatures will also produce this phase [42]. The production of the H phase can also be achieved under hydrothermal conditions and from a melt (if seeded with the same phase) [42]. The monoclinic structure of the H-Nb_2O_5, which contains 14 formula units per unit cell, is illustrated by Figure 1.12. The Nb atoms occupy the Wyckoff positions 1*g*, 2*i* (with half occupation), six 2*n* and seven 2*m*, while the O atoms occupy the 1*f*, 1*h*, sixteen 2*n* and eighteen 2*m* positions. This structure is described by layered 3×4 and 3×5 blocks of corner-sharing octahedra. These blocks are connected by edge-sharing octahedra, with a partly but systematic tetrahedral site, occupied by one Nb atom per unit cell [46,70].

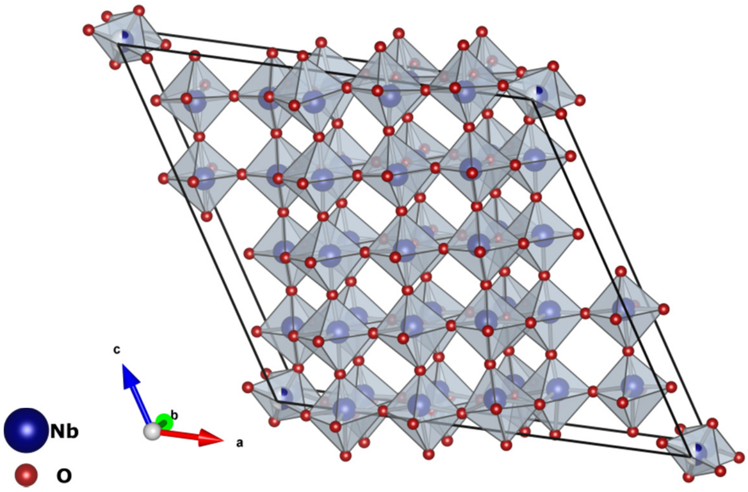

Figure 1.12 - Monoclinic structure of the H-Nb_2O_5 phase.

The B-Nb_2O_5 phase can be produced by chemical transport of Nb_2O_5 or $NbOCl_3$ at temperatures between 750 and 850 °C. However, it was observed that using this method other polymorphs are produced in addition, e.g. N and P-Nb_2O_5 [42]. It is possible to obtain an single phase sample of the B phase from molten Nb_2O_5 using a selected crystalline seed of the same phase [42]. Alternatively, it was reported that by heating between 500 and 800 °C metallic Nb or a lower stoichiometry niobium oxide (NbO or NbO_2 for instance), as well as the TT or the T-Nb_2O_5 polymorph, is a good method for producing the B phase [42]. The monoclinic structure of this polymorph, described by edge-sharing distorted NbO_6 octahedra blocks (each block linked in zigzag by corner-sharing) is illustrated by Figure 1.13. This structure contains 4 formula units per unit cell, with Nb atoms located at the Wyckoff position 8*f* and the O atoms at 4*e* and two 8*f* positions [70].

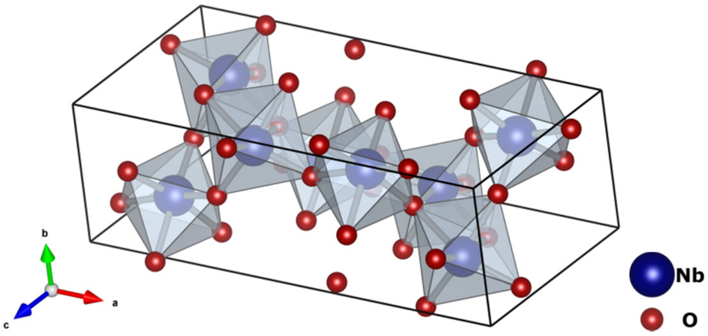

Figure 1.13 - Monoclinic structure of the B-Nb_2O_5 phase.

The N-Nb_2O_5 phase can be found, as mentioned, together with the M phase when synthesized from niobic acids. It can also be prepared by chemical transport of Nb_2O_5 at ~840 °C, but only in the presence of small amounts of fluoride, producing additional phases like the H and B polymorphs [42]. The N polymorph can also be produced under hydrothermal conditions where the OH^- groups may play the same role as the F^- [42]. It is also possible to prepare this polymorph by thermal decomposition of NbO_2F, at c.a. 1000 oC in high vacuum, though it is a very sensible method given that the formation of Nb_3O_7F or H-Nb_2O_5 can easily occur if the time and temperature are not optimal [42]. The monoclinic structure of the N-Nb_2O_5, illustrated by Figure 1.14, is described by 4×4 blocks of corner-sharing octahedra, where the blocks are interlinked by edge-sharing. The Nb and O atoms occupy, respectively, eight and twenty 4*i* Wyckoff positions [70].

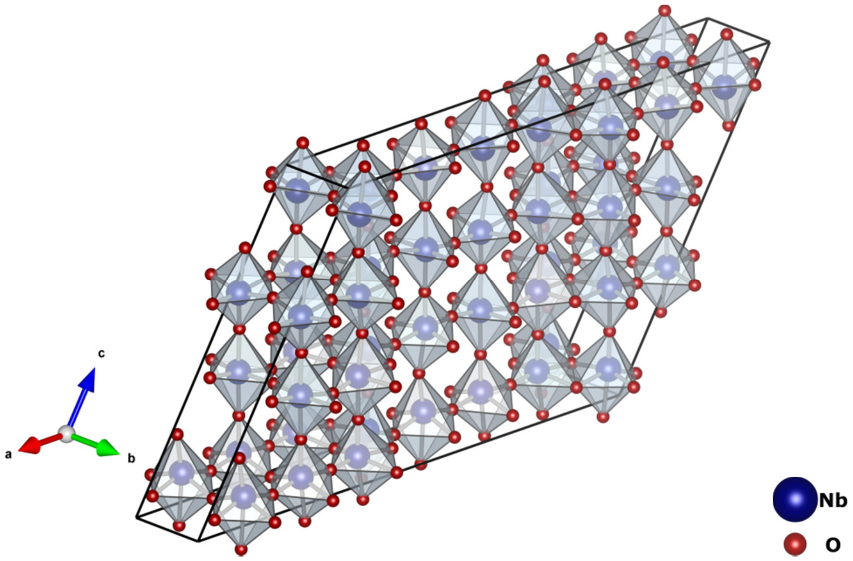

Figure 1.14 - Monoclinic structure of the N-Nb_2O_5 phase.

The M-Nb_2O_5 phase is usually formed by heating sulphate or chloride niobic acid between 900 and 950 °C for some hours (or even at higher temperatures but for shorter times). This phase can also be detected on oxidized Nb and Nb alloys when heat treated at 1000 °C in air [42]. Nevertheless, these methods also produce additional polymorphs, especially the N phase, hampering the preparation of a single phase sample of M-Nb_2O_5 [42]. Very recently, Dhawan *et al.* [85] were able to prepare spherical quantum dots of M-Nb_2O_5, by physical vapour deposition, with controllable sizes between 1 and 20 nm. For quantum dots with diameters below 5 nm, quantum confinement effects were observed [85]. The tetragonal structure of the M phase is illustrated in Figure 1.15. The unit cell contains 16 formula units, where the Nb atoms occupy two 8*i*, two 8*h* and three 16*l* Wyckoff positions, and the O atoms at two 8*j*, two 8*h* and three16*l*. The structure can be described by 4×4 blocks of corner-sharing octahedra, with adjacent blocks linked by octahedra edges [70].

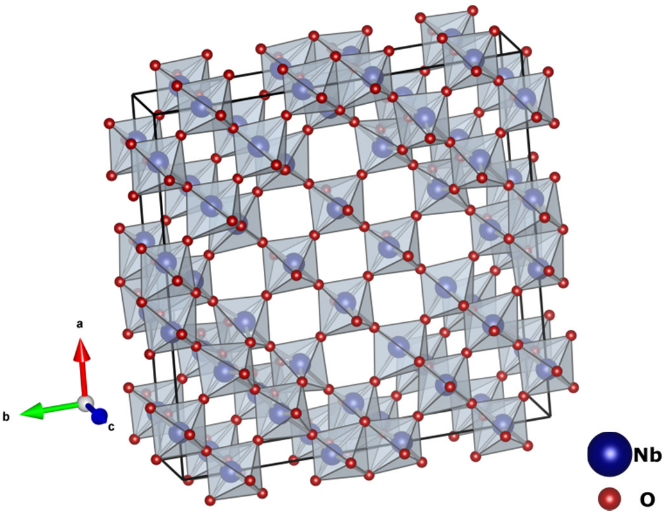

Figure 1.15 - Tetragonal structure of the M-Nb_2O_5 phase.

The P-Nb_2O_5 phase can be obtained by chemical transport, either in the chloride, bromide or iodide systems, at a temperature c.a 750 °C [42]. It was found that the presence of small amounts of water was fundamental to promote the growth of the P phase [42]. Alternatively, the P-Nb_2O_5 can be formed by very slow thermal decomposition of NbO_2F [42]. The idealized structure of the P polymorph, illustrated in Figure 1.16 (courtesy of Professor Osorio-Guillén from the Physics Institute of the University of Antioquia, Colombia), contains 4 formula units per unit cell where the Nb atoms occupy the Wyckoff position 8*c* while the O atoms occupy a 4*i* and two 8*c* positions [70]. The structure is composed by distorted octahedra organized in blocks of two edges-sharing, where the blocks are linked by corner-sharing [70].

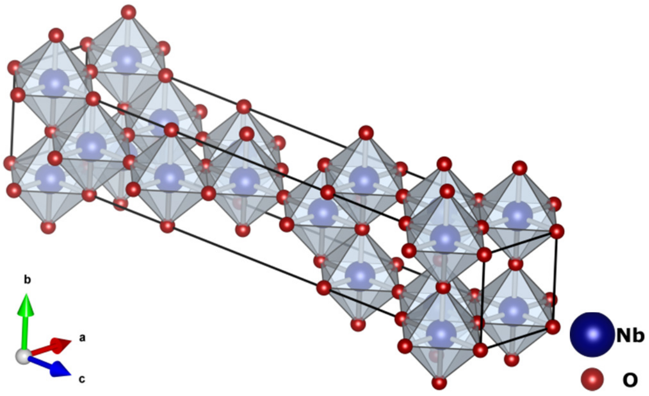

Figure 1.16 – Tetragonal structure of the P-Nb_2O_5 phase.

The R-Nb_2O_5 phase was first reported by Gruehn in 1966 [77]. It is not easy to find works which have identified this phase, though this polymorph is commonly referred in literature [70,86,87]. Originally, Gruehn obtained the R phase by chemical transport of Nb_2O_5 at temperatures between 600 and 800 °C. Using the same method with chloride niobic acid also produced this phase. Additionally, Gruehn said that the R-Nb_2O_5 was also found in the product of $NbOCl_3$ hydrolysis heated at 275 °C [77]. These methods, however, did not produce a single phase material, but constantly a mixture of R-Nb_2O_5 with other polymorphs (e.g. P or TT) [77]. The R phase has one of most simple structures among niobium pentoxides, illustrated in Figure 1.17. This monoclinic structure has two formula units per unit cell with the Nb atoms occupying the Wyckoff positions 4*i* and the O atoms the 2*a* and 4*i* [70]. This structure is described by distorted octahedra linked by edge-sharing, forming zigzag chains along the *b* direction which are interlinked by corner-sharing [77].

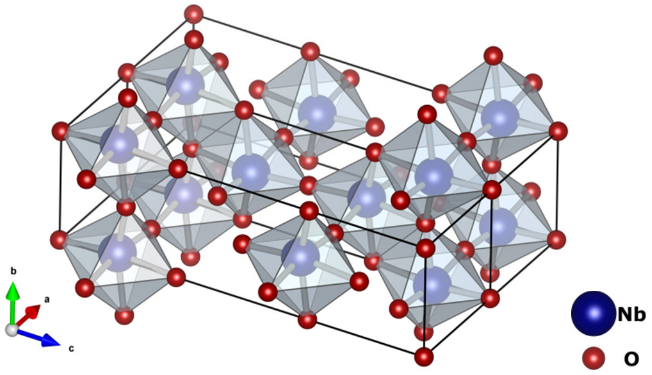

Figure 1.17 - Monoclinic structure of the R-Nb_2O_5 phase.

The Z-Nb_2O_5 phase was first reported by Zibrov *et al.* in 1998 [88]. This modification was identified, together with the B polymorph, after heat treating the H-Nb_2O_5 phase, between 800 and 1100 °C, in a high-pressure chamber at 8.0 GPa during 1-10 minutes [88]. The structure was determined and refined by the Rietveld method from the XRD measurements, and is illustrated is Figure 1.18. It was found that this monoclinic structure is one of the few niobium pentoxides without sixfold coordinated niobium, presenting mono-capped trigonal prisms with sevenfold coordination Nb atoms occupying the Wyckoff position 4*c*, while the O atoms occupy a 2*b* two 4*c* positions [70,88].

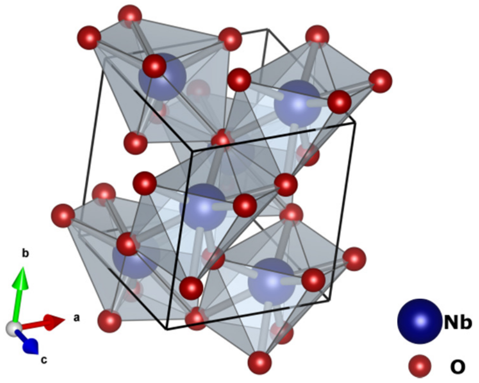

Figure 1.18 - Monoclinic structure of the Z-Nb_2O_5 phase.

The T-Nb_2O_5 phase is one of the most commonly studied niobium pentoxide phases and one of the first to be reported (originally by Brauer in 1941 [36]). This phase can be obtained by heating sulphate of chloride niobic acid between 600 and 800 ºC. Heating the TT-Nb_2O_5 polymorph, a lower niobium oxide (NbO_2 or NbO), or metallic Nb, to the same range of temperatures (600-800 ºC) does also produce the T phase [42]. Additionally, this polymorph can be obtained under hydrothermal conditions (starting from amorphous niobic acid), by quenching Nb_2O_5 into supercooled melts, or even by chemical transport of Nb_2O_5 [42]. The orthorhombic structure of the T phase, illustrated in Figure 1.19, is not simple and contains 8.4 unit formulas per unit cell. Nb atoms with six and sevenfold coordination produce distorted octahedra and pentagonal bipyramids, respectively. These polyhedra are linked both corner and edge-sharing along the [001] direction but are only connected by corner-sharing along the *c* axis [70]. There are 16 Nb atoms, distributed in parallel with the (001) plane and placed at four 8*i* Wyckoff positions with half-occupancy, while 0.8 Nb atoms are distributed in three 4*g* positions with 0.08, 0.08 and 0.04 occupancies [70]. The occupancy of the Nb atoms is represented in Figure 1.19 by the percentage of blue that each atom is coloured. The O atoms occupy one 2*b*, four 4*g* and six 4*h* Wyckoff positions [70].

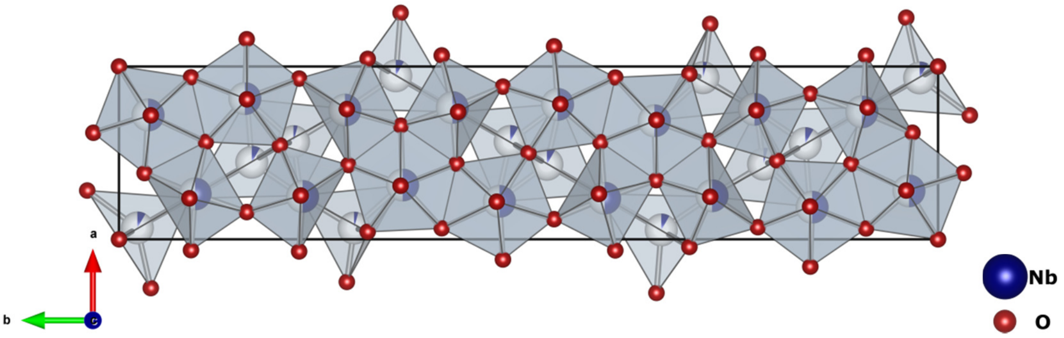

Figure 1.19 - Orthorhombic structure of the T-Nb_2O_5 phase.

Finally, the TT-Nb_2O_5 phase is also frequently reported in literature, and is commonly referred as a less crystalline form of the T phase, stabilized by vacancies or impurities, such as OH^- or Cl^- [46,70,76]. It is reported that the TT-Nb_2O_5 can be obtained by heating sulphate or chloride niobic acid to temperatures c.a. 500 °C, or by promoting the oxidation of lower niobium oxides by heating between 320 and 350 °C in air. In both methods, amorphous Nb_2O_5 is observed as an intermediate. This phase is also observed in oxidized Nb alloys at higher temperatures (~800 °C), and as one of the products of the reaction between NbO_2 and Cl_2 carried out between 270 and 320 °C. It is reported that the TT-Nb_2O_5 can crystallize in either monoclinic or pseudo-hexagonal structure [46,70,86,87,89], but the unit cell was never fully refined. It is affirmed, nevertheless, that the structure of the T phase is characterized by the presence of distorted octahedra, pentagonal and hexagonal bipyramids, i.e. NbO_6, NbO_7 and NbO_8 polyhedra [70,89], which are reported to be the same structural units as the amorphous phase of Nb_2O_5 [47,90].

A list of these Nb_2O_5 polymorphs (and other niobium oxides), with the respective crystal lattice parameters and space groups, is presented in Table 1.1.

Regarding the physical properties of niobium pentoxides, one should expect that, depending on the Nb_2O_5 polymorph, some of the properties may be different. In fact, not only the physical properties depend on the polymorph, but also on the synthesis method [42,47,69,71,91]. Because of this, it is common to find a wide range of values for some properties reported for Nb_2O_5.

Generally, independently on the polymorph, Nb_2O_5 is considered a wide band gap semiconductor (or insulator, depending on the classification criteria) [46,56,71].

Filho *et al.* performed photoelectrochemical studies and measured the band gap of thin films of amorphous niobium oxides, which was consistently around 3.4 eV, in agreement with results of previous works [92]. The authors also measured a high quantum yield on certain niobium oxides films and discussed the charge transfer model between this material and an electrolyte. Schultze & Lorengel [93] report niobium pentoxide passive films with band gap energies between 3.4 to 5.3 eV. Brayner & Bozon-Verduraz [76] report a nearly constant band gap of 3.4 eV for niobium pentoxide, in the amorphous, TT, T and H phases. However, the authors also report that, using a soft route method they were able to produce nanoparticles, with sizes between 40 nm and 4.5 nm, which band gap varied between 3.4 and 4.2 eV, respectively [76]. This variation was assigned to quantum confinement effects. It was also suggested that the local coordination of the Nb atoms can be a determinant factor in the band gap of niobium pentoxides and other niobates [76].

Additionally, it was reported that Nb_2O_5 particles heat treated at low temperatures (around 400 ºC) presented a brownish-white colour, turning into white after being heated, in air, to temperatures higher than 600 ºC (the characteristic colour of niobium pentoxide), which was assigned to oxygen vacancies originated during the synthesis process and respective vacancy filling with increasing temperature [76]. Soares *et al.* [71] reported about the effect of the processing method on the optical and electrical properties of niobium pentoxides. A band gap of c.a. 3.0 eV for Nb_2O_5 single crystals (H phase) at room temperature, increasing 100 meV when cooled down to 14 K, was observed. Additionally, photoconductivity measurements revealed identical band gap values for polycrystalline samples of H-Nb_2O_5, while for polycrystalline T-Nb_2O_5 two photoconductivity peaks at 3.4 and 4.7 eV were respectively assigned to the fundamental absorption edge and to a transition from the conduction band to a higher energy band structure of this phase [71]. Very recently, Dhawan *et al.* [85] observed, through optical absorption measurements, a variation of the band gap from 4.15 to 3.36 eV in M-Nb_2O_5 spherical quantum dots between 1 to 20 nm in diameter, respectively. While such variation was assigned to quantum confinement effects, it was only detected in quantum dots with less than 5 nm in diameter. For bigger sizes the band gap was nearly constant, therefore indicating that the exciton Bohr radius in the M-Nb_2O_5 phase should be c.a. 5 nm. Additionally, a small effective mass of the exciton $\mu \cong 0.532$ was reported [85].

It is occasionally stated that Nb_2O_5 presents n-type conductivity [70,91], but in fact this type of conductivity was reported, and it is today strongly accepted, as being associated to small stoichiometry deviations [46]. Nevertheless, reported values for conductivity of Nb_2O_5 are wide-ranging and inconsistent. For amorphous Nb_2O_5, Fischer *et al.* [94] reported electrical conductivities of 10^{-11} S/cm, while Cavigliasso *et al.* [95] reported 10^{-13} - 9×10^{-13} S/cm, and Macek and Orel [96] reported conductivities in the order of 10^{-12} - 10^{-11} S/cm, all at room temperature. Regarding crystalline Nb_2O_5 samples, Soares *et al.* [71] report conductivity values, at room temperature, that range between 3.7×10^{-10} S/cm (for the T phase) and 7.6×10^{-7} S/cm (for the H phase). Graça *et al.* [73], prepared polycrystalline Nb_2O_5 samples by the sol-gel method and observed conductivities ranging from 10^{-6} S/cm (for the H phase) to 10^{-13} S/cm (for the T phase). Schäfer *et al.* [97], by its turn, reported a conductivity of 3×10^{-6} S/cm is reported for the H-Nb_2O_5 phase. While all these results are in fact inconsistent, it appears that the H phase is often reported to be more conductive than other stoichiometric niobium pentoxides.

The reported values for the dielectric constant of the Nb_2O_5 are not consistent as well. For amorphous Nb_2O_5 films formed by anodization, depending on the forming electrolyte

Cavigliasso *et al.* [95] report dielectric constants between 49 and 120, while Schultze and Lorengel [93] report values between 41 and 46. For the T-Nb_2O_5, there are reported dielectric constants between 40 to 200 depending on the synthesis method and orientation [46,71,73]. For the H phase, values between 35 and 170 have been reported [46,71,73]. However, in many works, is not clear at which frequency and temperature these values are referring to. Despite this inconsistency, it is typically stated [31,47,98] that the dielectric constant of niobium pentoxide is 41, when comparing with other materials for the purpose of dielectric applications.

In fact, besides the reported potential [25,47,94,98] for the production of solid electrolytic capacitors explored in this work, as previously mentioned, the niobium pentoxides possess a wide range of interesting properties which makes this system suitable for many different applications. The high dielectric constant makes Nb_2O_5 an interesting material for complementary metal-oxide-semiconductor (CMOS) devices, or MIM tunnel diodes, or MIM capacitors [46,99]. Nb_2O_5 is also commonly reported for its photo and electrochromic properties [96,100–107] being possible to change the colour of thin films by applying a voltage. It has also been used as an electrode for dye-sensitized solar-cells (DSSCs) as an alternative to, or together with, TiO_2 [75,100,108,109]. Another active topic of research regarding the niobium pentoxides is their application as a catalyst [110]. Given its high catalytic activity, selectivity at low temperatures and stability, specially of amorphous hydrated $Nb_2O_5{\cdot}nH_2O$, it has been used to catalyse different types of reactions such as esterification, hydrolysis, dehydration, condensation or alkylation [46,90,110]. It has also been reported the use of niobium pentoxide for catalyst for the hydrogen storage [111]. The application of Nb_2O_5 in lithium batteries [74,100], humidity sensors [112], electrochemical biosensors [113], and as a biomaterial (given its chemical stability and low cytotoxicity) [114–116] have been reported. The incorporation of Nb_2O_5 in different glass systems [117–121] has been explored essentially for their interesting non-linear optical properties. The production of rare-earth doped Nb_2O_5 thin films for optical waveguides and amplifiers have also been recently reported [122]. The combination of rare-earths and niobium oxides systems will be further explored in section 1.4.3 regarding the rare-earth orthoniobates, which optical and electrical will be succinctly studied in this work (chapter 7). Niobium pentoxide also finds applications as hard coatings for optical glasses and lenses by taking advantage of its low optical absorption, high refractive index, chemical and thermal stability and mechanical resistance [46,123]. A very recent and promising application of Nb_2O_5, based on the resistive switching behaviour reported in niobium oxides in 1965 by Hiatt and Hickmott [38], is the application as resistive random access memories (ReRAM). This type of application and working principle fits the concept of a passive electronic component called *memristor*, which existence was first suggested in 1971 by Chua [124] and proved to exist only in 2008 by IBM Labs using TiO_2 [125]. The memristor is considered to be a fourth basic circuit element in electronics, along with the concept of resistor, capacitor and inductor, and is defined by the dependence of its resistance on the history (i.e. integral over time) of the current that passed through it. This is currently an active and fast-growing area of research [126–134], with many related works based on niobium oxides [135–143]. The topic of niobium oxide based memristors will be further explored in the last chapter of this thesis regarding the suggestions of future work.

Very recently, only a few months before the end of this work, a very good review paper was published by Rani *et al.* [144] regarding the fundamental properties, synthesis methods and recent applications of niobium pentoxides. Such work corroborates everything that was aforementioned, such as the inconsistencies on the identification of the Nb_2O_5 polymorphs, their wide range of applications and also stoichiometry issues.

1.3.5 Non-Stoichiometric Niobium Oxides

It is known that crystallographic shear and point defects are the most common types of defects that produce/accommodate stoichiometry changes in certain metal oxides (such as TiO_2) [80,81,145] but which are especially easy to occur in niobium oxides [82–84,146]. However, point defects cannot explain high variations of stoichiometry since their concentration in a crystal lattice is rather limited (usually not exceeding 10^{-4}) [82]. Crystallographic shear on the other side, leads to formation of planes where the metal oxide octahedra changed their linkage (e.g. from corner to edge-sharing) thus accommodating large oxygen deficiencies keeping the metal ion coordination [80,82]. In addition, the formation of such ordered defects can lead to the formation of different phases of the metal oxide. Citing Mrowec [81], "[…] *the mutual interaction between point defects results in formation of complexes and defect clusters called extended defects. These extended defects can become further ordered, which leads to superstructure ordering and to formation of intermediate phases. In some cases point defects can become eliminated in the process of crystallographic shear which is connected with formation of a whole series of intermediate phases.*"

It is possible to find several non-stoichiometric niobium oxides reported in literature. Essentially, these can be divided in two groups: one with stoichiometry between Nb and NbO, and other with stoichiometry between NbO_2 and Nb_2O_5, as illustrated before by Figure 1.7. There are three reported non-stoichiometric niobium oxides between Nb and

NbO, which were found to be metastable and were classified as NbO_x, NbO_y and NbO_z [46,147]. NbO_x was reported to be formed at 270-500 °C with a stoichiometry equivalent to Nb_6O, NbO_y was formed at 330-500 °C with stoichiometry equivalent to Nb_4O, and NbO_z was formed at 400-700 °C with an unknown exact stoichiometry [46,147]. There are very few works on this group of metastable non-stoichiometric niobium oxides.

Most of the reported non-stoichiometric niobium oxides are about those having a stoichiometry between NbO_2 and Nb_2O_5, and more precisely between $NbO_{2.4}$ and $NbO_{2.5}$. Schäfer *et al.* [42] referred the existence of such phases, with close but different stoichiometries, classified as *ox I* to *ox VI*, and suggested that all, or some of such phases might belong to the same mixed-crystal phase. Subsequent works, Schäfer *et al.* [97] and Kimura [148], reported the observation of measurable single phase ranges of non-stoichiometric niobium oxides, such as $Nb_{12}O_{29}$, $Nb_{22}O_{52}$, $Nb_{47}O_{116}$, $Nb_{25}O_{62}$ and $Nb_{53}O_{132}$ and others. Later studies, between 900 and 1300 °C, reported different results which were summarized and classified as "*incomplete and inconsistent*" by J.F Marucco [149].

Hence, Marucco [149] performed a critical review and a detailed study in order to clarify the thermodynamic existence of such phases, "*[...] by the method of equilibration between oxides and buffer gaseous mixtures, which is the most reliable*". However, between 1000 and 1100 °C, Marucco only found two stable phases within the same composition range ($2.4<x<2.5$) — $Nb_{12}O_{29}$ ($x = 2.42$) and $Nb_{25}O_{62}$ ($x = 2.47$) — suggesting that the previously reported non-stoichiometric phases were metastable or were associated with the sensitivity of the different methods that were used, or by the difficulty in keeping the phases unchanged after quenching. In a later study regarding the electrical resistance of niobium oxides, Marucco [150] explained that phases with very small stoichiometry deviations from the stable phases of Nb_2O_5, $Nb_{12}O_{29}$ and $Nb_{25}O_{62}$, were in fact possible to be found and that this deviation was not related to coherent intergrowth in the crystal, but instead to point defects, oxygen vacancies in stable phases, and niobium interstitials in metastable phases (e.g. $Nb_{22}O_{54}$ was found to be stable only above 1250 °C).

Overall, Marucco [150] concluded that the only stable phases of niobium oxides with a stoichiometry between $NbO_{2.4}$ and $NbO_{2.5}$ are Nb_2O_5, $Nb_{12}O_{29}$ and $Nb_{25}O_{62}$ where such variations in stoichiometry are possible to occur, and can be interpreted as single or doubly charged oxygen vacancies in their structure, resulting in significant variations of the electrical resistance. Since then, apart from the $Nb_{12}O_{29}$, there have been almost no reports on non-stoichiometric niobium oxide phases that could clarify these doubts about the stability of phases and their physical properties. Still, there is a recent work reporting the synthesis and structural characterization of the crystalline phase of $Nb_{22}O_{54}$ [151].

Digesting the available information to date, one can say that only three crystalline phases, stable at room temperature, of non-stoichiometric niobium oxides were reported: the monoclinic $Nb_{22}O_{54}$, and the monoclinic and orthorhombic $Nb_{12}O_{29}$ phases. The several other non-stoichiometric phases are reported to be metastable, i.e. to exist only at high temperatures.

The synthesis of these non-stoichiometric phases may be achieved by a controlled oxidation of lower niobium oxides (e.g. NbO_2, NbO or even metallic Nb), or by heat treating Nb_2O_5 sample in a reducing atmosphere at high temperatures (from 900 to 1300 ^oC) [42,97,149,150]. It was also recently reported the synthesis of crystalline $Nb_{12}O_{29}$ (both monoclinic and orthorhombic phases), in the form of thin films, by dc magnetron off-axis sputtering at room temperature, using metallic Nb as a target, after what they were annealed in vacuum at 1000 ^oC to promote the crystallization [152]. Moreover, McQueen *et al.* [151] successfully grown single crystals of orthorhombic $Nb_{12}O_{29}$ and $Nb_{22}O_{54}$ by mixing the right amounts of NbO_2 and Nb_2O_5 powders into the desired stoichiometry, and by subsequently melting the mixtures in a vacuum furnace back-filled with argon at 1425 ^oC.

The single crystals obtained by McQueen *et al.* [151], allowed them to refine and report, for the first time, the crystal structure of the $Nb_{22}O_{54}$. This phase crystallizes in a monoclinic structure (space group C_{2h}^1) with two formula units per unit cell, as illustrated in Figure 1.20. The structure is described by 3×3 and 4×3 blocks of NbO_6 octahedra linked by corner-sharing, and by Nb atoms in a tetrahedral coordination. The Nb atoms with octahedral coordination occupy six 2*m*, four 2*n* and one 1*e* Wyckoff positions, while the Nb atoms with tetrahedral coordination occupy a 2i, a 2n and a 2m positions with occupancies of 0.403, 0.068 and 0.029 respectively. The O atoms occupy thirteen 2*m*, thirteen 2*n*, one 1*c* and one 1*d* Wyckoff positions. It should be noticed that in the 3×3 and 4×3 blocks, the niobium atoms are displaced from the middle of the octahedra towards the centre of the block, forming an antiferroelectric ordering of the electric dipoles [151].

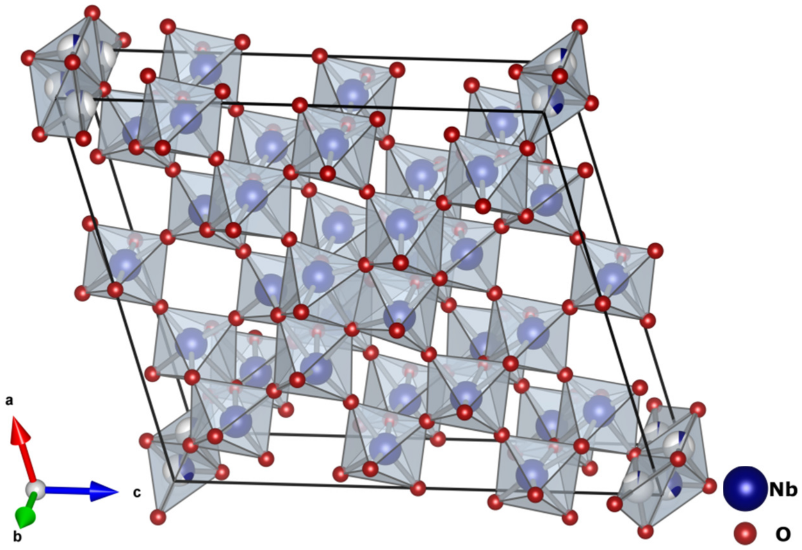

Figure 1.20 – Monoclinic structure of the $Nb_{22}O_{54}$ phase.

The $Nb_{12}O_{29}$ phase is the most commonly reported non-stoichiometric niobium oxide phase. This phase can crystallize into an orthorhombic structure (space group D_{2h}^{17}), or in a monoclinic structure (space group C_{2h}^{3}) [151,153]. The structures of $Nb_{12}O_{29}$, both orthorhombic and monoclinic polymorphs, are based on 4×3 blocks of corner-sharing NbO_6 octahedra, where the blocks are linked by edge-sharing. The orthorhombic structure of $Nb_{12}O_{29}$, illustrated in Figure 1.21, has six formula units per unit cell, where the Nb atoms occupy six 8*f* Wyckoff positions and the O atoms occupy thirteen 8*f* and three 4*c* positions [151,153]. The structure of the monoclinic polymorph of $Nb_{12}O_{29}$, illustrated in Figure 1.22, has three formula units per unit cell, with the Nb atoms occupying six 4*i* Wyckoff positions and the O atoms occupying one 2*d* and fourteen 4*i* positions [153]. Similarly to $Nb_{22}O_{54}$, both $Nb_{12}O_{29}$ have the Nb atoms displaced from the centre of the NbO_6 octahedra, towards the centre of each block. These displacements are typically responsible for a spontaneous polarization and electric polarization in ferroelectrics, but in this case they are arranged in such way that each block has no net electrical polarization, and therefore these materials are considered to be antiferroelectric [151].

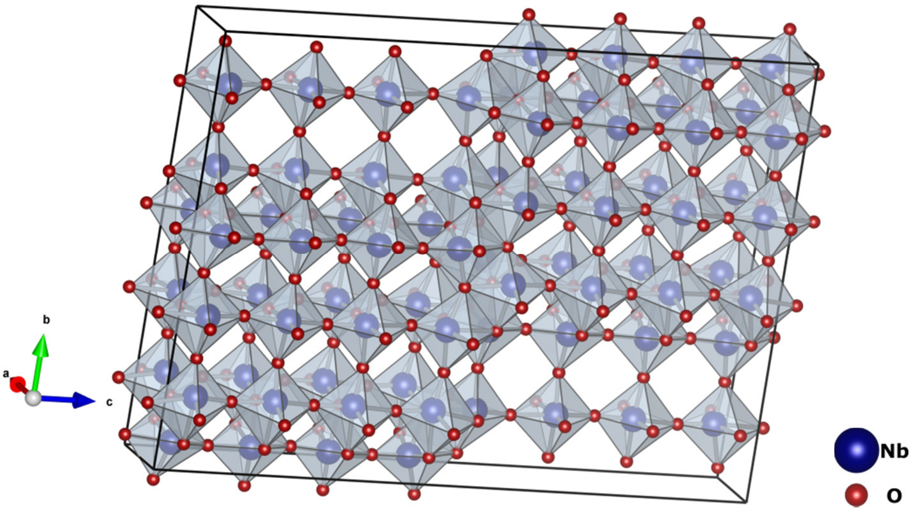

Figure 1.21 - Structure of the orthorhombic $Nb_{12}O_{29}$ phase.

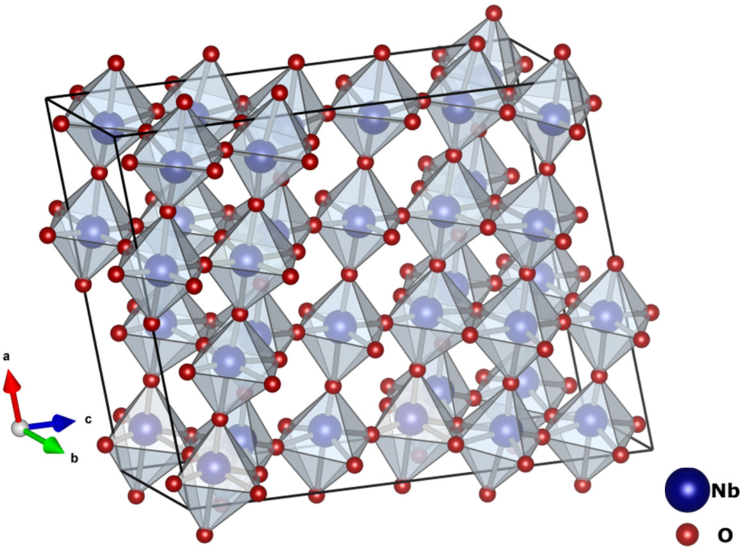

Figure 1.22 - Structure of the monoclinic $Nb_{12}O_{29}$ phase.

Even though the stoichiometry of these materials is near of the Nb_2O_5, which is a semiconductor, the electrical properties are quite different. Schäfer *et al.* [97], and later Marucco [150], investigated on the electrical properties of non-stoichiometric niobium oxides, verifying that even a small change of the O/Nb ratio produced a significant variation of the conductivity, showing a typical n-type conductivity. Schäfer *et al.* [97] reported a variation from 3×10^{-6}, to 4×10^{1}, and to 3×10^{3} S/cm, by changing the O/Nb ratios from 2.5, to 2.495, and to 2.489, respectively (at room temperature). Marucco [150] performed a more detailed study on the conductivity of niobium oxides, at high temperatures, in a broad range of stoichiometries between $Nb_{12}O_{29}$ and Nb_2O_5, as a function of oxygen pressure and temperature, also observing an increase of conductivity with the decrease of O/Nb ratio. Additionally, Marucco observed pronounced discontinuities of the electrical resistivity, depending on the non-stoichiometric phase, and also depending on the oxygen pressure, which allowed him to relate these observations with oxygen vacancies in the stable phases, and with niobium interstitials in the metastable phases [150]. Later studies [153,154] specifically about $Nb_{12}O_{29}$, report a typical metallic behaviour regarding the electrical conductivity, where Cava *et al.* [154] reports values in the order of 10^{-3} S/cm, but it does not become superconductive at least down to 0.25 K.

In 1991, Cava *et al.* [154] were the first to report on the magnetic properties of non-stoichiometric niobium oxides. While the Nb_2O_5 is diamagnetic, Cava *et al.* verified that the orthorhombic $Nb_{12}O_{29}$ phase shows an approximated Curie-Weiss behaviour, i.e. paramagnetic, and an antiferromagnetic ordering at 12 K. The fact that orthorhombic $Nb_{12}O_{29}$ shows, simultaneously, a Curie-Weiss behaviour, antiferromagnetism and metallic conductivity (even below the ordering temperature), which are characteristics of localized and delocalized electrons, led the author to suggest that the structure contained some Nb^{4+} ions with a localized $4d^1$ configuration, which give rise to the magnetism, while the other Nb^{5+} ions at other sites contribute with delocalized electrons, responsible for the conductivity. In 2001, Waldron *et al.* [155] further extend this explanation to monoclinic $Nb_{12}O_{29}$, but only in 2004 the same authors [153] experimentally verify for this phase an identical metallic conductivity, allied to a Curie-Weiss behaviour and a antiferromagnetic transition at 12 K, the same ordering temperature as the orthorhombic polymorph. However, the advanced structural study reported by McQueen *et al.* [151], in 2007, shows that based on bond valence results, no Nb^{4+} sites are detected in the orthorhombic $Nb_{12}O_{29}$ phase (at least at 200 K), which suggests that the magnetic behaviour observed in these materials is not related with the valence electrons of individual Nb atoms, but instead, as the authors speculate, "*[...] each magnetic electron may be delocalized across a 4×3 block [...]*". Up to date, this question about the magnetic nature of the $Nb_{12}O_{29}$ phases remains unclear. Moreover, it should be noticed that Cava *et al.* [154] verified that other non-stoichiometric niobium oxide phases displayed paramagnetic behaviour, but not any kind of ordering, at least down to 2 K.

Recently, in 2011, Ohsawa *et al.* [152] report the synthesis of a $Nb_{12}O_{29}$ thin films (with a thickness of 120 nm) which have shown a high transmittance in the visible range (~50 % in the red and ~70 in the blue regions), with a refractive index $n = 2.2$ at 400 nm. The films were deposited on a glass substrate with a transmittance between 90 and 95 %. The high transparency, allied to the high electrical conductivity of about 300 S/cm (even after annealing at 1000 °C in vacuum) without the need of doping, makes $Nb_{12}O_{29}$ a new class of transparent conductive oxides (TCO). Classified by the authors as an "*intrinsically doped d-electron-based TCO*" [152], and though there is no evidence if it has a direct or indirect band gap, the $Nb_{12}O_{29}$ may be a very interesting material for use in high-performance and low-cost optoelectronic devices.

With the description of the niobium oxides, the complexity of this system is evident. It also becomes obvious that an in-depth knowledge about the structures and stoichiometry of these oxides are fundamental for solid scientific research or towards any type of technological application. Table 1 summarizes all the stable niobium oxides phases reported to date. Some lattice parameters may slightly change depending on the preparation method or sintering temperature.

Table 1.1 - Niobium Oxides Crystalline Phases

Compound	*Crystal System*	*Lattice Parameters*	*Space Group*	*References*
NbO	Cubic	a = 4.210 Å	O_h^1	[41,47]
NbO_2	Tetragonal	a = 13.695 Å c = 5.981 Å	C_{4h}^6	[62,63]
	Rutile	a = 4.55 Å / a = 4.841 Å c = 2.86 Å / c = 2.992 Å	D_{4h}^{14}	[65,156]
	Monoclinic	a = 12.03 Å b = 14.37 Å c = 10.36 Å β = 121.17 °	C_{2h}	[59,60,64]
$Nb_{12}O_{29}$	Monoclinic	a = 15.686 Å b = 3.831 Å c = 20.71 Å β = 121.17 °	C_{2h}^3	[151,153,155]
	Orthorhombic	a = 3.832 Å b = 2.740 Å c = 28.890 Å	D_{2h}^{17}	[151,153,155]
$Nb_{22}O_{54}$	Monoclinic	a = 15.749 Å b = 3.824 Å c = 17.852 Å β = 102.03 °	C_{2h}^1	[151]
T- Nb_2O_5	Orthorhombic	a = 6.175 Å / a = 6.144 Å b = 29.175 Å / b = 29.194 Å c = 3.930 Å / c = 3.940 Å	D_{2h}^9	[86,87,89,157]
B- Nb_2O_5	Monoclinic	a = 12.73 Å b = 4.88 Å c = 5.56 Å β = 105.1 °	C_{2h}^6	[86,87,158,159]
H- Nb_2O_5	Monoclinic	a = 21.153 Å / a = 21.163 Å b = 3.8233 Å / b = 3.824 Å c = 19.356 Å / c = 19.355 Å β = 119.80 °	C_{2h}^1	[86,89,157–160]
N- Nb_2O_5	Monoclinic	a = 28.51 Å b = 3.830 Å c = 17.48 Å β = 120.8 °	C_{2h}^3	[86,87,158,159]
Z- Nb_2O_5	Monoclinic	a = 5.219 Å b = 4.699 Å c = 5.928 Å β = 108.56 °	C_2^1	[88]
R- Nb_2O_5	Monoclinic	a = 12.79 Å b = 3.826 Å c = 3.983 Å β = 90.75 °	C_{2h}^3	[86,87]
M- Nb_2O_5	Tetragonal	a = 20.44 Å c = 3.832 Å	D_{4h}^{17}	[86,87]
P- Nb_2O_5	Tetragonal	a = 3.876 Å c = 25.43 Å	D_4^{10}	[86,87]
TT- Nb_2O_5	Pseudohexagonal	a = 3.607 Å / a = 3.600 Å c = 3.925 Å / c = 3.919 Å	–	[74,86,87,89,157]
	Monoclinic	a = 7.23 Å b = 15.7 Å c = 7.18 Å β = 119.08 °		

1.4 Niobates

It was decided to explore materials others than niobium oxides, namely niobates. This choice was seen as an opportunity for extending the knowledge and experience acquired from niobium oxides, into a large group of materials with very interesting properties in the area of expertise of our research group.

If a bibliographic search for *niobates* is done in well-established scientific databases (such as ISI Web of Knowledge), one can find many recent papers that show us that there are several materials with a currently active research community and with great interest for different applications. From all the reported compounds, the alkali and columbite niobates are clearly the most actively studied. However, for this work, our choice fell on an interesting group of niobates that have been much less explored in literature but that present promising optical and electrical properties: the rare-earths orthoniobates.

1.4.1 Alkali Niobates

Lithium Niobate ($LiNbO_3$), Sodium Niobate ($NaNbO_3$) and Potassium Niobate ($KNbO_3$) are known as the alkali niobates. These oxides, structural classified as *perovskites*, have been reported by many of their interesting properties such as piezoelectricity, pyroelectricity, electro-optic and nonlinear optical behaviour [161,162].

More particularly, $LiNbO_3$, possibly the most studied of the alkali niobates, is a well-known transparent semiconductor (with a band gap of ~3.7 eV [163]) with an extremely technological importance. It presents large pyroelectric, piezoelectric, acousto-optic, nonlinear and electro-optic coefficients, and it is mainly used, in solid-state based optical devices, as optical modulators, for Q-switching, for second harmonic generation (SHG), optical filters, waveguides or acoustic-wave transducers, either in bulk or nanostructured forms [161,164]. Due to its wide band gap, $LiNbO_3$ has also been reported as an interesting host for achieving optically active lanthanides via suitable doping processes [165,166].

Similarly, $KNbO_3$ is reported for having large nonlinear optical coefficients which makes it suitable for SHG, frequency mixing, or optical parametric oscillators [164]. Moreover, $KNbO_3$ and also $NaNbO_3$ are pointed as promising alternatives to the currently used piezoelectrics ceramics, mainly based on lead zirconate titanate (PZT). The need of finding a substitute for PZT is essentially related with environmental and health concerns, since it presents a weight percentage of lead 600 times greater than the maximum limit imposed by governmental regulations [162]. Thus, the alkali niobate $(K,Na)NbO_3$, typically abbreviated as KNN, is probably the top candidate to replace PZT, with typical reported piezoelectric constant d_{33} around 80 pC/N for an optimal K/Na ratio ~1 [162]. The most common approach for property optimization of KNN involves forming solid solutions with other materials such as $LiNbO_3$, $LiTaO_3$, $LiSbO_3$, $BaTiO_3$, $CaTiO_3$, $(Bi_{0.5}Na_{0.5})TiO_3$, or a combination of these, resulting in d_{33} constants in the order of 200 and 300 pC/N [162]. The crystalline structure of KNN ceramics is not simple. While the pervoskite subcell of this material has a monoclinic symmetry (illustrated in Figure 1.23), the KNN crystalline structure is orthorhombic with a space group C_{2v}^{14}. The structure of $K_{0.5}Na_{0.5}NbO_3$ is not yet refined and does not have a standard JCPDS-ICDD file, and therefore compromises a correct crystal indexing literature. Furthermore, the KNN ceramics have different polymorphs depending on the temperature and on typically used dopants such as Li, Ta, Sb or others [162].

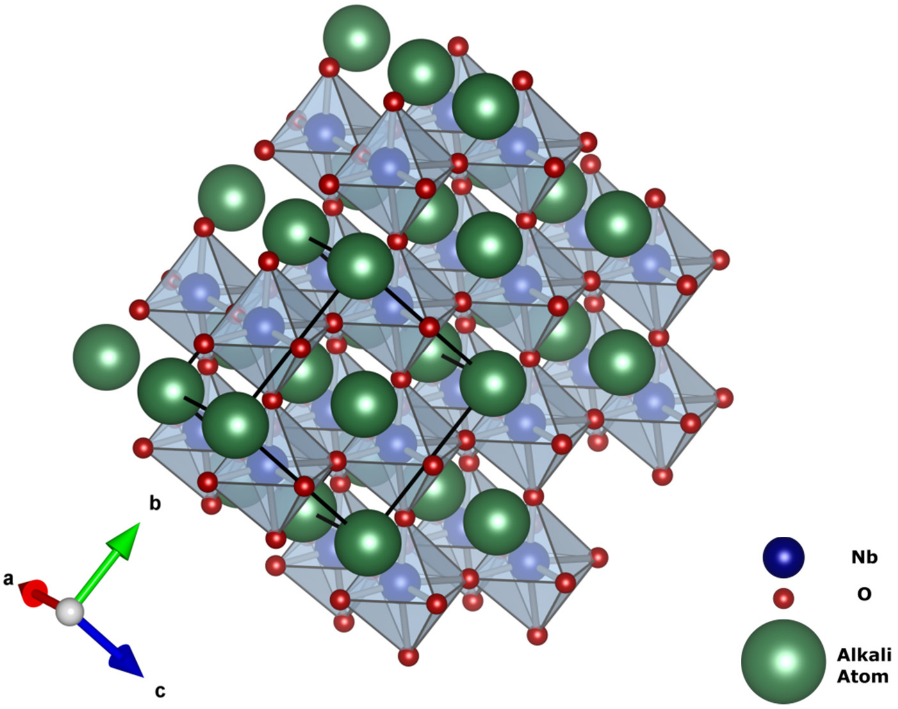

Figure 1.23 – Typical perovskite structure of an alkali niobate.

Despite the fact that these alkali niobates have been presenting extremely good piezoelectric properties, their application is still limited by difficulties in their synthesis. In fact, one of the current biggest challenges in the study of alkali niobates is the control and reproducibility of their properties, which are typically associated to the synthesis methods and sintering processes. It is known that small variations of the sintering temperature may easily result in deteriorated performance [167]. Additionally, there are two types of mechanisms that were proposed to justify the piezoelectric property enhancement - polymorphism phase transition (PPT) and morphotropic phase boundary (MPB). Summarizing, it becomes obvious that the investigation and control of the phase and crystalline structures of these materials is extremely important [162].

One of the most common precursors for the synthesis of niobates is some sort of niobium oxide, particularly Nb_2O_5. However, as explained above, due to the "memory of solids" the original synthesis method of the niobium oxide can be determinant in the properties of the final product, thus affecting the properties of the niobate in different ways. Furthermore, it is known [42] that there is a direct structural relationship between the form of Nb_2O_5 and the related ternary oxides. Moreover, Kuznetsova *et al.* [168] "[...] have demonstrated that the polymorphous phase state of Nb_2O_5 significantly influences the characteristics of the alkali metal niobate solid solution powders and determines the extreme variation of the properties of synthesized ceramics, which must be taken into account in development of the Nb-containing ferroelectric piezoceramics". Hreščaka *et al.* [169] have recently published a work on this issue, alerting for the need of a good identification of the Nb_2O_5 polymorph when reporting the synthesis of alkali niobates. This is why it is believed that the experience and knowledge acquired, while exploring the complex system of niobium oxides, may constitute an important basis in the research of different niobates.

Additionally, there have been also recent works regarding multiple hetero-nanostructures based on alkali niobates. This new class of materials are very interesting for the possibility of effectively coupling different properties. Due to their properties and multifunctional character, hetero-nanostructured systems can be more advantageous than single component systems. Particularly, Yan *et al.* [170] reported the synthesis of multiple $NaNbO_3$ nanoplates inside hollow Nb_2O_5 nanotubes. The authors classified these structures as a novel class of multiple ferroelectric/semiconductor heterostructures as they exhibit distinct ferroelectric switching due to the presence of the strain states at the $NaNbO_3/Nb_2O_5$ interface.

1.4.2 Columbite Niobates

The columbite niobates (which have their name from the same crystalline structure of the columbite mineral), have the general formula $M^{2+}Nb_2O_6$ where M^{2+} is a divalent cation of Mg or Ca or of a transition metal such as Cu, Cd, Zn, Ni, Mn, Co or Fe, and have been reported especially as microwave ceramics [171]. These materials crystallize in a orthorhombic structure (space group D_{2h}^{14}) characterized by zigzag chains linked by corner sharing, each chain formed by MO_6 and NbO_6 edge-sharing octahedra, as illustrated by Figure 1.24 [171]. The exceptions to this type of structure, in columbite niobates, are those which the divalent ion has a ionic radius higher than 1.0 Å, such as Ba^{2+} and Sr^{2+}, promoting the crystallization in other types of orthorhombic structure [171].

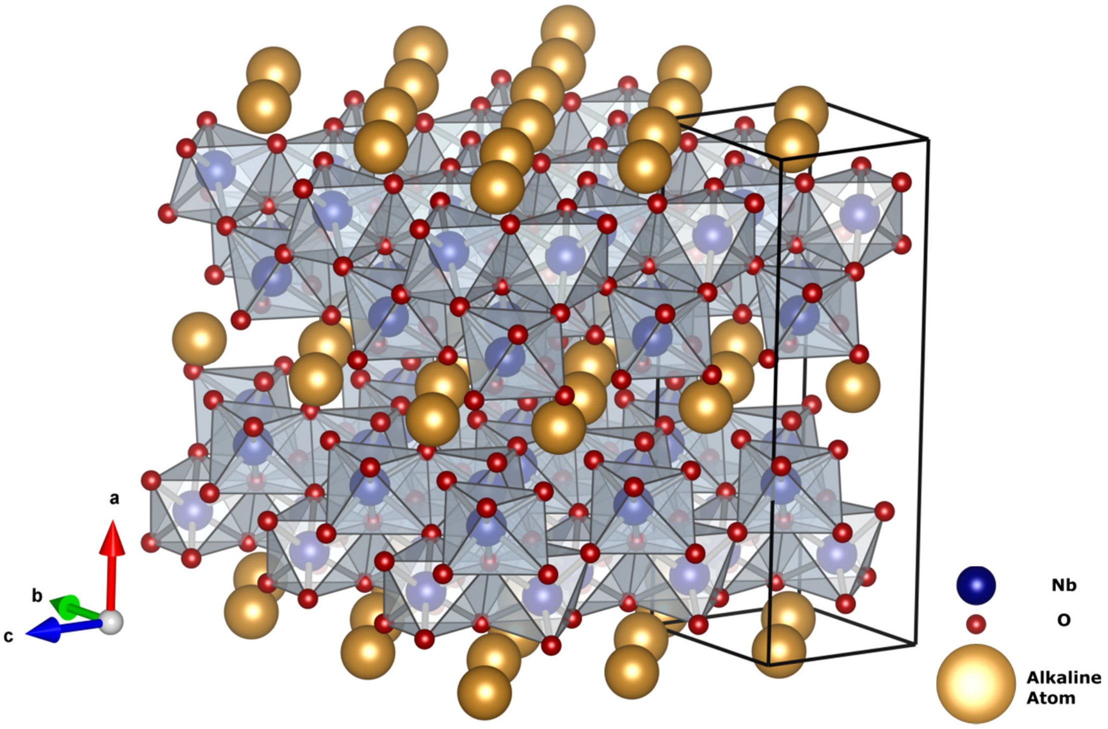

Figure 1.24 – Typical orthorhombic structure of most columbite niobates.

Microwave ceramics are characterized as being dielectric resonators with a frequency in the microwave region (500 MHz to 10 GHz), where a high dielectric constant and low dielectric losses are determinant characteristics. These materials find an important application in wireless communications which is, and has been, a highly demanding technology. Therefore, it is natural that there is a constant search for less expensive and high performance dielectric ceramics, especially because the materials currently used are tantalum-based complex perovskites, such as $BaZn_{0.33}Ta_{0.67}O_3$ (BZT) or $BaMg_{0.33}Ta_{0.67}O_3$ (BMT) [171].

As an alternative, there are niobium-based perovskites, such as $BaZn_{0.33}Nb_{0.67}O_3$ (BZN) or $Ba(Zn/Co)_{0.33}Nb_{0.67}O_3$ (BZCN), which are less expensive, but require high sintering temperatures (c.a. 1600 ºC) and times, and while the relative permittivity is superior, the overall dielectric properties are not yet competitive enough.

The reported interest in columbite niobates (especially $ZnNb_2O_6$) as microwave ceramics is related to their dielectric properties, similar to BZN or BZCN, and significantly better than columbite tantalates ($M^{2+}Ta_2O_6$). In contrast with the tantalate and niobate perovskites, these materials do not require sintering at such high temperatures, typically between only 1100 and 1200 °C, and also have just a superficial degree of ordering [171]. Additionally, because of the simpler chemistry of binary compounds, these materials require a less complex processing than the perovskites. Nevertheless, it can be concluded from the literature that many columbite niobates are not synthesized simply by one step. Difficulty in forming a single-phase samples or requiring two or more sintering steps are commonly reported. Furthermore, the occurrence of point defects in the lattice, dislocations, grain boundaries and porosity are pointed as frequent problems that compromise and justify the variation of the dielectric properties of these materials. It should be noticed that, also in these materials, non-stoichiometric phases are commonly produced as well. It was for instance reported that a slightly reduced manganese niobate ($MnNb_2O_{6-x}$) presents a much higher electrical conductivity, assigned to the production of delocalized electrons upon a small degree of Nb reduction [171]. Generally, it was observed that a small stoichiometry variation for columbite niobates produce huge variations in their dielectric properties, thus compromising their application [171]. It seems possible the cause of these type of observations may be closely related to the analogous behaviour of niobium oxides, and also related with the phase of niobium pentoxide used as precursor for the niobates, but further investigation is nevertheless necessary.

Besides the application as dielectric ceramics, columbite niobates have also been reported by their magnetic properties, which in general present antiferromagnetic ordering below temperatures 4-7 K with special interest on $CoNb_2O_6$ that shows some unusual magnetic ordering due to geometrical frustration [171]. The reported $NiNb_2O_6$ photocatalytic properties, for water hydrolysis, are quite interesting but it was shown that this material was easily corroded, thus compromising its application. On the other hand, Zn and Mn niobates were also reported to have interesting photocatalytic properties for isobutene oxidation, presenting a good chemical stability and selectivity.

The optical properties of both pure and rare-earth-doped columbite niobates have been reported in literature [171]. The pure columbite niobates (at least Ca, Zn, Cd and Mg niobates) have shown intrinsic blue luminescence with broad bands centred c.a. at 430-470 nm [171]. Hence, these materials were classified as self-activated phosphors. It was reported that the luminescence efficiency decreased with decreasing size of the divalent ion, i.e. Ca niobate was found to have the most intense emission. Particularly for Ca niobate, it was found that the 464.5 nm emission was preferentially excited with

200-260 nm wavelength radiation [171]. Partial substitution of Ca by other elements, such as Zn and Cd, were reported to enhance the blue luminescence intensity, which was assigned to the participation of the 4*d* electrons in the charge transfer within the NbO_6 octahedra [171]. Ca niobate has a high refractive index c.a. 2.07-2.2, is transparent in a wide spectral range (300 nm to 5.5 µm) and has relatively low phonon cut-off energy (~900 cm^{-1}). Additionally, single crystals of Ca niobate are rather easy to grow by laser-heated pedestal growth technique, which allied to these properties makes it a preferable host for rare-earth doping, aiming their application as optical devices [171]. Thus, there are works reporting laser action in Ca niobate doped with Nd, Ho, Pr and Tm, or even co-doped with Eu and Ti which was proposed as a low cost lamp phosphor [171]. Europium was found to be optically active in doped Cd niobate, showing higher intensity, when excited and detected under the same experimental conditions, compared with the Ca niobate host and with strong evidences of multiple Eu^{3+} emitting sites. Single crystals of $CaNb_2O_6$ doped with Nd have shown stimulated emission at 1064 nm, due to intraionic Nb^{3+} transitions, with a lifetime of only 145 µs; the samples doped with Er showed a pink coloration and an intense emission at 1550 nm at RT (due to transition between the fisrt excited multiplet and the ground one of the Er^{3+}), and similarly, those doped with Pr showed a sharp and intense band centred at 610 nm [171]. Additionally, $CaNb_2O_6$ was reported to have a strong blue mechanoluminescence, observed during grinding [171]. On the other hand, nanoparticles of Ni niobate doped with Dy, prepared by a sol-gel combustion method, did not show any characteristic luminescence of the lanthanide ion in its trivalent charge state, but it was found that the intrinsic blue emission of the host was enhanced, which was assigned to the energy transfer from the Dy^{3+} ion to the NbO_6 octahedra. This behaviour was observed also for Zn niobate doped with Dy, but it was also found that for >5 mol% Dy there was an opposite behaviour assigned to concentration quenching effect [171].

There has also been some works reporting on another type of niobate perovskite based on rare-earths with very interesting optical properties, particularly the $CaRENb_2O_{10}$ (where RE is a trivalent rare-earth ion) [172]. These materials are classified as triple-layered perovskites, as they are built by layers of corner-sharing octahedra. In a very recent work (2013), Qin *et al.* [172] report the synthesis and characterization of these “novel luminescent materials” with an estimated band gap of 4.42 eV. With 266 nm (~4.7 eV) laser excitation, and so above the material band gap, the authors observed a broad emission band which was assigned to the NbO_6 octahedra. Depending on the lanthanide, the intrinsic NbO_6 broad band varied its spectral position between 400 and 500 nm, from blue to greenish blue, which is preferentially excited at ~270 nm. The characteristic intra-4*f* emissions of the trivalent rare-earth ions were also observed under 266 nm excitation, namely for the Sm^{3+}, Er^{3+}, Dy^{3+} and Eu^{3+} ions, which shows that there was a charge transfer mechanism from host to the lanthanide. It is noted that these materials show a high critical point for luminescence concentration quenching effects. This, and the high luminescence intensity of the lanthanides characteristic emissions at RT, lead the authors to suggest these materials to be used as phosphors in near-UV or blue LEDs, especially the $CaEuNb_3O_{10}$ [172].

1.4.3 Rare-Earths Orthoniobates

There are works reporting rare-earth orthoniobates ($RENbO_4$), as well as rare-earth orthotantalates ($RETaO_4$), from decade of 1960 [173–177], but until recently these systems were not a research topic which has received much attention from the scientific community.

The $RENbO_4$ are known to crystallize in a *fergusonite*-type structure, i.e. in a monoclinic structure (space group C_{2h}^6), undergoing a pure and reversible ferroelastic phase transformation to a *scheelite*-type structure, with a tetragonal system lattice (space group C_{4h}^6), only stable at high temperatures (<700 °C) [177–179]. In the monoclinic phase the Nb and RE atoms occupy the Wyckoff positions 4*e* while the O atoms occupy the 8*f* position, which structure is illustrated by Figure 1.25 where it is possible to identify the NbO_6 octahedra linked by edge-sharing forming chains along the *c* axis.

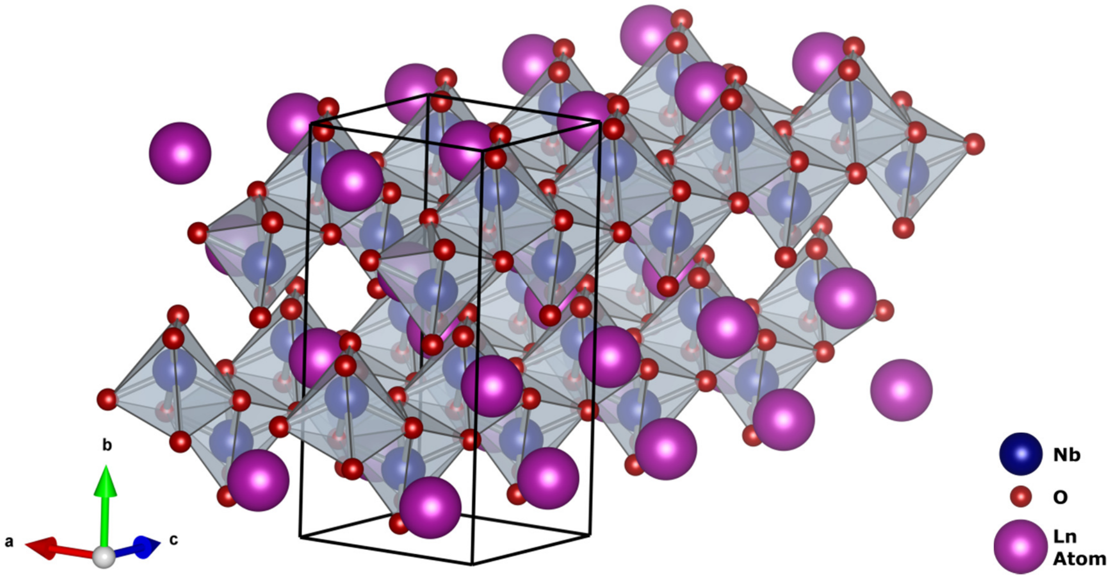

Figure 1.25 - Structure of the monoclinic phase of $RENbO_4$.

The tetragonal phase is not built on NbO_6 octahedra, but instead on unlinked NbO_4 tetrahedra, as illustrated in Figure 1.26, with the RE, Nb and O atoms occupying, individually and respectively, the 4*b*, 4*a* and 16*f* Wyckoff positions. The lattice parameters of the $RENbO_4$ compounds will obviously depend on the lanthanide ion.

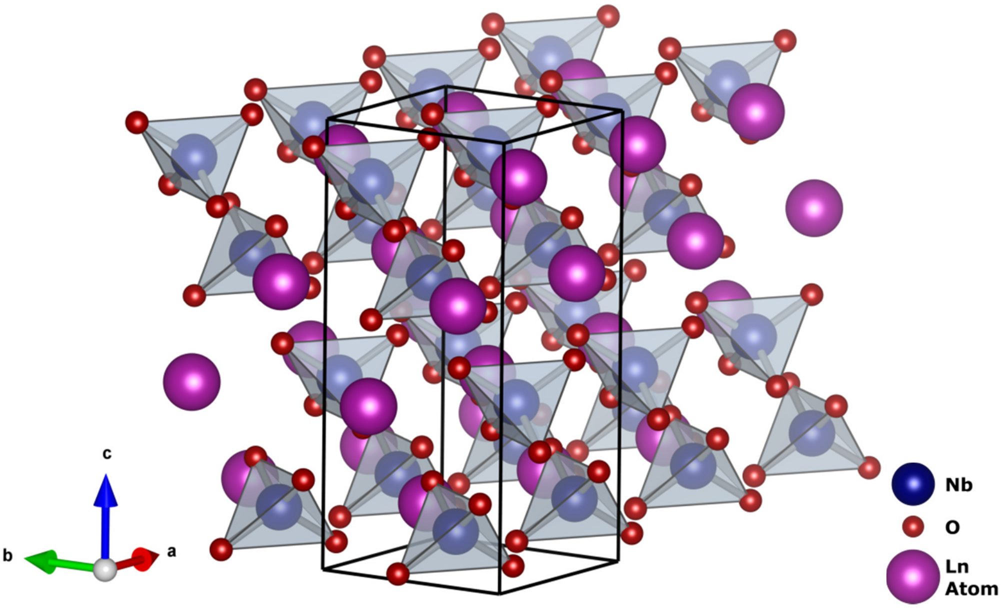

Figure 1.26 - Structure of the tetragonal phase of $RENbO_4$.

One of the most detailed structural studies on rare-earths orthoniobates, which covers all the lanthanide ions (from La to Lu, except Pm), is a work reported by Siqueira *et al.* [178]. The authors report the synthesis of rare-earth niobates by solid-state reaction (by mixing niobium pentoxide and rare-earths oxides), and their characterization by X-Ray diffraction and Raman spectroscopy. It was found that only for heat treatment temperatures above 1150 ^{o}C, the formation of secondary phases could be avoided. The Raman analysis on the $RENbO_4$ samples revealed very complex spectra, with 18 active modes, which was found to be in complete agreement with group theory calculations [178]. Furthermore, it was found that some of the modes follow a decrease of energy with the increase of the lanthanide ionic radii (which is a natural consequence of the unit cell expansion), while other modes followed the inverse trend (justified by a mass effect) [178]. Some bands in the range of 316 to 343 cm^{-1} showed a tendency to split for lower lanthanide ionic radii, which was assigned to a higher monoclinic distortion. From all the $RENbO_4$ samples, the Raman spectra of the Ce and La niobates were classified as an exception to the general trend because they presented a significant broadening and down-shifting of their modes. This was linked to the proximity of the transition temperature from the monoclinic to the tetragonal phase, since it decreases from the Lu to the La ion. The authors additionally refer the identification of 15 active modes by Fourier-transform infrared spectroscopy (FTIR) [178].

Rare-earth tantalates are known to have very similar properties and structures [178,180,181]. Still, besides the fergusonite-type structure, recent studies report on the identification of two additional different monoclinic polymorphs, of rare-earth orthotantalates stable at room temperature, depending on the lanthanide ion and on the synthesis/processing conditions [180,182]. Such polymorphs are mainly characterized by different arrangement and linkage of distorted TaO_6 octahedra, presenting different physical properties. The same was not observed for orthoniobates [178], but given the obvious similarities between these two systems, it would not be surprising that such polymorphs also exist for $RENbO_4$, and for that reason further research is necessary to clarify this point.

While the synthesis of $RENbO_4$ crystals has been previously reported by using Czochralski or flux growth methods [177], only in 2004 Octaviano *et al.* [183] report the synthesis of single crystals by a floating zone technique. The authors have grown single crystals of La, Ce, Pr, Sm, Eu, Dy Ho, and Er orthoniobates, and a few more doped with Er^{3+}, and mentioned the particular difficulty in controlling the crystal diameter during the growth. It was verified by X-Ray Laue diffraction analysis that the crystals tend to grow along the [110] direction. Octaviano *et al.* [183] mainly focused on the Er-doped $LaNbO_4$ material which showed very interesting optical properties, with high absorption coefficient and a strong luminescence of Er^{3+} when pumped with a green 514 nm laser line at 300 K. Recently, Graça *et al.* [184] report on the synthesis of $EuNbO_4$ crystals, grown by laser floating zone, and their optical and dielectric properties. The luminescence analysis of the $EuNbO_4$ crystals revealed intense red luminescence at room temperature with ultraviolet excitation, and the existence of multiple Eu-related optical centres whose emission is observed at low temperatures some of which are quenched at c.a. 50 K. Other authors, Xiao and Yan [185], report on the synthesis, by a modified in-situ chemical co-precipitation method, and the luminescence of different doped rare-earth orthoniobates. Very recently, from the end of 2013, a patent registered by Sandia National Laboratories [186] claims on the production of rare-earth niobates and tantalates, by an hydrothermal technique, aiming their application as nanophosphors to lighting and display technologies, which testifies the interesting optical properties of these materials.

Additionally, rare-earth orthoniobates have been reported to have a characteristic ferroelasticity attributed to the formation of domain walls during phase transitions [179,183]. The microwave dielectric properties and effects of such ferroelasticity on these properties were investigated by Kim *et al.* [179]. The authors estimated the mean static dielectric constants of several orthoniobates using the Clausius-Mossotti relation. The experimental dielectric constants of the $RENbO_4$ samples, however, were significantly lower: ~20, almost half than the estimated values. This was related to a monoclinic distortion which has its origin in the phase transformation from the tetragonal to the monoclinic structure, resulting in ferroelastic domain structure that resembles twinning, with two orientation states identical in structure but different in orientation [179]. Despite the low dielectric constants measured by Kim *et al.* [179], the $RENbO_4$ samples presented excellent quality factors, ranging between 33000 and 56600 GHz, depending on the lanthanide, and also high temperature coefficients of resonant frequency (τ_f) Particularly, $LaNbO_4$ presented a positive τ_f of 9 ppm/K. The transition temperature of several $RENbO_4$, listed by the authors, was found to be tunable by mixing two different lanthanides, thus allowing to control the strain induced by the lattice distortion, and therefore the dielectric properties. The high-temperature stability of the resonant frequency and quality factor, make the rare-earth orthoniobates interesting ceramics for microwave applications [179]. In other frequency range, from 100 Hz to 2 MHz, Graça *et al.* [184] verified that, for $EuNbO_4$ crystalline fibres, the dielectric constant depends on the crystal growth speed, being highest ($\varepsilon' \cong 40$) for the slowest pulling rate. Furthermore, it was found that from 80 to 400 K the dielectric constant of the $EuNbO_4$ samples remained constant in a remarkable way, which may be interesting for dielectric applications which require stable operation in a wide temperature range.

Probably, the major interest in the rare-earth orthoniobates is related to the reported proton conductivity, thus having the potential application in sensors and fuel cells electrolytes [181]. The first work reporting on the protonic conduction on these materials is from 2006 by Haugsrud and Norby [181], and though the authors have studied both Ca and Sr-doped rare-earth orthoniobates (and also orthotantalates), the main focus was on proton conductivity and solubility of protonic defects in wet H_2 atmospheres of Ca-doped $RENbO_4$ samples. The authors clearly identified a pure protonic conductivity for these samples, increasing with the temperature between 400 and 1200 °C. Generally, between 400 and 600 °C it was possible to notice a break in the slope of the conductivity, which was associated with the phase transformation from monoclinic to tetragonal. The Ca-doped $LaNbO_4$ material presented the highest conductivity, reaching ~10^{-3} S/cm. The analogous orthotantalates were found to behave similarly to the niobates but with a protonic conductivity almost half an order of magnitude lower. Additionally, since their phase transition is much higher, the tantalates remained with the monoclinic structure up to 1200 °C. The authors refer that "*the tetragonal polymorph of the niobates, in general, shows more exothermic (more negative) hydration enthalpies and is thus more easily hydrate than the monoclinic polymorph of the tantalates*". Still, since the phase transformation may lead to thermal expansion, Haugsrud and Norby [181] suggest a partial substitution of Nb by Ta in order to minimize this effect. The fact that these materials are the oxides (without Ba or Sr as the main components) with the highest reported protonic conductivities, make them particularly interesting for fuel-cell electrolytes and humidity sensors, as aforementioned [181]. It is therefore no surprise that, since this work, there have been many other reported studies on the protonic conductivity of these materials, especially on $LaNbO_4$ [187–195].

It is also known that some $RENbO_4$ present antiferromagnetic ordering at temperatures below 4 K, while most of them follow a Curie-Weiss law [176]. Additionally, in 1998, Baughman *et al.* [196] report a large negative Poisson's ratio (in at least one direction) for $LaNbO_4$, thus being classified as an *auxetic* material. This type of property makes these materials interesting for high pressure applications as, for instance, optical line systems installed at deep sea level.

For these reasons, it is believed that the research on these materials is a good opportunity as a consequence of the study of niobium oxides. Hence, this work will also focus us on the synthesis and in the structural, electrical and, especially, the optical properties of the $RENbO_4$, which results are presented and discussed in chapter 7 of this work.

Chapter 2

Synthesis and Characterization Techniques

2. Synthesis and Characterization Techniques

This chapter will describe the routes and techniques that were used to synthesize and prepare the different samples studied in this work. Experimental procedures which took place in the scientific research laboratories of the University of Aveiro will be addressed. The description of the industrial manufacturing of the solid electrolytic capacitors, which took place in the production facilities of Kemet Electronics Portugal, will be focused on the next chapter.

This chapter begins by presenting the synthesis techniques, explaining their basic principles and major advantages and disadvantages. Then, the several advanced characterization techniques, their fundamental principles, characteristics, applications and limitations will be covered as well as the type of information that is possible to obtain directly or indirectly. The mathematical formalism applied for the data interpretation of some techniques will also be presented. The order in which these techniques will be described is an attempt to follow the most common sequence adopted during the study of the different materials presented in this work. The most common approach was to begin with a structural along with morphological analyses, followed by different types of optical and electrical characterizations.

2.1 Synthesis and processing techniques

2.1.1 Solid State Reaction

Solid state reaction is one of the most known and common techniques to synthesize ceramic materials [197]. Typically, this method requires the mixture of solid compounds with the desired elements, usually oxides, nitrates, acetates or fluorides, with the desired stoichiometry

Most ceramics (and inorganic solids in general) are chemically stable and inert at ambient temperatures. This is mainly due to the strong covalent bonds between the atoms composing the material. With enough time and energy, it is possible to promote the reaction of a solid with a gas, liquid or another solid. The temperature should not, however, be raised up to the melting point of the compounds in order to promote the *reaction* only in the *solid state*.

This type of reaction generally begins at the surface of the solids, progressing to the bulk as the reactants diffuse inwards [197]. Therefore, in order to optimize the efficiency of the reaction and the quality of its product, this method requires a pre-processing of the precursor materials, increasing the contact area and homogeneity of the mixture. To do this, a thorough process of grinding the reactants must take place, by using a mortar and a pestle or a planetary ball mill.

In order to promote the contacting degree, the distance between the grains of the solid solution must be decreased down to a minimum, being common to press the powders into pellets for that purpose (uniaxially, isostatically or hot pressing). The prepared mixture of reactant powders is then taken into an electric heating furnace to promote the reaction. Depending on the material and objective, the temperatures can range from c.a. 300 to 2000 ^{o}C. Usually, alumina crucibles are used as recipients of the material during the heat treatment since it has very good refractory properties and chemically inert up to very high temperatures (c.a. 2000 ^{o}C). Containers made of silica, zirconia, magnesia, or some metals such as platinum and tantalum, are also commonly used [197]. In this work, alumina crucibles were used as a compromise of chemical inertia, maximum temperature of the heat treatments and price/availability.

Besides the area of contact between the reactants, there are other factors that influence the rate of reaction between solids as the diffusion and nucleation phenomena [198].

The rate of diffusion of ions can be greatly enhanced by increasing the temperature, or by the presence of crystal defects, such as point defects (e.g. vacancies and interstitials, intrinsic of the reactant crystals or intentionally induced through the introduction of impurities), structural defects (e.g. dislocations) and grain boundaries [198]. The usage of alternative types of reactants, such as carbonates or nitrates of the desired element, can also be helpful since they usually decompose at lower temperatures (or faster) when compared with oxides, for example [198].

The rate of nucleation mainly depends on the crystal lattice similarities between one, or both, reactants and the reaction product. There are two types of orientational reactions – topotactic and epitactic. While the epitactic reactions depends on a two dimensional similarity to promote the nucleation, the topotactic reaction, is more restricted and a bulk similarity between the crystals lattice parameters is required. If the reactants have similar lattice parameters and/or structure, the structural reorganization needed to obtain the product is lower, therefore facilitating the rate of nucleation. It is estimated that, in order to promote an orientational nucleation, a maximum of 15 % of difference between the interfacial lattice parameters is tolerated [198]. Furthermore, another important aspect is the reactivity of lattice planes. Since most crystals do not have the same structure in all their surfaces, i.e. different orientations, the reactivity and therefore the rate of nucleation will vary. Citing Anthony R. West [198], "*A general guideline to crystal growth and morphology is that those surfaces that are most prominent in a crystal are those that grow more slowly*".

While the solid state reaction method allows us to produce large amounts of crystalline samples in a relatively simple way, it has, however, several disadvantages. It usually requires very high temperatures and/or time, and therefore large energy consumption. Other consequences of using high temperatures is the difficulty of incorporating ions that are easily volatilized, and also the difficulty of achieving low temperature, or metastable, crystalline phases.

The atmosphere in a solid state reaction is also a crucial factor. For instance, if one wants to promote the oxidation of a certain material, an O_2 rich atmosphere is desirable. Moreover, if one of the reactants elements has more than one oxidation state, one can introduce an oxidizing or reducing atmosphere in order to achieve the desired oxidation state. Pressure and concentration do play an important role here.

A process that is very common to follow the solid state reaction is the sintering process and grain growth of the reaction product. Sintering is governed by diffusion processes but it cannot be considered a reaction since there is no change of phase or composition. During this process, many of the grains are in contact between them and, upon heating (below the fusion temperature, so any liquid phase is present), neck growth is promoted in such region of contact between adjacent particles [199]. The transport of mass that gives rise to the neck growth happens by atomic diffusion from the grains into the neck region. At the beginning, pores and non-spherical shapes are produced, but as the sintering process continues such pores tend to disappear and spherical shaped grains (larger than before sintering) are preferentially promoted, in order to reduce the effective area of the particles which is energetically more favourable [199]. The sintering and growth of grains are particularly important to improve the density of the sample (in some cases undesirable), reduce interfacial defects and improve the crystallinity of the final product.

2.1.2 Sol-Gel Method

The sol-gel process has been widely used in the synthesis of ceramics in different forms – glasses, powders, films or fibres [200–202]. In the most simplified way, the sol-gel process can be summarized by the preparation of a *sol*, *gelation* of the *sol* and removal of the solvent. A *sol* can be defined as a colloidal suspension of solid particles in a liquid, while an *aerosol* is a suspension of particles in a gas, and an *emulsion* a suspension of droplets of liquid in another liquid [200]. Any type of these colloidal suspensions can be used to produce gels from which ceramic materials can be synthesized.

This method is based on precursors containing a metal or a metalloid element bonded to either on organic or inorganic ligands which do not contain other metals or metalloids. The use of metal alkoxides is traditionally more common, but metal salts such as nitrates or chlorides are also used [200,202]. A metal alkoxide has the general chemical formula $M(OR)_z$ where *z* designates the valence state of the metal M bonded to an oxygen atom O of the alkoxide, which by its turn is bonded to an alkyl R, with general formula C_nH_{2n+1}. The fact that the metal atom is bonded to the oxygen, and not directly to the organic molecule, distinguishes the metal alkoxides from the organometallic compounds. The reason why metal alkoxides are so used in the sol-gel process is essentially because of how easy they react with water, by hydrolysis. Depending on the amount of water (*x*), the hydrolysis reaction can be more or less complete:

$$M(OR)_z + xH_2O \rightarrow (OH)_xM(OR)_{z-x} + xROH \qquad \text{Eq. (2.1)}$$

The several partially hydrolysed molecules can polymerize into larger and larger molecules in a condensation reaction such as:

$$(OR)_{z-x}M(OH)_x + (OH)_xM(OR)_{z-x} \rightarrow (OR)_{z-x}M - O - M(OR)_{z-x} + xH_2O \qquad \text{Eq. (2.2)}$$

or

$$M(OR)_z + (OH)_xM(OR)_{z-x} \rightarrow (OR)_{z-x}M - O - M(OR)_{z-x} + xROH \qquad \text{Eq. (2.3)}$$

This process is called *hydrolysis* which produces the colloidal suspension (*sol*) of several small molecules [200]. Afterwards, the process of polymerization and gelation is characterised by the growth of these molecules, reaching macroscopic dimensions throughout the solution (commonly catalysed by decreasing the pH of the sol), until the point when no more molecules can be bonded, producing solid porous network containing a liquid phase – this is called a *gel* [200,203]. Typically, the interest is to isolate the *gel* from the liquid phase to be processed, thus obtaining a dry gel (*xerogel*) or an *aerogel*. These types of gels are interesting because of their high porosity and surface area which makes them useful for catalytic substrates or filters, but traditionally the purpose is to process them into ceramics [200]. The gels are generally amorphous (even after being dried and calcinated), therefore requiring a heating process at a temperature high enough to promote the sintering and the crystallization of the ceramic. Figure 2.1 is a scheme inspired in many similar illustrations [200] that synthesizes most of the sol-gel different stages and processes.

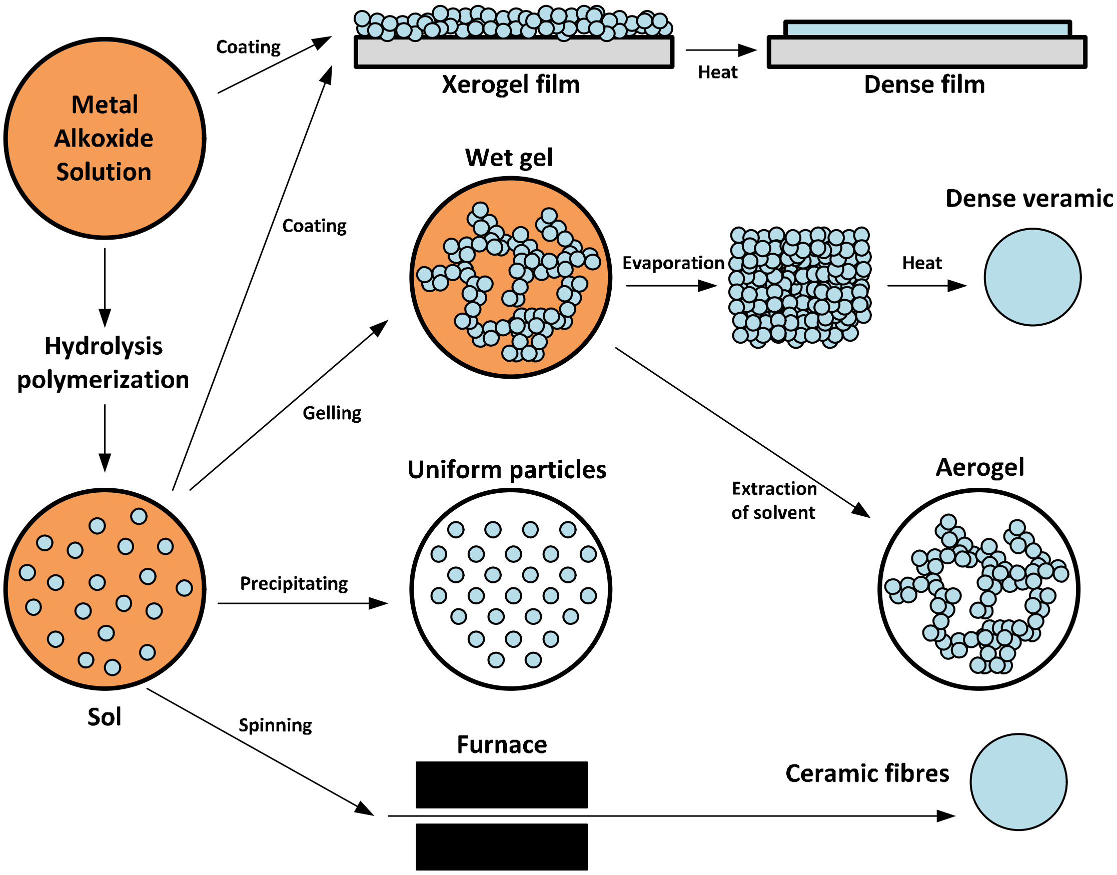
Coating
Xerogel film
Heat
Dense film
Metal Alkoxide Solution
Wet gel
Dense veramic
Coating
Evaporation
Heat
Hydrolysis polymerization
Gelling
Uniform particles
Extraction of solvent
Aerogel
Precipitating
Sol
Spinning
Furnace
Ceramic fibres

Figure 2.1 – Schematic representation of common routes of the sol-gel process (inspired in a similar scheme from Brinker and Scherer [200]).

Despite the common use of metal alkoxides as precursors, many of them are hard to obtain and handle because of their high hygroscopic properties and difficulty in controlling their hydrolysis rate, which is essential to prepare multi-component ceramics [202]. As stated previously, metal salts are an alternative. These compounds, which include chlorides, nitrates, sulphides and acetates, are usually cheaper and easier to handle, and therefore very interesting for the sol-gel route. In this case, the metal salts can form metal complexes by promoting the chelation of the metal ions by organic ligands [202].

Pechini's method, patented in 1967 by Maggio Pechini [204], was originally developed as an alternative method to improve the production of dielectric materials in the thin-film form, composed by two or more metal oxides, for the capacitor industry. This method is one of the of sol-gel process type. Traditionally, metal salts are used as precursors along with citric acid to promote the complexation into metal citrates. Citric acid is generally used because of the high stability of the metal complexes, due to the strong coordination between the metal cations and the citric ion, but other hydrocarboxylic acids may also be used [202]. The polymerization of these complexes is then promoted using a glycol, such as ethylene glycol, which happens along with a condensation reaction [202]. This reaction process is promoted by heating the sol at low temperatures, usually below 100 ^{o}C. After the gel point is reached (defined by the point in time when the mixture forms a rigid substance, removable from its recipient), the compound is dried and calcinated to obtain a crystalline ceramic, or deposited into a substrate to obtain a ceramic film. A modified Pechini's method is also commonly used, characterized by the replacement of the chelating agent, such as the citric acid, by ethylene diamine tetraacetic acid (EDTA), justified by its stronger chelating power, which generally results in an improved uniformity of the metal ions in the solution [202].

Because of low temperatures, the simplicity of the experimental apparatus, the versatility and possibility of depositing highly homogeneous thin-films, this route is an attractive and energy-saving alternative in preparation of ceramic materials (but also glasses). More specifically, it offers the possibility of having highly pure materials with homogeneous compositions, since the mixing of metal cations is done at a molecular level [202]. There have been numerous works in literature regarding the synthesis of materials with different properties using the Pechini's method [73,120,166,205,206].

2.1.3 Laser Floating Zone

Single crystals are basic elements of many of the modern technological devices. They are used in lasers, electro-optic, piezoelectric, electronic devices, and even in a simple wristwatch.

The interest in the production of single crystals, in the context of this work, is related with the knowledge of the fundamental properties of the materials in bulk, having them as reference for comparison with samples synthesized through other methods. When synthesizing a crystalline material, the nucleation and growth of particles happen through the three-dimensional addition of atoms that form the crystals. However, these small crystals, which eventually get merged, into what is called a "crystallite", do not mandatorily organize themselves along the same crystal direction and do preserve lattice defects that are related to their surface or grain boundaries. The existence of structural defects usually produces non-optimized, or even undesirable, physical properties. Furthermore, a random crystal orientation does not allow us to take advantage of an anisotropic property. Silicon, which is the basis of Electronics and also used in solar-cells [207], as well lithium niobate which is generally used as an optical modulator [208], are good examples of how single crystalline materials are important.

In polycrystalline samples, each crystallite in a grain can be seen as a single-crystal. Therefore, the actual difference between a single and a polycrystalline sample is the size of the crystal [209].

The methods to grow single crystals are considerably different than for polycrystalline and amorphous samples. Since the purpose is to restrict the growth of a single nucleus, most of these methods are typically based in the growth from a melt material using a seed crystal. One of the most used methods to grow single crystals was developed by the Polish scientist Czochralski in 1916. His eponymous process, is widely used for the electronic industry in the production of silicon ingots, which are cut into wafers afterwards, but also for the production of niobate based semiconductors such as $Ca(NbO_3)_2$ [198,209].

In the Czocharslki method, the material which is aimed to be grown is kept melted, slightly above its melting point, in a heated crucible. Then, a crystalline seed of that material is put into contact with the surface of the melt and gradually pulled out, which will make the melt to cool and grow along the crystalline orientation of the seed. During this process, the melt and the growing crystal are usually being rotated in order to keep the melt uniform and at a constant temperature [198].

Among others, the Laser Floating Zone (LFZ) method (also known as Laser Heated Pedestal Growth (LHPG)), which is similar to the Czochralski process, also allows the production of high quality single crystals under controlled growth parameters. Particularly, it is a very popular technique for growing materials from the melt in a crucible free device, thus avoiding most of the contaminations. On the other hand, the maximum diameter and length of the crystals grown by LFZ is technically limited. In the system used in this work, it is possible to grown fibres with diameters approximately between 1 and 5 mm of diameter and ~10 cm of length in the best cases. The most important considerations that have been reported and discussed in the literature, regarding the stability of the crystal growth in LFZ, are typically the conservation of mass, balance of heat transfer, the capillary shaping stability and also segregation [210]. These considerations are related to several factors such as the feed rod characteristics, power of the laser, atmosphere and gas pressure, pulling rates, rotation speeds, the radius of the rods and molten zone length. Furthermore, alignment problems in LFZ can produce internal tensions between the crystal and the molten zone resulting in a low quality crystal, cracks formation or simply growth failure by breaking one of the rods [210,211].

The LFZ method requires two rods – one is the crystalline *seed*, and the other the *feed rod* made of the precursor material which is melted by the focused laser beam. Figure 2.2 illustrates a simplified scheme of the LFZ technique with the type of apparatus as used in this work. A CO_2 laser source with 200 W of maximum power, with controllable output, is directed to reflexicon, which is a reflecting system based on conic mirrors that turns a linear laser beam into an annular beam. Using flat and parabolic mirrors, the laser beam is focused on the feeding rod as illustrated by the red arrows in Figure 2.2. Controllable step motors coupled to metallic beams, are responsible for the rotational and translational movement of the rods.

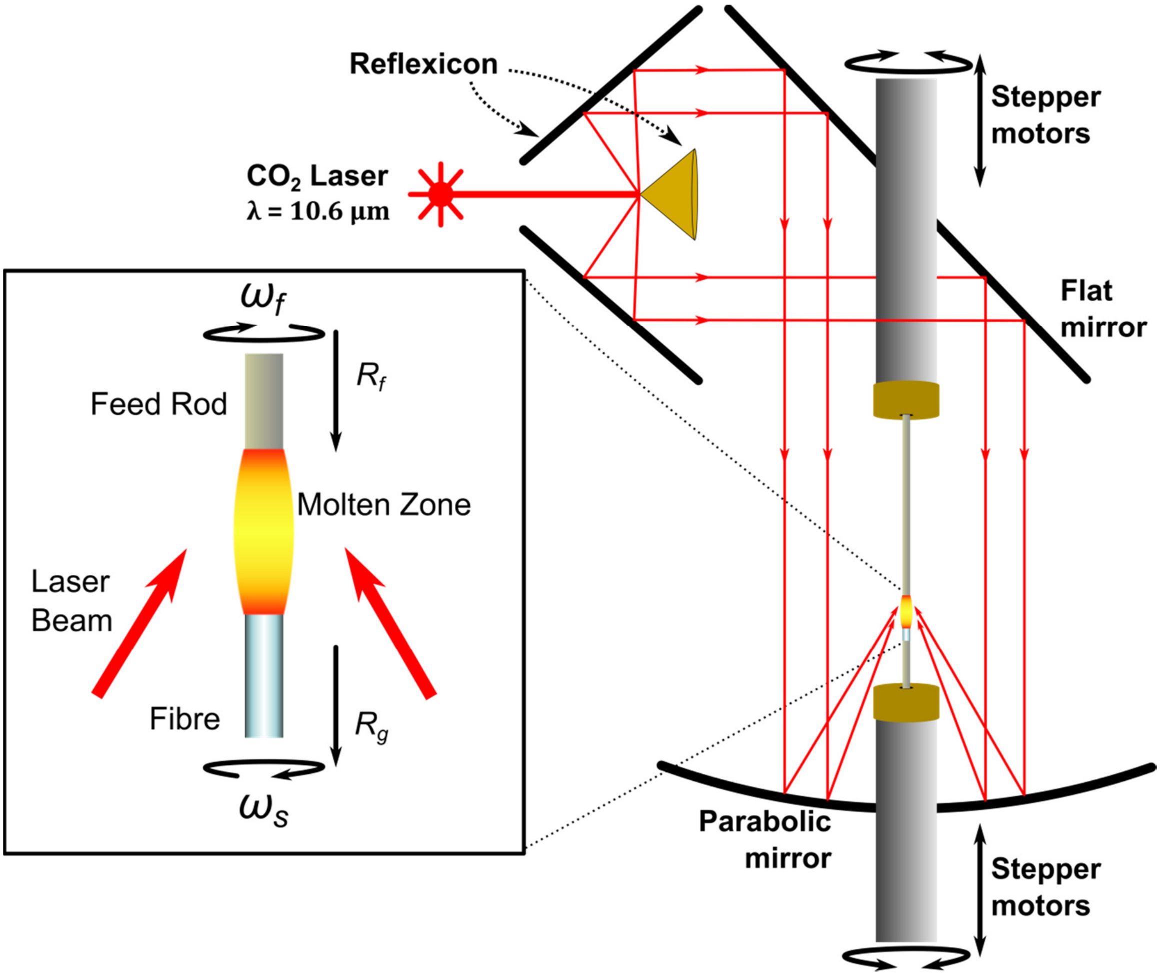
Reflexicon
CO_2 Laser
$\lambda = 10.6\ \mu m$
Stepper motors
Flat mirror
Parabolic mirror
Stepper motors
ω_f
R_f
Feed Rod
Molten Zone
Laser Beam
Fibre
R_g
ω_s

Figure 2.2 – Schematic representation of the Laser Floating Zone (LFZ) technique.

As the melted zone is pulled out by the seed, at a certain rate of growth R_g, it will cool and form a crystalline fibre. The feed rod is pulled in the same direction of the seed but not necessarily at the same rate. The rate of feeding R_f is actually common to be higher than the rate of growth, since the density of the crystal is usually higher than the feeding rod and also because there are material losses, in the form of gases, in the molten zone. In LFZ, the growth of the crystal can be done upwards or downwards, mostly depending on the material it is intended to grow. Generally, the lower the growing rate the greater the quality of the crystal, since the time available for the atoms to organize is higher. However, it is possible to achieve single crystalline fibres with speeds of several dozens or even hundreds of mm/h, which is considerably faster than the maximum speeds achievable with other methods [212]. As in Czochralski method, in LFZ the seed and the feeding rod are usually, but not always, rotating with angular speeds of ω_s and ω_f, respectively, with the same purpose of homogenising the mixture and temperature in the molten zone. The molten zone is sustained by the two solid rods, seed and precursor, and by its own surface tension.

The precursors are prepared by mixing the powders of the desired compound with a mechanical binding agent, in this case polyvinyl alcohol (PVA), in order to form an homogenous and consistent dough. This dough is subsequently cold extruded into a cylindrical fibre, and put immediately after in a support with grooves which helps the wet extruded fibres to get dry without getting bended. This drying process usually takes about one week and it is performed at air and at room temperature.

The LFZ system available in the UA Physics Department laboratories was developed and built by the research group of Professor Florinda Costa and is fully electronically controlled through a graphical interface. Before starting the growing process, it is very important to assure a good alignment between the two rods. This is done with the help of a digital video camera pointed to the focus point of the laser, where the molten zone will be created. After this, the chamber is closed, the laser is turned on and a security shutter is opened. The minimum power output of the CO_2 laser is 14 W. With this power, it is already possible to notice the rod becoming incandescent, but not melted. The power is slowly increased until a drop is formed, which can vary from 20 W up to close to 200 W (the maximum power output of laser), depending on melting point of the material and viscosity of the drop. This process is usually performed with the rod rotating to homogenize the temperature. The drop is then put into contact with the seed rod, after which the growing process can begin – the pulling and feeding rates, and also the rotating speeds, are defined. It is possible all these parameters have to be tuned during the first minutes of the growth until the stability is achieved. To end the crystal growth, the laser power can be simply turned off, or gradually decreased if the material is sensitive to abrupt changes of temperature (originating internal tensions or cracks).

2.2 Characterization techniques

2.2.1 Differential Thermal Analysis

A thermal analysis is based on the measurement of physical or chemical properties of a certain material as a function of temperature. In solid state science, this type of analysis is particularly important in the study of solid state reactions, thermal decompositions, phase transitions and determination of phase diagrams. There are different types of thermoanalytic techniques. The thermogravimetric analysis (TGA) is a technique that allows us to measure the change of mass of a sample as a function of temperature and time. The differential thermal analysis (DTA) measures the difference of temperature ΔT between the sample and an inert reference as a function of temperature. The differential scanning calorimetry (DSC), similar to DTA, allows us to measure quantitatively the enthalpy change of a sample as a function of temperature. The thermodilatometric analysis (TDA), also known as dilatometry, is another useful thermoanalytic technique that records changes in the dimension of the sample with temperature [198].

DTA is generally a more versatile technique than the TGA since it is able to detect the same phenomena that the TGA (which involve mass change) and in addition detects structural changes (crystallizations and polymorphs changes). DTA can thus detect every phenomenon that has an effect in the sample temperature, while TGA detects only phenomena that involve mass change. This does not mean that TGA is not useful, on contrary, because this type of analysis helps us to identify the *type* of phenomena if both techniques (DTA *and* TGA) are performed. Furthermore, TGA may give us the information of the average stoichiometry of a sample at a certain temperature if we know the initial stoichiometry and that the mass gain is only due to an oxidation (or reduction). This is particularly useful in the case of niobium oxides study. However, it was not possible to have access to a TGA equipment during this work.

To perform a DTA, it is necessary not only the sample to be analysed but also one reference sample (inert sample) in a heating system placed side by side, to minimize temperature differences, which will be heated (or cooled) at a constant rate. Two identical thermocouples must be connected in a *back to back* configuration and placed in each sample holder. Figure 2.3 illustrates a typical DTA setup. In our laboratory we have available a *Linseis Aparatus* DTA equipment, that can measure from RT up to 1600 °C. We use alumina crucibles to hold the sample and the reference. The system needs to be calibrated, typically with 20 to 40 mg of Al_2O_3, submitted to a constant heating rate. Using the same mass of sample and the same heating rate as in calibration, the difference of potential between the thermocouples, as illustrated in Figure 2.3, is recorded as a function of temperature of the furnace (recorded by a third separate thermocouple). In this way, it is possible to identify endo and exothermal phenomena by correlation with the difference of potential (ΔV) between the thermocouples (i.e. a difference of temperature ΔT), which positive or negative signal will depend on the thermocouples connection setup.

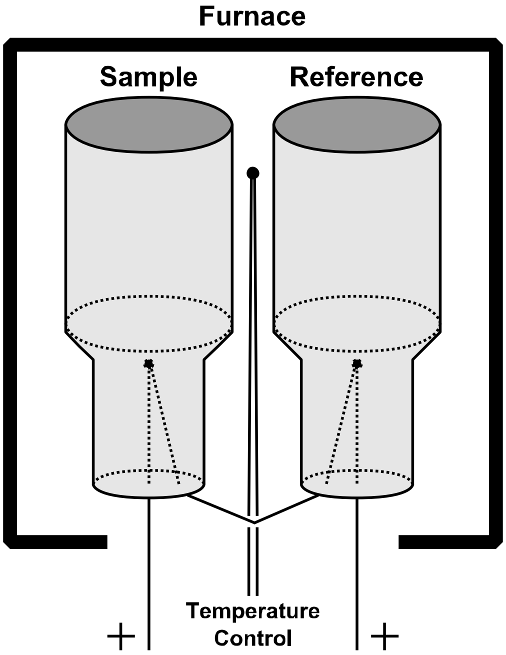

Figure 2.3 – Typical DTA experimental arrangement.

Essentially, the information that we want to obtain with the DTA is to identify and understand at which temperatures, or temperature range, it occur oxidations, crystallizations and phase transitions for a certain sample, crossing the acquired data with other types of characterizations. This type of information is essential in the first steps of a certain material's study, in this case niobium oxides.

2.2.2 X-Ray Diffraction

X-Ray diffraction (XRD) is one the most important experimental techniques in solid state science research. This type of analysis gives us crystallographic information such as crystallinity, crystal orientation, phase identification, and with advanced analysis, other types of information such as lattice parameters or semiquantification of phases [198,213,214].

The type of information we can get with XRD is ultimately related with the distance between the crystalline planes of our sample. We can get a quantitative measure of this distance based on the diffraction phenomenon. Since the distance between atoms in a crystalline structure is typically in the order of angstroms (Å), we should use wavelengths in that order of magnitude, such as X-Rays. There can be different sources of X-Rays, but maybe the most common is to accelerate highly energetic electrons (in the order of keV) into a copper (Cu) target. As some of the *1s* electrons of the Cu atoms are removed from their orbital, a radiative transition occurs thus producing an X-Ray photon. In this work, all the XRD experiments were performed with the K_α line of Cu, with a wavelength λ = 1.5418 Å. One should notice that, despite all the filters and cares to make the X-Ray beam monochromatic, it never is.

The X-Rays are directed into the sample, where they are diffracted into different directions. In order to have the waves, in this case electromagnetic, interfering constructively they must reach the detector in phase. Thus, the diffraction of a wave in a crystal follows the Bragg law [213], given by:

$$2d \sin\theta = n\,\lambda \qquad \text{Eq. (2.4)}$$

where *d* is the crystal interplanar distance, θ the diffraction angle, *n* is order of the diffraction and λ the wavelength. Figure 2.4 help to interpret this condition.

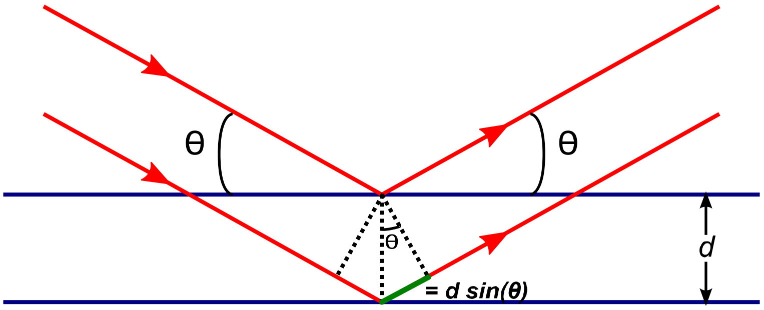

Figure 2.4 - Bragg's Law graphical interpretation (adapted from [213]).

We can interpret the Bragg law trough a geometrical formulation called Ewald's sphere (Figure 2.5), which radius is given by the reciprocal of the wavelength, helping us to understand if the diffraction by a certain indexed *hkl* plane may be observed, depending on crystal structure and orientation and wavelength.

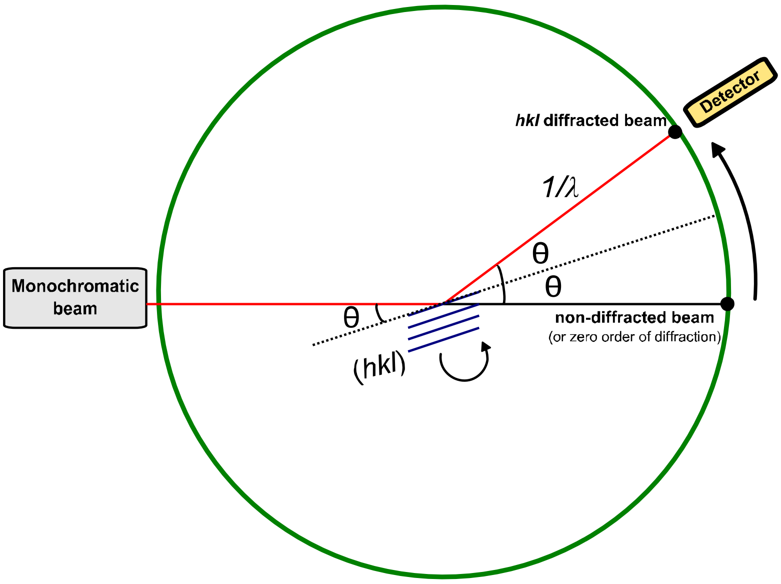

Figure 2.5– General representation of Ewald's sphere (adapted from [213]).

Depending on the type of sample (powder or single crystal) and the type of detector and recording methods, there are different methodologies for the structural characterization based on the same XRD principle [198,213]. One of the most common techniques is the powder XRD which, using a Philips X'Pert powder difractometer, was one of the most frequently used in this work. In powder XRD the sample is in the form of powder and therefore we can consider that the crystals are arranged randomly in every direction. Thus, not all the crystals will be contributing for diffraction, but for a certain Bragg angle θ there should be at least a set of crystal planes oriented in such a way that produce a diffraction maximum.

In a powder XRD system measurement, the X-Rays source is usually fixed at a position, as both sample and detector rotate to change the angle of incidence and detection, at the same rate, so we can cover a certain range of diffraction angles. That is why the intensity of the scattered X-Rays is measured as a function of 2θ (the angle between the non-diffracted and diffracted beam) and not θ, as Figure 2.5 illustrates. In most cases, an XRD pattern recorded between 10 and 60 º is typically enough to get most of the information it is needed. Measurements for high 2θ angles (more than 90 º) are possible to perform, though one should avoid the sample to fall out from the sample holder, but it is also an angle after which the negative orders of diffraction will start to be detected. Below 10 º the signal/noise ratio is typically very low.

The most common data treatment performed after recording a XRD pattern is to identify the crystalline phase of the samples by using a database and an analysis software that crosses information regarding the relative intensity and position of the diffraction maxima. In this work, a database from International Centre for Diffraction Data (ICDD) was used. This analysis may help to identify one or more crystalline phases present in the studied samples but, with advanced analysis, it is possible to get more types of information, such as the lattice parameters of the crystals.

The structure factor F_{hkl}, which gives the amplitude of the wave scattered along an *hkl* direction [213] (result of the constructive and destructive interferences of the waves scattered by the crystal), is given by

$$F_{hkl} = \sum_{j=1}^{N} f_i \, e^{i\,2\pi\,(hx_j+ky_j+lz_j)} \Rightarrow \; F_{hkl} = A_{hkl} + iB_{hkl}$$

$$A_{hkl} = \sum_{j=1}^{N} f_i \cos\left[2\pi\left(hx_j + ky_j + lz_j\right)\right] \qquad \text{Eq. (2.5)}$$

$$B_{hkl} = \sum_{j=1}^{N} f_i \sin\left[2\pi\left(hx_j + ky_j + lz_j\right)\right]$$

One can verify that for a face centred cubic lattice, where each atomic position (x,y,z) has the (x,y+1/2,z+1/2), (x+1/2,y,z+1/2) and (x+1/2,y+1/2,z), the structure factor is zero for planes defined by combinations of odd and even Miller indices, for instance (1,0,0), (1,1,0), (2,1,0) or (2,1,1). A presence of a forbidden diffraction maximum may indicate a structure with defects, distorted and/or with tensions [213].

With the indexing of the powder patterns, we can perform a unit cell refinement. This consists in calculating the lattice parameters of our crystal unit cell by determining the interplanar distance of an indexed plane *(hkl)*. The interplanar distance can be simply calculated using Bragg's law, Eq. (2.4), where 2θ is the centre of the respective diffraction maximum [213]. Depending on the crystal system, we may need at least one, two or three planes. In the case of the cubic system, given its symmetry we only need to measure one interplanar distance to calculate the lattice parameter a:

$$\frac{1}{d^2} = \frac{1}{a^2}\left(h^2 + k^2 + l^2\right) \qquad \text{Eq. (2.6)}$$

The precision of these calculations are highly dependent on the quality of the recorded XRD spectra, i.e. angular step and signal/noise ratio.

In 1918, Scherrer [215] suggested a method of correlating the broadening of the diffraction peaks with the crystallites size L responsible for that diffraction maximum. The general Scherrer formula is given by:

$$L = \frac{K\lambda}{\beta \cos \theta} \qquad \text{Eq. (2.7)}$$

where K is the Scherrer constant (or shape factor) which value depends on the sphericity of the crystallites [216] (typically considered 0.9 [198,213]), λ the wavelength of the X-Ray radiation, θ the Bragg angle and β the line broadening obtained from the Warren formula:

$$\beta^2 = \beta_M^2 - \beta_S^2 \qquad \text{Eq. (2.8)}$$

where β_M is the measured peak width in radians at half peak height and β_S the width peak of a standard material (commonly LaB_6) as a correction for the intrinsic system broadening [198].

The Scherrer formula was very commonly used and it is still a popular method, but recent works [217] have shown that it is in fact not reliable and is strongly suggested that its use should not be considered (as other similar methods).

The Rietveld refinement is a very popular and powerful advanced analysis technique, but relatively hard to use [218]. Essentially, the Rietveld refinement consists in the adjustment a theoretical model to fit the acquired XRD pattern, by a least squares approach. To perform this fit, the theoretical model encompasses several parameters that take into account different factors from which we can obtain information such as crystal lattice parameters, stress on the lattice or semiquantification of phases [213,214,218].

2.2.3 Scanning Electron Microscopy

The microstructural analysis of a sample is particularly important to allow us to correlate certain properties of a material with the synthesis parameters and techniques, and processing methods. The simple analysis of the structure and dimensions themselves may be essential regarding the aimed application, especially if it is micro or nano patterned.

Therefore, one should appeal to microscopic techniques to perform topological and morphological analyses. Optical microscopy is undoubtedly insufficient, constricted by physical and technological aspects, to offer a clear and detailed observation of features below the micron scale. The main disadvantages of optical microscopy are related to the low resolution limited by diffraction, and low depth of field. At best, a conventional optical microscope using visible light is limited to a maximum resolution of c.a. 200 nm. A way of overcome this would be using shorter wavelengths [219].

As an alternative to photons, high energy electrons can be used to obtain a microscopic image. The principle of the image formation is the same as for photons. The wavelength of the electrons is controllable by the acceleration voltage applied to the electron gun (typically in the order of kV), while the focus is assured by electromagnetic lenses which are usually more flexible and less limited than optical lenses. Thus, electron microscopy offers us the possibility of high resolution imaging and with a greater depth of field [219].

When a beam of electrons with a high and well defined energy is directed to a sample, electrons may or may not lose energy, i.e. they can be elastic or inelastic scattered. The ones which lose energy are responsible for different phenomena such as the emission of secondary electrons or Auger electrons, emission of electromagnetic radiation such as X-Rays or visible light, or even the production of plasmons (collective vibration of electrons) [219,220]. These phenomena have characteristic energies that range from few to hundreds of eV. The fact that these energies are characteristic of our sample makes their detection a useful characterization tool. For instance, the Energy-Dispersive X-Ray (EDX) analysis detects the emitted X-Rays thus allowing the chemical elements identification of the sample [219,220]. Figure 2.6 illustrates and synthesizes these different interactions and usefulness.

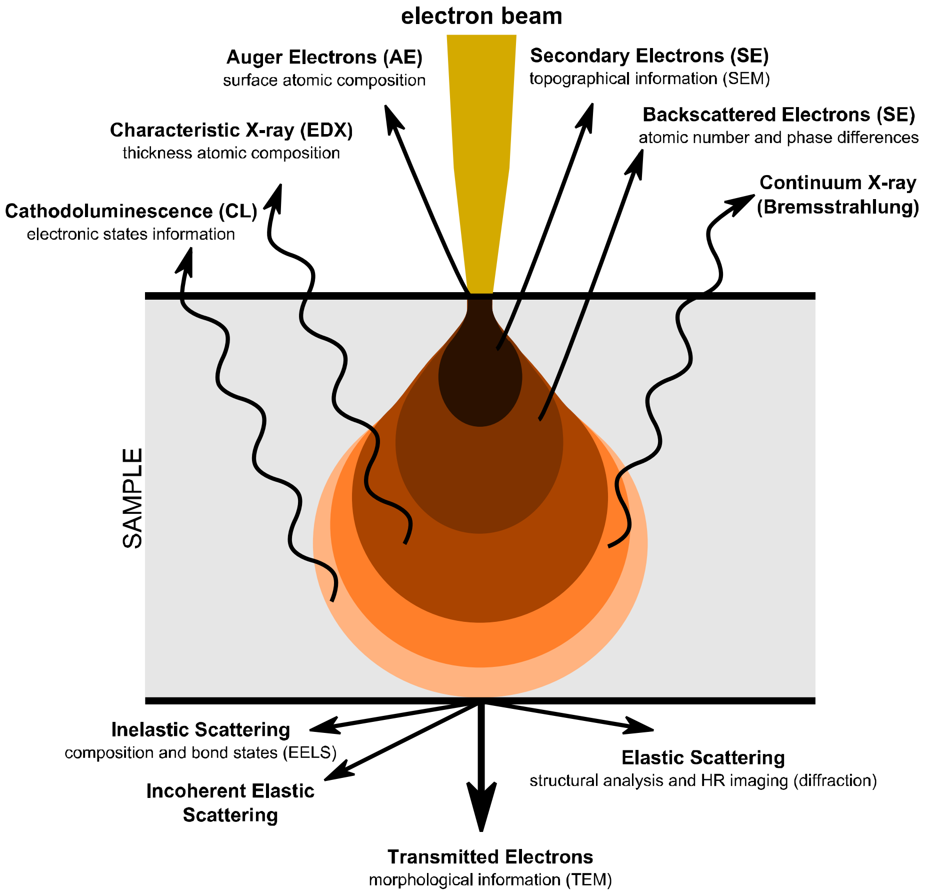
electron beam
Auger Electrons (AE)
surface atomic composition
Secondary Electrons (SE)
topographical information (SEM)
Characteristic X-ray (EDX)
thickness atomic composition
Backscattered Electrons (SE)
atomic number and phase differences
Continuum X-ray
(Bremsstrahlung)
Cathodoluminescence (CL)
electronic states information
SAMPLE
Inelastic Scattering
composition and bond states (EELS)
Incoherent Elastic
Scattering
Elastic Scattering
structural analysis and HR imaging (diffraction)
Transmitted Electrons
morphological information (TEM)

Figure 2.6 – Phenomena resulting of the interaction of high energy electrons with a sample (adapted from [221]).

Scanning electron microscopy (SEM) takes advantage of the secondary electrons emitted from the surface of the sample to form an image. Figure 2.7 shows a scheme of the fundamental components of a typical SEM microscope. At the top of the microscope column, a high voltage is applied to the electron gun (typically between 10 and 25 kV) in order to accelerate the electrons [219,220]. A set of controllable electromagnetic lenses, which consist on coils with high currents (water cooled), allow to focus the electron beam into the sample. Given the high energy of the electrons, it is extremely important that high vacuum is constantly kept inside the microscope column. This is usually assured by an ion pump. A secondary electron detector is responsible for obtaining the image of the surface of the sample and transmitting it to the computer. Similarly, the information that the backscattered electrons and the characteristic X-Rays may offer, can be obtained by specific detectors [219,220]. If the sample which is being studied in an electronic microscope is not electrical conductive enough, the electrons from the focused beam tend to accumulate at its surface, thus creating a charge barrier that prevents us to obtain a high quality image. To avoid this, the sample can be covered by a very thin layer of a conductive material such as carbon (from a graphite bar), or gold, typically using the sputtering technique [219,220]. In this work, the SEM microscopes that were used were a S4100 from Hitachi and also a Vega3 SB from TESCAN.

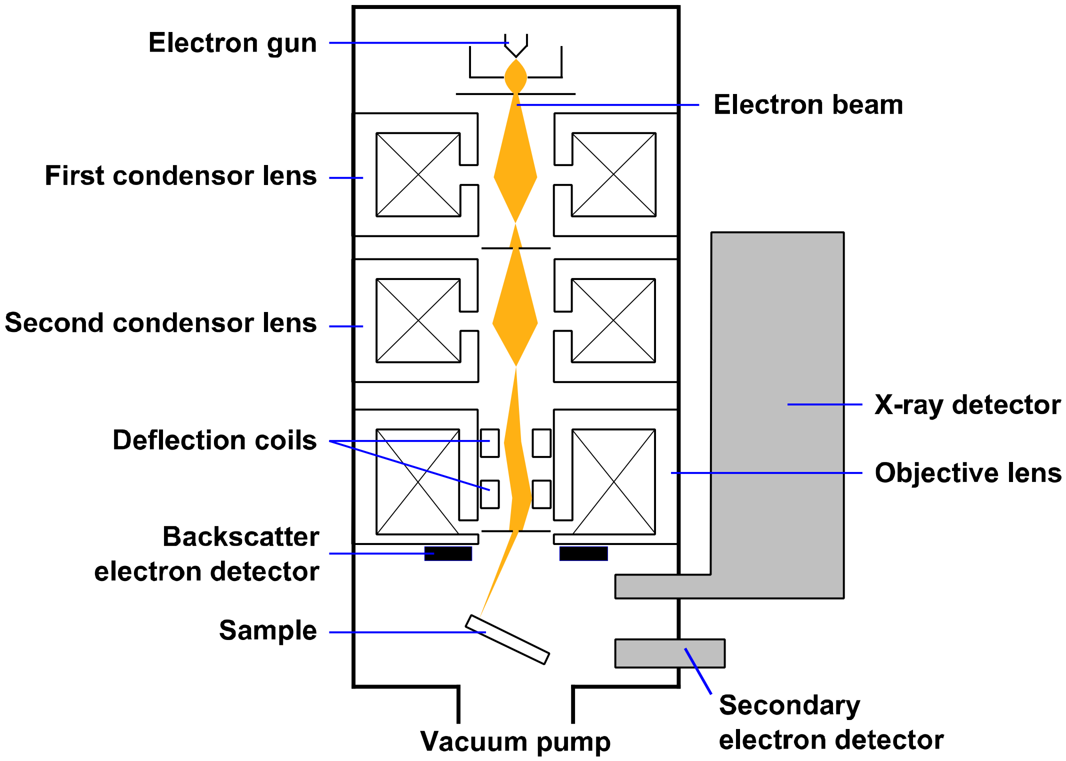
Electron gun
Electron beam
First condensor lens
Second condensor lens
X-ray detector
Deflection coils
Objective lens
Backscatter electron detector
Sample
Secondary electron detector
Vacuum pump

Figure 2.7 - Scanning Electron Microscope scheme [222].

2.2.4 *Raman Spectroscopy*

Raman spectroscopy along with infrared spectroscopy, are optical techniques that allow the study of the vibrational modes of crystal lattices. These normal modes of atomic vibrations, *phonons*, have characteristic energies depending on the local symmetry, structural defects or tensions, chemical elements, bonding states and neighbouring atoms, which justifies the fact that Raman spectroscopy is one of the most important techniques in materials physics and chemistry. The fact that it is a non-destructive technique and that it does not require a sample pre-processing to perform the analysis, make this technique particularly interesting.

In order to explain the physical principles on which Raman spectroscopy is based, it is common, to use as an example the simple case of an isotropic crystalline material with an electric susceptibility χ [223,224]. Considering a classic description of an intense monochromatic beam of radiation (focusing on such material) with a wavevector $\boldsymbol{k}_i$ and frequency ω_i, the sinusoidal plane electromagnetic field $\boldsymbol{F}(\boldsymbol{r},t)$ will induce a polarization $\boldsymbol{P}(\boldsymbol{r},t)$ [224]:

$$\boldsymbol{F}(\boldsymbol{r},t) = \boldsymbol{F}_i(\boldsymbol{k}_i,\omega_i)\, cos(\boldsymbol{k}_i \cdot \boldsymbol{r} - \omega_i t) \qquad \text{Eq. (2.9)}$$

$$\boldsymbol{P}(\boldsymbol{r},t) = \chi(\boldsymbol{k}_i,\omega_i) \cdot \boldsymbol{F}_i(\boldsymbol{k}_i,\omega_i)\, cos(\boldsymbol{k}_i \cdot \boldsymbol{r} - \omega_i t) \qquad \text{Eq. (2.10)}$$

However, due to the thermally excited atomic vibrations, with a wavevector $\boldsymbol{q}$ and frequency ω_0, described by

$$\boldsymbol{Q}(\boldsymbol{r},t) = \boldsymbol{Q}(\boldsymbol{q},\omega_0)\, cos(\boldsymbol{q} \cdot \boldsymbol{r} - \omega_0 t) \qquad \text{Eq. (2.11)}$$

the electric susceptibility χ will suffer small variations. Assuming that the atomic vibrations are much slower than the electronic vibrations (quasi-static approximation), and considering that, at room temperature, the amplitudes of the atomic vibrations are very small, one can consider the Taylor expansion of χ as a function of $\boldsymbol{Q}$ [223]:

$$\chi(\boldsymbol{k}_i,\omega_i,\boldsymbol{Q}) = \chi_0(\boldsymbol{k}_i,\omega_i) + \left(\frac{\partial\chi}{\partial\boldsymbol{Q}}\right)_0 \boldsymbol{Q}(\boldsymbol{r},t) + \cdots \qquad \text{Eq. (2.12)}$$

Thus, replacing Eq. (2.12) in Eq. (2.10), one can prove [224] that the induced polarization by the electromagnetic wave is given by:

$$\boldsymbol{P}(\boldsymbol{r},t,\boldsymbol{Q}) = \boldsymbol{P}_0(\boldsymbol{r},t) + \left(\frac{\partial \chi}{\partial \boldsymbol{Q}}\right)_0 \boldsymbol{Q}(\boldsymbol{q},\omega_0)\, cos(\boldsymbol{q}\cdot\boldsymbol{r} - \omega_0 t)$$
$$\times\, \boldsymbol{F}_i(\boldsymbol{k}_i,\omega_i)\, cos(\boldsymbol{k}_i\cdot\boldsymbol{r} - \omega_i t)$$
$$\Leftrightarrow\; \boldsymbol{P}(\boldsymbol{r},t,\boldsymbol{Q}) = \boldsymbol{P}_0(\boldsymbol{r},t) + \frac{1}{2}\left(\frac{\partial \chi}{\partial \boldsymbol{Q}}\right)_0 \boldsymbol{Q}(\boldsymbol{q},\omega_0)\, \boldsymbol{F}_i(\boldsymbol{k}_i,\omega_i) \qquad \text{Eq. (2.13)}$$
$$\times \{\, \cos[(\boldsymbol{k}_i + \boldsymbol{q})\cdot\boldsymbol{r} - (\omega_i + \omega_0)\cdot t$$
$$+\;\; \cos[(\boldsymbol{k}_i - \boldsymbol{q})\cdot\boldsymbol{r} - (\omega_i - \omega_0)\cdot t]\;\; \}$$

The induced polarization is therefore described by $\boldsymbol{P_0(r,t)}$ that correspond to dipoles oscillating at the same frequency ω_i as the incident radiation (Rayleigh scattering), and to dipoles oscillating at frequencies $\omega_i - \omega_0$ and $\omega_i + \omega_0$ corresponding to the radiation classified as Stokes Shift and Anti-Stokes Shift, respectively. In this case, the energy and momentum are conserved, if the scattered photons have energy and moment respectively expressed by [223,224]:

$$\hbar\omega_{scattered} = \hbar\omega_i \pm \hbar\omega_0 \qquad \text{Eq. (2.14)}$$

$$\hbar\boldsymbol{k}_{scattered} = \hbar\boldsymbol{k}_i \pm \hbar\boldsymbol{q} \qquad \text{Eq. (2.15)}$$

Therefore, Stokes scattering requires a phonon creation, while Anti-Stokes requires a phonon annihilation [223,224]. Since the wavevector of a phonon is very small (typically about 1/100 of the size of the Brillouin zone in a semiconductor) [224], it can be considered that $\boldsymbol{q} \cong 0$ and hence that the first order Raman spectra probes phonons only in the zone-centre of the first Brillouin zone [224].

The origin of the Raman scattering processes can be analysed as energy transitions between vibrational states and virtual states, promoted by the optical excitation, as illustrated by the diagram Figure 2.8. The Anti-Stokes scattering requires the optical excitation of phonons at a higher energy vibrational state than the Stokes scattering. Therefore, since the population N of a certain vibrational level with energy E follows a Boltzmann distribution, it is expected that the intensity of the Anti-Stokes scattering is smaller than the Stokes scattering. Thus, the ratio between the Stokes and Anti-Stokes scattering intensities I_S/I_{AS}, is a temperature dependent function and is described by [225]:

$$\frac{I_S}{I_{AS}} = \left(\frac{\omega_i - \omega_0}{\omega_i + \omega_0}\right)^4 e^{\frac{\hbar\omega_0}{K_B T}} \qquad \text{Eq. (2.16)}$$

where K_B is the Boltzmann constant. In Figure 2.8, it is illustrated an example of a Raman spectrum, showing the Rayleigh dispersion (at Raman Shift equal to zero) and the Stokes and Anti-Stokes scattering at $-\hbar\omega_0$ and $\hbar\omega_0$ Raman Shifts, respectively.

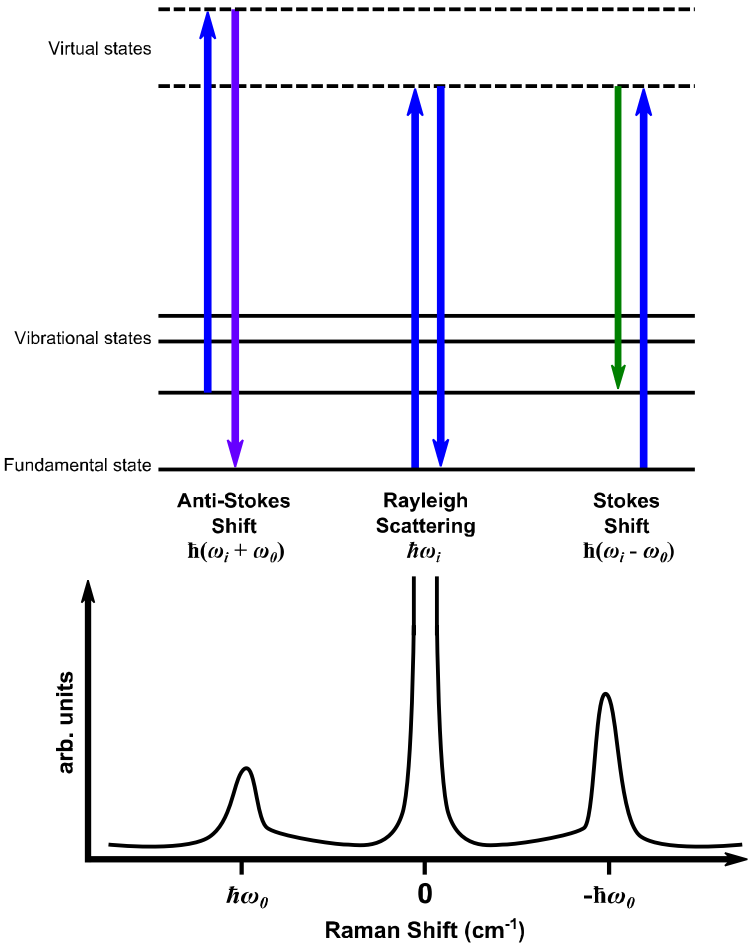
Virtual states
Vibrational states
Fundamental state
Anti-Stokes
Shift
ħ(ωi + ω0)
Rayleigh
Scattering
ħωi
Stokes
Shift
ħ(ωi - ω0)
arb. units
ħω0
0
-ħω0
Raman Shift (cm-1)

Figure 2.8 - Simplified energy level diagram showing the transitions involved in Raman signal (Stokes and Anti-Stokes) as well as the Rayleigh dispersion, and an example of a Raman spectrum.

The energies involved in the crystal vibrations are usually between 10 and 1000 cm^{-1} depending on the material (low energy vibrations corresponding to the inelastic scattering by acoustic phonons, Brillouin scattering, and the optical phonons at higher energies). Furthermore, the intensity of the Raman signal is typically very low when compared with the intensity of the elastic Rayleigh scattering. For these reasons, the Raman spectrometers typically comprise high quality and sensitive optical components. The Raman spectrometer of the Physics Department of UA, used in this work, is a *HR-800 Jobin Yvon (Horiba)* spectrometer which works in a backscattering geometry. Figure 2.9 illustrates a simplified schematic of this system, similar to other typical Raman spectrometers.

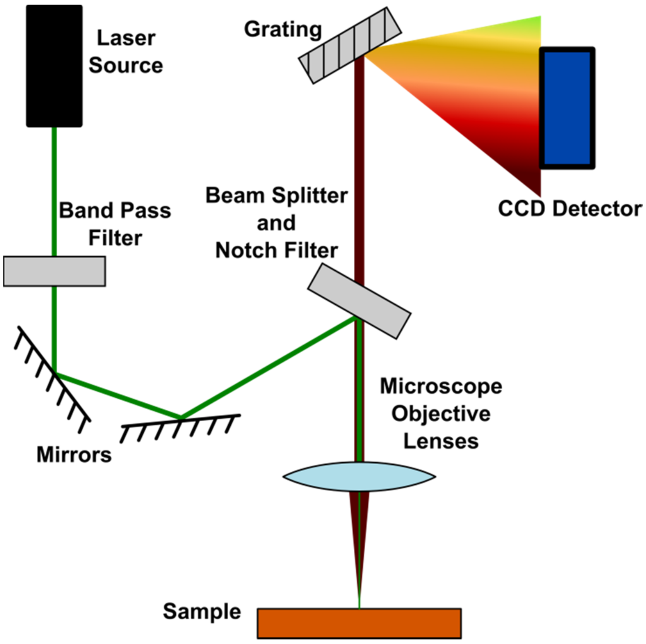

Figure 2.9 – Schematic of Raman spectrometer in a backscattering geometry.

Generally, the major components that comprise a Raman spectrometer are a continuous-wave laser (as the excitation source), a set of optical filters, mirrors and lenses (which allow to direct and to capture the light to and from the sample), a grating and a detector. The most recent systems typically use CCD detector as they allow fast and quality spectra acquisition. The light focusing and capture are usually assured by a microscope incorporated into the spectrometer, as they offer a ready-to-use and versatile optical system. In the case of the spectrometer used in this work, a band-pass filter is used to improve the monochromaticity of the excitation laser source. Another component which acts both as a beam splitter and notch filter is the key which allows us to work in a backscattering geometry, since it reflects the laser wavelength but allows other wavelengths to be transmitted to the grating.

2.2.5 Photoluminescence Spectroscopy

Luminescence spectroscopy may be described as the study of the radiation emitted from a sample as a result of electronic energy levels transitions, when excited by some sort of mechanism. While almost any type of material can produce some sort of luminescence, the most interesting and commonly studied are semiconductors and insulators. According on the type of excitation mechanism, we may classify the type of luminescence, i.e. *photo*luminescence (PL) with photon excitation (typically in the UV-Visible-IR range), *cathodo*luminescence with an electron beam (commonly associated with a SEM or TEM), *radio*luminescence with X-, α-, β-, or γ-rays, *thermo*luminescence with heat, *electro*luminescence with an electric field or current, *chemi*luminescence with a chemical reaction, *iono*luminescence with an ion beam, among others.

Focusing on photoluminescence, we should consider the interaction mechanisms of light with matter and understand how the radiation emitted by a given sample can be interpreted. When an electromagnetic wave reaches a sample it can be reflected at the surface, scattered elastically or inelastically (as described in chapter 2.2.4), or absorbed. The study of the absorption is particularly important for photoluminescence analysis since it allows us to know which frequencies of incident radiation are resonant with the electronic energy levels present in a semiconductor or insulator. To measure an absorption spectrum we need a light source emitting in a broad spectral range, a monochromator to select the wavelengths which will pass through the sample into the detector. The reflectance analysis is commonly performed as an alternative (or complementary technique) to absorption, especially when the sample is too thick or too thin, i.e. when the intensity of the absorbed or transmitted radiation is close to zero. When this happens, the reflectance analysis offers the possibility of obtaining correlated spectra, which can be related using the Kramers-Krönig relations [226]. The reflectivity measurement may be performed in a direct geometry, collecting the light reflected along the same direction of the incident radiation, or measuring the diffuse reflectivity where the light reflected on the sample along all directions is collected. For the latter, an integrating sphere is used, which assures that almost every light (entering through a pinhole into the sphere and into the surface of the sample where it is reflected) suffers multiple reflections in the sphere walls until it eventually reaches the sensor.

The analysis of PL spectra is a complex task. The luminescence of a semiconductor or insulator generally involves transitions between several electronic states related with the intrinsic or extrinsic material. Knowing which electronic states are being populated, from which states, through which mechanisms and their quantum efficiency, is the ultimate goal of a luminescence advanced analysis. Photoluminescence Excitation (PLE) spectroscopy is an extremely useful technique. While simple PL is usually performed with a monochromatic excitation source, while recording the emission intensity for different wavelengths, PLE consists in fixing the detection wavelength and record its intensity as a function of the excitation wavelength, typically using a broad spectral range source such as an incandescent or arc lamp. This allows us to determine which excitation wavelengths favour a certain electronic transition, i.e. emission band. Ultimately, it is possible to perform a PL/PLE analysis where both excitation and detection wavelengths are varied in order to obtain a three dimensional data of excitation vs. emission vs. intensity. Figure

2.10 illustrates such PL/PLE system, but it can also be interpreted as a schematic of a simple PL or PLE system, depending only on the acquisition procedure as explained before.

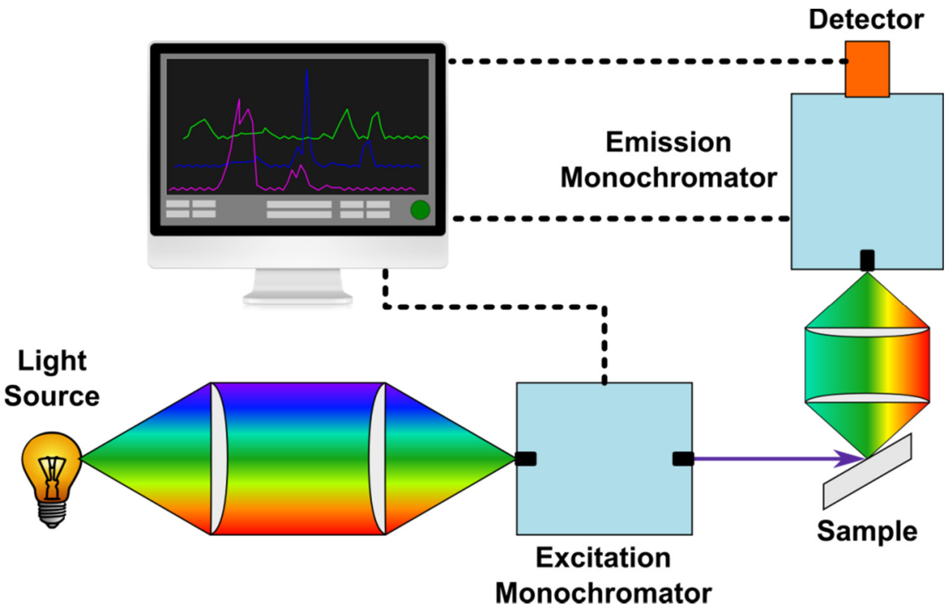

Figure 2.10 - Schematic of a typical PL/PLE experimental arrangement.

Photoluminescence spectroscopy is particularly interesting in the study of insulator and semiconductors, as some of them are particularly efficient in the emission from the conduction to the valence band and suited for light emitting devices. Semiconductors such as diamond, Si, Ge, SiC, GaN, ZnSe, CdS, CdSe, GaAs, and ternary and quaternary alloys, such as AlGaAs, InGaN, AlGaIN, AlGaAsP, and a series of oxides are broadly used in the industry of optical devices. With the development of nanotechnology, many of these materials gained a new interest as the ability to produce particles and structures at the nanoscale allows us to explore new materials functionalities mainly related to quantum confinement effects.

However, many interesting luminescent properties of inorganic materials come from the presence of lattice defects and doping which originate energy levels within the band gap. This type of centres, which can give rise to optical transitions at energies lower than the intrinsic energy gap of the host, are called optically active centres [226,227]. The interpretation of the optical features of a doping ion requires a good understanding of how its energy levels are affected by the local environment [226,227]. Generally, the energy levels E_i of a given optical centre require solving the Schrödinger equation:

$$H\psi_i = E_i\psi_i \tag{Eq. (2.17)}$$

where H is the Hamiltonian that represents the several interactions of the valence electrons of the optical centre and ψ_i the eigenfunctions [226].

In a real crystal, the optical centre should be considered a part of a dynamic lattice where the ion can participate in the collective vibrating modes. The fact that the ion is coupled to the vibrating lattice affects the electronic states of the centre and, reciprocally, the environment may be affected by the electronic states of the ion. The Hamiltonian should thus represent the interactions that the ion-lattice coupling comprises [226]:

$$H = H_L + H_{CF} + H_{FI} \tag{Eq. (2.18)}$$

where H_L describes the kinetic and potential energies of the lattice, H_{CF} the crystalline field which couples the electronic and ionic motion (thus depending on the coordinates r_i of the valence electrons and the coordinates R_l of the ligand ions), and H_{FI} which is related to the free ion and is expressed by:

$$H_{FI} = H_0 + H_{ee} + H_{SO} \tag{Eq. (2.19)}$$

where H_0 reflects the central electric field, from the nucleus and the inner and outer-shell electrons, acting on the valence electrons; H_{ee} the Coulomb interactions between the valence electrons; and H_{SO} the spin-orbit interaction [226].

The consideration of all these interactions, and consequently the fact that that the eigenfunctions depend both on r_i *and* R_l, make the solution of the Schrödinger equation quite complex. Therefore, two useful and reasonable approximations can be made. The adiabatic approximation [226] suggests that the ions move very slower that the valence electrons, since the nuclei are much heavier, and therefore we can consider that these motions can be represented independently:

$$\psi = f(r_i, R_l) \cdot \chi(R_l) \tag{Eq. (2.20)}$$

where $f(r_i, R_l)$ are the electronic wavefunctions and $\chi(R_l)$ the vibrational wavefunctions. This representation can be further simplified with a second approximation . If only one vibration mode is considered – the *breathing mode* – we can describe the radial vibration of the ligand ions with only one nuclear coordinate Q – the *configurational coordinate* [226]:

$$\psi = f(r_i, Q) \cdot \chi(Q) \tag{Eq. (2.21)}$$

Under these assumptions, the solution of the Schrödinger equation can be schematized as illustrated by Figure 2.11. The parabolas are approximations (at distances close the to the equilibrium coordinate) to Morse potential energy curves, which represent the interionic interaction, while the straight lines represent the discrete phonon levels [226].

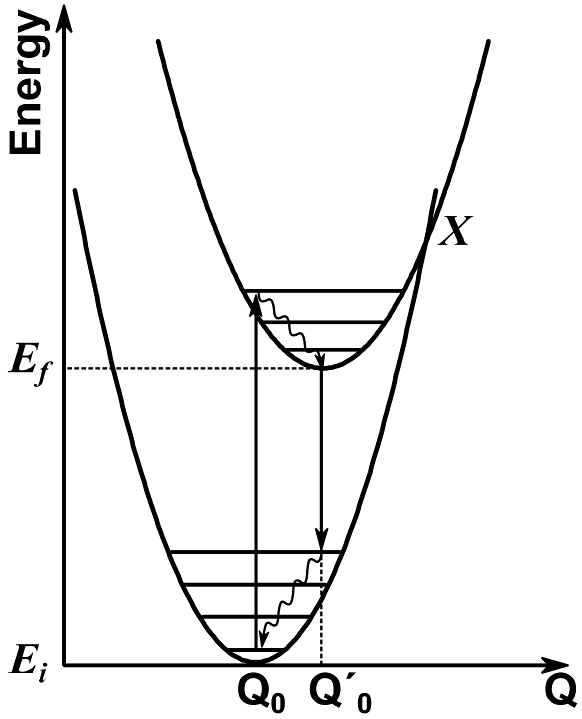

Figure 2.11 – Configurational coordinate diagram (adapted from [226]).

The upward straight arrow in Figure 2.11 represents an excitation of the optical centre from an initial at the equilibrium coordinates Q_0, to the final state. According to the adiabatic approximation, this type of transitions occurs very fast and therefore it should be considered at a constant coordinate Q (the Franck-Condon principle) [226]. As a consequence, when excited to the final state, the electron will need to relax non-radiatively to lowest energy E_f at Q'_0, from where it will go back to the initial state resulting in a radiative emission. The crossover point (marked with an X) is where the parabolas of both states cross, and its relative position is particularly important to evaluate the non-radiative phenomena for a given emitting centre [226,227]. The higher the difference between Q_0 and Q'_0 (usually expressed by the Huang-Rhys parameter S), the higher the electron-lattice coupling and, generally, the lower the energy of the crossover point X. The non-radiative processes are slower and therefore follow a change in the nuclear coordinate. Because of this, and the level degeneracy at X, if the electron is excited to an energy higher than the crossover point, the probability of de-excitation through phonon states of the initial state is higher, therefore decreasing the probability of a radiative emission. Similarly, the increase of temperature may decrease the radiative probability. The thermal population of higher energy phonon states increase the probability of reaching the energy of the crossover point, resulting in a thermally quenched luminescence [226,227].

If we consider other centres that are close enough to the optical active centre, such that a direct overlap of their electronic wavefunctions occurs, there can be an energy transfer without photon emission. These energy transfers may result in a different radiative or non-radiative emission, depending on the centres. Again, depending on the crossover point between the states of the two centres, energy transfer may be thermally promoted [226,227].

Defining the quantum efficiency, η, of a certain radiative transition, as the ratio between the radiative and total decay probabilities (A/A_T) [226]:

$$\eta = \frac{A}{A + A_{nr}} \qquad \text{Eq. (2.22)}$$

where A_{nr} is the non-radiative probability which (considering a classical approach model) follows a Boltzmann dependency with temperature, the quantum efficiency as a function of temperature may be expressed by:

$$\eta(T) = \frac{A}{A + C \cdot exp^{-\frac{E_A}{K_B T}}} \qquad \text{Eq. (2.23)}$$

where C is the temperature independent frequency factor, K_B is the Boltzmann constant and E_A the activation energy of the thermal extinction process. Assuming that at low temperatures the non-radiative transitions are negligible ($A_{nr} \cong 0$), i.e. $\eta = 1$, and that the intensity of the emission is proportional to the probability radiative transition, we can write [226]:

$$\frac{I(T)}{I_0} = \frac{1}{1 + C \cdot exp^{-\frac{E_A}{K_B T}}} \qquad \text{Eq. (2.24)}$$

Therefore, the study of photoluminescence at low temperatures and/or as a function of temperature is an important source of information which allows us to understand the non-radiative mechanisms and how do they affect the luminescence efficiency of a certain sample [226].

The previous analysis was considering a continuous wave excitation, in time, of a sample – *steady state photoluminescence*. However a time dependent photoluminescence analysis can give important information [226]. Considering an excited electronic state of an optical centre, the evolution of the population N of that level with time may be expressed by:

$$N(t) = N_0 e^{-A_T t} \quad \text{Eq. (2.25)}$$

where A_T is the total decay rate (or probability) which, as aforementioned, is the sum of both the radiative and non-radiative rates, A and A_{nr}:

$$A_T = A + A_{nr} \quad \text{Eq. (2.26)}$$

Since the emitted intensity $I(t)$ is proportional to the rate of de-population of a certain centre, one can write [226]:

$$I(t) = I_0 e^{-A_T t} \quad \text{Eq. (2.27)}$$

Therefore, performing a time-dependent photoluminescence analysis, we can find the total decay rate A_T, which can be expressed as the inverse of the luminescence lifetime τ:

$$\frac{1}{\tau} = \frac{1}{\tau_0} + A_{nr} \quad \text{Eq. (2.28)}$$

where τ_0 is the radiative lifetime of the respective transition. Therefore, from Eq. (2.22) one can write [226]:

$$\eta = \frac{\tau}{\tau_0} \quad \text{Eq. (2.29)}$$

Thus, lifetime measurements may give us information not only about the lifetime of a state, which can help to identify the type of state responsible for a certain radiative emission, but also about the non-radiative lifetime of a transition if quantum efficiency measurements are performed [226].

Furthermore, a time-dependent photoluminescence study may help to identify emissions with weak intensity masked by other emissions. If a strong emission and a weak radiative emission are superimposed, but having different lifetimes, it is possible to observe them separately at different time windows [226].

2.2.6 Electrical Measurements and Impedance Spectroscopy

Since one of the main subjects of this work is the study of materials with the potential application in electronic passive components, it becomes obvious the need of performing different types of electrical characterizations.

Coulomb's law describes how electrical charges interact and more generally defines that the charge carriers under a constant electrical field (or DC voltage) are submitted to a constant force, thus creating an electrical current. Ohm's law states that the current I passing through a sample is linearly related to the applied voltage V, changing at a constant rate which we call resistance R [228]:

$$V = R \cdot I \qquad \text{Eq. (2.30)}$$

Most, but not all, materials do follow Ohm's law, at least at a certain range of temperatures and current magnitudes. These are called *ohmic conductors*. Having this definition of resistance, we should define it as a function of the dimensions of a sample (considering it with a shape of a right prism):

$$R = \frac{\rho L}{A} \qquad \text{Eq. (2.31)}$$

where A is the area of the electrical contacts (base faces of the prism), L and is the length, and ρ the resistivity which is a physical characteristic of the material and independent of the sample shape and dimensions. This property is also commonly specified in terms of its inverse, i.e. the conductivity $\sigma = 1/\rho$, which relates the current density $\boldsymbol{j}$ and the electrical field $\boldsymbol{E}$:

$$\boldsymbol{j} = \sigma \boldsymbol{E} \qquad \text{Eq. (2.32)}$$

Another important electrical property of materials is their ability to be polarized. Any material presents this ability but is especially relevant in low conductive materials. There are different known mechanisms that are responsible for polarization [228]. As an applied voltage will force the electrons and nucleus of an atom towards opposite directions, this will create an electric dipole – this is called electronic polarization. In an ionic compound, the cations and anions will also be pushed in opposite directions under an applied voltage thus producing an additional contribution to the polarizability of the dielectric – ionic polarization. Similarly, polar molecules in a liquid can give rise to orientational polarization. The concentration of charged particle (electrons or ions) at interfaces such as grain boundaries can also originate what is called interfacial polarization. Finally, there are some materials classified as *ferroelectrics* (a sub class of *piezoelectric* materials) which present a spontaneous polarization, i.e., without applying an external electric field.

The polarization of a material as a function of the electrical field is expressed by:

$$\boldsymbol{P} = (\varepsilon - \varepsilon_0)\boldsymbol{E} \qquad \text{Eq. (2.33)}$$

where ε_0 is the vacuum permittivity and where ε is called the dielectric permittivity, characteristic of the material. On the other hand, the density of the current $\boldsymbol{j}$ is expressed as the variation of polarization with time:

$$\boldsymbol{j} = \frac{d\boldsymbol{P}}{dt} \qquad \text{Eq. (2.34)}$$

However, considering that the electric potential, i.e. the electric field, is constant with time (DC), the polarization will not change with time and therefore $j = 0$. From Eq. (2.32), this means that the conductivity σ will be zero for a DC voltage, which is a characteristic of an ideal capacitor, thus allowing to store energy in the form of polarized electric dipoles. Conventionally, regarding the capacitance property, the material at issue is classified as the dielectric. This ability of accumulating energy in the form of charge is called *capacitance* and expressed by:

$$C = Q/V \qquad \text{Eq. (2.35)}$$

where C is the capacitance for a voltage V, allowing to accumulate the amount of charge Q. Considering a parallel plate capacitor, with a certain dielectric material, and assuming that the width of the plates is much larger than the thickness of the dielectric (i.e. the electric field is uniform along the capacitor), the capacitance is given by:

$$C = \varepsilon_0 \varepsilon_r A/d \qquad \text{Eq. (2.36)}$$

where ε_r is the relative dielectric constant defined by $\varepsilon_r = \varepsilon/\varepsilon_0$, A the area of each parallel plate and d the distance between them [228].

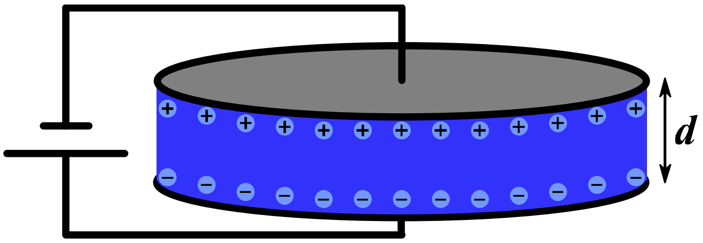

Figure 2.12 – Schematic representation of parallel plate capacitor

Ideally, if we apply a constant DC voltage to a capacitor, the charged particles on the sample will orientate along the electric field, but without allowing an electrical current to flow, i.e. $I_{DC} = 0$, thus accumulating charge. However, an AC voltage applied to a capacitor would make the dipoles on the dielectric to change their polarization. Therefore, a capacitor should ideally be highly resistive to DC current and highly conductive to an AC signal.

With an AC electric field the concept of resistance, as the relation between voltage and current, should be extended to the frequency/time domain into what is called impedance, designated by Z. Considering a general AC signal, with angular frequency ω, it can be described as a complex number for calculus simplification, using Euler's formula, by the following expression:

$$V(t) = V_0 \cdot \mathrm{e}^{i\omega t} \tag{Eq. (2.37)}$$

In an ideal resistance, we should consider $1/\omega \gg \tau$ (where τ is the average collision time of the charge carriers), and therefore the current in the resistance (I) follows Ohm's law [229]. Therefore, the impedance of a resistance Z_R can be expressed by:

$$Z_R = \frac{V(t)}{I(t)} = R \tag{Eq. (2.38)}$$

In the opposite case, when $1/\omega \ll \tau$, the time between collisions is much larger than the period of the AC signal. This means that we can assume a good response to polarization without dc conductivity, i.e. an ideal capacitor. Since the current is the variation of charge per unit time (dQ/dt), and the charge in a capacitor is given by Eq. (2.35), we can deduce and express the current that flows in an ideal capacitor by [230]:

$$\begin{gathered} I(t) = \frac{dQ}{dt} = \frac{d(CV)}{dt} = C\frac{dV}{dt} = C \cdot \ i\omega \cdot V_0 e^{i\omega t} \\ \Leftrightarrow I(t) = C \cdot \ i\omega \cdot V(t) \end{gathered} \tag{Eq. (2.39)}$$

Therefore, the impedance of a capacitor Z_C is expressed by:

$$Z_C = \frac{V(t)}{I(t)} = \frac{1}{C \cdot i\omega} \tag{Eq. (2.40)}$$

However, in a real sample, we do not know in principle if $1/\omega \ll \tau$ or if $1/\omega \gg \tau$ and we should not consider it to be a perfect resistance or capacitor. Instead we should admit that the electric properties of the sample are a combination of the properties of both a capacitor and a resistance. This means that we can and should describe the impedance Z of a sample as a generic complex number:

$$Z = Z' - i \cdot Z'' = |Z| \cdot e^{i\phi} \tag{Eq. (2.41)}$$

where Z' and Z'' are the real and imaginary components of the impedance, respectively, and where ϕ is defined by:

$$\phi = arctg\left(\frac{Z''}{Z'}\right) \quad \text{Eq. (2.42)}$$

This is more easily described by a phasor diagram as illustrated in Figure 2.13:

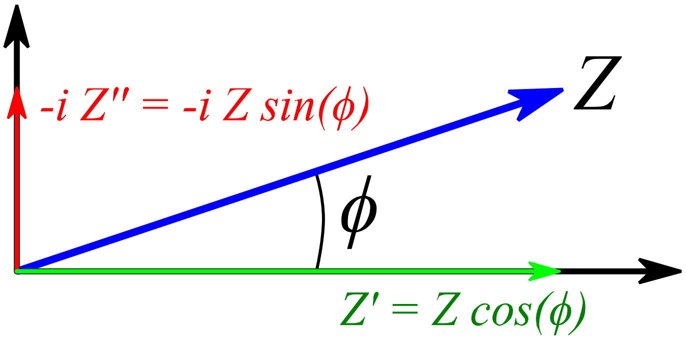

Figure 2.13 - Phasor Diagram of a generic electrical impedance.

If we describe the current in a material generally by:

$$I = I_0 \cdot \mathrm{e}^{i\omega t} \quad \text{Eq. (2.43)}$$

from Eq. (2.41) we can therefore write:

$$V(t) = Z \cdot I(t) \Leftrightarrow V_0 \cdot \mathrm{e}^{i\omega t} = |Z| \cdot I_0 \cdot \mathrm{e}^{i(\omega t+\phi)} \quad \text{Eq. (2.44)}$$

where ϕ is therefore interpreted as the difference of phase between the voltage and the current. The difference of phase ϕ and amplitude of voltage and current, V_0 and I_0, can be directly measured which allows us to calculate the real and imaginary components of impedance (*Z'* and *Z''*), relating Eq. (2.41) and Eq. (2.44). The contribution of inductive elements in the total impedance *Z* was intentionally not included in the previous description since in many practical cases it can be neglected (which was the case of the analyses performed in this work).

Impedance spectroscopy (IS) is particularly sensitive to intermolecular interactions and is able to monitor cooperative processes at the molecular level. Analysing the IS data based on different dielectric relaxation models such as Debye, Cole-Cole or Havriliak-Negami (HN) can provide different types of structural and microstructural information regarding, for instance, homogeneity, grain boundaries, lattice defects, dopants or chemical groups. Therefore, IS *"[...] provides a link between the investigation of the properties of the individual constituents of the complex material via molecular spectroscopy and the characterization of its bulk properties"* [231].

Relating the IS data with an equivalent capacitance and an equivalent resistance for the sample is useful regarding the description for a technological application, but also facilitates the calculation of physical parameters of the samples, such as the dielectric permittivity or electrical conductivity. To do this, we need to define an equivalent electrical circuit for the IS measurements that is defined based on the relative impedance magnitude of the sample (but also on its geometry). Two common equivalent circuits used in IS imply a resistance R and a capacitor C connected in parallel (C_pR_p), or connected in series (C_sR_s), as illustrated by the Figure 2.14:

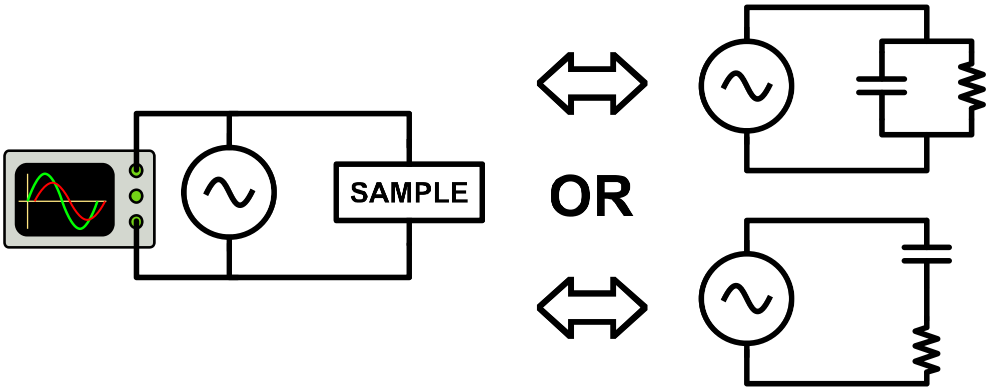

Figure 2.14 - Two common equivalent RC circuits used in impedance spectroscopy.

From Eq. (2.38) and Eq. (2.40), and based on Kirchhoff laws, we can define the equivalent impedance for C_pR_p and C_sR_s respectively by:

$$Z_{CpRp} = \left(\frac{1}{R_p} + i\omega C_p\right)^{-1} \qquad \text{Eq. (2.45)}$$

$$Z_{CsRs} = R_s + \frac{1}{i\omega C_s} \qquad \text{Eq. (2.46)}$$

These expressions can thus be easily associated with Eq. (2.41) in order to calculate the equivalent resistance and capacitance of the sample as a function of frequency. However, many modern equipment already allow to select an equivalent RC circuit, thus automatically calculating the C and R values. This is the case of the Agilent 4294A Precision impedance analyser that was used in this work.

Looking back to Eq. (2.34), which defines the current density as the variation of polarization with time, it becomes obvious that with a AC voltage we should have a non-zero $\boldsymbol{j}$ defined by:

$$\boldsymbol{j} = \frac{d\boldsymbol{P}}{dt} = i\omega\boldsymbol{P} \qquad \text{Eq. (2.47)}$$

Substituting *j* and *P*, from Eq. (2.32) and Eq. (2.33), we can show that:

$$\begin{gathered} \sigma = i\omega\varepsilon_0(\varepsilon_r - 1) \\ \Leftrightarrow \varepsilon_r = 1 + \frac{\sigma}{i\omega\varepsilon_0} \end{gathered} \qquad \text{Eq. (2.48)}$$

This means that we should describe the conductivity and the dielectric constant as:

$$\sigma = \sigma' + i\sigma'' \qquad \text{Eq. (2.49)}$$

$$\varepsilon_r = \varepsilon' + i\varepsilon'' \qquad \text{Eq. (2.50)}$$

which values may be calculated from the resistance *R*, from Eq. (2.31), and capacitance *C*, from Eq. (2.36). The complex part of the dielectric constant ε'' is therefore related with a conductive behaviour against the ideal of a dielectric, and can be interpreted as energy loss in the form of heat. A semi-quantification of the energy dissipated in a dielectric is commonly expressed by the *tan δ*, typically known as *dielectric loss,* where δ represents the phase shift between the electric displacement and the electric field [228].

$$\tan\delta = \frac{\varepsilon''}{\varepsilon'} \qquad \text{Eq. (2.51)}$$

Depending on the frequency, the different types of polarization mechanisms will have different responses to the applied electric field. Generally, as the frequency of the signal increases the real part of the dielectric constant (ε') decreases which can be easily understood with an analogy to a damped harmonic oscillator. Following this analogy, at certain resonant frequencies we expect that the dissipated energy (ε'') to reach a maximum, along with a strong decrease of ε'. This phenomenon is typically called a *dielectric relaxation*. As the entities responsible for the polarization (molecules, ions and electrons) have different masses, it is expected that the frequency range at which the dielectric relaxation happens is different. Typically, we should expect to have orientational polarization up to $\sim 10^9$ Hz (microwave range), ionic polarization up to $\sim 10^{13}$ Hz (infrared range), and electronic polarization up to $\sim 10^{15}$ Hz (visible-UV range) [228]. Figure 2.15 illustrates a generic trend of the real and imaginary parts of the dielectric constant for a material with different polarization mechanisms, emphasizing their dielectric relaxation phenomena at different frequencies. Interfacial or ferroelectric polarization mechanisms mainly involve long-range motion of ions or ferroelectric domain walls [228], and cannot be simply analysed through a damped harmonic oscillator scenario. Usually, these mechanisms can produce dielectric relaxations at frequencies in the range of kHz or MHz [228].

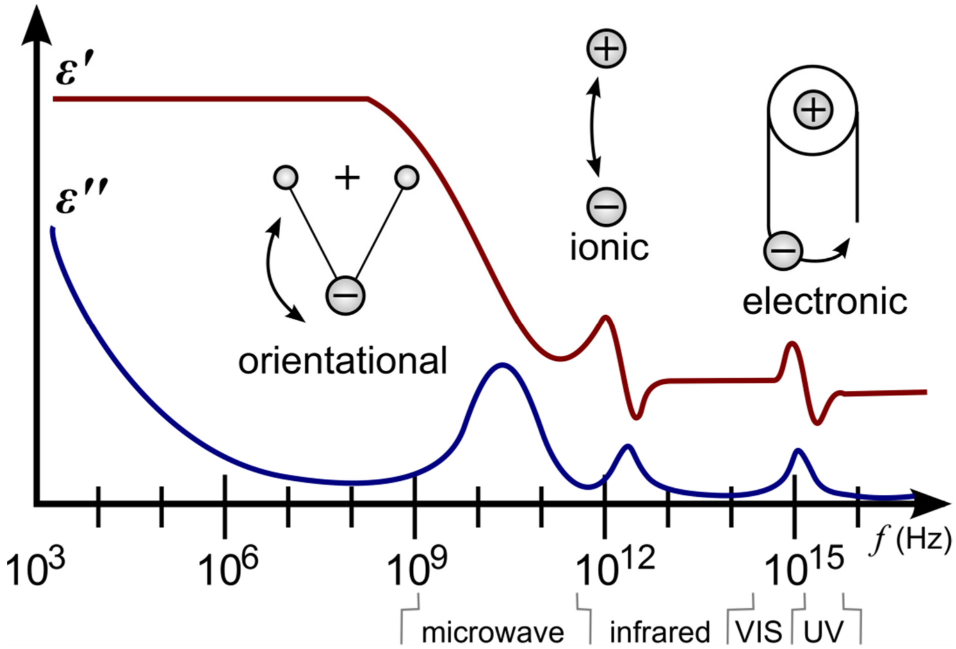

Figure 2.15 - Representation of the real and imaginary parts of the dielectric constant of a material with contributions from different polarization mechanisms (adapted from [232]).

Regarding the technological application of a dielectric material, knowing the value of the real part of dielectric permittivity at a certain frequency is insufficient. We should know how the dielectric permittivity (both real and imaginary parts) changes with frequency and with temperature. Generally, if the purpose of the material is not to heat, it is desirable to have low dielectric losses. However, since ε' and ε'' do depend both on frequency, a certain material may be highly suited in a certain range of frequencies but extremely unsuited for others. Also, the dielectric properties may be quite constant in a certain range of temperatures but change when the material is heated or cooled. Generally, materials with mainly ionic polarization can have higher ε' but varying significantly with frequency, and can also present higher dielectric losses at some frequencies. On the other hand, materials with only electronic polarization can present less variation with frequency and lower losses. This is how IS comes as an important tool to study the dielectric properties of materials as a function of frequency and temperature.

Chapter 3

Solid Electrolytic Capacitor

3. Solid Electrolytic Capacitor

In this chapter, a brief description of which types of capacitors exist and how they are classified depending on the constituent materials, building structure and electrical characteristics, will be presented. Additionally, the type of applications they meet, which electrical properties and limitations they have, will be explored.

A special focus will be given to the tantalum solid electrolytic capacitors, explaining in detail their structure and manufacturing method. The mass production of tantalum capacitors involves several processing steps which will be described as performed in the facilities of the largest capacitor producers [233,234].

For this work, the attempt to produce niobium oxide based capacitors was based on the approach of adapting the tantalum manufacturing steps and parameters, in order to keep the same production line and equipment. Therefore, in the following chapters, it should be noted that the samples of niobium oxides studied for the purpose of capacitor development, were produced by the same type of techniques here described in this chapter for the tantalum.

Because of confidentiality motives, there are some details and parameters of the manufacturing process which were intentionally left unclear, but that do not interfere with the analysis and interpretation of this work.

3.1 Types of Capacitors

A capacitor is one of the four fundamental passive electrical components, along with the resistors, inductors and memristors. An "Historical Introduction to Capacitor Technology" is presented in an article written by Ho *et al.* [235]. It is generally considered that the first capacitor-like device was the *Leyden jar*, invented by Ewald von Kleist in 1745. A more sophisticated design of a capacitor was only achieved in 1876, when Fitzgerald invented a wax-impregnated paper dielectric capacitor, and later in 1909 when William Dubilier invented a mica dielectric capacitor in a time where the demand for capacitors was increasing due to the need of signal filtering for the early radio receivers [235].

Currently, there are many types of capacitor technologies which are schematically categorized by Figure 3.1. Capacitors can generally by classified into two main groups: the non-polarized and the polarized capacitors. This classification depends essentially on the construction design and is linked to the type of materials which the capacitor is made of. The structure of a non-polarized capacitor can be simply described by a symmetrical construction of a dielectric material between two metallic electrodes in such way that the two terminals can be indifferently connected in either polarization. The non-polarized capacitors can be further separated into different categories depending if the material of the dielectric is a ceramic, a paper film or a polymer film. Furthermore, is also common to sub-classify the capacitors in *classes* (e.g. class 1 or class 2) in order to distinguish ranges of capacitances (higher classes means higher capacitances).

The polarized capacitors englobe two different types: the electrolytic capacitors and the super-capacitors (also classified as *electrochemical*). The electrolytic capacitors (the type that it studied in this work), are typically built by oxidizing a thin layer of a metallic anode. The anode is generally made of aluminium, tantalum or, more recently, niobium. The thin layer of metal oxide is used as the dielectric and is chemically bonded to the anode. The cathode can be either a solid (typically MnO_2 or a conductive polymer such as polypyrrole) or a non-solid (*wet*) electrolyte (such as ethylene glycol, sulphuric acid or others). Non-solid electrolytes are generally less expensive but, on the other, have an electrical conductivity significantly lower than solid electrolytes. Even so, MnO_2 has a relatively lower conductivity (~0.1 S/cm) [236] when compared to polypyrrole (typically from 10-100 S/cm) [237], but has a particularity that makes it very interesting: when a dielectric breakdown happens, it can actuate as a self-healing agent in such high leakage current points by changing the phase (by heating through Joule effect) from MnO_2 to Mn_2O_3 which is highly insulator. The type of electrolyte typically depends on the final application, nominal voltage of the capacitor, maximum temperature under operation and leakage current maximum tolerance.

In terms of energy storage comparison, super-capacitors are placed between typical capacitors and the lowest capacity rechargeable batteries [238]. These capacitors are not based in the principle of electrostatic storage by a solid dielectric layer. Instead, the storage of charge is classified as electrochemical type, and can be achieved through either, or both, principles which define their sub-classification. The electrical double-layer capacitors (EDLC) rely, as the name indicates, on the formation of an extremely thin double layer of positive and negative ions accumulated at the interface between the solid electrode and the electrolyte (also known as Helmholtz layer) [238]. The so-called pseudocapacitors owe their prefix to the energy storage mechanisms based on electron transfer between the electrode and the electrolyte through electrosorption, surface redox reactions, and/or intercalation processes [238], which are more often associated with batteries than with capacitors. Typically, carbon, or carbon derivative electrodes tend to show double-layer capacitance, while metal oxides or conductive polymers tend to have pseudocapacitance. However, there are also hybrid capacitors, such as lithium-ion capacitors, which have significant contributions of both types of electrochemical capacitance.

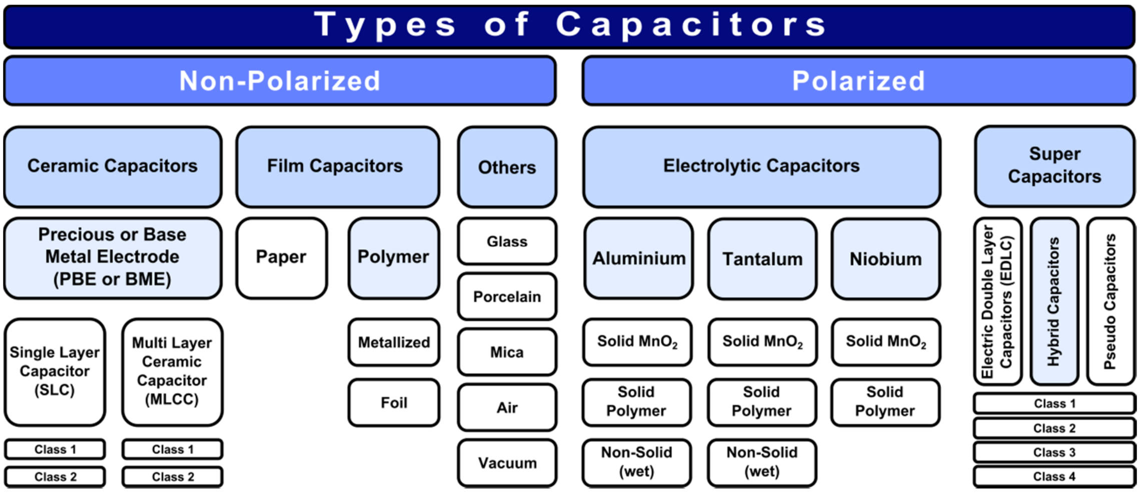
Types of Capacitors
Non-Polarized
Polarized
Ceramic Capacitors
Film Capacitors
Others
Electrolytic Capacitors
Super Capacitors
Precious or Base Metal Electrode (PBE or BME)
Paper
Polymer
Glass
Porcelain
Mica
Air
Vacuum
Metallized
Foil
Single Layer Capacitor (SLC)
Multi Layer Ceramic Capacitor (MLCC)
Class 1
Class 2
Class 1
Class 2
Aluminium
Tantalum
Niobium
Solid MnO$_2$
Solid MnO$_2$
Solid MnO$_2$
Solid Polymer
Solid Polymer
Solid Polymer
Non-Solid (wet)
Non-Solid (wet)
Electric Double Layer Capacitors (EDLC)
Hybrid Capacitors
Pseudo Capacitors
Class 1
Class 2
Class 3
Class 4

Figure 3.1 – Classification of different types of capacitor technologies (adapted from [239] and [240]).

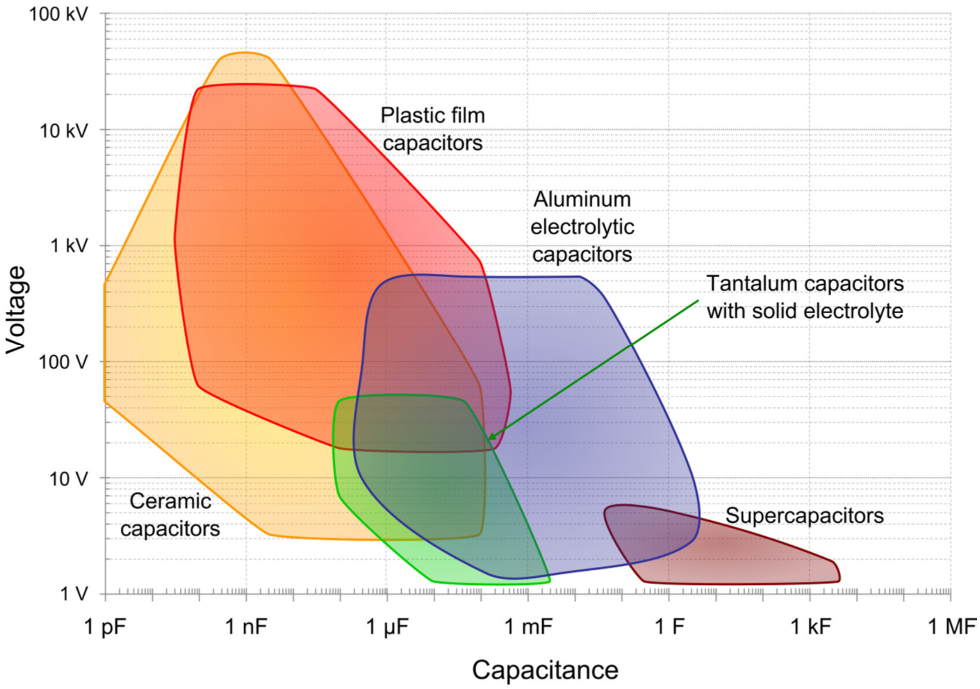

Figure 3.2 – Operating voltages and capacitance ranges for different types of capacitors available in the market (adapted from [239] and [241]).

The thickness of the dielectric layer of non-polarized capacitors can vary, typically between 0.5 and 10 µm. In contrast, the polarized capacitors have a much thinner dielectric thickness (between 10 and 100 nm). Furthermore, the microstructure of the anode is usually very rough and porous, with a high surface area, thus offering relatively large capacitance values within a reasonable size. The super-capacitors have the highest capacitance values, with Helmholtz layers as thin as 5-10 Å (achieving electric fields in the order of 10^6 V/cm) and with highly porous electrodes to increase its effective surface area [242]. Figure 3.2 illustrates the ranges of capacitances and operating voltages that each type of capacitor covers.

On the other hand, the dielectric losses and leakage currents, determined by the equivalent series resistance (ESR), are usually higher in electrolytic capacitors and super-capacitors than in ceramic and film capacitors (non-polarized). Typically, the dielectric losses ($tan\ \delta$) of supercapacitors are around 1, while electrolytic capacitors can range from 10^{-1} to 10^{-2}. Ceramic capacitors can have losses from 10^{-3} to 10^{-4}, while film capacitors can be within the range between 10^{-4} and 10^{-5} [239]. The inductance in capacitors is typically small (between 1 and 20 nH) and can be neglected for most purposes. Only at high frequencies the inductance in such components may become important, and it increases for bigger lengths of the conductive electrodes [239].

The final applications of capacitors can cover a wide range of technologies, but essentially capacitors are used for *coupling* (blocking DC component of an AC signal), *decoupling* (protecting a system from sharp variations of voltage), *filtering* (allowing or blocking certain frequencies of an AC signal), and *wave-shaping* (controlling the voltage amplitude versus time, thus giving the ability to introduce delays or changes in the waveform of a signal). Each application has certain criteria that define the type of capacitor that will be used. Such criteria cover parameters such as capacitance, operating voltage, ESR, size of the capacitor, frequency response, maximum operating temperature, flammability and also the price.

Ceramic capacitors cover a wide range of capacitance values, sizes and shapes but are mainly suited for high-frequency, high-voltage applications, where stability and precision are essential requirements. The film capacitors are essentially used in applications where very low energy dissipation and a resistance to high currents are required, such as motors, snubbing or lighting ballasts.

Regarding the electrolytic capacitors, which is the main focus of this chapter, their main advantage is the high capacitance to volume ratio. Therefore, these capacitors are typically useful in low frequency systems, where dissipation of energy is not a major concern but where high capacitance values, reduced size, self-healing properties, stability and reliability are required. Electrolytic capacitors are well suited for surface mounted devices (SMD), in computers, mobile phones, audio systems, DC buffering, and several space and military applications.

3.2 Manufacturing

The several steps of manufacturing a tantalum capacitor with a solid electrolyte of MnO_2 will now be described, as performed in the industrial facilities of any modern capacitor manufacturer [233,234]. As explained before, one of the objectives of this work is to adapt an existing processing line of tantalum capacitors to niobium oxide and therefore these are the processing steps that were followed for the production of the niobium oxide samples.

3.2.1 Pressing

The first step is the anode fabrication, which entails the pressing of metallic tantalum powders around a metallic tantalum wire. While the wire will provide an easy contact for the terminal, the powders will allow a great effective surface area for the growth of the dielectric layer.

At this step there are different parameters that will determine the final characteristics of the capacitor. Depending on the desired capacitance, Ta powders with different granularities are chosen accordingly (the smaller the average grain size, the higher the surface area and the capacitance). However, small granularities lead to lower thermal and electrical stability and are typically used for capacitors operating at lower voltages. There are also different standard *case sizes*, typically classified alphabetically (from the smallest to the largest) [243].

The Ta powder is mixed with a small amount of an organic binder which will promote the aggregation of the powders during the pressing, but also will act as a lubricant to avoid damaging the surface of the press.

The chosen Ta powder, mixed with the organic binder, is therefore added to the pressing mould (with the defined case size) and pressed uniaxially to form the pressed tantalum anode. This process is schematically illustrated by Figure 3.3.

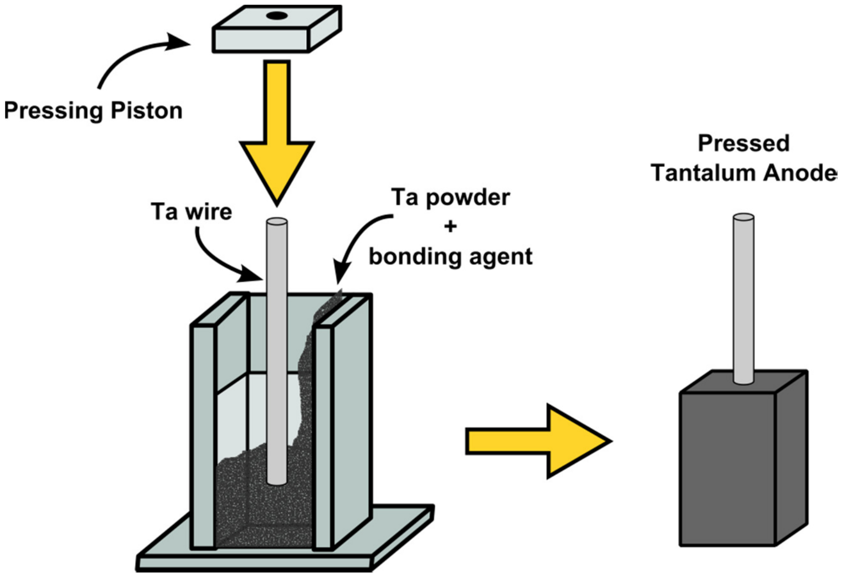
Pressing Piston
Ta wire
Ta powder
+
bonding agent
Pressed
Tantalum Anode

Figure 3.3 – Illustration of the pressing of the tantalum powders to form the capacitor anode.

3.2.2 *Sintering*

After the powders are pressed, the anodes are sintered in vacuum at high temperatures (typically higher than 1300 ^{o}C [244]). This step is crucial because it improves the contact between the Ta grains (and also the wire), without oxidizing. Otherwise, if there were grains that were not coalesced they would be isolated from the voltage applied to the anode at the Ta wire. This process is also important to remove the organic binder from the previous step and also to increase the mechanical consistency. On the other hand, this process reduces the effective surface area which is undesirable, and therefore a compromise must be achieved by making a good choice of the sintering temperature and time. Figure 3.4 illustrates this process and also the Ta grains before and after sintering.

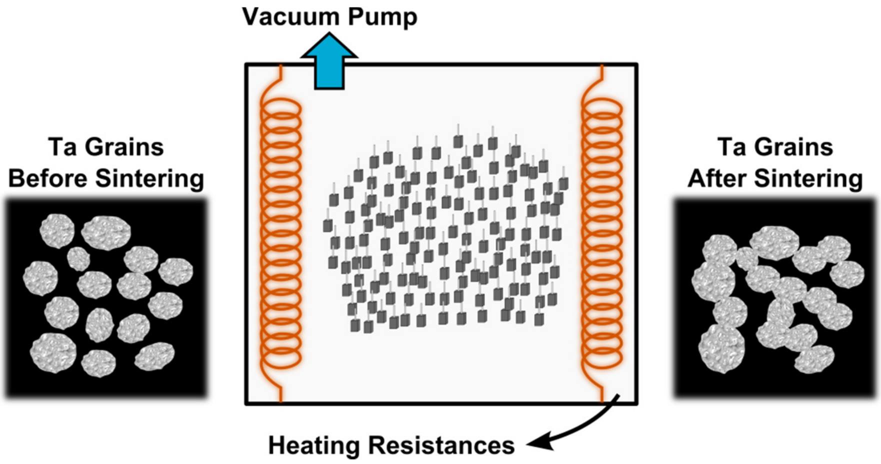
Vacuum Pump
Ta Grains
Before Sintering
Ta Grains
After Sintering
Heating Resistances

Figure 3.4 – Illustration of the sintering process of the Ta anodes in vacuum.

3.2.3 Bar Welding

To facilitate the production in large scale, avoiding individual processing, the anodes are welded into aluminium bars by the Ta wire, staying well aligned and equally spaced, as illustrated in Figure 3.5. Large sets of these bars are stored and handled together during the next processing steps.

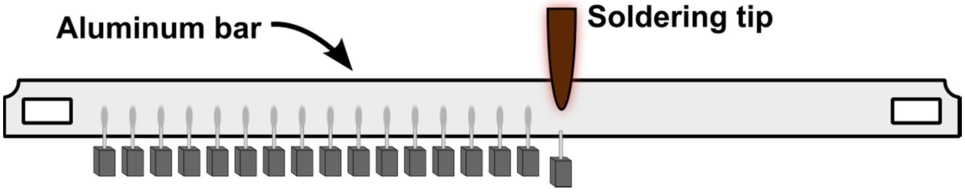

Figure 3.5 – Illustration of Ta anodes being welded into an aluminium bar.

3.2.4 Teflon ring (Primer)

Since the manufacturing processes of a capacitor involve the contact with different wet chemicals [234,245], the Ta wire could be become unintentionally processed by such chemicals which could extend their contact area by capillarity action. Furthermore, since one of the last steps will involve the cathode formation and also conductive baths [234,245], the Ta wire should not be in contact with such processes otherwise the capacitor would be short-circuited. Hence, a chemically inert and electrical insulating ring made of a certain type of Polytetrafluoroethylene (PTFE), commonly known as Teflon, is deposited near the bottom of the Ta wire, as illustrated in Figure 3.6. This process is also commonly known in the industry as *primer*.

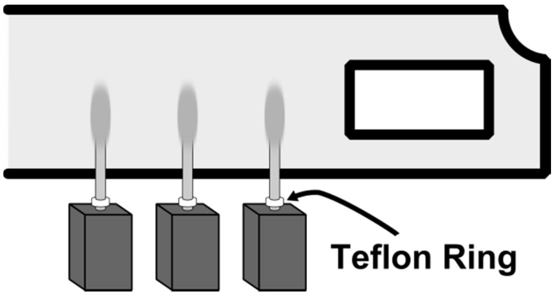

Figure 3.6 – Teflon ring incorporation around the Ta wire of the anodes.

3.2.5 *Dielectric Forming (Pre-Forming)*

At this point, the anodes are ready to be subjected to the formation of the dielectric layer. This process requires the oxidation of a thin layer at the surface of the crystalline Ta grains, into amorphous tantalum pentoxide (Ta_2O_5). This is achieved by a process called *anodization* which is very common in many types of industries as, for instance, creating a protective layer of Al_2O_3 in metallic pieces of aluminium [246,247].

The anodization process consists in placing the metallic Ta anodes dipped in a conductive bath, typically an acid solution of low concentration, while a DC electrical current is applied between the aluminium bar (i.e. the anodes) and the solution (where a metallic contact, the cathode, is dipped). When the electrical current is applied, with the negative terminal always applied at the anodes, the Ta grains will start to oxidize into amorphous Ta_2O_5, while H_2 gas bubbles will form at the cathode. The following chemical equations describe the reactions that occur during the anodization process at the anode and cathode [233]:

Anode

$$2\,Ta \rightarrow 2\,Ta^{5+} + 10\,e^{-}$$
$$2\,Ta^{5+} + 10\,OH^{-} \rightarrow Ta_2O_5 + 5\,H_2O \qquad \text{Eq. (3.1)}$$

Cathode

$$10\,H_2O + 10\,e^{-} \rightarrow 5\,H_2 + 10\,OH^{-} \qquad \text{Eq. (3.2)}$$

This is the reason why these capacitors are polarized: applying a voltage with the opposite polarization would reverse the oxidation reaction, leading to an increasing conductivity of the dielectric layer and, consequently, to short-circuits [233]. In the correct polarization, but with relatively lower voltages, the formation of the dielectric will not occur (at least not significantly) because the current is typically low, thus allowing the capacitor to operate normally.

In the beginning of this process, when there is no dielectric layer formed, there is almost no electrical resistance between cathode and anodes. So, to avoid extremely high current due to short-circuit, a controllable source of current is used to apply and limit to a certain maximum current (I_{max}). While the current is inducing the formation of the Ta_2O_5 layer, and its thickness is increasing, the resistance will increase and therefore the voltage between the terminals will increase. The thickness of the grown dielectric layer, which will determine the capacitance, is considered to be proportional to the forming voltage ($V_{forming}$) [233]. Therefore, when the voltage between the anodes and the cathode achieves a certain $V_{forming}$ value, which is chosen beforehand to match the desired capacitor properties, the system will switch from the current source to the voltage source in order to keep the voltage constant. At this point, not all the Ta grains may have the desired thickness of dielectric layer and therefore the current is still too high [233]. After some time, the dielectric layer with achieve the desired thickness and thus the current between cathode and anodes will reach a minimum (I_{min}) at which point the anodization process is considered to be completed [233]. The anodization process is illustrated by Figure 3.7 with a schematic representation of the experimental apparatus and the time evolution of the applied voltage and current.

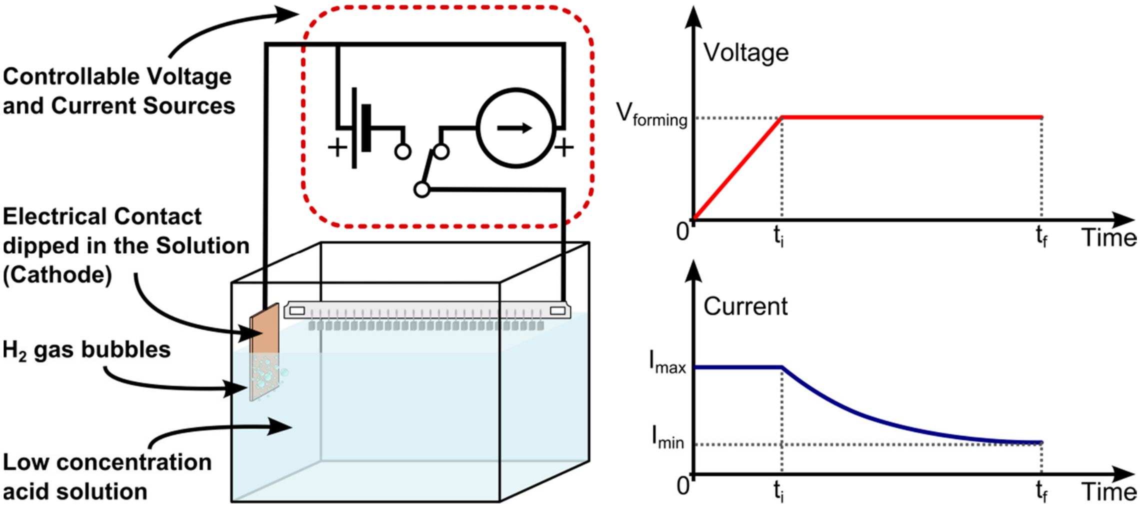
Controllable Voltage and Current Sources
Electrical Contact dipped in the Solution (Cathode)
H_2 gas bubbles
Low concentration acid solution
+
+
Voltage
$V_{forming}$
0
t_i
t_f
Time
Current
I_{max}
I_{min}
0
t_i
t_f
Time

Figure 3.7 – Schematic representation of the experimental apparatus of the anodization process and the time evolution of the applied voltage and current.

The leakage current of the anodes, measured at this point of the process, is highly affected by inhomogeneous (or still incomplete) dielectric formation and also by metallic contaminations in the conductive solution [233]. Hence, after this process the anodes are typically washed in hot distilled water and dried. This step is called the *pre*-forming because the formation of the dielectric layer will be "repeated/corrected" along the manufacturing process (always at lower voltages than the $V_{forming}$) in order to assure a better homogeneity and heal damages caused by other processing steps.

3.2.6 Tempering and re-forming

After the pre-forming of the dielectric layer of amorphous Ta_2O_5, the anodes are taken to a heat treatment at air (and only at some particular cases in vacuum). The purpose of this process is to *temper* the dielectric layer, i.e. to improve its hardness and cohesion. This tempering process is typically done at temperatures below 500 °C [233,248].

During the tempering, some points of the dielectric layer may also become damaged and therefore, as previously mentioned, the anodes are taken to *re-forming*. The re-forming is essentially another anodization, as described in section 3.2.5, but more simplified. Since most of the dielectric layer is already formed, there is no need at this point to control the current and therefore a voltage source is used to apply a slightly lower voltage (compared to the $V_{forming}$ of the pre-forming) until the measured current reaches I_{min} [233]. After this process the anodes are again washed and dried. Figure 3.8 illustrates the microstructure of the anodes at this point of the process, showing a network of sintered metallic Ta grains with an amorphous Ta_2O_5 dielectric layer around.

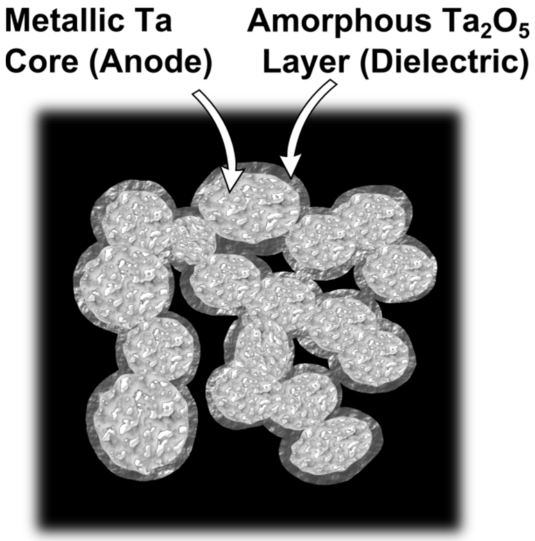

Figure 3.8 – Illustrative representation of the microstructure of a Ta anode with the formed dielectric layer of amorphous Ta_2O_5.

3.2.7 MnO_2 Impregnation

As previously explained, manganese dioxide (MnO_2) is the material used as the cathode layer for these type of capacitors. The impregnation of such MnO_2 layer into the porous and complex microstructure of the anodes, assuring that the dielectric is completely and homogeneously covered, is not a simple process [233,249].

The MnO_2 impregnation relies essentially on a pyrolysis reaction described by the following chemical equation [233]:

$$Mn(NO_3)_2 \xrightarrow[heat]{} 2\,NO_2 + MnO_2 \qquad \text{Eq. (3.3)}$$

This reaction requires the use of manganese nitrate, which has the advantage of being easily dissolved in water thus allowing a good penetration into the porous anode. This is one of the main reasons why along this process are used solutions with different concentrations of manganese nitrate: lower concentration offer a better penetration power while higher concentrations offer a large amount of material to assure a complete and homogeneous deposition [233]. Furthermore, a type of slurry, with both manganese nitrate solution and a suspension of solid particles of manganese dioxide, is used in this impregnation process [233,249]. Essentially, in this process, the anodes are taken to several manganese nitrate baths where they dipped, each bath followed by a heating system to promote the pyrolysis reaction, as illustrate by Figure 3.9. This cycle is repeated several times, but the number of cycles and parameters will depend on the desired properties of the capacitor [249]. At each pyrolysis reaction, the anodes are exposed to heat, as it happens in the tempering process. Therefore, at the end of each pyrolysis cycle there is a re-forming process, at slightly lower voltages than the previous re-forming [249].

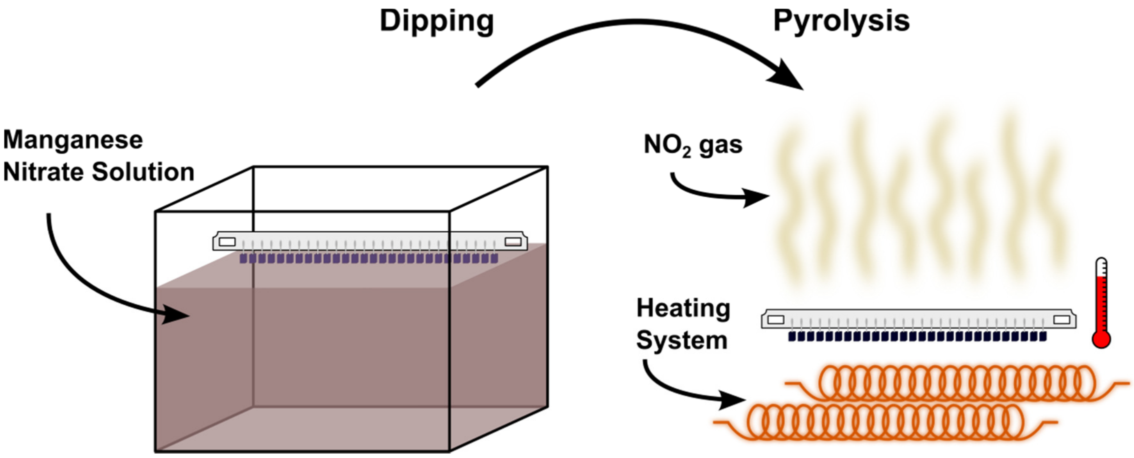

Figure 3.9 – Illustration of a dipping and pyrolysis cycle to the impregnation of MnO_2.

3.2.8 Contacting of the Cathode

At this point, the basic capacitor structure is completed (anode, dielectric and cathode). However, to improve the electrical contact of the cathode and facilitate its soldering with a metallic terminal, some conductive baths are performed. More specifically, the capacitors are covered with graphite particles and silver paint [233,249]. Particularly the graphite layer will prevent the silver to be in contact with the manganese dioxide, what could lead to the oxidation of Ag into AgO (which is a material more electrically insulating) [233].

As Figure 3.10 illustrates, this is done by dipping the capacitors into a suspension of graphite in ammonia and water under continuous stirring [233,234]. The capacitors are taken to a drying station and dipped into a silver paint bath afterwards. Lastly, the capacitors are washed in hot distilled water. The final microstructure of the capacitors is also illustrated in Figure 3.10 including the MnO_2 and the other conductive layers.

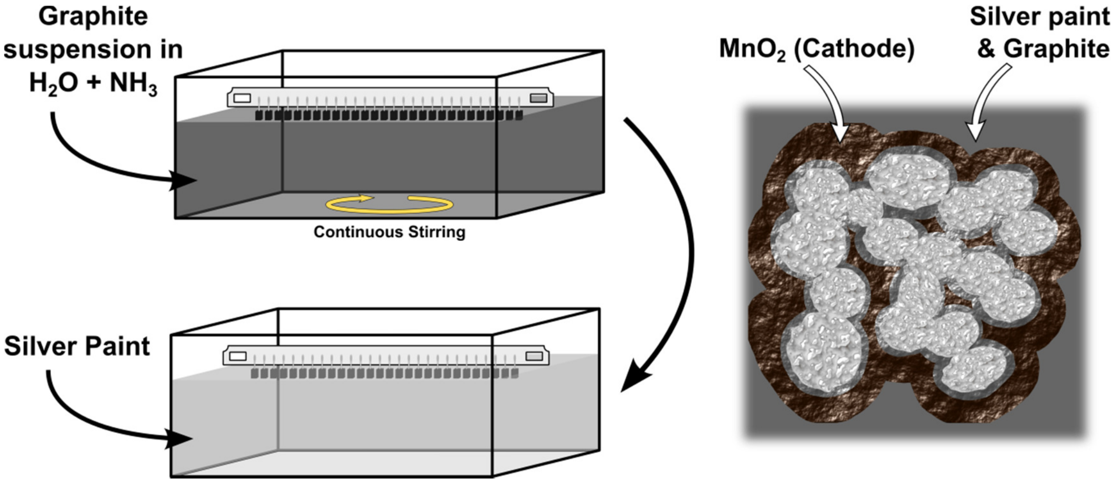

Figure 3.10 – Illustration of the conductive baths around the MnO_2, and a schematic representation of the final microstructure of the capacitors.

3.2.9 Assembly

Once the capacitors microstructure is completely finished and defined, they are taken to the last manufacturing steps – the assembly. The assembly of the capacitor comprises several sub-processes [233,234]. The first is the *terminal connection* which is basically the soldering of a metal terminal to the Ta wire (anode) and other terminal to the body of the capacitor with silver (cathode). After this, the capacitor is encapsulated with an epoxy resin in order to protect the body of the capacitor for commercial usage [233,234]. This impregnation implies a thermal hardening of the epoxy at temperatures below 200 °C. Afterwards, the epoxy is marked with a laser to label the capacitor.

Finally, in order to assure the stability and fidelity of the capacitors, all of them are submitted to an *aging* process [233,234]. The aging consists in placing the capacitors under normal operating voltage at a temperature between 100 and 150 °C for about an hour, in order to simulate their initial lifetime [234]. This process will make the defects that still exist in the capacitors to be healed with the help of the manganese dioxide, thus reaching a stable operation with time. The capacitors that do not survive this process are eliminated [234].

Figure 3.11 illustrates, at the left, a cross section view of a solid electrolytic capacitor at the final stage of its manufacturing and, at the right, a real picture of one capacitor welded into a PCB.

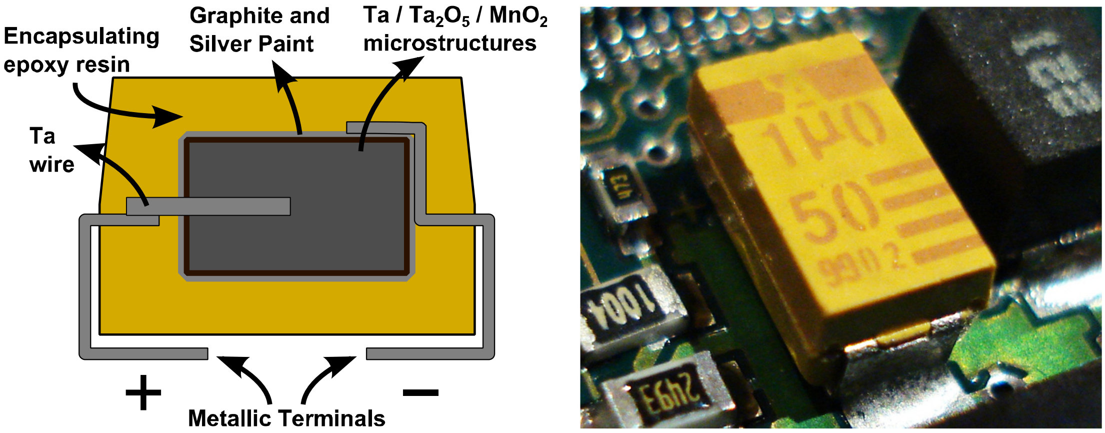
Encapsulating epoxy resin
Graphite and Silver Paint
Ta / Ta_2O_5 / MnO_2 microstructures
Ta wire
+
−
Metallic Terminals

Figure 3.11 – Cross-section view of a tantalum solid electrolytic capacitor (at left) and a picture of a capacitor welded into a PCB.

Chapter 4

Niobium Oxides prepared by sintering NbO powders

4. Niobium Oxides prepared by sintering NbO powders

In this chapter the first studies, performed during this work, on niobium oxides will be presented. At the starting point of this study, little was known about these materials and the main purpose was to explore fundamental properties and processing techniques of the niobium oxides.

It was decided that the starting materials should be the powders of niobium monoxide (NbO) that were considered suitable for the production on niobium solid electrolyte capacitors.

4.1 Experimental Procedure

Two different types of commercially available niobium monoxide (NbO) powders doped with nitrogen (~ 3000 ppm) were used as start materials. The powders were considered suitable for electrolytic capacitors with a charge per unit weight (CV/g) of 80,000 μC/g (NbO-80K) and 120,000 μC/g (NbO-120K), approximately. Differential Thermal Analyses (DTA) in a *Linseis Aparatus* from room temperature (RT) up to 1200 ^{o}C were performed in order to define the heat treatment (HT) temperatures. For the HT, the NbO powders were pressed into disc pellets (∅ = 5 mm; thickness = 9 mm). The HT was carried out in air, with a first step of 3 hours at 150 ^{o}C. A second temperature step of 1 hour at 200 ^{o}C was made, in order to remove all organic impurities that may remain. The last step, corresponding to the different sintering temperatures, was made during 1 hour at 300, 450, 700, 800, 900 and 1100 ^{o}C. The same pellets were used for all characterizations, though the results are reproducible for pellets prepared under the same conditions.

The crystalline structure of the sintered pellets were studied, at room temperature (RT), by *ex-situ* X-Ray diffraction (XRD), with an X'Pert MPD Philips difractometer (CuK$_{\alpha}$ radiation, λ=1.54056 Å). The microstructure and morphology of the pellets was analysed by SEM on a Hitachi S4100-1. The structural characterization of the pellets was complemented with optical measurements such as Raman spectroscopy, which is particularly important in this kind of structures since it is very sensible to distortions of the NbO_6 octahedrons. *Ex-situ* Raman spectroscopy was performed at RT, in a backscattering geometry with a 325 nm line of a He-Cd laser.

Steady state PL was measured using the same He-Cd laser as excitation source. The samples emitted light was dispersed by a Spex 1704 monochromator (1 m, 1200 grooves/mm) and fitted with a cooled Hamamatsu R928 photomultiplier. The samples were mounted in a cold finger of a closed cycle helium cryostat and the sample temperature was controlled in the range from 14 K up to RT.

The impedance spectroscopy measurements ($Z^*=Z'-jZ''$) were carried out at RT by applying a ac signal of 500 mV of amplitude, sweeping the frequency from 40 Hz to 110 MHz, using an Agilent 4294A Precision Impedance Analyser and measuring in the Cp-Rp configuration. These measurements allowed to calculate the real (ε') and imaginary (ε'') part of the complex permittivity, and also the dielectric losses ($tan\ \delta$) using the equations discussed in section 2.2.6. The electrodes of the analysed samples were made by painting the opposite faces of the pellets with silver conductive epoxy.

4.2 Results and Discussion

The DTA spectra of the NbO-80K and NbO-120K powders are shown in Figure 4.1. Two exothermic phenomena, between RT and 1100 °C for both NbO powders can be clearly identified. The first, at 430 °C and 390 °C, for NbO-80K and NbO-120K, respectively, is associated to the phase transition from NbO to Nb_2O_5, as it would be concluded ahead. A large exothermal band between ~550 °C and 1100 °C was detected in both samples, as a result of a phase transition from the orthorhombic to monoclinic structure of Nb_2O_5. This kind of large exothermal band, without clear crystallization peaks, was previously reported in a similar work [74]. The thermal annealing temperatures were defined based on the DTA data: 300, 450, 700, 800, 900 and 1100 °C. Representative pictures of the samples are shown in Figure 4.2 where the untreated samples are dark grey, the samples treated at 300 °C are blue, while the sample treated at 450 °C is white and has the same look as the samples treated at higher temperatures. Pictures of the NbO powder before pressing and a NbO powder treated at 1100 °C in air are also shown.

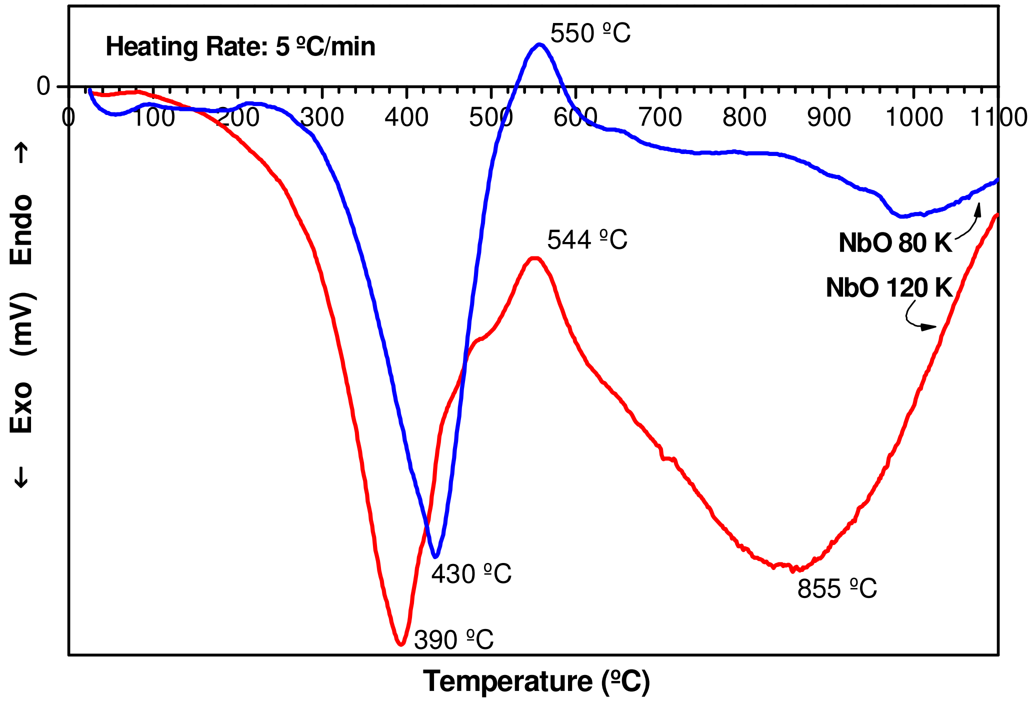

Figure 4.1 - Differential Thermal Analysis of NbO-80K and NbO-120K powders.

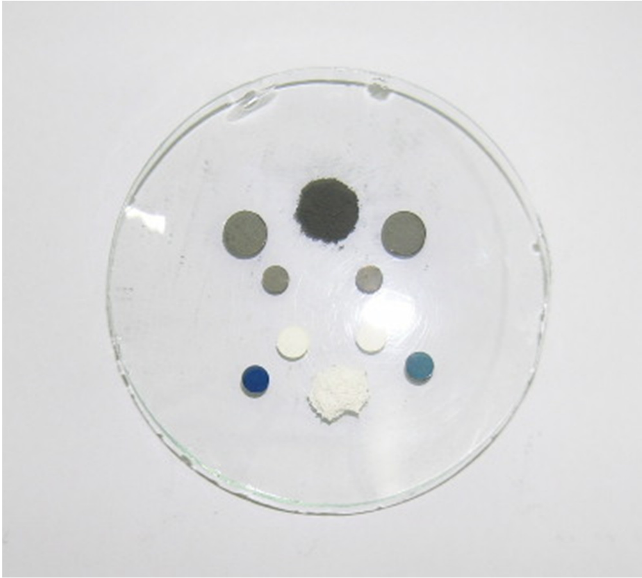

Figure 4.2 – Photograph of some of the NbO pellets before (grey) and after heat treatment at 300 ºC (blue) and at higher temperatures (white).

The XRD patterns of the sintered pellets were indexed using the ICDD reference cards, and are shown in Figure 4.3. It is possible to observe that the heat treatment at 300 ºC does not modify the initial cubic NbO crystal structure (ICDD Ref. 71-2146), though the colour of the pellets changes from grey to dark blue. In fact, although this colour is associated to NbO_2 phase [250], any diffraction maxima corresponding to such niobium oxide phase was identified. The heat treatment at temperatures between 450 ºC and 900 ºC, promote the formation of Nb_2O_5 with a diffraction pattern corresponding to the orthorhombic structure T-Nb_2O_5 (ICDD Ref. 30-0873) [22,33,74,251]. All the diffraction maxima assigned to the T polymorph suffered a slight shift to lower angles as the HT temperature increases which indicates a dilation of crystalline lattice. These pellets become completely white, as expected for a wide band gap semiconductor. In the pellets treated at 900 ºC, besides the orthorhombic crystalline phase, the monoclinic B-Nb_2O_5 phase was also identified (ICDD Ref. 26-0885). For heat treatment temperatures above 900 ºC, the XRD patterns revealed a new monoclinic phase with larger lattice parameters, corresponding to the H-Nb_2O_5 polymorph (ICDD Ref. 37-1468), as expected [22,33,74,251].

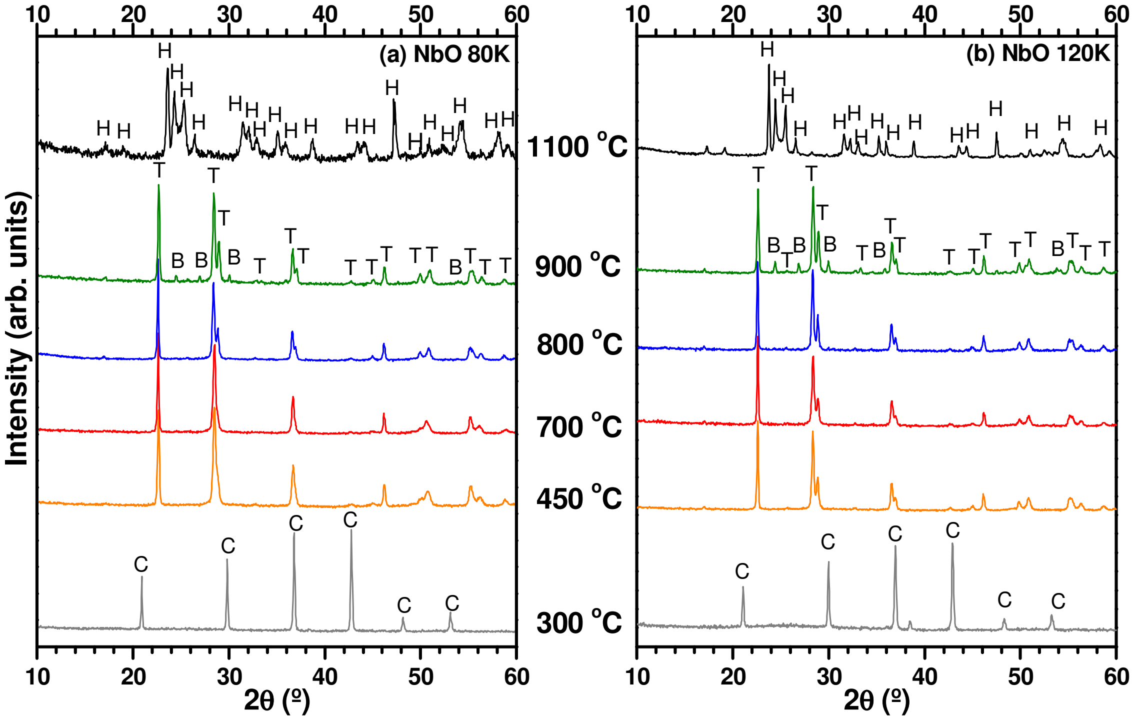

Figure 4.3 - XRD patterns of the NbO-80K and NbO-120K sintered pellets (C - Cubic NbO; T - Orthorhombic T-Nb_2O_5; B - Monoclinic B-Nb_2O_5; H – Monoclinic H-Nb_2O_5).

Interestingly, the NbO XRD pattern shows more diffraction maxima that would be normally expected for a cubic structure. As explained in section 2.2.2, a face-centred cubic structure would have destructive interference (i.e. forbidden reflections) of the planes defined by combinations of odd and even Miller indices, as the (1,0,0), (1,1,0), (2,1,0) or (2,1,1). In the analysed NbO samples, diffraction maxima corresponding to these planes were detected. However, using the crystallographic data that describes the defective rock-salt structure of NbO (see section 1.3.2), it is possible to simulate the XRD diffraction pattern of the NbO powders (which in this case was done using VESTA 3 software [252]), and it was observed exactly the same diffraction maxima, as illustrated by Figure 4.4. There is a small deviation between the simulated and the experimental patterns (~0.22 °). Because such deviation is the same for every diffraction maxima (i.e. for different planes) such fact is probably related to an experimental miscalibration.

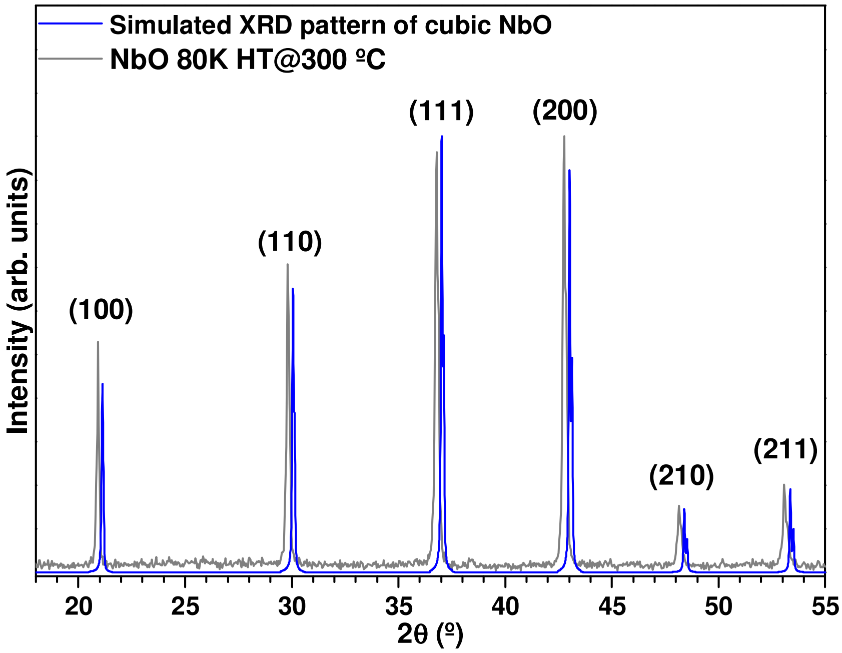

Figure 4.4 – Simulated powder XRD pattern for the cubic NbO structure.

The observation of such diffraction maxima, could suggest a defective or deformed structure of the NbO samples. However, the fact that this is observed in the simulated XRD pattern suggests that this is related to the particular cubic structure of the NbO. Indeed, this is most likely related to the 25 % ordered vacancies in both sublattices of Nb and O of the NbO structure [46,56], as also described in section 1.3.2.

The SEM micrographs of the pellets treated at 300 °C, with NbO cubic structure, show grains with spherical shape and with 200 nm in diameter (Figure 4.5). This morphology remains the same for the orthorhombic T-Nb_2O_5 crystalline phase, even with the HT at 900 °C, where an intermediate monoclinic crystalline phase (B-Nb_2O_5) is also present. The increase of the heat treatment temperature promotes an increase of the grain size from 200 nm to 1 µm, approximately. Also, an abrupt change in the grain morphology was observed in the pellets heat treated at 1100 °C. The grains of the monoclinic H-Nb_2O_5 phase exhibit a parallelepiped shape with some local preferential orientation.

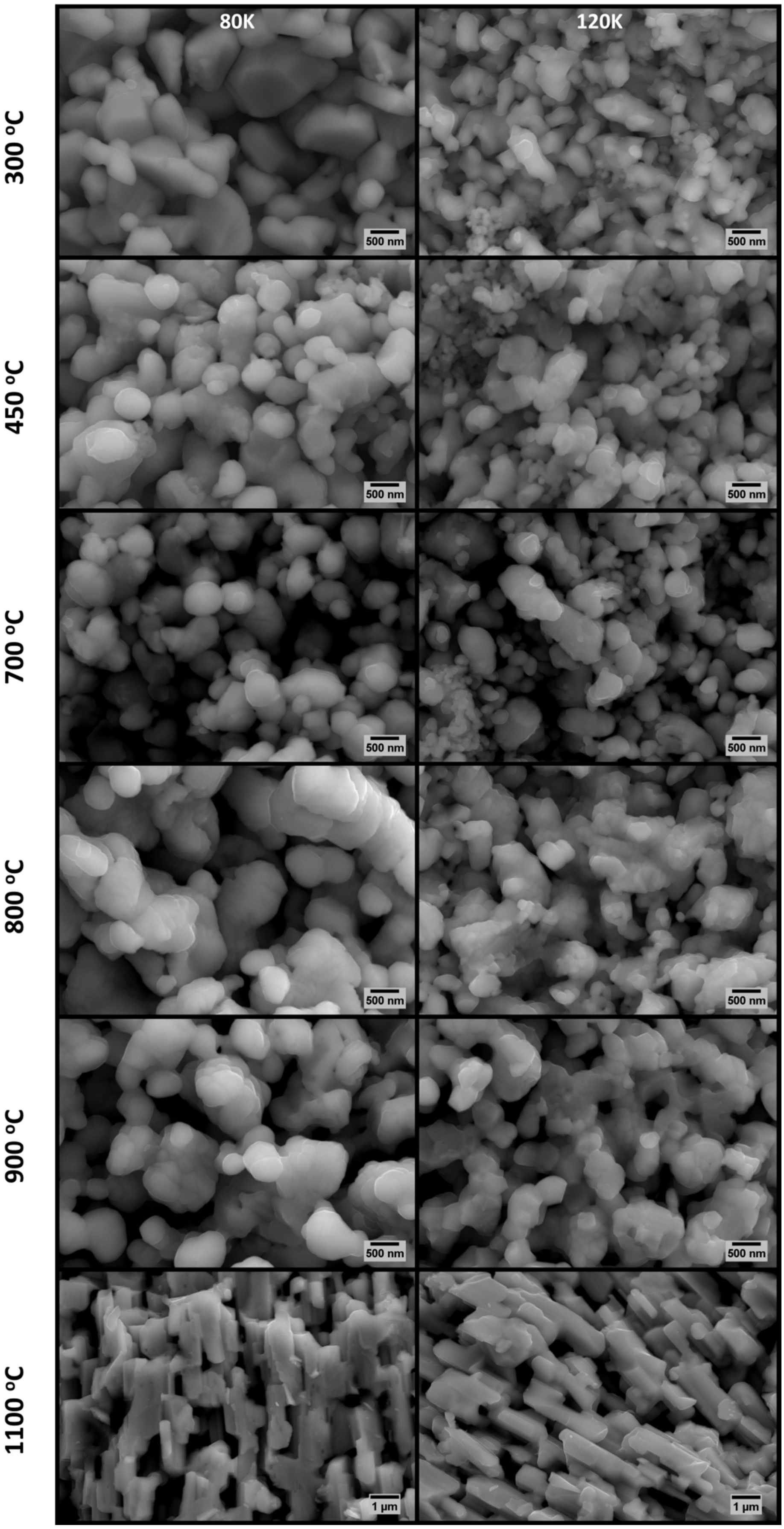
80K
120K
300 °C
450 °C
700 °C
800 °C
900 °C
1100 °C
500 nm
1 µm

Figure 4.5 - Scanning Electron Micrographs for the NbO-80K and NbO-120K sintered pellets.

Figure 4.6 shows the RT Raman spectra of all NbO-80K and NbO-120K treated samples. Independently of the used photon wavelength excitation, 325 nm or 532 nm (not shown) the pellets treated at 300 ºC exhibit a large band centred at ~641 cm^{-1}, suggesting the existence of an amorphous, Nb_2O_5 phase [157], not detectable by XRD. For pellets heat treated between 450 ºC and 800 ºC, which display orthorhombic T-Nb_2O_5 phase, the expected vibrational modes for this Nb_2O_5 polymorph [89,157] were found at 684, 235 and 100 cm^{-1}, approximately. The phonons identified on the sample heat treated at 900 ºC are the ones corresponding to the B-Nb_2O_5 and T-Nb_2O_5 crystalline phases [158,159]. These phases are not homogenously distributed on the sample volume as evidenced by the Raman spectra taken in two different sample regions. A distinct vibrational spectrum is taken for the pellets heat treated at 1100 ºC, as expected due to the presence of the H-Nb_2O_5 phase [89,157–159].

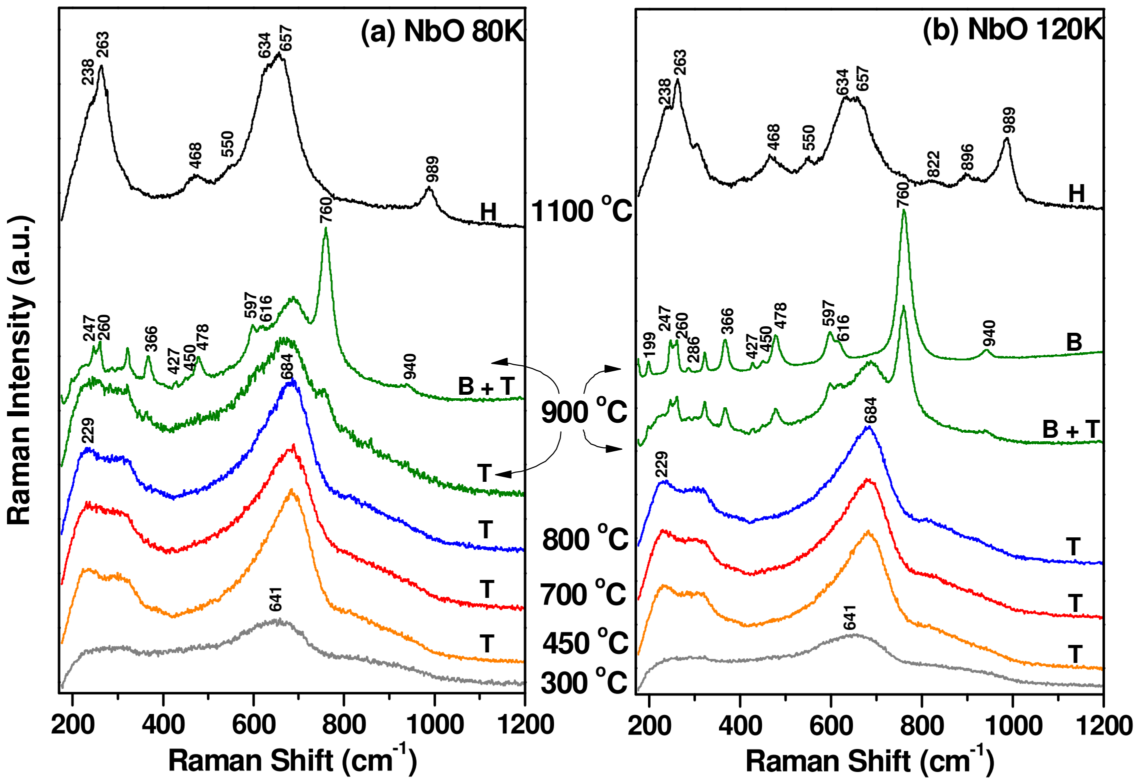

Figure 4.6 - RT Raman spectra of NbO-80K and NbO-120K sintered pellets, obtained with the 325 nm He-Cd laser line (T, B and H polymorphs are assigned to the corresponding spectra).

The absorption in the infrared region of the electromagnetic spectra can be an important technique to obtain information about the structure of the materials. Therefore, in order to have reference spectra for different phases of niobium oxides it was performed absorption measurements in the infrared, illustrated in Figure 4.7.

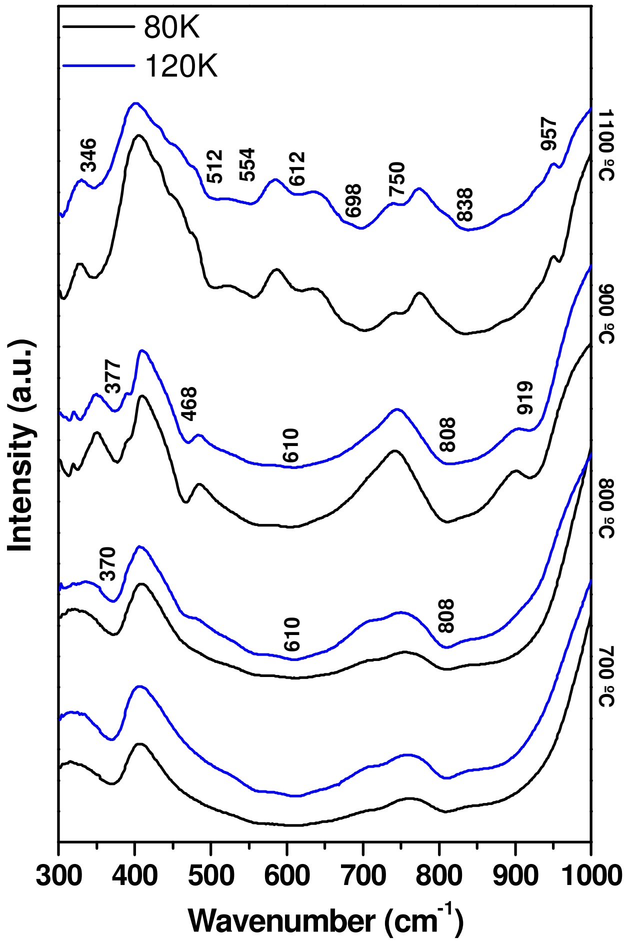

Figure 4.7 – IR absorption spectra of the NbO 80K and 120K samples.

Figure 4.8 (a) shows the low temperature PL spectra for pellets sintered at different temperatures, with the T-Nb_2O_5 and B-Nb_2O_5 crystalline phases. With 3.8 eV photon energy excitation (an energy close to the band gap of the material, as discussed in section 1.3.4 and experimentally determined ahead), all the samples evidence broad luminescence bands in the visible spectral region due to optically active defects. Yellow (maxima ~2.25 eV) and blue (maxima ~2.55 eV) luminescence are exhibited by the pellets heat treated at lower and higher treatment temperatures than 900 ºC, respectively. Broad emission bands located in the middle of the band gap energy of wide band gap oxides are usually associated with the presence of native defects such as the anion and cation vacancies or interstitial defects [253]. The observation of these broad luminescence bands in the niobium oxide based structures suggests that the native defects could assume an important role on the control of the electrical properties for the passive components, namely by carrier trapping.

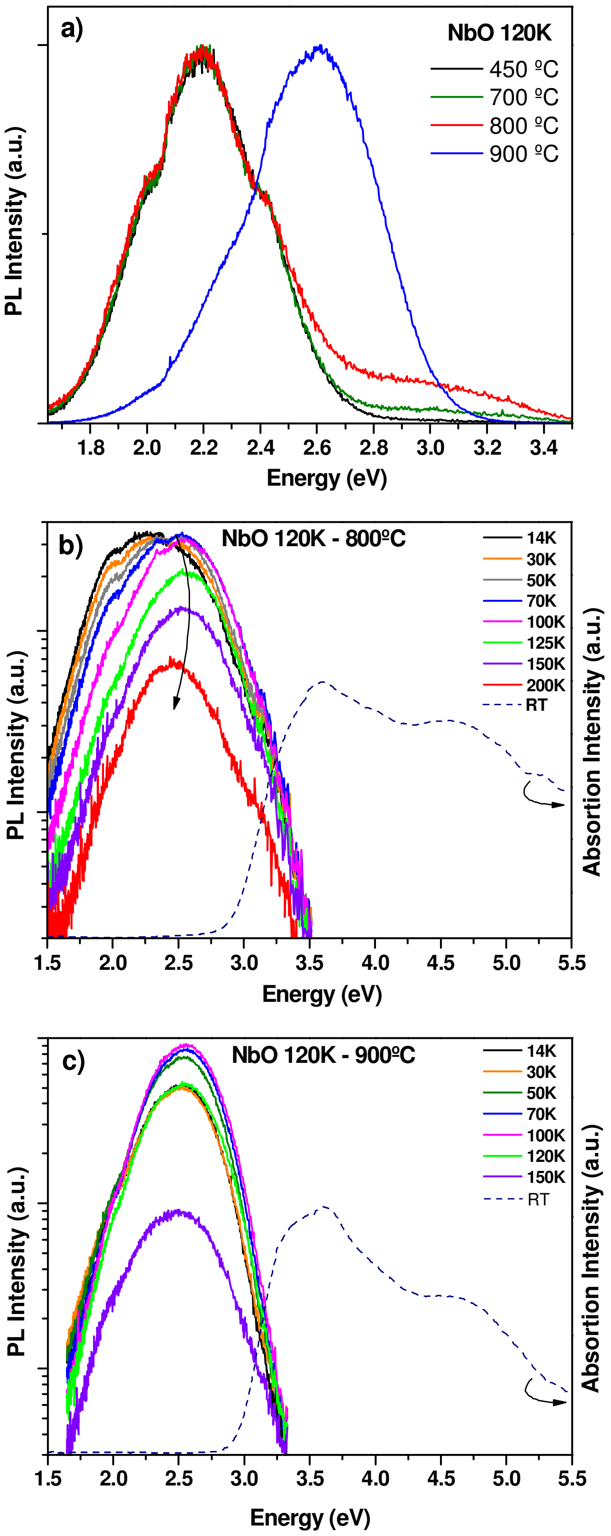

Figure 4.8 - (a) 14 K PL spectra of the 450, 700, 800 and 900 °C sintered pellets of NbO-120K; (b) Temperature dependent PL spectra and RT absorption of the 800 °C sample and (c) The same as in (b) for the 900 °C sintered pellets of NbO 120K.

Figure 4.8(b) and (c) shows the temperature dependent PL spectra for the 800 °C and 900 °C sintered pellets, the ones with the highest PL intensity. For the 800 °C T-Nb_2O_5 sample a nearly persistent intensity is detected from 14 K to ~100 K which is accompanied by a ~300 meV high energy shift of the band maximum. Typically, for the same optical centre, high energy shifts with increasing temperatures could be explained by a thermal population of the high energy states. However, such a high energy shift in the aforementioned temperature region is unlikely to be assigned to a thermal population ($K_BT \cong 26$ meV at RT). A probable explanation is that the broad emission band is an overlap of two emitting centres with maxima near 2.25 eV and 2.55 eV. A faster quenching of the intensity for the 2.25 eV band promotes the overall shift of the band maxima, with the high temperature PL spectrum dominated by the 2.55 eV band, as observed in Figure 4.8(b). Further increase of the temperature leads to the overall luminescence intensity quenching due to additional nonradiative processes (an intensity ratio of 5 was observed between 100 K and 200 K). The quenching is accompanied by a ~80 meV low energy shift, suggesting that shallow energy levels are involved in the recombination process. This is also the expected behaviour for a band gap shrinkage in semiconductor materials, suggesting a decrease of ~80 meV for the orthorhombic T-Nb_2O_5 crystalline phase. Similar band gap shrinkage of ~100 meV was recently reported for the H-Nb_2O_5 samples [71]. Figure 4.8(b) also shows the RT absorption spectra of the sintered pellet. The peak position around 3.5 eV is consistent with the reported band gap energy in films produced by sol-gel with similar crystalline phase discussed in section 1.3.4 [254]. The additional absorption maximum at 4.7 eV was also observed in T-Nb_2O_5 sintered by a different route and from the observation of the same band in the photoconductivity experiments it was suggested that the high energy intrinsic absorption could be related with transitions from different critical points in the conduction band for the T-Nb_2O_5 band structure as it happens in other metal oxide semiconductors with similar crystalline structures [71]. Different RT band gap energies were recently reported for Nb_2O_5 polymorphs [75]. In agreement with the reported values in the literature [71,91], Viet *et al.* found band gap energy values in the 3.4 to 5.3 eV energy range [75]. However, an expansion of the absorption spectra for both low and high energies indicates that for H-Nb_2O_5 and T-Nb_2O_5 onset absorptions at ~3.1 eV and ~3.5 eV (with an additional onset at 4.7 eV) can be found at RT, respectively [71]. Different oxygen stoichiometry on samples processed by the different routes could also explain the band gap variations, including the presence of distinct Urbach tails [71,75].

A distinct temperature dependent PL behaviour was found for the sample with mixed T+B Nb_2O_5 crystalline phases sintered at 900 °C. Here, with the same excitation conditions, the dominant recombination has a maximum at ~2.55 eV at low temperatures rather than at 2.25 eV, as found for the T-Nb_2O_5 sample. Increasing the temperature between 14 K and 100 K leads to an increase in the PL intensity meaning that the 2.55 eV optical centre is thermally populated. For higher temperatures a faster decrease of the luminescence intensity was found (I_{100K}/I_{150K} ~10 and no signal was observed for temperatures above 200 K) suggesting that the presence of the additional phase induces extra nonradiative processes that compete with the luminescence. In a similar way to the one found for the heat treated sample at 800 ºC (T-Nb_2O_5) a low energy shift of the broad band maxima due to the band gap shrinkage was observed at higher temperatures. In both the analysed systems besides the role of the native defects in the optical active defects it cannot be ruled out the participation of nitrogen as a potential acceptor in these niobium-oxide systems which could be responsible for the identified shallow levels. Additionally, as commonly observed in metal oxides, surface related defects could also have an important role on the optical properties.

The addition of nitrogen to the NbO powders makes them more stable toward oxidation and improves its thermal stability and dielectric strength [25]. Figure 4.9(a) shows the dielectric characteristics, measured at room temperature, of the NbO-80K pellets treated at 800, 900 and 1100 ºC. The results obtained with the NbO-120K pellets, treated at the same temperatures, are shown in Figure 4.10(a). It was observed that the sample with orthorhombic (T-Nb_2O_5) structure (treated at 800 and 900 ºC) exhibit a dielectric constant value of ~ 25 at 100 kHz, increasing to ~ 55 for the sample heat treated at 1100 ºC with a monoclinic structure (H-Nb_2O_5). This increment can be related to the formation of the parallelepiped morphology, which gives rise to an evident preferential grain orientation (Figure 4.5). These results suggest that the development of a distorted unit cell structure, which is the case of the formation of polymorphic H-Nb_2O_5 (Figure 4.3), facilitates the formation of a microstructure with grains oriented in a preferred direction. Thus, the presence of a preferential orientation promotes an increase of the dipole moment [205], experimentally observed by the increase of the dielectric constant value (Figure 4.9(a), Figure 4.10(a)). The presence of the B-Nb_2O_5 monoclinic phase in the sample NbO-80K treated at 900 ºC, does not influences significantly the dielectric results due, probably, to its low content. For the sample NbO-120K, treated at 900 ºC, the amount of the B-Nb_2O_5 phase is, according to the XRD patterns, higher than in sample NbO-80K. The SEM micrographs (Figure 4.5) revealed that the grain size of the 120K samples is always lower than that of the 80K samples. Moreover, in pellets treated at 900 ºC it was not observed parallelepiped grain morphology, related with the B-Nb_2O_5 structure, which indicates that these particles have a much smaller size. A possible justification for the decrease of ε', on the 120K sample, with the increase of the heat treatment temperature from 800 to 900 ºC, is the presence of a sufficient quantity of B-Nb_2O_5 particles that can promote with their interaction with the T-Nb_2O_5 particles, a dielectric non-cooperative effect [255,256] leading to a decrease of ε´. The high value of ε´ at low frequencies, for all samples, is due to the polarization of sample-electrode interfacial dipoles, which number increases with the rise of the heat treatment temperature (Figure 4.9(a), Figure 4.10(a)).

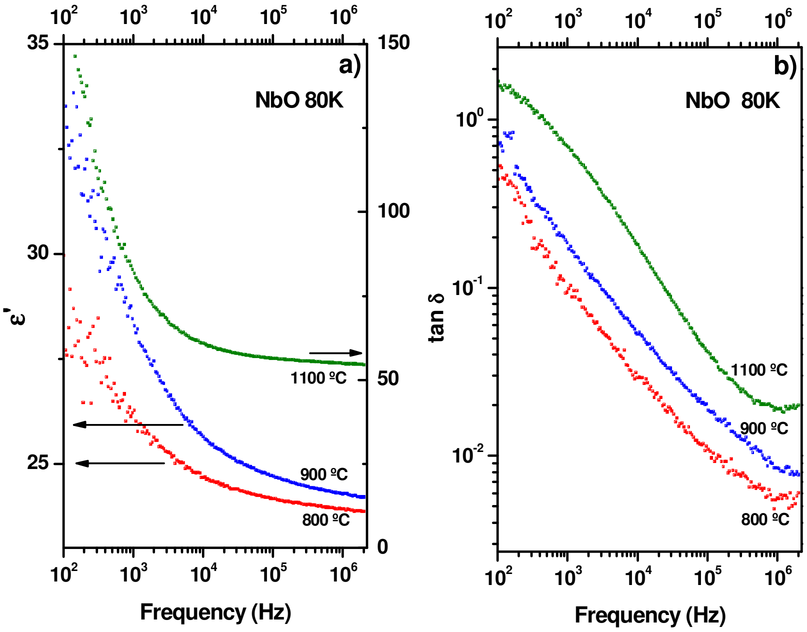

Figure 4.9 - (a) Dielectric constant and (b) dielectric loss, measured at 300 K for the NbO-80K pellets sintered at 800, 900 and 1100 ºC.

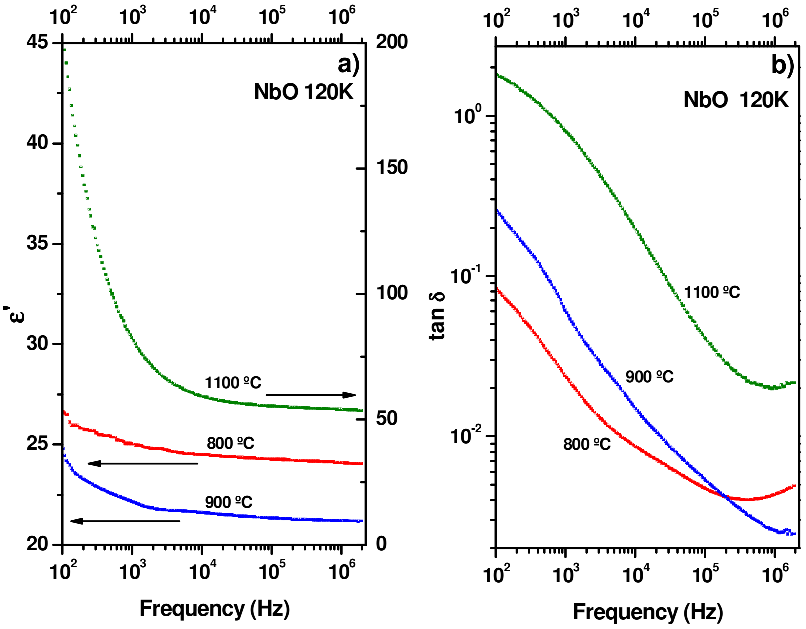

Figure 4.10 – (a) Dielectric constant and (b) dielectric loss, measured at 300 K for the NbO-120K pellets sintered at 800, 900 and 1100 ºC.

The dielectric loss (tan δ - Figure 4.9(b)) presents its higher value for the 1100 ºC pellets, which can be ascribed to the increase of the percolation path between the grains. This percolation path increase is justified by the preferential grain growth, observed through SEM, on the 1100 ºC treated pellets.

The graph of imaginary part of the dielectric modulus (M´´) [120] in function of frequency revealed the presence of a dielectric relaxation phenomenon in all pellets heat treated at 900 and 1100 ºC (Figure 4.11). The increase of the heat treatment temperature promotes a shift of the M´´ peak to higher frequencies, indicating a decrease of the relaxation time. This result shows that for the pellets treated at high temperatures their dielectric dipoles can follow the applied external ac field more easily promoting a high polarizability, already observed through the ε´ values discussion.

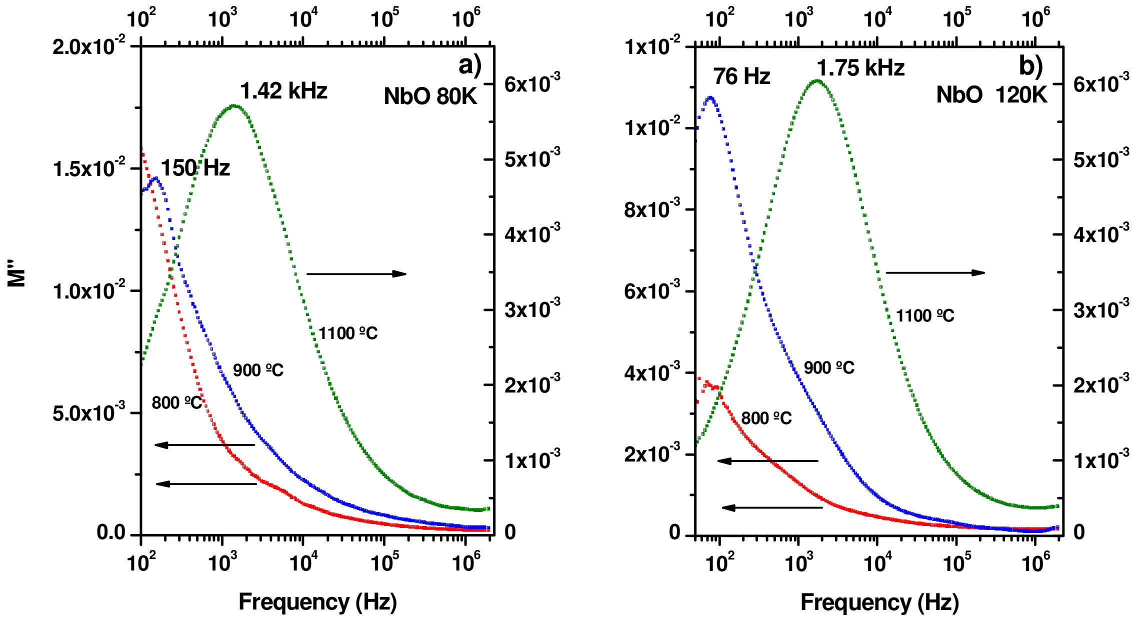

Figure 4.11 - M´´ versus frequency, at 300 K for the pellets NbO-80K (a) and NbO-120K (b) sintered at 800, 900 and 1100 ºC.

In Figure 4.12 it is illustrated the comparison of the dielectric constant and dielectric losses between the NbO-80K sample heat treated at 300 ºC and the sample heat treated at 450 ºC. Curiously, while the sample treated at 450 ºC has a behaviour and absolute values very close to the sample treated at 800 ºC (which has the same T-Nb_2O_5 polymorph), it is possible to observe that the sample treated at 300 ºC has a much larger dielectric constant (around 1100 at low frequencies, decreasing to ~350 at 2 MHz). This is particularly interesting because it was only detected the crystalline phase of cubic NbO on this sample, even considering the amorphous niobium pentoxide detected by the weak signal in the Raman spectroscopy analysis (Figure 4.6).

This behaviour will be explained in the next chapter, where it will be shown that this huge dielectric constant is related to the formation of a thin layer of amorphous Nb_2O_5 around the NbO grains in the range of temperatures between 300 and 500 °C. Such effect was not so pronounced for the NbO-120K powders. This can be explained by the fact that these powders tend to oxidize at lower temperature, which inferred by the DTA analysis (Figure 4.1) and by the signal-noise ratio in the XRD pattern and Raman spectra (Figure 4.3 and Figure 4.6), from which one should conclude that the amount of amorphous Nb_2O_5 is higher comparing with the NbO-80K powders heat treated at the same temperature (300 °C).

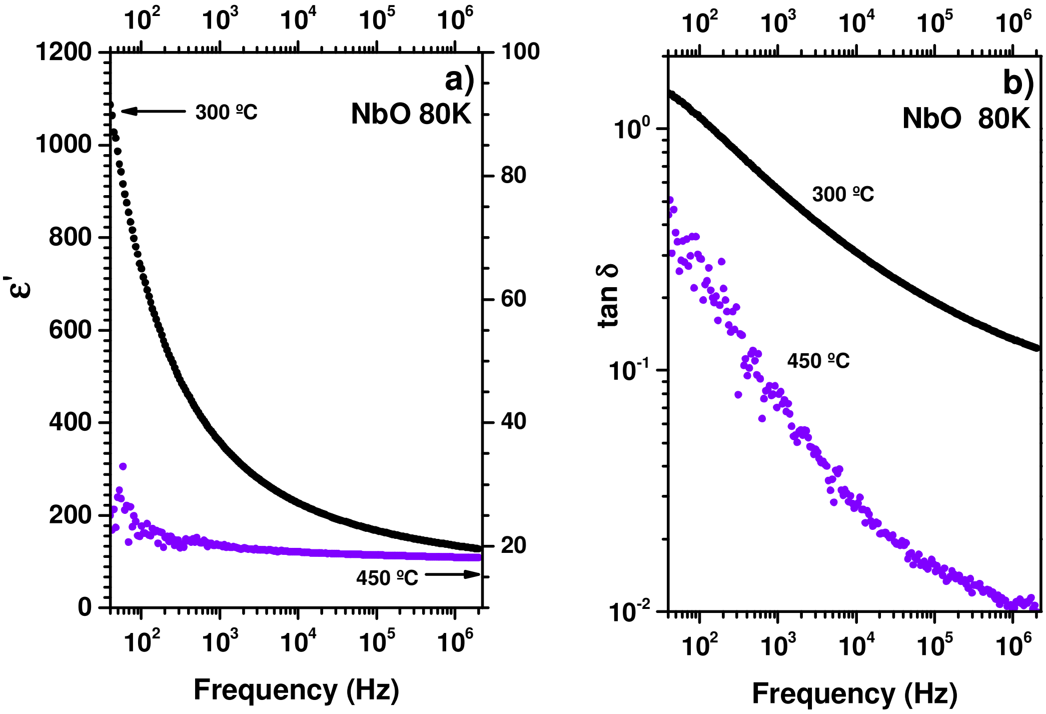

Figure 4.12 - (a) Dielectric constant and (b) dielectric loss, measured at 300 K for the NbO-80K pellets sintered at 300 and 450 °C.

4.3 Summary

The XRD analysis performed to the sintered pellets showed an evolution from cubic NbO to orthorhombic T-Nb_2O_5 and then to monoclinic H-Nb_2O_5, as the sintering temperature rises. It was also identified an intermediate monoclinic phase (B-Nb_2O_5) with smaller lattice parameters than the H- polymorph for pellets treated at 900 ºC. The XRD measurements were fully corroborated by the Raman data. All the sintered pellets, with exception of the heat treated at 900 ºC, evidence a broad emission band peaked at ~2.25 eV. For the 900 ºC sample the emission is blue shifted. The temperature dependent PL analysis suggests that an overlap of emitting centres is responsible for the broad emission and that thermally population occurs between the two emitting defects. The analysis puts forward that shallow energy levels must be involved in the recombination processes and, besides considering the native defects as responsible for the broad bands, it cannot be ruled out that nitrogen, or even surface related defects, can assume an important role on the luminescence. Furthermore, for higher temperatures a band gap shrinkage of ~80 meV was found in samples where the T-Nb_2O_5 crystalline phase is dominant. The dielectric constant of ~55 (at high frequencies), for the samples with the H-Nb_2O_5 monoclinic structures, is approximately the double of the orthorhombic samples. Furthermore, a huge dielectric constant was measured for the 80K sample treated at 300 ºC, but not at 450 ºC. This behaviour will be explained in the next chapter where it be shown that it is related to the formation of NbO-Nb_2O_5 core-shell structures in this range of temperatures. These results show that the treatment temperature is a very important parameter for the production of solid electrolytic capacitors where the Nb_2O_5 is the dielectric material.

Chapter 5

Thermal Oxidation of NbO Anodes

5. Thermal Oxidation of NbO Anodes

In this chapter, the oxidation of Niobium Oxides by heat treating at air NbO powders pressed into parallelepiped pellets will be explored in more detail. These will constitute the anodes of the capacitors studied in the next chapter.

An *in-situ* XRD study will be shown, which allowed to have a much better accuracy and understanding of the NbO oxidation and phase transformation mechanisms. The range of temperatures between RT and 500 ºC was particularly studied in this chapter, where a video and Raman spectra were recorded *in-situ* during the heat treatment. SEM pictures of anodes treated within this range of temperatures, and also *in-situ* reflectance spectra were acquired to understand the appearance of different sample colours. The explanation for the extremely high dielectric constant measured for the NbO samples treated at 300 ºC in chapter 4 was also found.

5.1 Experimental Procedure

A commercially available niobium oxide (NbO) powder, stabilized with nitrogen (~3000 ppm), suitable for electrolytic capacitors with a charge per unit weight (CV/g) of 80000 µC/g (information given by the supplier), was used for this work. The powders were pressed into a pellet with an embedded tantalum wire, to form the capacitor anode, and then sintered in high vacuum ($<10^{-5}$ mbar) at a temperature >1000 ºC to improve the coalescence between the grains.

It was performed an *in-situ* X- ray diffraction (XRD) analysis of the powders, with an *X´Pert MPD Philips* difractometer (Cu K_α radiation, λ=1.54056 Å), from 100 ºC to 1100 ºC in air, in a heating chamber *Anton Paar HTK16*. From 100 to 500 ºC the analysis was made with a step of 10 ºC, and from 500 to 1100 ºC with a step of 20 ºC, with a heating rate of 2 ºC/min between steps, and an acquisition time of ~20 minutes.

A differential thermal analysis (DTA) was performed from RT to 1200 ºC in a *Linseis Aparatus* using 40 mg of milled powder from a NbO anode. The same amount of alumina was used as reference.

The structural characterization was complemented with *in-situ* Raman spectroscopy, performed on a pressed anode in a backscattering geometry with a 532 nm laser line, using a *HR-800 Jobin Yvon (Horiba)* spectrometer, from RT to ~550 ºC using a *Linkam HFS91* heating stage with a heating rate of 2.5 ºC/min. The spectra were acquired sequentially, while the temperature was rising, with an acquisition time of 45 seconds for each spectrum.

Two sets of the same type of anodes were heated at rates of 2.5 and 20 ºC/min, respectively, from RT to ~550 ºC. A movie of this process was recorded, at 4 frames per second, with a USB camera (*IDS UI-1460SE*) connected to an *Olympus SZH10 Microscope*. The videos were then accelerated to ease the observation of the colours shifting phenomenon, and can be visualized on the online version of the reference [257]. To translate this colours shifting information to a static representation, a small area of every frames of the video was selected to create a continuous image stack of those cut pieces, vertically stretching the final image for a better visualization. The sample was placed on the top of a glass lamella, which by its turn, was placed on the top of the heating stage, thus acting as a thermal barrier. The temperature difference between the stage and the sample was measured with a thermocouple in contact with the top of the glass lamella. The measured temperature difference was not constant, but the maximum was around 40 to 50 ºC at highest temperatures. It was found that showing the measured temperatures at the surface of the sample would not be an accurate information. Therefore, it is important to notice that the heat treatment (HT) temperatures mentioned in this work are related with the heating stage, not with sample temperature. It should always be assumed that the samples are at a slightly lower temperature than the one indicated by the heating stage.

Heat treatments were then performed on 4 samples, using an heating rate of 2.5 ºC/min, at 320, 360, 400 and 440 ºC, respectively, during 1 hour. The purpose of preparing these samples was to observe, by scanning electron microscopy (SEM), how the thickness of the shell changed with the HT temperature. First attempts to make transgranular fractures of the samples were not successful, always resulting in intergranular fractures, thus not letting us to check the inner structure of the grains. Therefore, the samples were impregnated in an epoxy resin (Buehler EpoKwick®), which allowed us to polish them with silicon carbide sandpaper (120 grit), and finally with a diamond paste of 1 μm. The microstructure and morphology of these samples were then re-analysed by SEM on a *Hitachi S4100-1*, in secondary electron (SE) and backscattered electron (BSE) modes.

Optical reflectance spectroscopy was also performed on these anodes, using an *Ocean Optics USB4000* operating from 300 to 800 nm, from RT up to 550 ºC.

5.2 Results and Discussion

The *in-situ* XRD and DTA analyses are shown in Figure 5.1 by a colour map plot of the data. The blue gradient refers to XRD patterns and the black line to the DTA spectrum. This type of representation was chosen because it eases the interpretation of the evolution of the spectra with temperature without losing relevant information of the XRD spectra.

For lower temperatures, between 100 and ~370 ºC, the observed diffraction maxima are assigned to the cubic phase of NbO. Between ~300 and 500 ºC it was observed the appearance of an amorphous band followed with a decrease of the intensity of the NbO diffraction maxima with the increase of temperature, leading to a gap/absence of crystal phases before the formation of the orthorhombic T-Nb_2O_5 phase. Between ~450 and ~1000 ºC the orthorhombic T-Nb_2O_5 phase is detected. It was also possible to observe the appearance of the monoclinic B-Nb_2O_5 phase around 850 ºC. For the highest temperatures (above 1000 ºC) the monoclinic H-Nb_2O_5 phase predominates. The DTA curve has two main exothermic phenomena between 300 and 500 ºC, probably related to the oxidation of NbO (giving rise to the amorphous Nb_2O_5) and the crystallization of the pentoxide phase, respectively. Between 550 and 800 ºC, the T-Nb_2O_5 phase is very stable. At ~800 ºC, an endothermic phenomenon is detected which is probably related with the formation of the monoclinic phase of B-Nb_2O_5, followed by another exothermal event around 1000 ºC related to the crystallization of the monoclinic phase H-Nb_2O_5. These results are in total agreement with previous works [71,72], as for the present phases, as for the temperature ranges in which they appear. However, the most important information that is acquired from this analysis is the wider and clearer view of the phase changing dynamics, mainly in the range of temperatures in which the oxidation of NbO to Nb_2O_5 would occur. It is also possible to identify a small shift of the two first diffraction maxima of the T-Nb_2O_5 phase, the first one for higher and the second to lower diffraction angles likely to be related to small lattice distortions, probable consequence of tensions created by temperature.

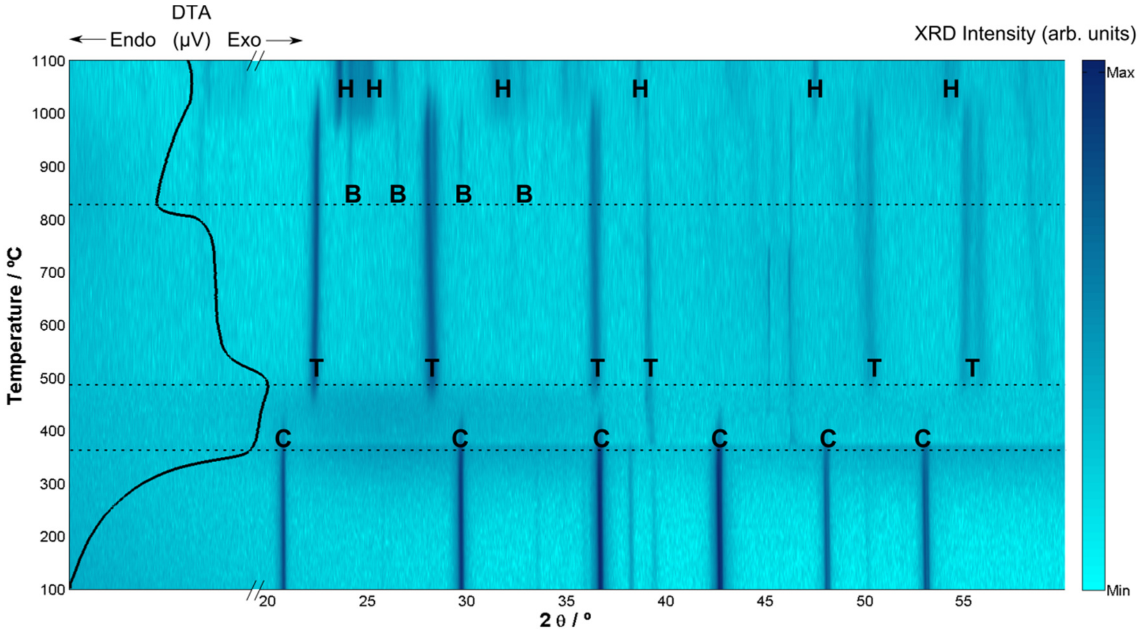

Figure 5.1 - In-Situ XRD and DTA analyses performed to the NbO powders.

Figure 5.2 shows some of the recorded movie snapshots from the NbO anode subjected to a HT with a heating rate of 20 °C/min (full video is can be visualized in the online version of reference [257]). In this experience, it is possible to observe how the NbO anodes change their colours with increasing temperature, between RT and 550 °C. The anodes quickly changed in a wide range of colours, non-homogeneously, and ended with a catastrophic destruction after approximately 20 minutes counting from the beginning of the experience.

In order to clarify this colour change effect, a slower heating rate (2.5 °C/min) was used. The results are shown in Figure 5.3 (full video is can be visualized in the online version of reference [257]).

Before the HT, the anodes are dark grey, characteristic of the NbO. With increasing temperature, the NbO begins to oxidize to amorphous Nb_2O_5 and the anode becomes brown (may be interpreted as red/orange + grey), followed by blue, green, orange, violet, blue, green, and finally light grey to completely white for higher temperatures, as the Figure 5.4 illustrates. These samples were also treated in a furnace at a fixed temperature (300 °C) during 10 and 24 hours. From that, it can be concluded that sample colour is also dependent on the duration of the treatment at a fixed temperature.

One cannot fail to notice that the change of colours seems to be cyclic and following the same sequence of the visible spectra. For higher temperatures the colours shifting is faster (sharper colours bands in Figure 5.4) than for lower temperatures. This behaviour, and the fact that for higher temperatures the amount / thickness of formed Nb_2O_5 if higher, suggests that optical interference is responsible for the phenomenon of the colours shifting in a similar way to the one observed in thin films. The white colour, observed at the highest temperatures, is due to the Nb_2O_5 phase characteristic of this oxide.

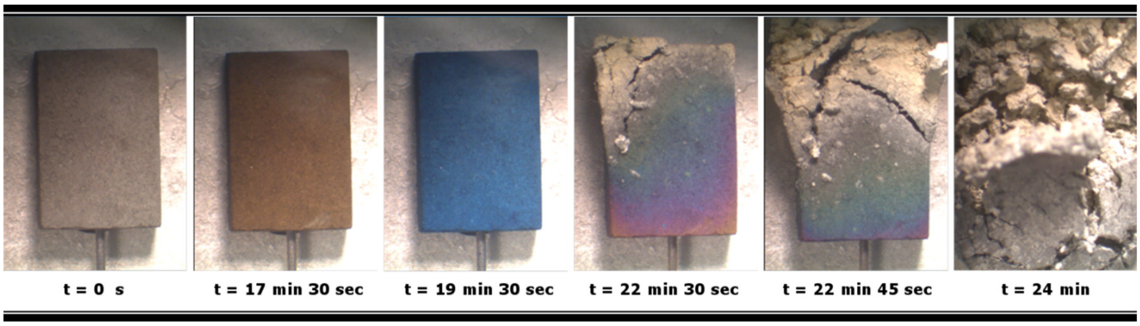
t = 0 s
t = 17 min 30 sec
t = 19 min 30 sec
t = 22 min 30 sec
t = 22 min 45 sec
t = 24 min

Figure 5.2 – Snapshots of the anode at different times (between 0 and 24 min) of the HT with a heating rate of 20 °C/min.

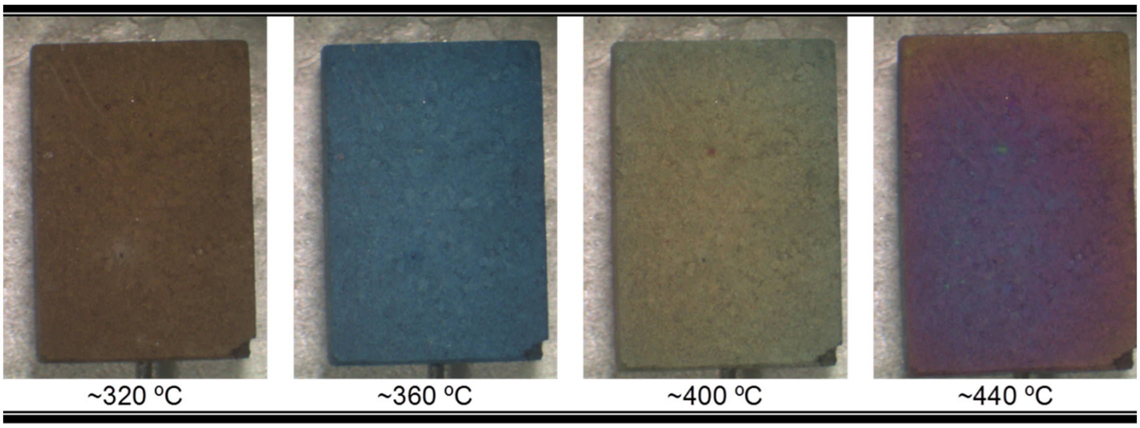
~320 °C
~360 °C
~400 °C
~440 °C

Figure 5.3 – Snapshots of the anode at different times of the HT with a heating rate of 2.5 °C/min.

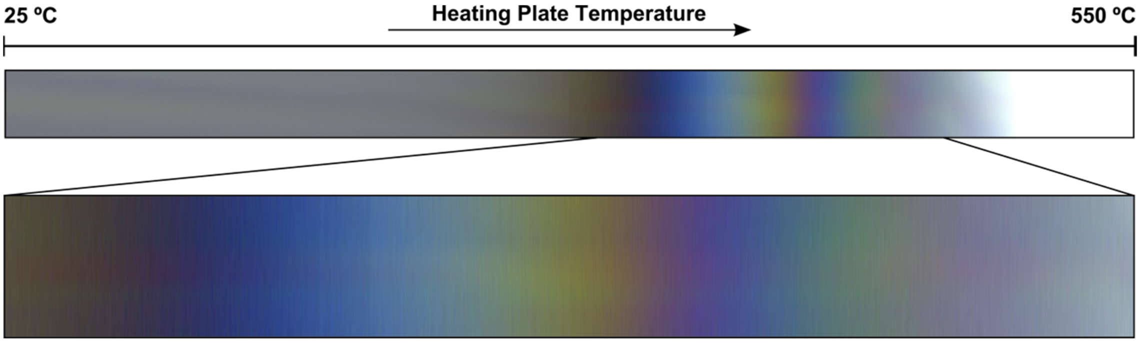
25 °C
Heating Plate Temperature
550 °C

Figure 5.4 - Stack of representative frame fractions from the video of niobium oxide anode heated at 2.5 °C/min (increase of temperature from left to right).

In-situ Raman spectroscopy analysis was performed with the same HT conditions, i.e. 2.5 ^{o}C/min, using a 325 nm He-Cd laser as excitation source. Figure 5.5 shows the spectra obtained from this analysis.

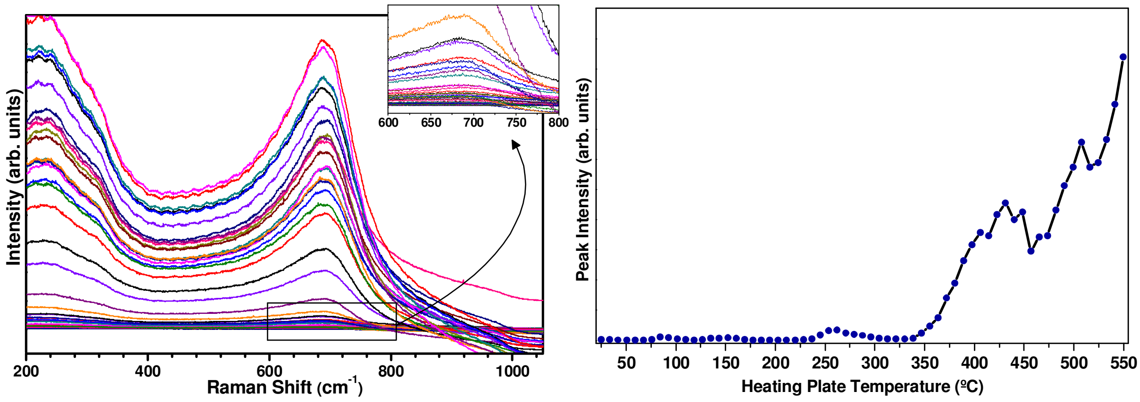

Figure 5.5 – *In-situ* Raman analysis of the NbO anode (left); Representation of the variation of the maximum intensity of the Raman peak (~690 cm^{-1}) with the HT temperature (right).

The Raman spectra of the starting NbO anode show a very low signal, almost residual, as expected since the NbO phase crystallizes in a cubic structure and is known by its metallic properties (Figure 5.5). The signal becomes very intense for higher HT temperatures, near the saturation limit of the detector (at 550 ^{o}C), under the used experimental conditions. The inset graph in Figure 5.5 shows, in detail, the main Raman peak at the lowest temperatures. The position of the vibration mode peaked at ~690 cm^{-1}, related to the T-Nb$_2$O$_5$ phase [71,72,76,157], does not shift, though its shape becomes sharper and more defined with increasing temperatures. Figure 5.5 also puts in evidence variation of the peak intensity, at ~690 cm^{-1}, with the temperature. A weak intensity for low temperatures (with slight oscillations) is observed, starting to grow in intensity as the temperature rises (probably related to formation of the Nb$_2$O$_5$ phase and its crystallization). For higher temperatures, the trend is clearly a raise of the maximum intensity, despite some oscillations that may be related to the increase of volume of the sample, as it oxidizes, and consequently defocus the laser beam from the sample surface.

Figure 5.6 shows the SEM images, in both SE and BSE modes, of the four samples treated at 320, 360, 400 and 440 ^{o}C, where it can be observed a uniform coverage of the grains with a glassy type substance which it is believed to be the amorphous niobium pentoxide. It may be hard to see clearly the expected core-shell structure since there is no difference in the present elements – only the stoichiometry and density is different. However, one can see in some pictures that the contrast is high enough to distinguish a core and a shell.

It is also possible to see that the core tends to decrease in size as the amount of shell tends to increase (Nb_2O_5 formation at the expense of NbO oxidation). Comparing the images acquired in SE and in the BSE mode, one can clearly see that the shell has a very lower intensity in BSE mode, thus indicating a lower average atomic number and/or lower density which is the case of the Nb_2O_5 phase. Even though that is clear that the thickness of Nb_2O_5 tends to increase, it is not possible to indicate an average thickness of the samples with enough precision, given its high standard deviation.

Recording the reflectance spectra of the anodes under an increasing heating temperature, it was possible to observe the optical interference pattern occurring because of the formation of the amorphous Nb_2O_5 thin layer. Figure 5.7 shows a graph with only some of the spectra acquired during this experience, between 340 and 500 ^{o}C, in order to ease the visualization and interpretation of the data (a video showing all the spectra with temperature can be visualized in the online version of reference [257]).

The existence of an interference maximum in the yellow and red region of the visible spectra at lower temperatures can be observed. The appearance of another interference maximum around 400 nm is observed, and its position begins to shift to longer wavelengths as the temperature increases (increase of the layer thickness). This trend is visible for higher temperatures, and it is even possible to distinguish a third interference maximum for the highest temperatures.

The *Commission internationale de l'éclairage* (CIE) colour coordinates of each spectrum were calculated, and these data were plotted on a CIE colour diagram, shown in the inset of Figure 5.7. It can be seen that it approximately matches the cycling sequence of colours previously observed with the optical microscope under the same circumstances.

Therefore, it is concluded that these colours are related to optical interference phenomena, resulting from changes in the thickness of the NbO/Nb_2O_5 core-shell structures.

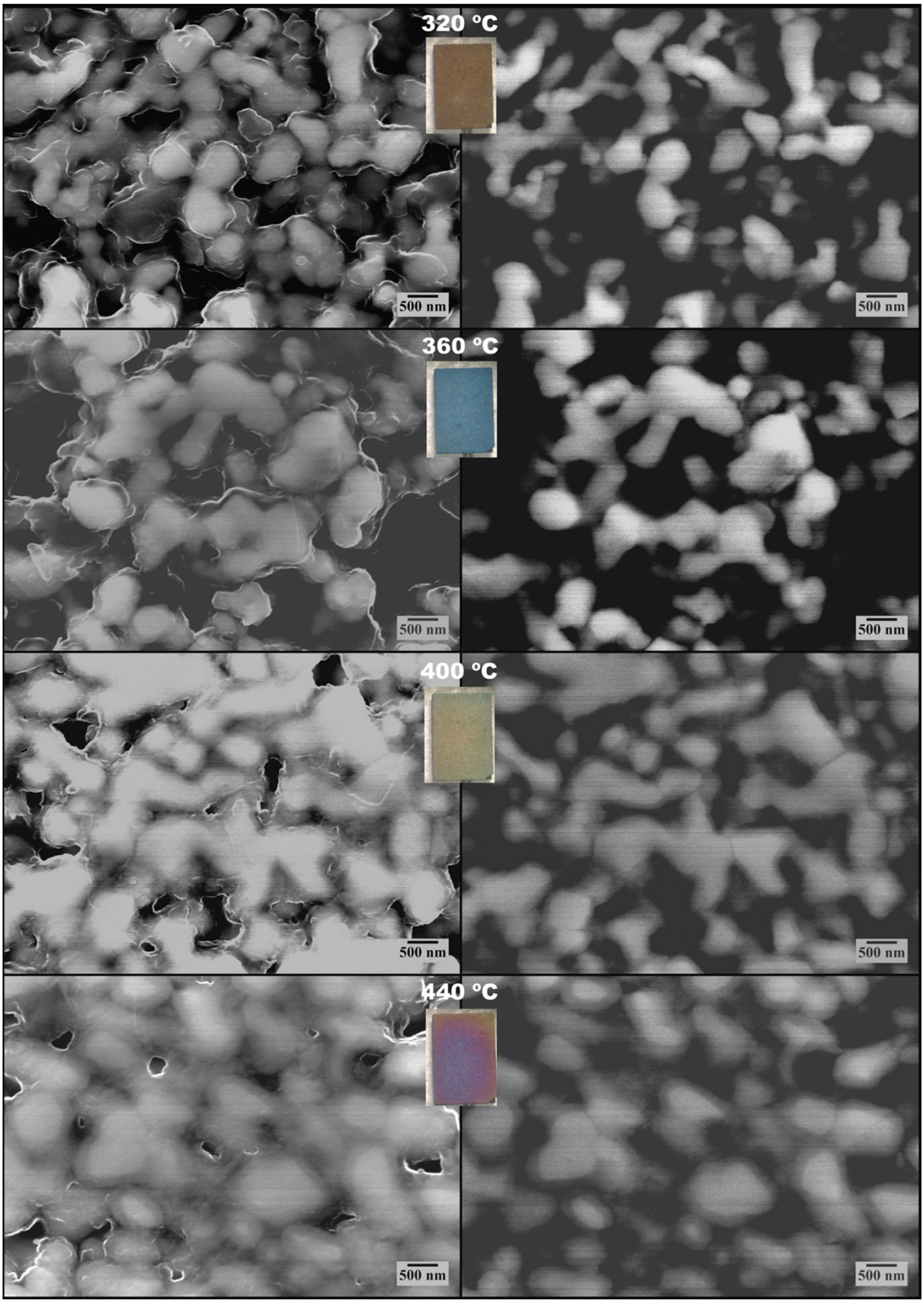
320 °C
500 nm
500 nm
360 °C
500 nm
500 nm
400 °C
500 nm
500 nm
440 °C
500 nm
500 nm

Figure 5.6 - SEM analysis of four NbO anodes heat treated at different temperatures, in SE mode (at left) and BSE mode (at right).

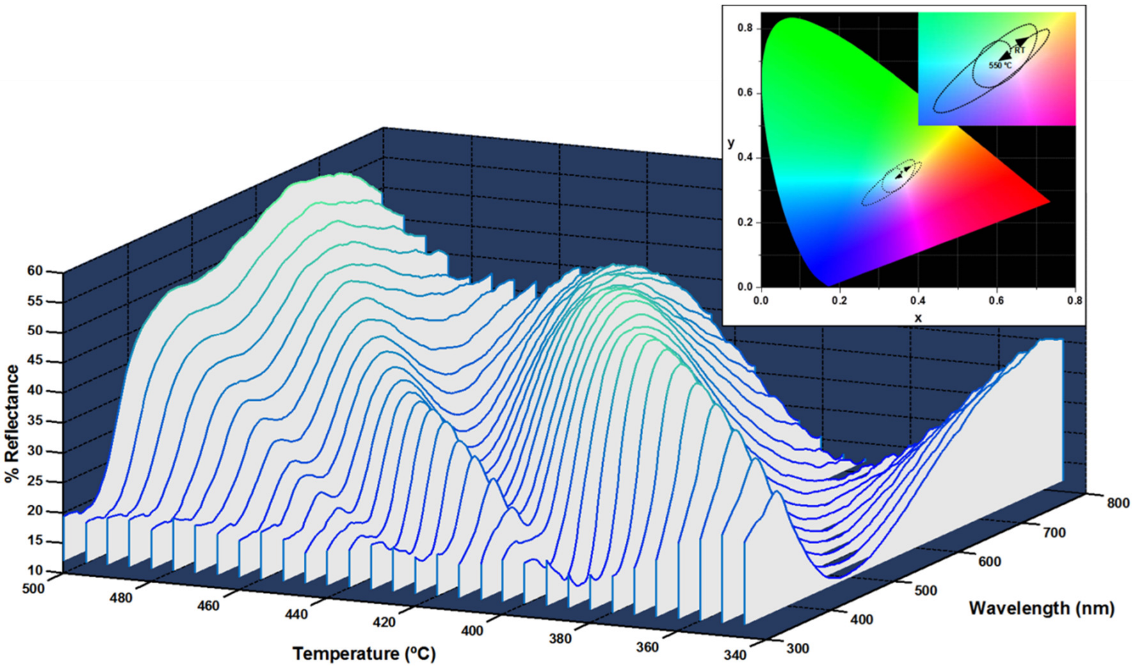

Figure 5.7 - Optical interference patterns of the NbO samples obtained between 340 and 500 °C. The colour coordinates calculated from the spectra are plotted in the CIE colour diagram shown in the inset.

5.3 Summary

The *in-situ* XRD allowed us to identify an interesting region of temperatures where the crystalline NbO oxidizes to Nb_2O_5 followed by amorphization before it becomes crystalline again. The oxidation in the range of temperatures between 300 and 500 °C was studied, using *in-situ* Raman and a video camera. The *in-situ* Raman helped to prove that the formation of amorphous Nb_2O_5 happens before crystalline T-Nb_2O_5 with the increase of temperature. The video, recorded during the oxidation with different heating rates, showed a cyclic colour change which it is believed was caused by interference of a thin layer. These results, allied to the images acquired by SEM, helped us to prove that NbO/Nb_2O_5 core-shell structures were formed. The Nb_2O_5 shell layer is the responsible for the interference colours, which thickness increases with the temperature, as it was proven by recording the optical interference patterns with the temperature.

The formation of such thin layer of Nb_2O_5, which can be considered a dielectric, around the NbO grains does also explain the high dielectric constant measured at the NbO samples heat treated at 300 °C shown in chapter 4. In detail, to calculate the dielectric constant of the sample, the thickness of the dielectric was considered to be the thickness of the pellet, which is inaccurate because in fact is an overestimation since the thickness of the Nb_2O_5 shell is much smaller than the thickness of the NbO grains. Therefore, it becomes clear that one cannot use the parallel plate capacitor model to estimate the dielectric constant of this type of microstructures.

Knowing these structural colours may be useful not only from a decorative/aesthetic point of view, but also as a qualitative measurement of the thickness of the layer. The thickness of the shells obtained by thermal oxidation was not homogeneous, but this may be more accurately controlled via anodization process. Furthermore, knowing that the formation of core-shell structures occurs in this range of temperatures is essential for the interpretation of the physical properties of this type of materials.

Chapter 6

Niobium Oxides based Capacitors

6. Niobium Oxides based Capacitors

In this chapter it will be presented the results regarding the development of niobium oxide based capacitors. The samples presented in this chapter were produced and processed in KEMET facilities in Évora, and analysed at the University of Aveiro.

At first, it will be presented the characterization of the pressed NbO anodes, with different densities, followed by study of the anodization process.

After that, the results regarding the study of the tempering processes, with different temperatures and atmospheres, will be presented.

Lastly, it will be shown the study of the impregnation of the MnO_2 through pyrolysis and the electrical characterization.

6.1 Pressing and Sintering

For this study, the same powders studied in chapter 4 were used, i.e. NbO powders doped with nitrogen (~3000 ppm). These powders were specified by the manufacturer, H.C. Stark to be well suited to the production of solid electrolytic capacitors which, depending on the granulometry, could enable specific capacities of 80000 μC/g and 120000 μC/g. The morphology of these powders is illustrated in Figure 6.1

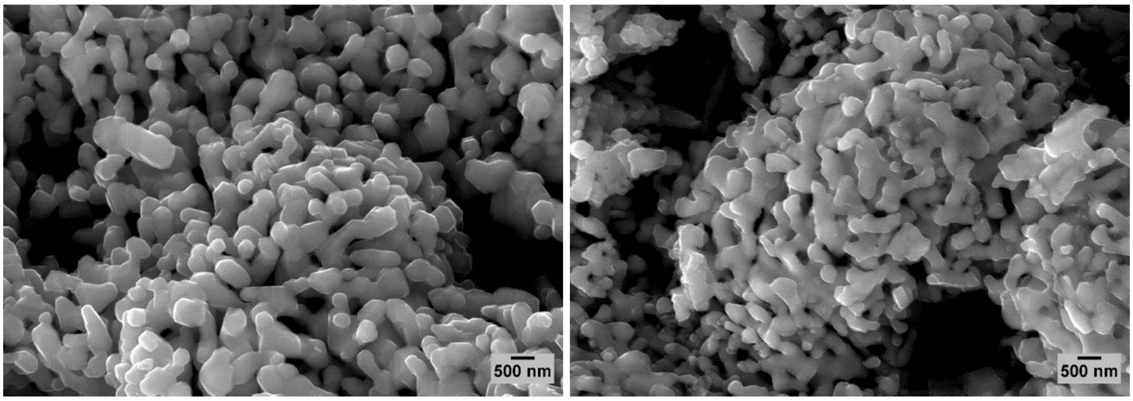

Figure 6.1 – SEM pictures of the NbO 80K and 120K powders.

These NbO powders were characterized by XRD where it was possible to identify the cubic phase of niobium monoxide (indexed with a *C*) and also some less intense diffraction maxima which were assigned to niobium nitrides (indexed with * and º), as illustrated in Figure 6.2. A diffraction maximum at ~26 º was observed but it could not be assigned to any crystalline phase. Such maximum was also detected in many of the following diffraction patterns, but it was never possible to be indexed.

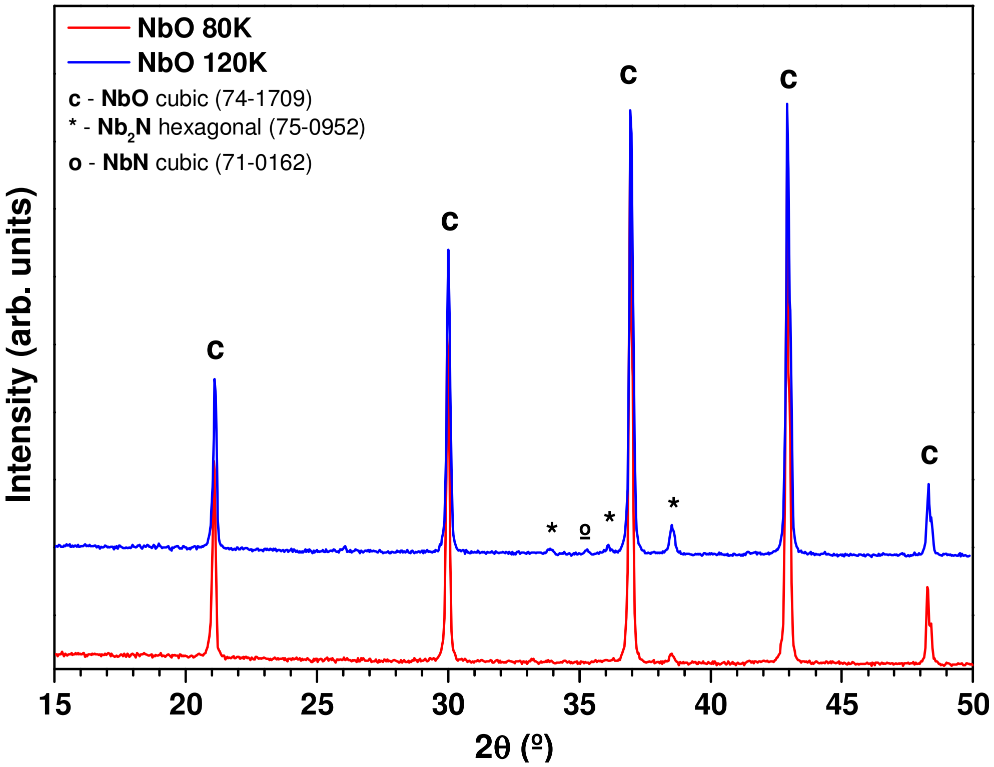

Figure 6.2 – XRD patterns of the NbO 80K and 120K powders.

Hence, at the beginning of the process (similar to the tantalum capacitor production as described in section 3.2), the NbO powders were mixed with a small weight percentage of an organic bonding agent. Subsequently, the powders were pressed uniaxially around a Ta metallic wire (~0.2 mm of diameter and ~10 mm in length) into a parallelepiped pellet, in order to form the capacitor anode.

The dimensions of these pellets, designated as *case size*, vary according the desired nominal capacitance and operating voltage of the final capacitor. The Ta capacitors with a nominal capacitance of 150 µF at 6.3 V have a case size of 3.2×0.85×4.7 mm^3 and are classified as *V case* [258]. The Ta capacitors with 22 µF at 10 V have a smaller case size with the dimensions of 1.7×0.55×2.7 mm^3 and are classified as *C case* [258].

Hence, NbO 80K powders were pressed into anodes using V cases, while NbO 120K powders were pressed using C cases, with different densities, as enumerated in Table 6.1.

Table 6.1 – List of the pressed NbO anodes.

Code	Powder	Case Size	Pressing Density (g/cm^3)
V2.8	NbO 80K	*V case* 3.2×0.85×4.7 mm^3	2.8
V3.0			3.0
V3.2			3.2
V3.4			3.4
C2.3	NbO 120K	*C case* 1.7×0.55×2.7 mm^3	2.3
C2.5			2.5
C2.8			2.8

Noteworthy, the walls of the pressing mould became slightly scratched and damaged after pressing the NbO powders into a significant number of anodes, which was not verified while pressing the Ta powders. Additional problems with the pressing were observed, with the surface of the NbO anodes being rather rough and sometimes with heterogeneous look and with fissures. These difficulties in the pressing were more common while pressing the NbO 120K powders. In an attempt to avoid this, larger amounts of organic bonding agent were used during the pressing, but without success. The presence of niobium nitrides (NbN_x), identified in XRD, may be an explanation for these pressing problems. Niobium nitrides are known for their relatively high toughness and friction coefficient [259], which can therefore damage the steel of the pressing mould. Finding a compromise of the amount of doping nitrogen to the NbO powders, in order to assure oxidation stability and low NbN_x content, may be a key to solve these pressing issues.

After being pressed, the anodes were taken to a sintering process at a temperature between 1200 and 1400 ^oC at high vacuum, to promote the coalescence, and thus the electrical contact, between the NbO grains while avoiding their oxidation. The XRD pattern of the sintered NbO anodes is shown in Figure 6.3. After the sintering process, the anodes were then welded into an aluminium bar to facilitate their handling for the following processing steps, as Figure 6.4 illustrates. The NbO anodes pressed into the C case size, with the 120K powder, with densities higher than 2.5 g/cm^3 were not mechanically stable enough to proceed with the following processing steps, particularly the bar welding and anodization. Therefore, the only type of anodes with NbO 120K powder pressed with a C case size that continued the studies was the C2.5 (with a density of 2.5 g/cm^3).

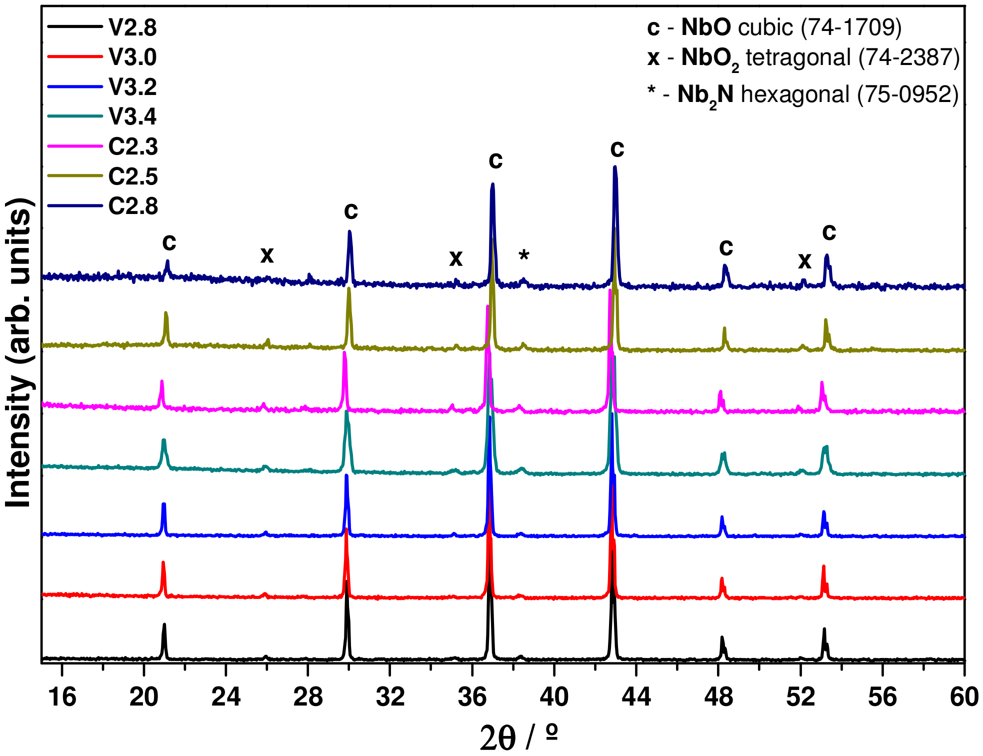

Figure 6.3 – XRD patterns of the sintered NbO 80K and 120K anodes.

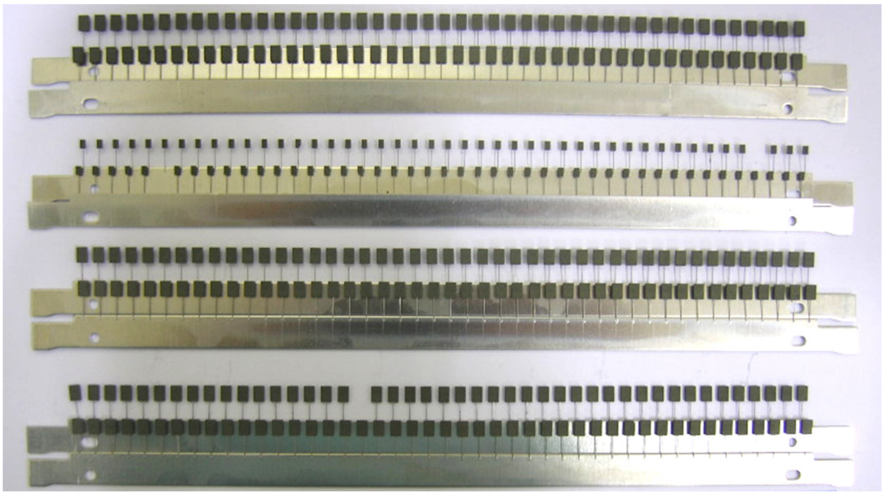

Figure 6.4 – Pressed and sintered NbO anodes welded into an aluminium bar.

The detection of the NbO_2 is undesirable and also not expected since the sintering process was performed in high vacuum where the Ta anodes are also sintered without problems. Therefore, a sintering process at the laboratory scale, using a tubular furnace connected to a vacuum pump was performed to replicate the industrial process. The sintering process was performed at 1000 ºC (with an heating rate of 2.5 ºC/min) during 1 hour at a pressure in the order of 10^{-4} mbar, to NbO 80K and 120K pellets. The XRD pattern of the NbO pellets treated in vacuum is shown in Figure 6.5.

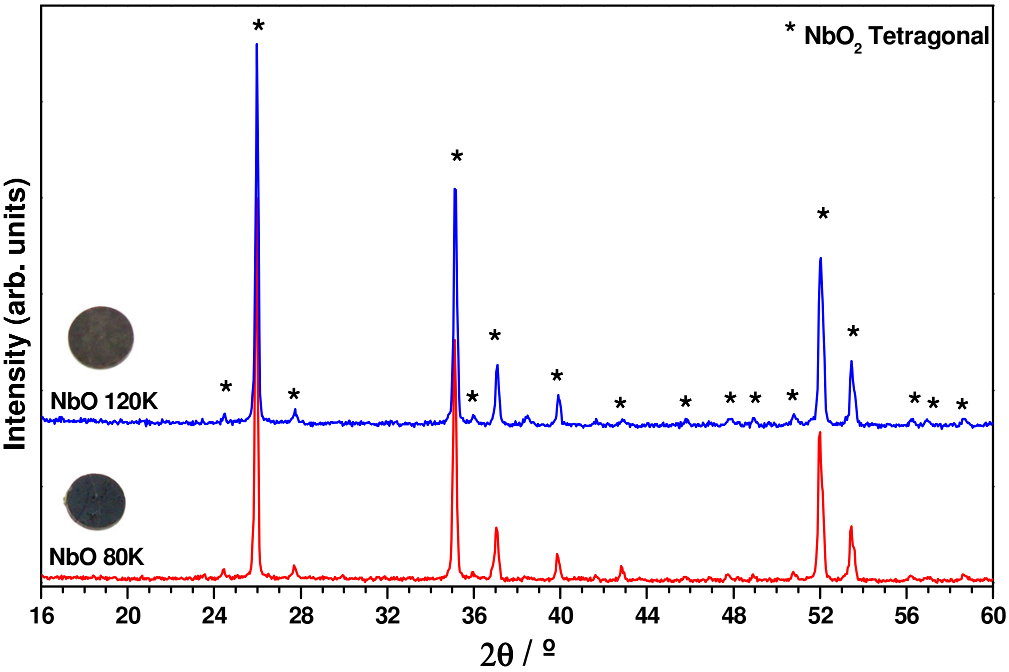

Figure 6.5 – XRD pattern of the NbO pellets sintered in vacuum in the UA laboratory.

It was possible to verify that even in a highly controlled system, as it was in our laboratory, assuring a good vacuum (c.a. 10^{-4} mbar), the NbO pellets oxidized into NbO_2 when heat treated at 1000 ºC. The fact that in this case only the NbO_2 phase was detected, in opposition to the anodes sintered in the industrial process which had still much of the cubic NbO phase, may be related to the time of the process. While in the industrial process the sintering takes about half an hour and the furnace heating process uses a very fast rate (>50 º/min), may explain why in this case the NbO_2 has been more extensively formed. However, the source of oxygen that allows the NbO to oxidize was not identified. Nevertheless, it is suggested that this may be related to air trapped between the grains during the pressing, which is not easily extracted during the evacuation of the furnace. It is however possible to conclude that the formation of NbO_2 can be restricted, to some degree, if the sintering process is completed in shorter time.

The acquired Raman and IR absorption spectra of these samples, are shown in Figure 6.6 and Figure 6.7 respectively. While the energy of the vibrational modes matched well with previous works on of tetragonal NbO_2 thin films [63] and nanowires [67], the relative intensities between peaks is not exactly the same, which can be related to a preferential crystal orientation of the reported samples. It was not possible to find any IR absorption spectra of this phase for comparison, and therefore the spectra illustrated in Figure 6.7 can be used as future reference for the identification of the tetragonal phase of NbO_2.

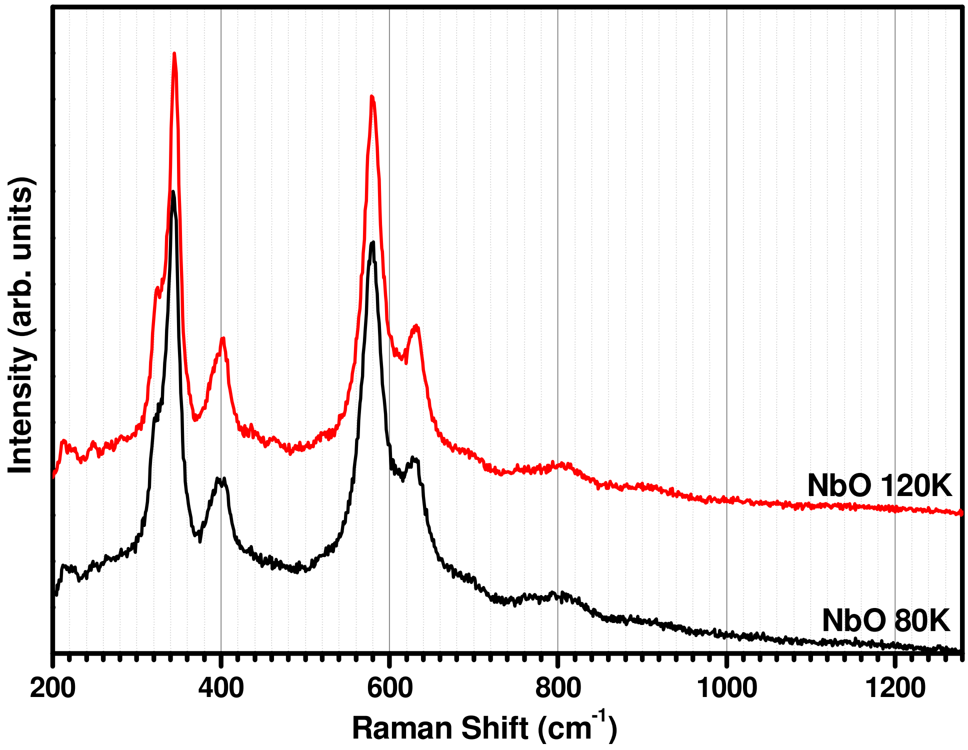

Figure 6.6 – Raman spectra (under 325 nm laser excitation) of the NbO 80K and 120K samples oxidized into NbO_2

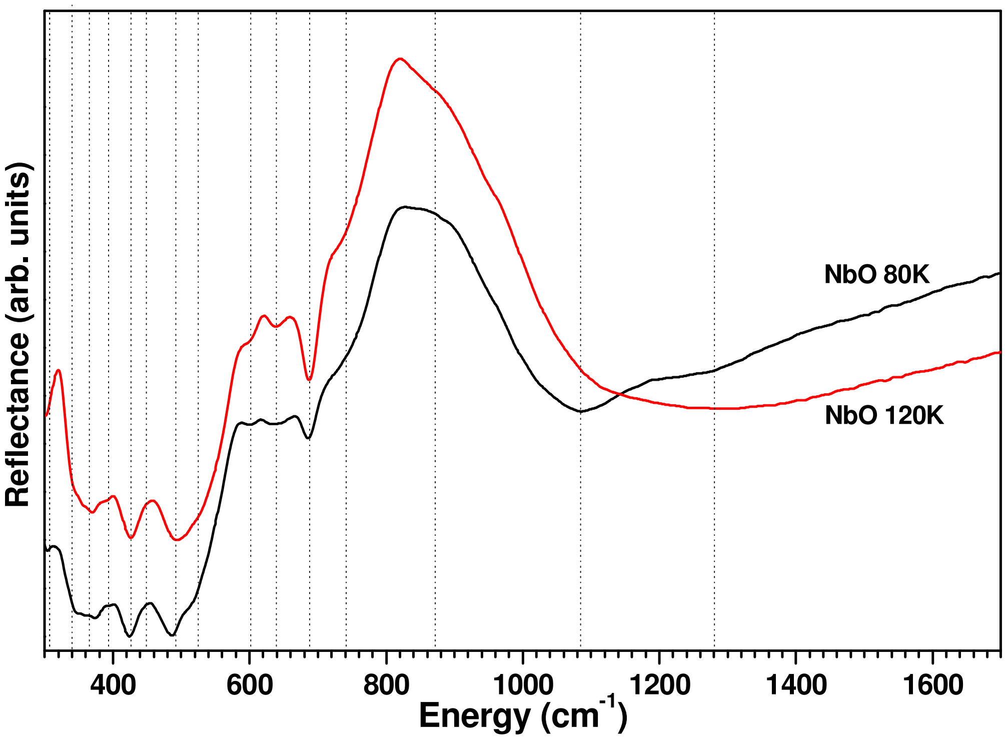

Figure 6.7 – IR absorption spectra of the NbO 80K and 120K samples oxidized into NbO_2.

6.2 Anodization

The NbO anodes sintered in vacuum were then welded into an aluminium bar and were taken to the anodization process as described in chapter 3.2. The Table 6.2 enumerates the anodes that were submitted to anodization and the current and voltage used to form the dielectric layer. The forming voltage values were chosen depending on the pressing density, following a similar relation established for the Ta capacitors, in order to achieve a capacitor with 150 µF (V case) and with 22 µF (C case). Figure 6.8 shows the colours of the anodized NbO anodes and also representative pictures to show their general aspect. From the conclusions of chapter 5, it is known that such colours are due to the surficial oxidation of the NbO grains into Nb_2O_5 with different thicknesses.

Table 6.2 – List of the anodes submitted to the anodization process and the respective forming current and voltage.

Code	Forming Current (A)	Forming Voltage (V)	Powder	Case Size	Pressing Density (g/cm³)	Specific Current (A/[g/cm³])
V2.8_1.5	1.50	24	NbO 80K	*V case*	2.8	0.54
V3.0_1.5		29			3.0	0.50
V3.2_1.5		30			3.2	0.47
V3.4_1.5		34			3.4	0.44
V3.4_1.4	1.40	34			3.4	0.41
V3.0_1.2	1.18	29			3.0	0.39
V3.4_0.2	0.25	34			3.4	0.07
C2.5_0.4	0.39	38	NbO 120K	*C case*	2.5	0.16

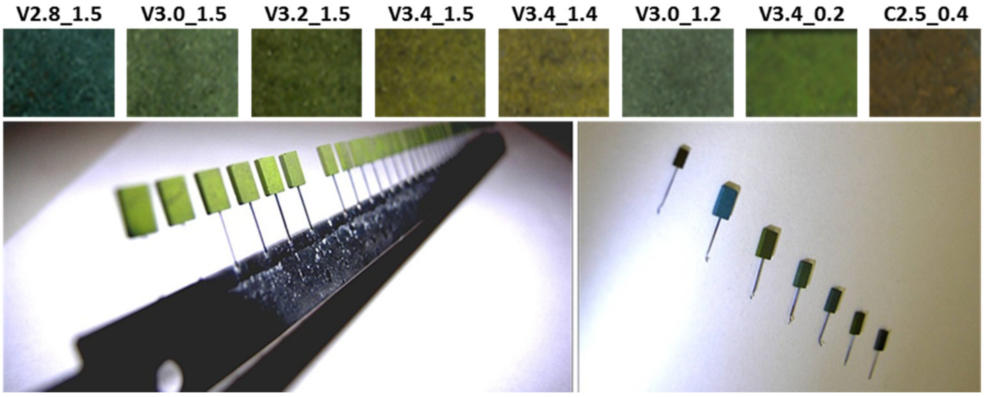

Figure 6.8 – Pictures of the anodized NbO anodes, showing their different colours.

The anodized NbO anodes were analysed by XRD (Figure 6.9). It was possible to detect the cubic phase of NbO, but also traces of NbO_2 and niobium nitride. The XRD patterns are in fact very similar to the anodes before anodization, which is not entirely unexpected since only a small amount of NbO should have become oxidized into amorphous niobium pentoxide. However, the patterns illustrated in Figure 6.9 do not suggest the presence of an amorphous phase since it was not observed any broad diffraction band and the signal/noise ratio is relatively high (with exception of the C2.5_0.4 sample which is related to the small amount of powder). The diffraction maximum at ~28 º was once again observed but kept unassigned to a crystalline phase.

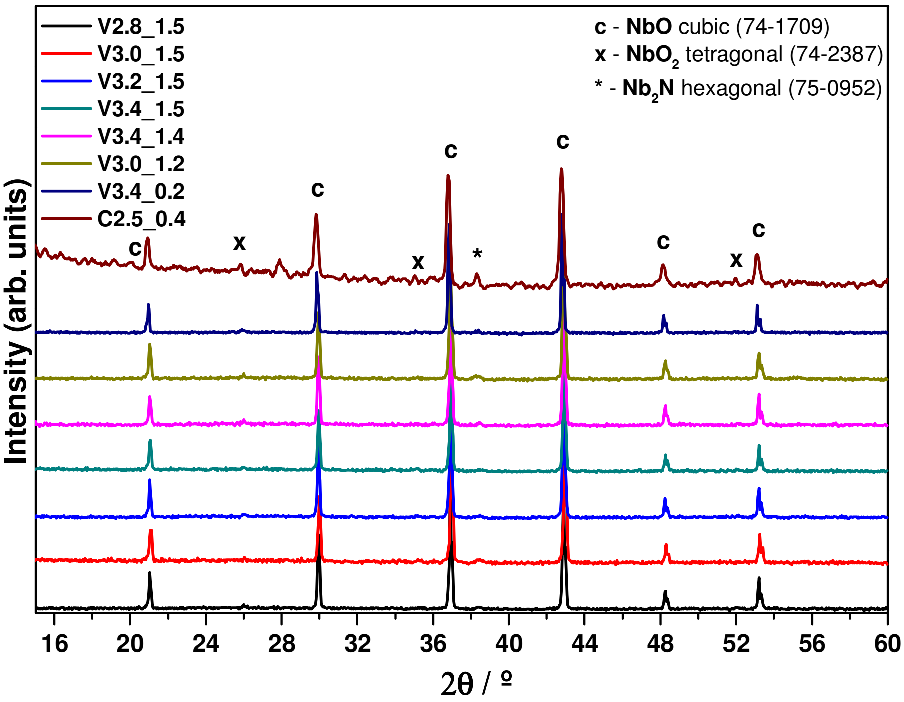

Figure 6.9 – XRD patterns of the anodized NbO anodes.

The micro Raman spectra of these anodes under 325 nm laser excitation, shown in Figure 6.10, allow us to detect the broad band characteristic of the amorphous Nb_2O_5 (centred around 640 cm^{-1}), thus confirming the presence of the desired dielectric material. There were regions of anodes surface where it was possible to detect slightly different spectra, with a broad band centred around 250 cm^{-1} and other mode at ~972 cm^{-1}. Also, in these samples, the band at 640 cm^{-1} suffered an asymmetrical broadening. It was not possible to identify the cause of these additional vibrational modes, but it is reported that the bending modes of Nb-O-Nb linkages have vibrational bands in the range of energies between 200-300 cm^{-1}. The Raman modes between 800 and 1000 cm^{-1} can be associated to highly distorted NbO_6 octahedra and/or NbO_4 species [76,89,251]. Such modes can eventually be related to an incipient crystallization of a niobium pentoxide phase, such as TT-Nb_2O_5 polymorph [76], though it would be expected that the formation of such phase would only occur upon heating. The low intensity peak observed at ~320 cm^{-1} is characteristic of the Raman spectrometer, particularly detectable for long acquisition times and low signal/noise ratio, and it is not related with the analysed samples.

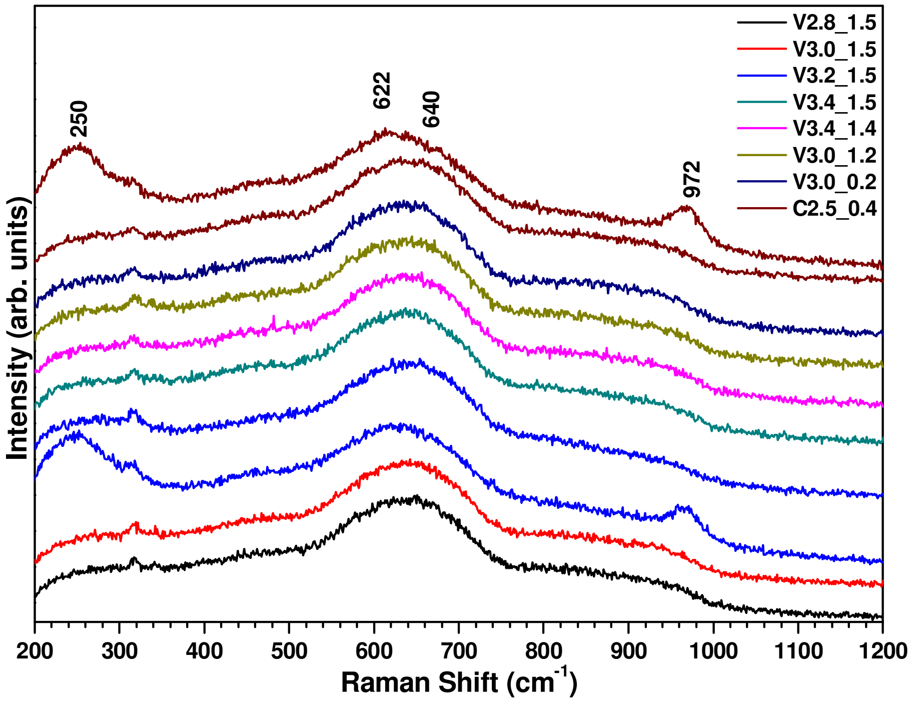

Figure 6.10 – Raman spectra of the anodized NbO anodes under 325 nm laser excitation.

The measurements of capacity and resistance of the anodized NbO anodes (respectively shown in Figure 6.11), were performed by impedance spectroscopy, as described in chapter 2.2.6, using the Cp-Rp model. The experimental apparatus used to perform these measurements consisted in dipping an individual anode into an electrical conductive solution of distilled water with 0.1 wt% of H_2SO_4, which acts as the cathode. The electrical measurements were performed by applying an *ac* signal with 500 mV of amplitude with zero DC bias between the two terminals: a gold contact dipped into the solution, and the Ta wire connected to the NbO anode.

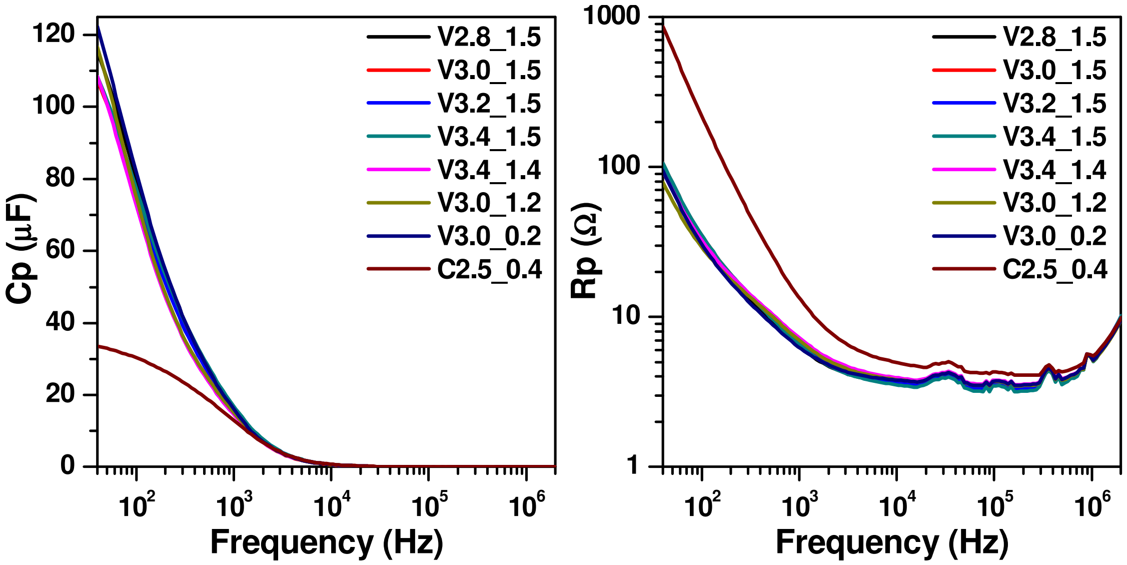

Figure 6.11 – Capacitance and Resistance, as a function of frequency, of the NbO anodized anodes.

It is possible to observe that the balance between the pressing density and the forming voltage was successfully adapted from the Ta technology, since the capacitance and resistance values of the anodized anodes, using the same forming current, are extremely close. As it can be observed in Figure 6.11, at 40 Hz (the lowest measured frequency) the capacitance of the V case size anodized anodes ranged between 105 and 120 µF, decreasing and converging at higher frequencies, being almost negligible after 10 kHz. The resistance ranges between 80 and 100 Ω at 40 Hz and decreases with frequency. Between 10 kHz and 1 MHz it can be observed a systematic behaviour of small bands and peaks in the resistance for all measured samples. Hypothesis that can justify such patterns are related to the connecting cables, to the conductive solution or to the equipment, which should be excluded since it was not observed in other type of low resistive samples. So, this behaviour must be related to intrinsic characteristics of the samples, though at this point it is not possible to understand. The C case size anode shows a lower capacitance, as desired, of about 32 µF at 40 Hz decreasing to higher frequencies. The resistance of this anode was surprisingly high, almost 1 kΩ at 40 Hz, which makes it completely unsuitable for its use as a capacitor. It is possible to see that the forming current value does not play a major role in the electrical properties, but still it is possible to observe a small increase of the capacitance with the decrease of the current. This observation can be justified by the fact that using lower currents during the anodization leads to a slower formation of the dielectric, which can promote a more homogeneous and stable dielectric layer.

It is important to compare and correlate these electrical measurements with the samples density, anodization parameters and the thickness of the dielectric layer. Thus, the microstructure of the anodes was analysed by SEM, and the micrographs are shown in Figure 6.12. It was expected that one could observe core-shell structures with an NbO core and a thin Nb_2O_5 layer around it. However, such structures were not easily observed, which is likely related to the difficulty in promoting intragranular breaking while preparing the specimen for observation. Furthermore, since both the core and shell are niobium oxides, i.e. they only differ in the Nb/O ratio, the contrast between these two phases is quite low, as it was also observed in chapter 5. Still, it was possible to measure, for each anode, the thickness of the outer layer (dielectric). Table 6.3 enumerates the average dielectric thickness for each NbO anodized anode (calculated from a statistical relevant sample of measurements), as well as the standard deviation. A parameter that relates the forming voltage with the thickness of the Nb_2O_5 layer was also calculated for each NbO anode, ranging from 2.8 to 4.3 nm/V. The average value can therefore be referred as a characteristic parameter for the NbO anodization: the Nb_2O_5 is formed at an average rate of 3.3 nm/V. However, calculating the truncated mean, i.e. not considering the value of 4.3 nm/V, one gets the value of 3.1 nm/V.

It would be expectable that the thickness of the dielectric layer would increase with the forming voltage, but the measurements performed with the SEM images did not exactly reflect this. In fact, from Table 6.3, it is possible to observe that the measured thickness of the dielectric of the V2.8_1.5 anode (formed at 24 V) is higher than for the V3.0_1.5, V3.2_1.5, V3.0_1.2 and V3.4_0.2, all of them anodized at higher voltages. Also, the V3.2_1.5 anode (submitted to 30 V) showed a thickness larger than the V3.4_0.2 which was anodized at 34 V.

Furthermore, it is possible to see the dielectric thickness of samples anodized at the same voltage, but with different currents, is not consistent. While the V3.0_1.5 and the V3.0_1.2 anodes have shown a very similar dielectric thickness (~87 nm), the measurements of the V3.4_1.5, V3.4_1.4 and V3.4_0.2 were significantly different. Thus, it is not possible to establish a trustful relation between these SEM measurements and the anodization parameters.

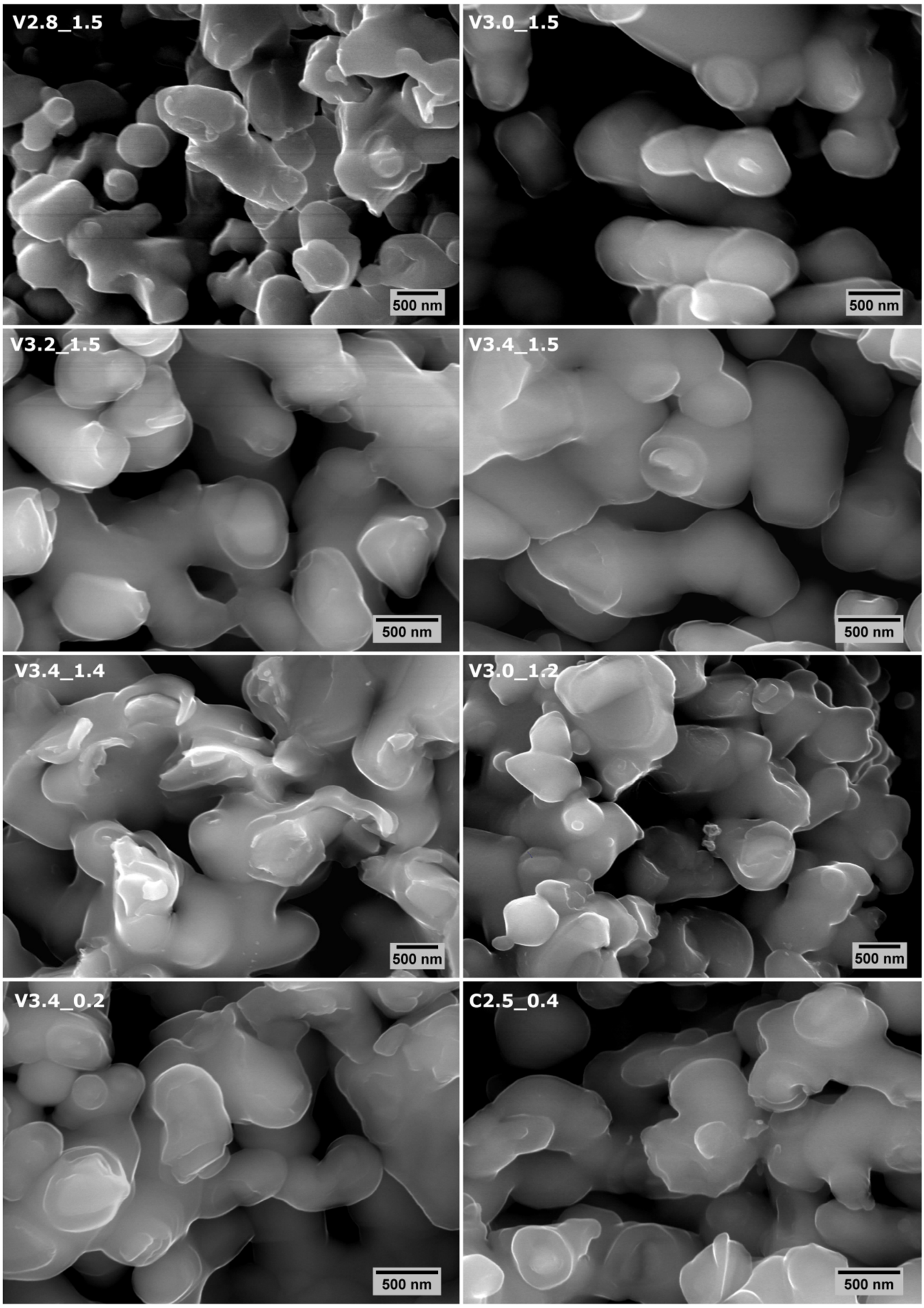
V2.8_1.5
500 nm
V3.0_1.5
500 nm
V3.2_1.5
500 nm
V3.4_1.5
500 nm
V3.4_1.4
500 nm
V3.0_1.2
500 nm
V3.4_0.2
500 nm
C2.5_0.4
500 nm

Figure 6.12 – SEM images of the anodized NbO anodes.

Table 6.3 – Average thickness of the dielectric layer of each anodized NbO anode and the calculated ratio thickness/voltage.

Anode	Average Dielectric Thickness (nm)	Standard Deviation (nm)	Forming Voltage (V)	Thickness/Voltage (nm/V)
V2.8_1.5	102.6	10.6	24	4.3
V3.0_1.5	86.5	7.7	29	3.0
V3.2_1.5	98.2	11.0	30	3.3
V3.4_1.5	112.3	17.5	34	3.3
V3.4_1.4	118.4	10.3	34	3.5
V3.0_1.2	87.4	8.0	29	3.0
V3.4_0.2	96.0	13.3	34	2.8
C2.5_0.4	112.1	19.7	38	3.0

However, while these SEM measurements are clearly unreliable to define the thickness of the Nb_2O_5 dielectric layer (and are also not in agreement with the electrical measurements) such results should not be disregarded. These observations, and the high standard deviation, are possibly related to the difficulty in acquiring clear images and having a clear identification of the interface between the NbO core and the amorphous Nb_2O_5 dielectric layer. Additionally, it is possible that the formation of intermediate stoichiometries, i.e. oxygen deficient Nb_2O_5 (or even NbO_2) can be formed at the interface between dielectric and anode. While such intermediate layers would not significantly contribute for the capacitance and resistance values, they could be observed with almost equal contrast in a SEM image, thus misleading the thickness measurements. Comparing the colours of the anodes shown in Figure 6.8 and the thicknesses listed in Table 6.3, one can see that similar colours tend to match similar thicknesses. This could mean that the oxygen defective Nb_2O_5 intermediate layers, which are likely to have similar refractive index as the stoichiometric amorphous Nb_2O_5, may in fact exist and be wrongly observed as the dielectric layer in SEM.

In such case, it is possible that the formation of such intermediate layers is related not only with the forming voltage, but also with the forming current. That would explain, for instance, why the V2.8_1.5 anode (formed at the lowest voltage) has shown a higher dielectric thickness, because since there are less NbO grains, they will be subjected to a higher local current than an anode with higher density, as listed in Table 6.2. Therefore, the forming current should also be adapted as a function of the pressing density.

6.3 Tempering

From the experience acquired from the study of the anodized NbO anodes, a new set of samples was prepared to proceed to the tempering studies. It was chosen the same forming current, 1.5 A, with different pressing densities (from 2.8 to 3.4 g/cm^3) with the V case size, and the respective forming voltages, in order to reproduce the same conditions of the V2.8_1.5, V3.0_1.5, V3.2_1.5 and V3.4_1.5 samples. Hence, such anodes were tempered at 320 and 350 °C in air, and at 390 °C in vacuum. Table 6.4 enumerates all these anodes submitted to the tempering process and also the pictures showing their general aspect. It is possible to observe from such pictures that the colour of the anodes changed as a function of the tempering parameters (temperature and atmosphere) which, as it was explained, is an indication of the variation of the thickness of the Nb_2O_5 layer (with or without oxygen deficiency).

Table 6.4 – List of the anodes submitted to the tempering process at different temperatures and atmospheres, and respective pictures.

Code	Pressing Density (g/cm^3)	Tempering Temperature (°C)	Atmosphere	Picture
2.8_320	2.8	320	Air	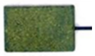
2.8_350		350	Air	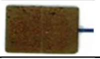
2.8_390		390	Vacuum	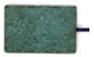
3.0_320	3.0	320	Air	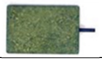
3.0_350		350	Air	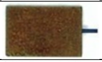
3.0_390		390	Vacuum	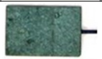
3.2_320	3.2	320	Air	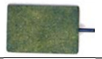
3.2_350		350	Air	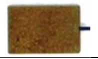
3.2_390		390	Vacuum	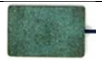
3.4_320	3.4	320	Air	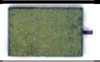
3.4_350		350	Air	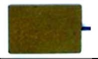
3.4_390		390	Vacuum	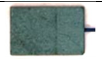

Figure 6.13 shows the XRD of all anodized NbO anodes before and after tempering with different conditions. No changes of the crystalline phases were observed in any case. The most intense diffraction maxima were assigned to the cubic NbO phase, which was still

expected to be the majority phase but, similarly to the samples in previous processing stages, minor peaks corresponding to the tetragonal niobium dioxide and niobium nitride were assigned. While the signal/noise ratio did not significantly vary, it was possible to observe, for the anodes tempered at 350 ºC at air, a low intense large band, approximately between 20 and 32 º (shown in detail in Figure 6.14),which may indicate the presence of an amorphous phase. From this observation, and from the conclusions reached in chapter 5, it is possible to assume that such band is related to the amorphous Nb_2O_5 since that at this temperature (in air) it was expected that the formation of such phase would have increased.

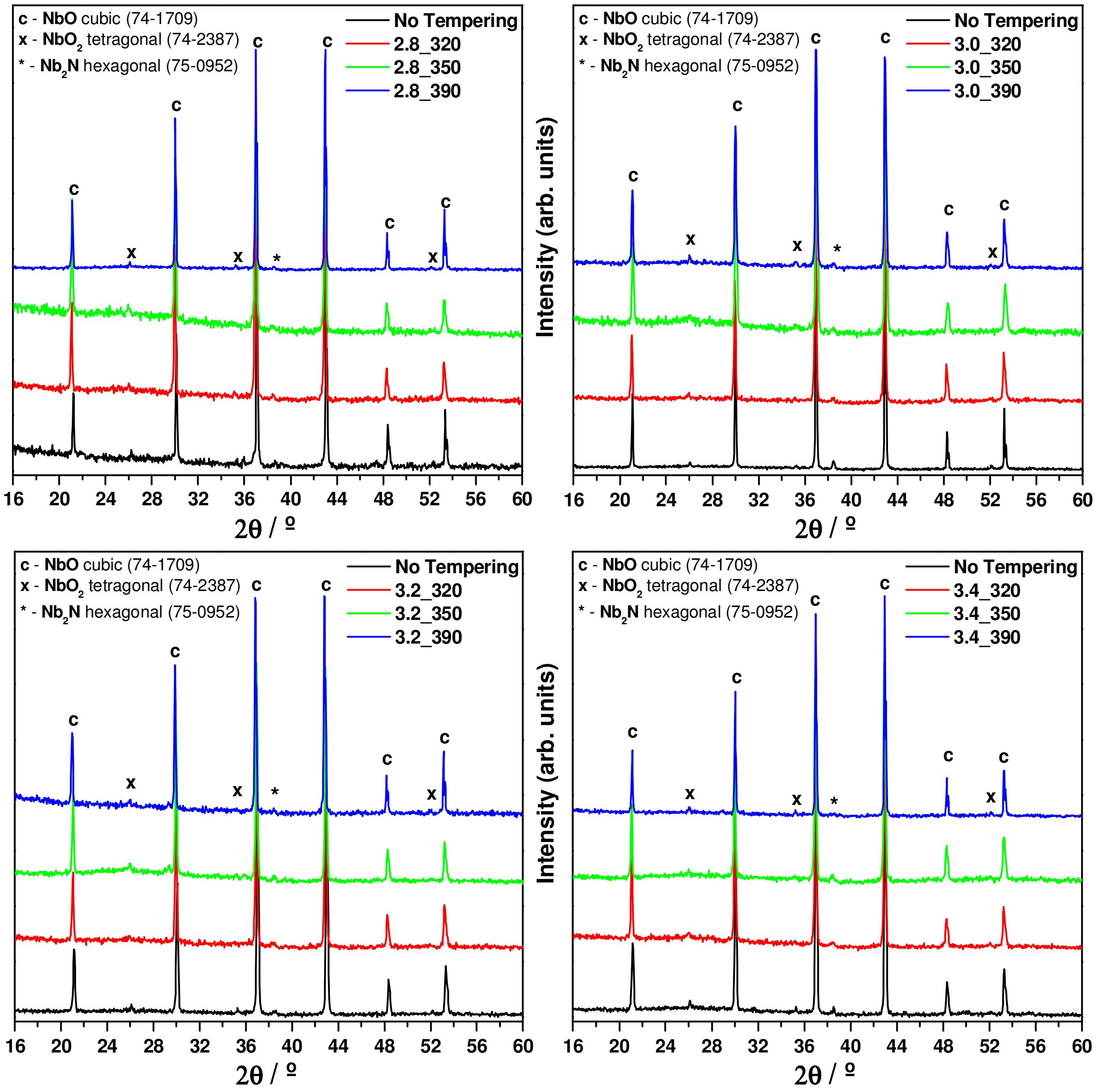

Figure 6.13 – XRD patterns of the anodes before and after the tempering process.

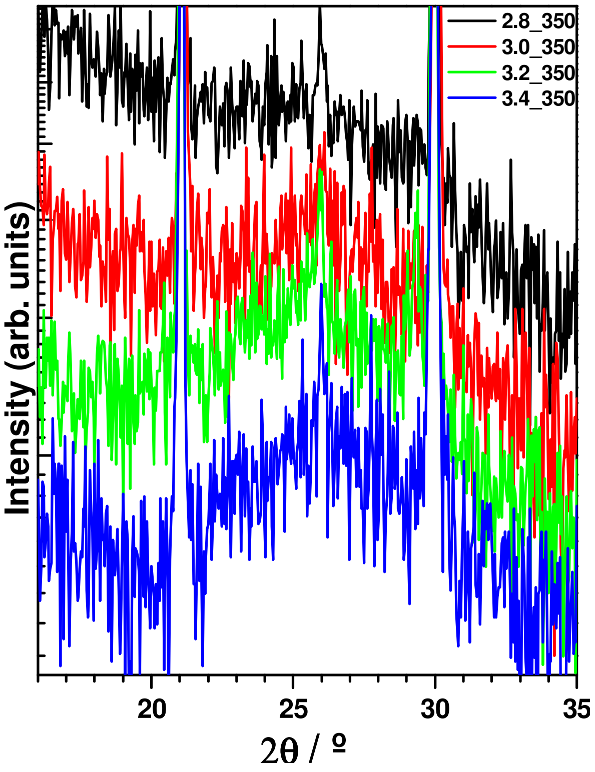

Figure 6.14 – Detail of the bands observed by the XRD patterns of the anodes tempered at 350 ºC, assigned to the presence of an amorphous phase.

Figure 6.15 shows the Raman spectra, using a 325 nm laser as excitation source, of all anodized NbO anodes before and after tempering with different conditions. All the samples revealed extremely similar spectra, with a large band centred at ~640 cm^{-1}, with other band at ~260 cm^{-1}, typical from the aforementioned amorphous phase of Nb_2O_5. The intensity of the signal was generally very low and it was necessary to use large acquisition times to acquire all spectra. It is expected that the samples tempered at 350 ºC in air would have a higher amount of amorphous Nb_2O_5, and therefore a more intense signal. However, such observation was not clearly evidenced due to some drawbacks associated with the technique and sample heterogeneity. The recorded signal was very low and small variations of the intensity were more due to focus issues or to the sample region that was being analysed.

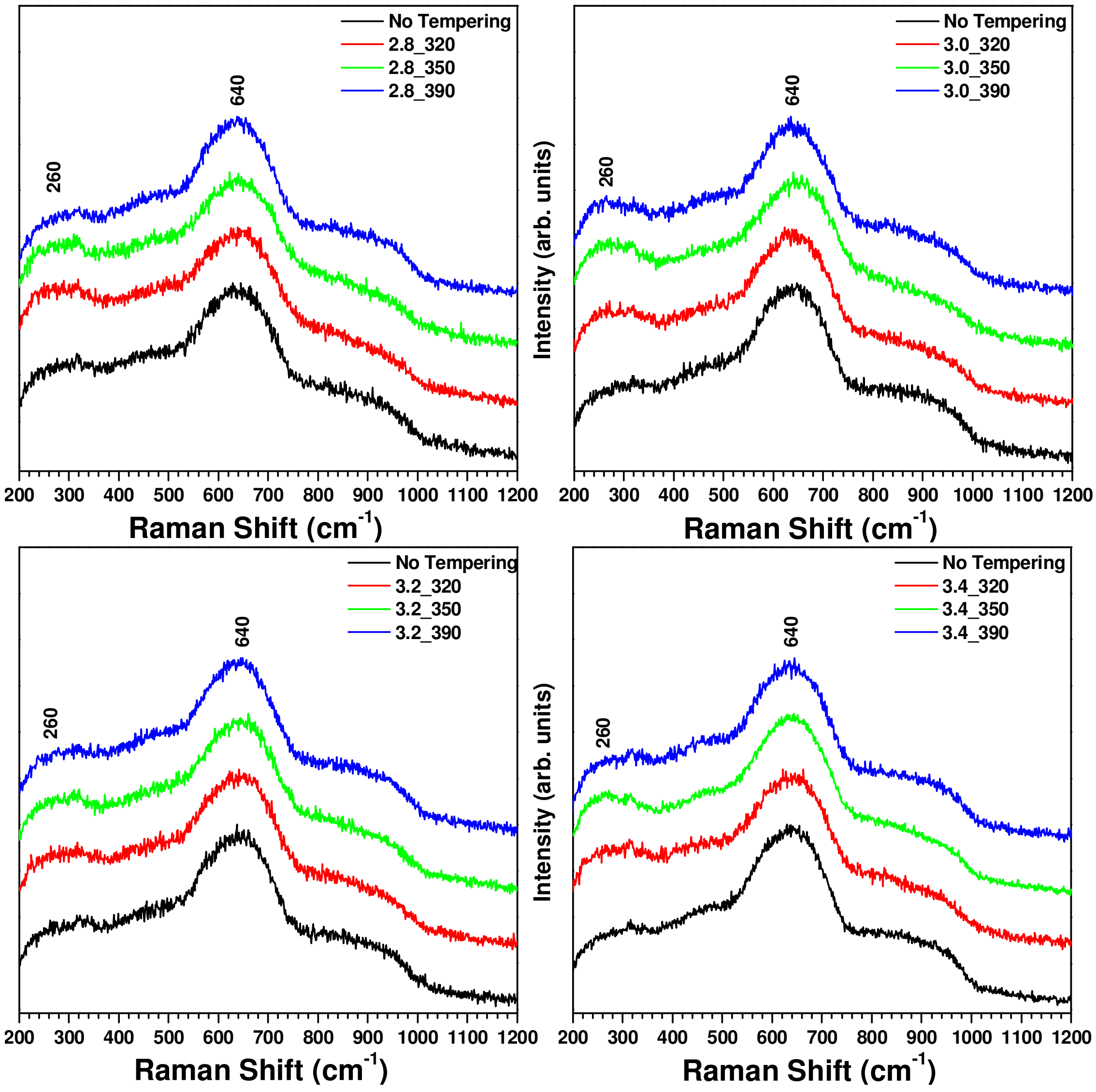

Figure 6.15 – Raman spectra, under 325 nm laser excitation, of the anodes before and after the tempering process.

The measurements of capacity and resistance, as a function of frequency, of the anodized NbO anodes, before and after tempering, are shown in Figure 6.16 and Figure 6.17. The electrical measurements were made under the same conditions and with the same type of apparatus as described in previous section. In Figure 6.16, it is possible to see that the capacitance of the NbO anodes before tempering is between 130 and 160 μF (depending on the pressing density) at 40 Hz. After the tempering process in air, at 320 ºC, the capacitance decreases significantly, to values between 60 and 90 μF at 40 Hz. The capacitance decreased even further for the anodes tempered at 350 ºC (in air), to ~2 μF. However, the tempering at a higher temperature (390 ºC) in vacuum, led to an increase of the capacitance to values between 180 and 200 μF.

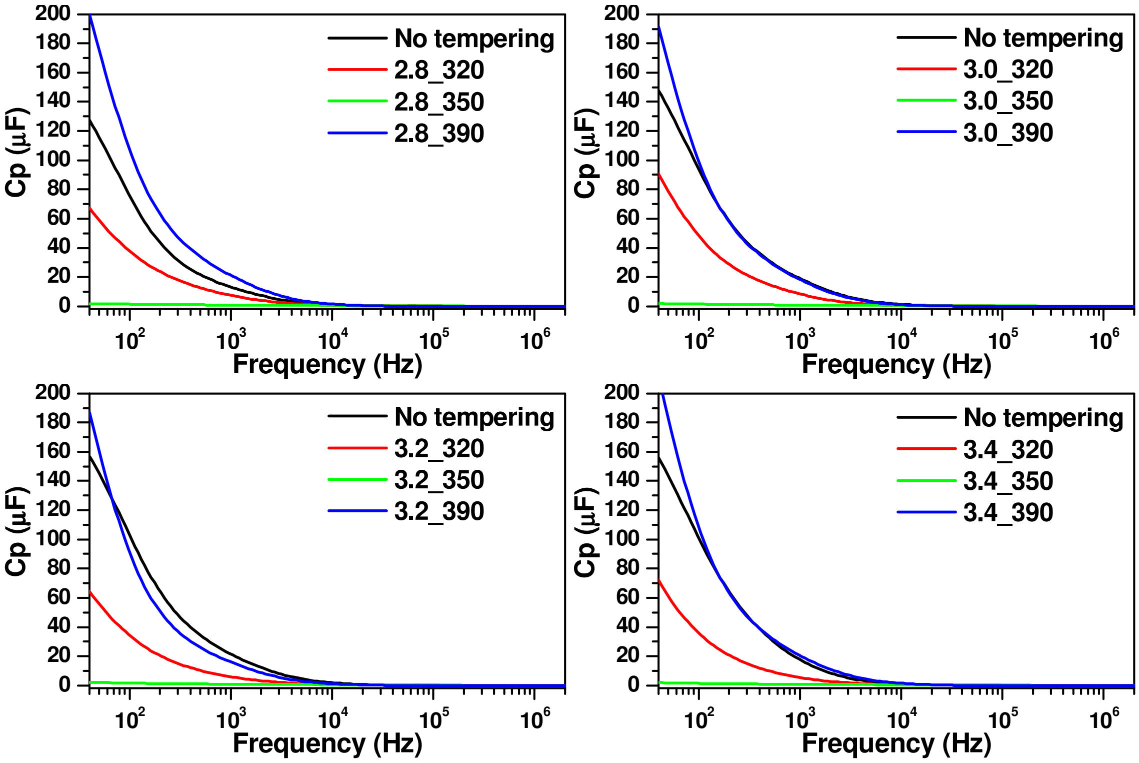

Figure 6.16 – Capacitance of the anodes before and after the tempering process.

Thus, after the capacitance measurements, the resistance results shown in Figure 6.17 were not surprising. Comparing with the anodized NbO anodes, which have shown a resistance around 50 Ω at 40 Hz, it was observed an slight increase to 60-80 Ω (at the same frequency) after being tempered at 320 °C in air. However, at higher frequencies this difference was higher, and the previously observed patterns (bands and peaks) between 10 kHz and 1 MHz were much less pronounced. Regarding the anodes tempered at 350 °C, the resistance was significantly higher reaching values between 1.8 and 2.5 kΩ at 40 Hz but decreasing to higher frequencies (about 2 orders of magnitude at 1MHz). The aforementioned patterns at high frequencies were not detected in these samples. Finally, the anodes tempered at 390 °C in vacuum have shown a decrease in the resistance, comparing with the non-tempered anodes, to 15-20 Ω at 40 Hz, generally converging at higher frequencies. Overall, the non-tempered anodes and those tempered in vacuum have shown very similar resistance values and behaviour with frequency, also regarding the bands and peaks between 10 kHz and 1 MHz.

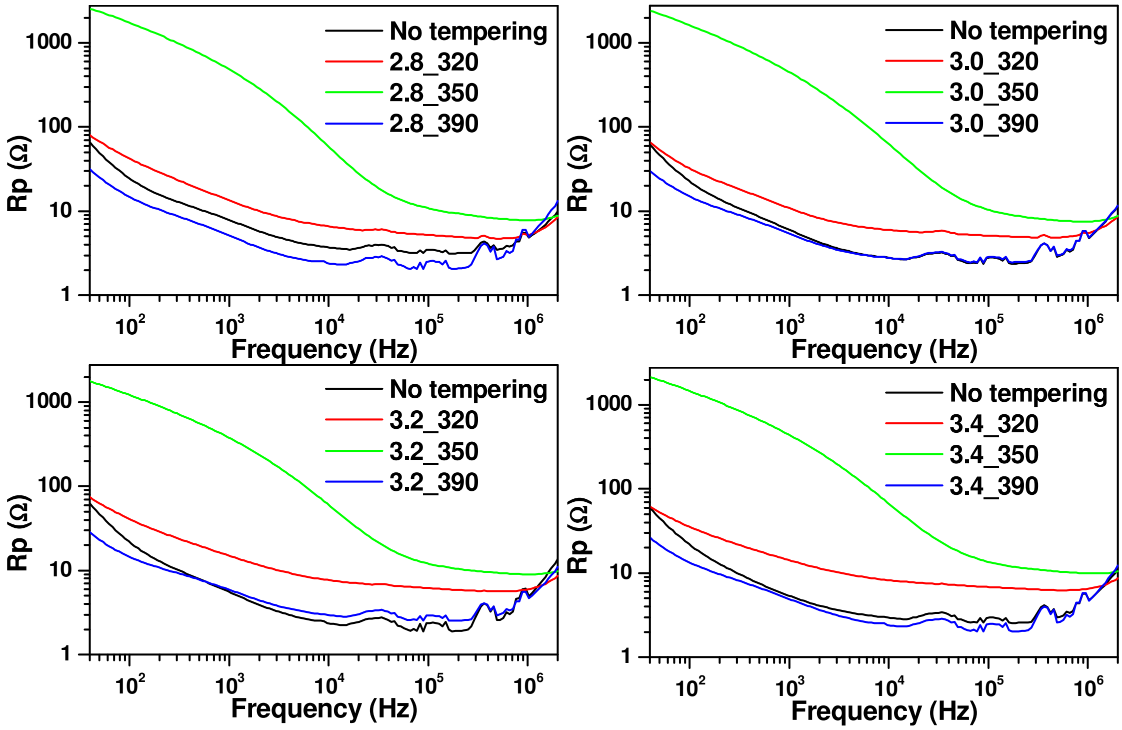

Figure 6.17 – Resistance of the anodes before and after the tempering process.

At this point, it is possible to suggest an explanation to the observed behaviour of the tempered NbO anodes, and the effect of the temperature and atmosphere on their properties. As explained, from chapter 5, it is known that a heat treatment in air at temperatures higher than ~300 °C lead to the oxidation of the NbO into Nb_2O_5. Therefore, while the non-tempered NbO anodes have a layer of Nb_2O_5 formed by anodization with a controlled and uniform thickness, the anodes which have suffered a tempering process in air (at 320 and 350 °C) should have an increased amount of niobium pentoxide, i.e. a thicker dielectric layer. Hence, it becomes obvious why with the increase of the tempering temperature, in air, the capacitance of the anodes decrease and the resistance increases. On the other hand, the anodes tempered in vacuum at an even higher temperature (390 °C) seemed to show an opposite behaviour, i.e. increased capacitance and decreased resistance. In an analogy, such observation can indicate that the thickness of the dielectric (Nb_2O_5) can slightly decrease with the tempering in vacuum. Knowing that niobium monoxide can be easily oxidised at these temperatures, and since there was no external source of oxygen, and allied to the fact that niobium pentoxide can easily accommodate oxygen deficiencies, it is highly probable that oxygen diffusion occurs from the dielectric layer of Nb_2O_5 into the NbO. In this way, it can be justified why the thickness of the dielectric becomes thinner, as the oxygen is diffused, but leading to the increase of the oxygen deficient Nb_2O_5 intermediate layer, as also suggested by Störmer *et al.* [31]. It is also possible that the patterns of bands and peaks observed at high frequencies may be related to the presence of such oxygen deficient Nb_2O_5. However, further studies focused on such phases are unquestionably required to reach a definite conclusion.

In order to check on morphological changes during this tempering process, a SEM analysis was performed to all the tempered anodes. The images are shown in Figure 6.18.

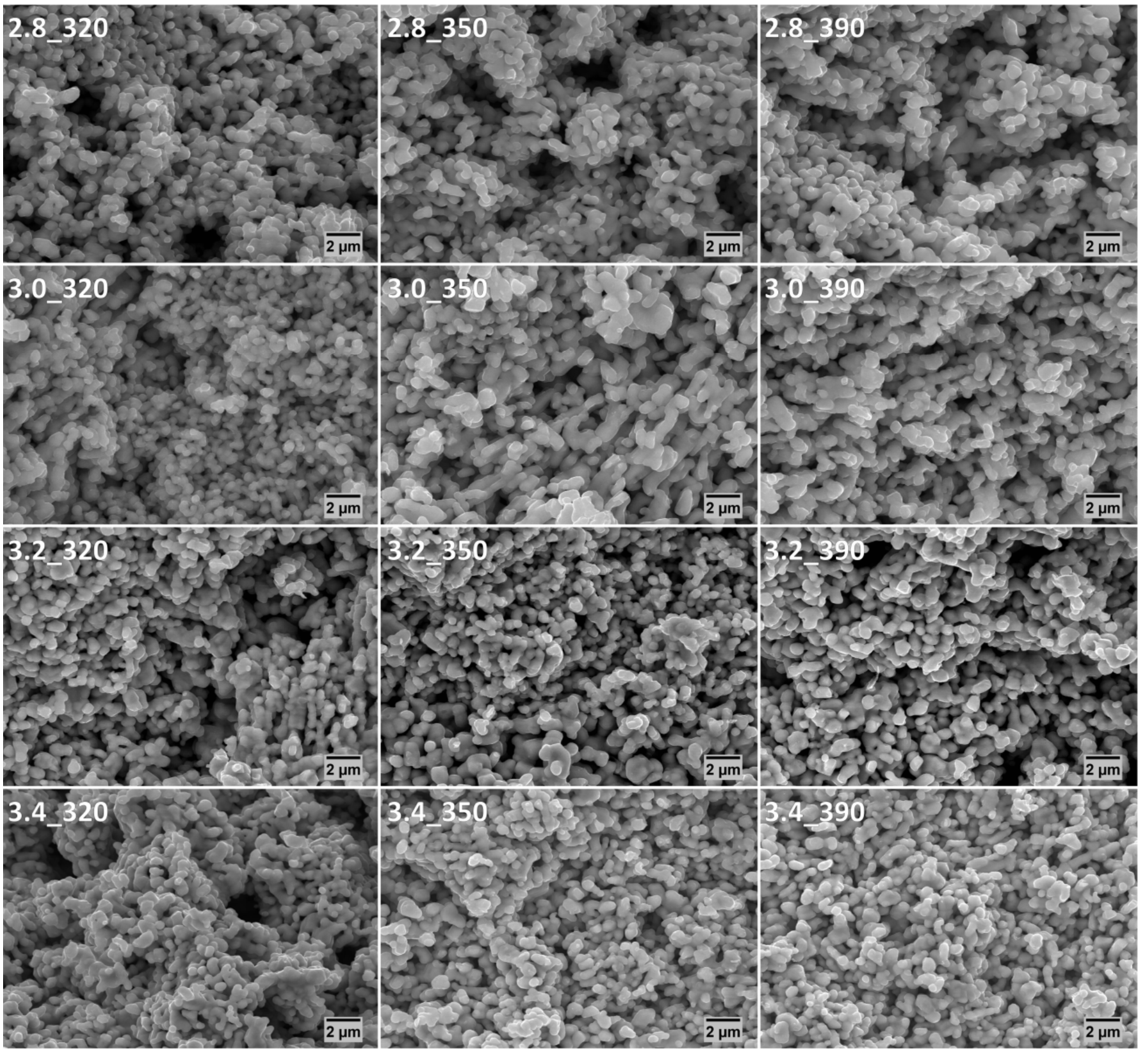

Figure 6.18 – SEM images of the anodized NbO anodes after the tempering process.

Generally, all the samples looked extremely similar. It was possible to see that the morphology of the anodes does not change significantly with the tempering temperature and atmosphere. However, no fractured grains were observed, in any of the analysed samples. Several attempts to create intragranular fractures were made, but without success. It was attempted to observe these samples through atomic force microscopy (AFM), but given the high roughness and porosity of the specimens, such attempts were unsuccessful. This was a big inconvenient, because it does not allow to see the effect of the tempering process on the thickness and microstructure of the Nb_2O_5/NbO core-shells. On the other hand, one can say this problem assures that the temper was successful, providing a higher hardness and cohesion of these structures as it was desired.

Overall, it can be concluded that, for the production of capacitors, the tempering of NbO anodes should be done in vacuum, not in air. Variations of the electrical properties were observed with any of the tempering temperature or atmosphere. However, the case of the anodes tempered in vacuum, where an increase of capacitance was observed, is more easily corrected by making a re-forming of the dielectric through an anodization process, as mentioned in section 3.2.6.

6.4 MnO_2 impregnation

As explained in section 3.2, one of the last steps of the manufacturing process of a solid electrolytic capacitor is the MnO_2 impregnation which will act as the cathode. This is done by dipping the anodes into a manganese nitrate solution and then heated to promote the pyrolysis reaction into MnO_2.

Hence, following the previous manufacturing step, the anodized NbO anodes submitted to the tempering process were taken into the MnO_2 impregnation line. In this case, the anodes with 2.8, 3.0 and 3.4 g/cm^3 tempered in air at 320 and 350 ^oC and in vacuum at 390 ^oC were selected. Because the thickness and adhesion of the MnO_2 formed layer depends on the temperature, two different pyrolysis reactions were tested at 230 and 270 ^oC. The morphology of the MnO_2 particles formed around the Nb_2O_5/NbO core-shell structures, were analysed by SEM. The images acquired for the anodes submitted to a pyrolysis at 230 ^oC are shown in Figure 6.19, while Figure 6.20 shows the anodes submitted to a pyrolysis at 270 ^oC. It should be noted that the images depicted in Figure 6.19 and Figure 6.20 are from the inner body part of the anodes after being broken apart.

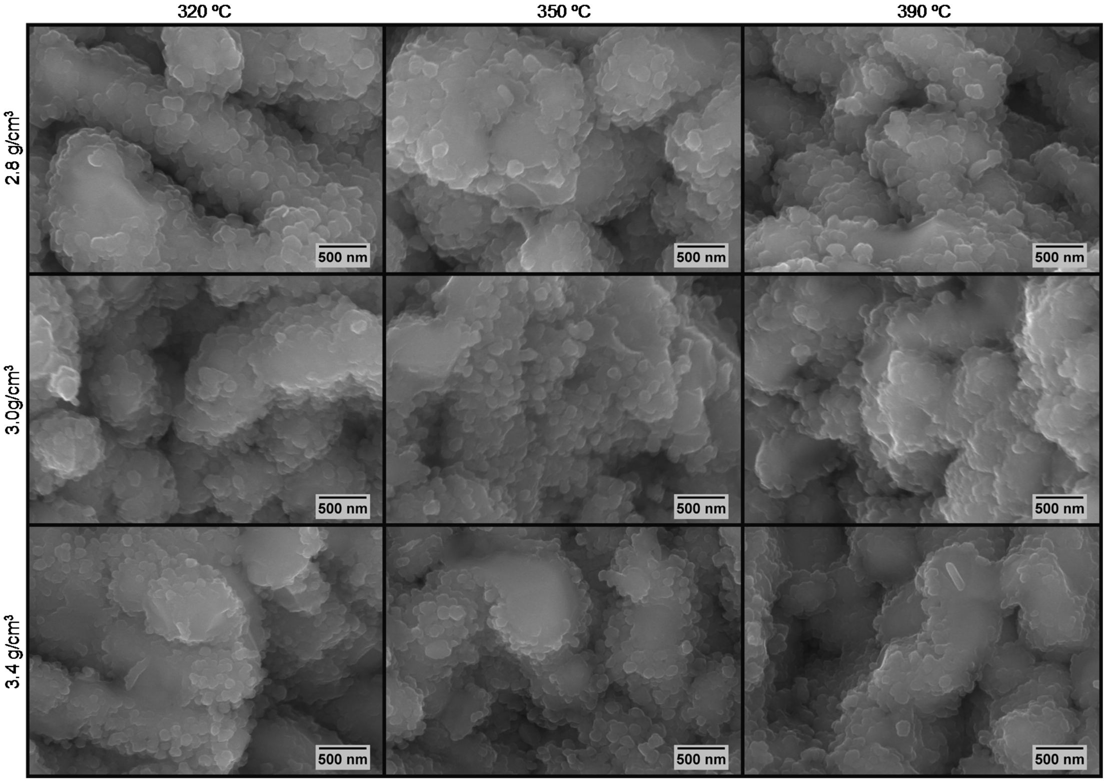
320 ºC
350 ºC
390 ºC
2.8 g/cm³
3.0g/cm³
3.4 g/cm³
500 nm

Figure 6.19 – SEM images of inner body part of the NbO anodes after MnO_2 impregnation through a pyrolysis at 230 ºC.

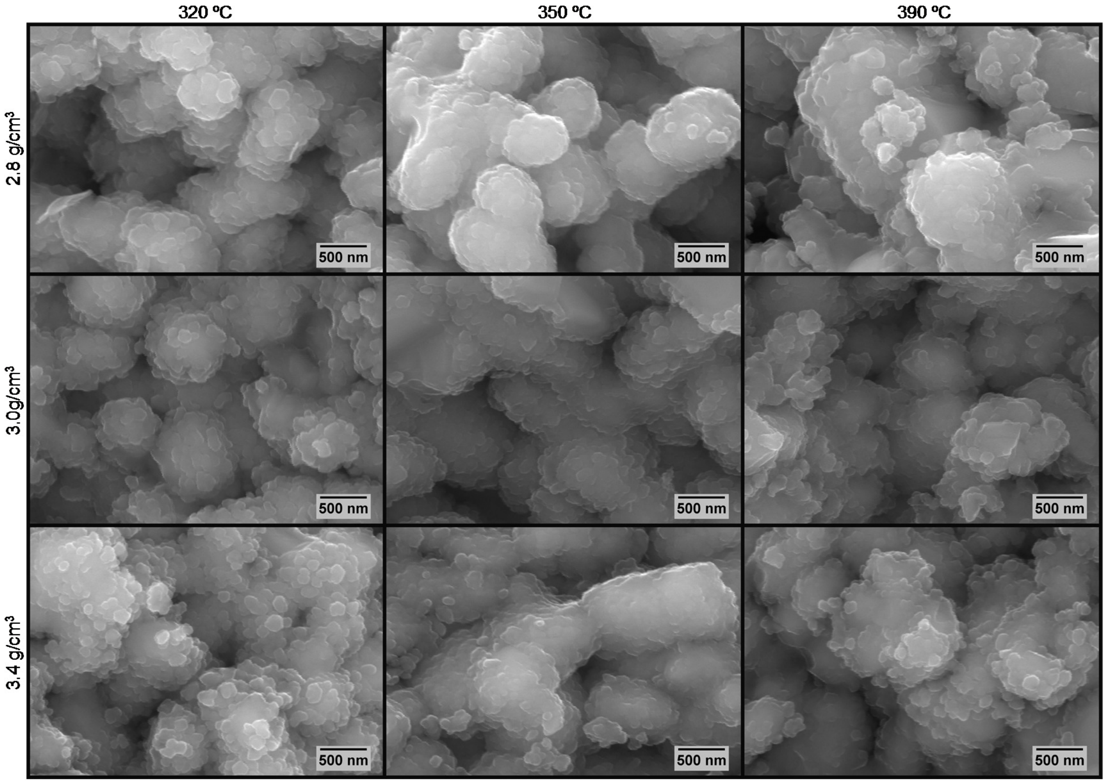
320 ºC
350 ºC
390 ºC
2.8 g/cm³
3.0g/cm³
3.4 g/cm³
500 nm

Figure 6.20 – SEM images of inner body part of the NbO anodes after MnO_2 impregnation through a pyrolysis at 270 ºC.

It is possible to see that the MnO_2 particles were produced with grain sizes between 100 and 300 nm. An EDX analysis performed to these particles confirmed that they were rich in manganese. Both pyrolysis temperatures, 230 and 270 ^oC, have produced a uniform coverage of the niobium oxide grains, but in some images it seems that at 270 ^oC there are slightly more MnO_2 particles formed around the Nb_2O_5/NbO structures.

The SEM analysis of the surface of the anodes submitted to a pyrolysis at 230 ^oC revealed a morphology completely identical to the morphology observed in the inner body part depicted in Figure 6.19. However, that was not the case for the samples with the pyrolysis at 270 ^oC. The surface of these anodes appeared much rougher than the ones with the pyrolysis at 230 ^oC, and it was possible to observe peculiar structures rich in manganese with a morphology may resemble mushrooms. Figure 6.21 and Figure 6.22 shows some examples of such manganese oxide structures observed at the surface of the anodes, which were computationally coloured (for an artistic purpose only).

This type of "mushroom" structures are undesirable for the production of solid electrolytic capacitors because they compromise the incorporation and adhesion of conductive layers of graphite particles and silver paint. Therefore, while it is important to assure a good coverage of the dielectric with MnO_2 particles, the pyrolysis must take place at lower temperatures (e.g. 230 ^oC) to avoid the formation of such structures at the surface of the anode.

As a curiosity side note, near the Ta wire, it was observed a different type of manganese particles with a hexagonal pyramid shape with a central spiral, as can be observed in Figure 6.23. This type of structures are most likely due to defects at the surface of the crystal that give rise to, during crystal growth, screw dislocations [198].

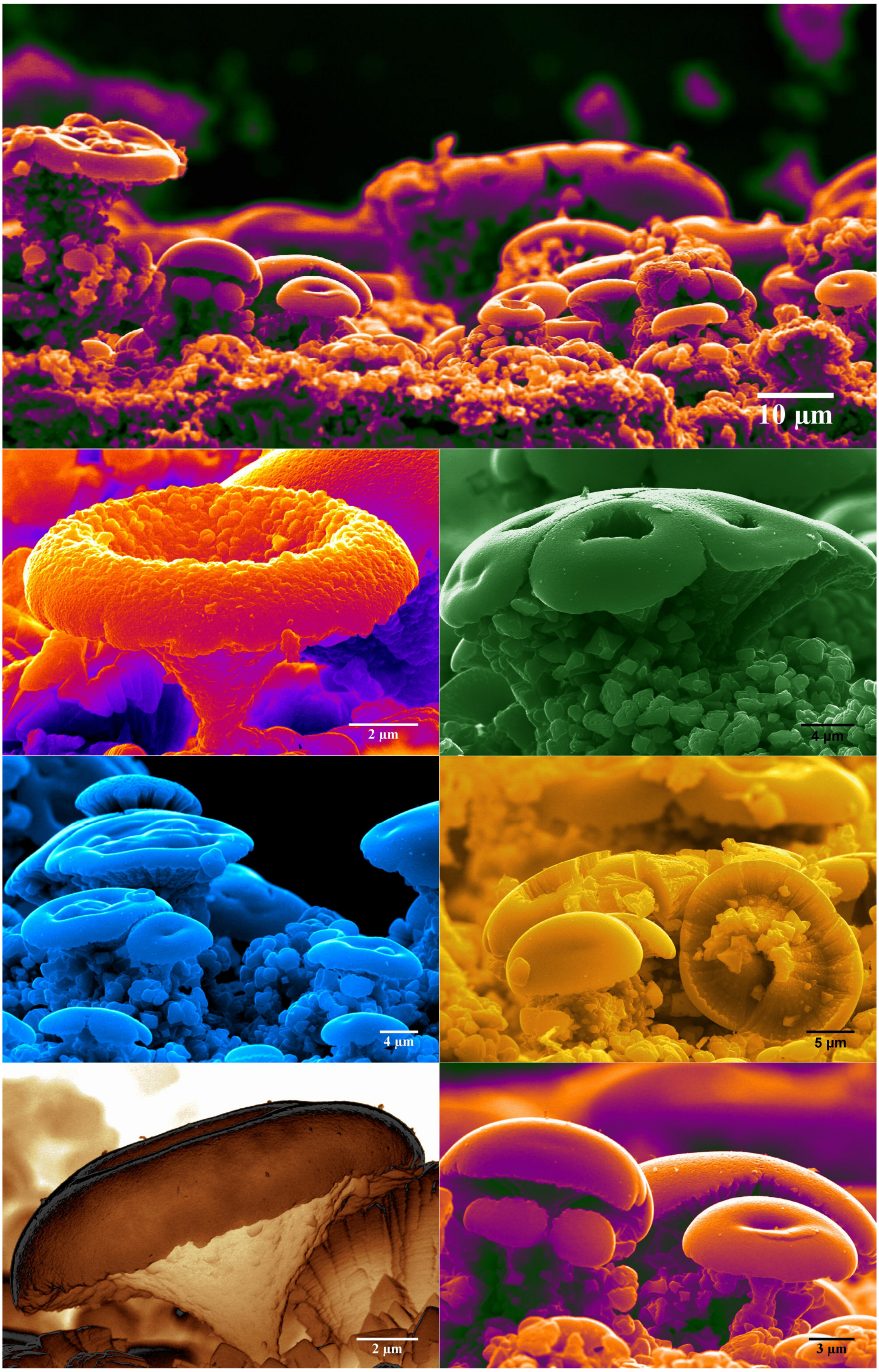
10 µm
2 µm
4 µm
4 µm
5 µm
2 µm
3 µm

Figure 6.21 – Manganese oxide particles with mushroom shape observed at the surface of the NbO anodes after a pyrolysis at 270 °C.

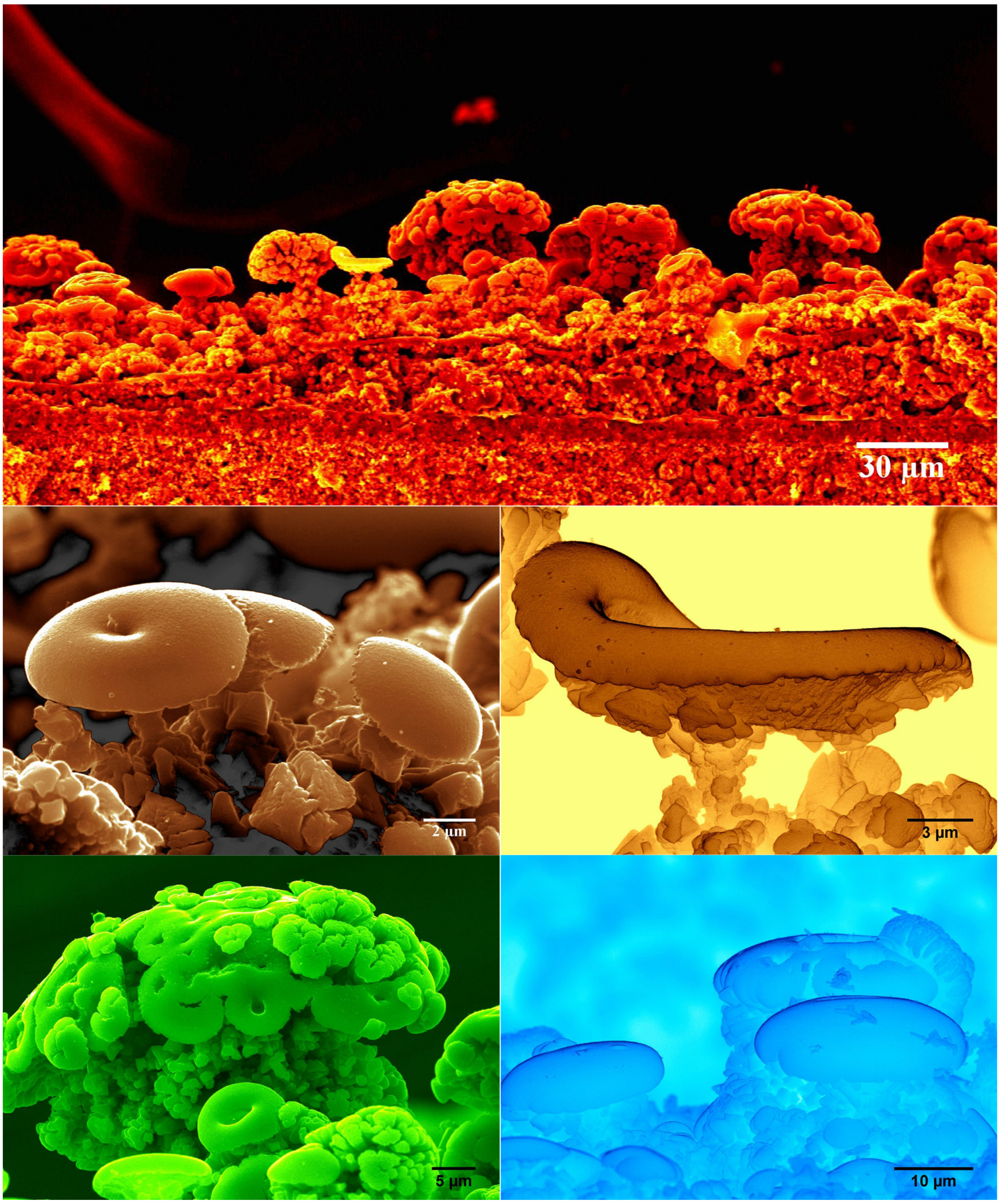
30 µm
2 µm
3 µm
5 µm
10 µm

Figure 6.22 – Manganese oxide particles with mushroom shape observed at the surface of the NbO anodes after a pyrolysis at 270 ^{o}C.

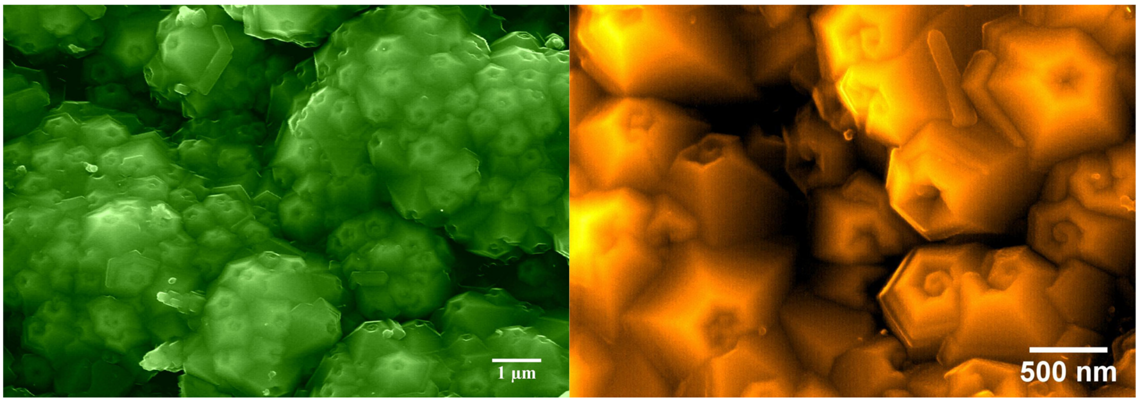

Figure 6.23 – Manganese oxide particles a hexagonal pyramid shape, observed next to the Ta wire of the NbO anode after a pyrolysis at 270 °C.

6.5 Summary

The purpose of this work was, using the already existent production line and processes for the tantalum technology, to adapt it into the niobium oxides. Thus, NbO anodes were pressed with different densities and sintered in vacuum. While the sintering of the NbO grains was successfully promoted, the formation of a small amount of NbO_2 was observed. In a future work, it is suggested that an improved vacuum or a slightly reducing atmosphere, such as nitrogen, is used.

In the anodization process different forming voltages and currents were tested. The voltage was controlled accordingly to the pressing density as an attempt to achieve a similar capacitance value. This control was based on the same proportion known for the Ta technology, and as the electrical measurements have shown it was successful. However, measurements of the thickness niobium pentoxide layer, using SEM images, have shown a disagreement with the electrical properties. This led to the conclusion that oxygen deficient niobium pentoxide, which is conductive, must be formed in a non-controlled way. It is suggested that the forming current may play a significant role in the diffusion of oxygen, and thus the formation of such oxygen deficient phases.

The tempering process revealed that the growth of the dielectric layer of Nb_2O_5 is promoted by the thermal oxidation at air, as expected from the conclusions of chapter 5, which leads to a decrease of capacitance and increase of resistance. Therefore, the tempering process at 390 °C in vacuum seems to be well suited as it increases the capacitance which can be corrected by a re-forming process afterwards. Nonetheless, it appears that this heat treatment may induce the diffusion of oxygen towards the NbO core leading to an increase of oxygen deficient niobium pentoxides.

The pyrolysis process, to cover the dielectric with MnO_2 particles, was successful. Both pyrolysis temperatures, 230 and 270 °C, produced a good and homogeneous coverage of the niobium oxides grains. However, at the surface of the anodes with a pyrolysis performed at 270 °C, it was possible to observe mushroom shaped manganese oxide structures which can lead to difficulties in future steps of the process, specifically in the incorporation and adhesion of conductive layers. It would be interesting to test other materials to be used as a cathode, namely the polypyrrole mentioned in section 3.1.

Further tests are definitely required to achieve a functional prototype of a niobium oxide based capacitor, but these results appear to indicate that such device is close to be achieved. One should note that the analysis of the electrical measurements was performed based on a simple model of a capacitor and a resistance connected in parallel. Even if it does not strongly affect the interpretation of the results, it is suggested that using a more complex model to analyse these same results (i.e. considering the capacitance and resistance of the interfaces) could provide a more clear and detailed insight of the observed electrical behaviours.

Chapter 7

Rare-Earth Orthoniobates

7. Rare-Earth Orthoniobates

As explained in the first chapter, the choice of studying of rare-earth orthoniobates ($RENbO_4$) was related to a combination of several facts. While these materials are not yet well studied, there are works that report very interesting optical and electrical properties. Additionally, it is believed that the experience and knowledge acquired with the study of niobium oxides can bring new insights to the properties of these materials. Moreover, the previous experience of the research group in the study of the optical properties of lanthanides in different hosts (e.g. oxides and glasses) is also an important advantage.

The synthesis of three different RE niobates: Erbium Niobate ($ErNbO_4$), Europium Niobate ($EuNbO_4$) and Samarium Niobate ($SmNbO_4$) was decided. The choice of these lanthanide based hosts is essentially related with the relevance of such trivalent charged ions for red and green light, and the experience of the research group in studying them as dopants in different hosts. Single-crystalline and polycrystalline samples were prepared by the LFZ and by the Pechini methods, respectively. These samples were then characterized structurally, optically and electrically.

7.1 Synthesis

As mentioned, samples of $RENbO_4$ were prepared by two different methods: by LFZ, in order to obtain single crystalline samples, and by Pechini method, to obtain polycrystalline powders.

The LFZ method, described in section 2.1.3, allows growing highly crystalline samples with few contaminations. Thus, H-Nb_2O_5 powders (Merck) and RE_2O_3 for the RE elements Eu, Er and Sm (Aldrich) were mixed in a 1:1 ratio and placed in a planetary ball mill during 4 cycles of 30 minutes at 300 rpm, inverting the rotation direction at each cycle. The powders mixture was then mixed with a PVA solution (prepared beforehand) which will act as a bonding agent to obtain a dough that will be extruded into the precursor rods. These rods were left in acrylic tracks to dry at room temperature and air during one week.

After the precursor rods have become well dried and mechanically consistent, two of the straightest ones were selected to initialize the growth of the crystals. Before reaching the parameter values (i.e. power, rotation, pulling and feeding speeds) that allowed growing each of the three $RENbO_4$ crystals, several attempts were made until it was possible to have a stable and uniform growth. At the beginning of each growth, the alignment of the laser beam was verified and corrected, but it was observed that even minor misalignments significantly influence the power that reaches the precursors. For this reason, the growing parameters may be taken as a reference for future works if the LFZ system and laser are kept the same and its alignment is well optimized.

Table 7.1 enumerates the parameters used for the growth of the $RENbO_4$ fibres by LFZ. The minus sign signifies the downward direction in the case of the pulling and feeding rates, while for the rotating speeds, opposite signals imply opposite directions. In the case of $ErNbO_4$ and $EuNbO_4$ fibres, a re-growth process (i.e. using already grown crystalline fibres) was performed in order to improve the crystallinity of the samples. Hence, a $ErNbO_4$ fibre was first grown using 40 W with a feeding and pulling rate of 250 and 100 mm/h respectively, which was re-grown afterwards using 50 W of power and equal feeding and pulling rates (2.5 mm/h). In neither case the fibres were rotating because it was observed that it would compromise the stability of the growth. A $EuNbO_4$ fibre was first grown using 70 W of laser power, feeding at 250 mm/h and pulling at 100 mm/h, while rotating the feeding rod at 10 rpm and the crystal at 5 rpm in opposite directions. Using the same rotating parameters and power, the $EuNbO_4$ fibre was re-grown with a feeding and pulling rate of 2.5 mm/h. The $SmNbO_4$ fibre was possibly the most hard to grow, and the only successful attempt was using 34 W of laser power, without rotation and with equal feeding and pulling rates of 10 mm/h. All the mentioned parameters suffered fine tunes during the growth to compensate instabilities throughout the process.

Table 7.1 – Growth parameters of the $RENbO_4$ fibres.

		$ErNbO_4$	$EuNbO_4$	$SmNbO_4$
Growth	**Power**	40 W	70 W	34 W
	R_f	-250 mm/h	-250 mm/h	-10 mm/h
	R_g	-100 mm/h	-100 mm/h	-10 mm/h
	ω_f	0 rpm	10 rpm	0 rpm
	ω_g	0 rpm	-5 rpm	0 rpm
Re-Growth	**Power**	50 W	70 W	
	R_f	+2.5 mm/h	-2.5 mm/h	
	R_g	+2.5 mm/h	-2.5 mm/h	
	ω_f	0 rpm	10 rpm	
	ω_g	0 rpm	-5 rpm	

The Pechini method used to prepare the polycrystalline samples of $RENbO_4$, consisted in using niobium chloride salts ($NbCl_5$) and also rare-earth nitrate salts ($RE(NO_3)_3{\cdot}xH_2O$), weighted in a 1:1 mol ratio. The $NbCl_5$ salt was dissolved with a hydrogen peroxide (H_2O_2) solution, with a concentration of 3 % in volume, and placed into continuous magnetic stirring during 15 minutes at c.a. 50 ºC, obtaining a yellow transparent solution. The $RE(NO_3)_3{\cdot}xH_2O$ salt was dissolved using distilled water and left for stirring at RT during 1 hour. The used amount of H_2O_2 and H_2O was slightly more than the necessary to assure a good dissolution of the salts. Next, an aqueous solution of citric acid ($C_6H_8O_7$) was prepared, by weighting a 3:1 mol ratio relatively to $NbCl_5$, and adding just about the enough amount of water to assure the complete dissolution of the acid, which was then added to the $NbCl_5$ solution and stirred for 25 minutes at 50 ºC. The same amount of citric acid was also added to the $RE(NO_3)_3$ solution and left for stirring during 25 minutes at RT. Afterwards, ethylene glycol ($C_2H_4(OH)_2$) was weighted in a 3:2 mass ratio relatively to the citric acid, and added to the $NbCl_5$ and to the $RE(NO_3)_3$ solutions. Each of these two solutions were stirred for 12 hours at RT before being mixed together and stirred for 24 hours, also at RT, until an homogeneous gel is obtained. Figure 7.1 schematically illustrates this process in a simple and concise way.

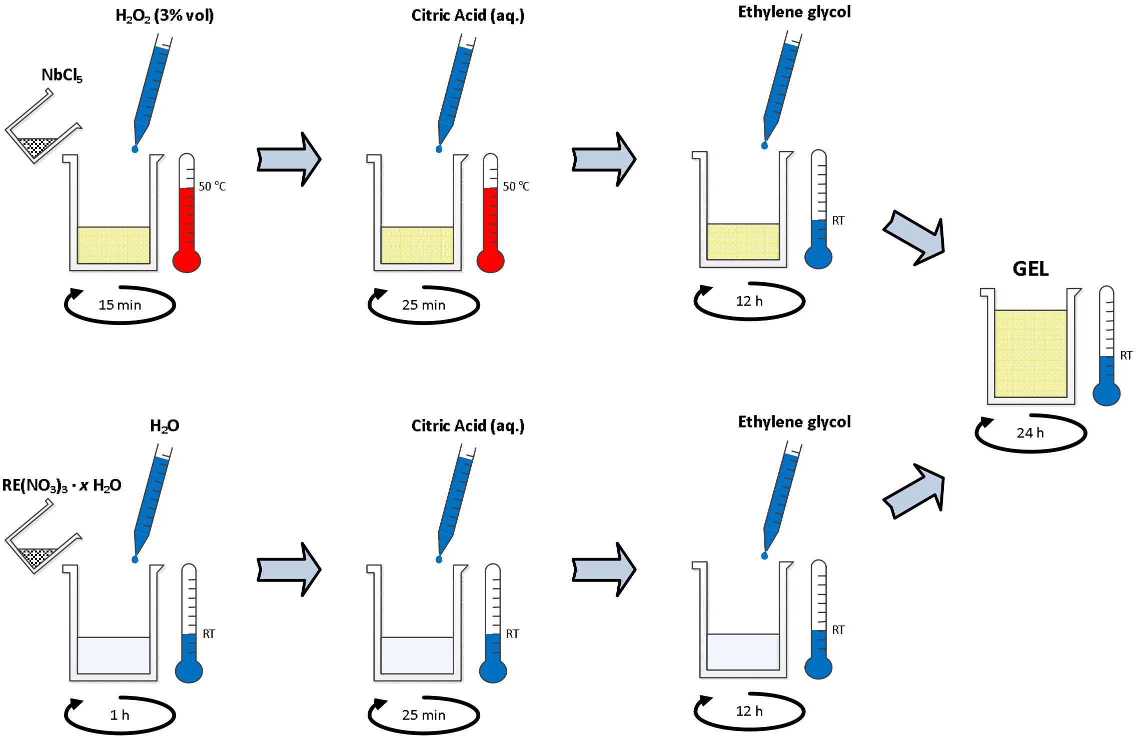

Figure 7.1 – Schematic illustration of the followed Pechini route for the synthesis of the $RENbO_4$ gel.

After the gel was formed, it was taken into a heating furnace for drying at air, in order to obtain a powder. The heat treatment will promote the growth of organic polymeric chains, leading to a significant increase of the sample volume, which may be a practical problem. Hence, in order to minimize such effect, a slow heating rate (2.5 ºC/min) was used from RT to 400 ºC, with progressive HT at intermediate temperatures, as illustrated by Figure 7.2.

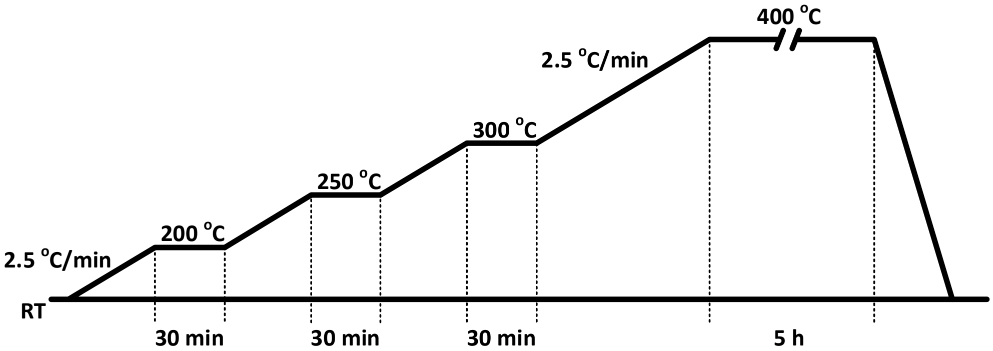

Figure 7.2 – Heating profile followed during the gel drying process.

The obtained powders were agglomerated into a single piece, but it was easily crumbled. After being smashed and milled with a mortar and pestle, the powders were placed into an alumina crucible and taken to a furnace and heat treated in air at 1400 ºC for 10 hours (heated at 5 ºC/min). Such temperature was chosen based on previous experiences [260] which had shown the formation of highly crystalline $RENbO_4$ pellets.

After synthesizing $ErNbO_4$ and $SmNbO_4$ powders and heat treating them at 1400 ºC, XRD and Raman analyses were performed, as shown in Figure 7.3.

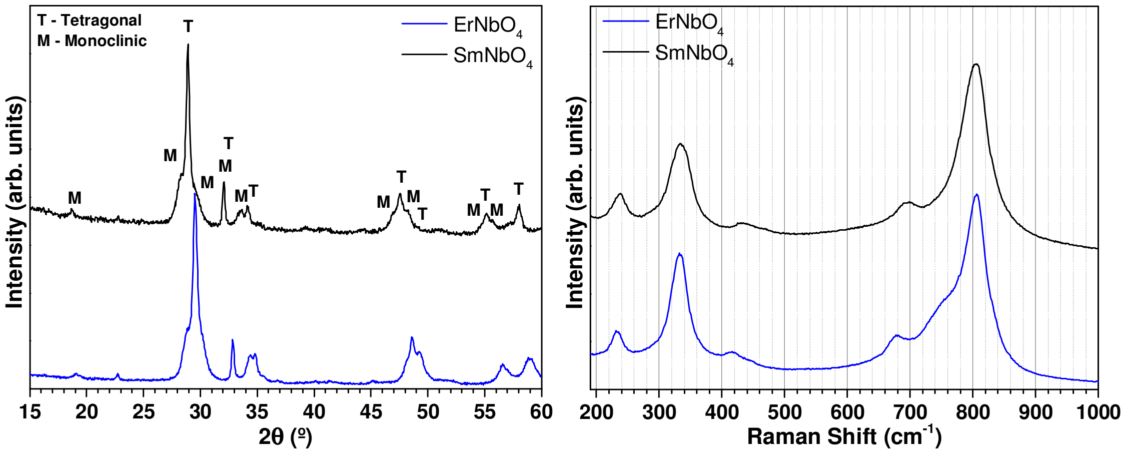

Figure 7.3 – XRD patterns (left) and Raman spectra under 325 nm laser excitation (right) of the $ErNbO_4$ and $SmNbO_4$ powders.

The XRD revealed the existence of two different phases of $RENbO_4$. Not only the expected monoclinic phase was identified (as it was referred in section 1.4.3 as the only phase stable at RT), but also a phase with a tetragonal structure, which is not the same scheelite phase stable at higher temperatures referred in section 1.4.3. While the formation of this phase is not commonly observed in $RENbO_4$, it was reported and identified by Mather and Davies [261] as a nonequilibrium, or metastable, phase not only in $RENbO_4$ (synthesized by sol-gel) but also in other fergusonite-related compounds as rare-earth orthotantalates ($RETaO_4$). Such tetragonal phase has a fluorite distorted structure (D_{4h}^{15} space group), similar to the tetragonal zirconia (ZrO_2), with two RE atoms and two Nb atoms at the Wyckoff positions 2*b* and eight O atoms at the 4*d* position [261]. Furthermore, the authors verified that the formation of such metastable phase was more common for smaller grain sizes and gave rise to the typical monoclinic structure as the size increased. While kinetics *"[...] are responsible for the existence of all metastable phases [...]"* it did not became clear if the formation of this tetragonal metastable phase at RT could be explained by either, or a combination of, the three mechanisms discussed by Mather and Davies [261]: "[...] *topotactic crystallization, intrinsic effect of grain size due to surface energy differences, or additional hydrostatic pressure imposed by the Gibbs-Thomson effect*".

The Raman spectrum of the $SmNbO_4$ powders revealed bands centred at c.a. 232, 332, 414, 676 and 806 cm^{-1}, and also a shoulder at ~760 cm^{-1}, thus totalizing 6 vibrational modes. The $ErNbO_4$ powders have shown an identical spectrum, with 6 vibrational modes, but with the bands slightly shifted towards higher energies, and the shoulder at ~770 cm^{-1} was less pronounced. Following a group theory analysis for the previously described tetragonal metastable phase, one can show that for the six atoms per unit cell, a total of eighteen vibrational modes in the irreducible representation $\Gamma = 1A_{1g} \oplus 2A_{2u} \oplus 2B_{1g} \oplus 1B_{2u} \oplus 3E_g \oplus 3E_u$ at the centre of the Brillouin zone ($\mathbf{k} = 0$) occur. According to the character table of the D_{4h} group, from these modes $1A_{2u}$ and $1E_u$ pair are acoustic modes (corresponding to the translations), and the remaining fifteen are optical modes. $1A_{2u}$ and $2E_u$ pairs are active in the IR, and $1A_{1g}$, $2B_{1g}$, and $3E_g$ pairs are active in Raman. Therefore, it is consistent with the 6 vibrational modes that were observed. Additionally, the most intense Raman active vibrational modes of the monoclinic phase may be superimposed with the modes of the tetragonal phase, since their energies are very similar, as it will be shown in the next section.

These powders were also analysed by SEM where it was possible to observe large particles with the shape of leaves/flakes, and also some smaller grains mixed together, as illustrated by the images in Figure 7.4, which are representative of all the synthesized

$RENbO_4$ powders. While the surface of such flakes seemed very smooth at a first glance, it was possible to see that these particles were formed by highly coalesced round particles with diameters ranging between approximately 50 and 150 nm.

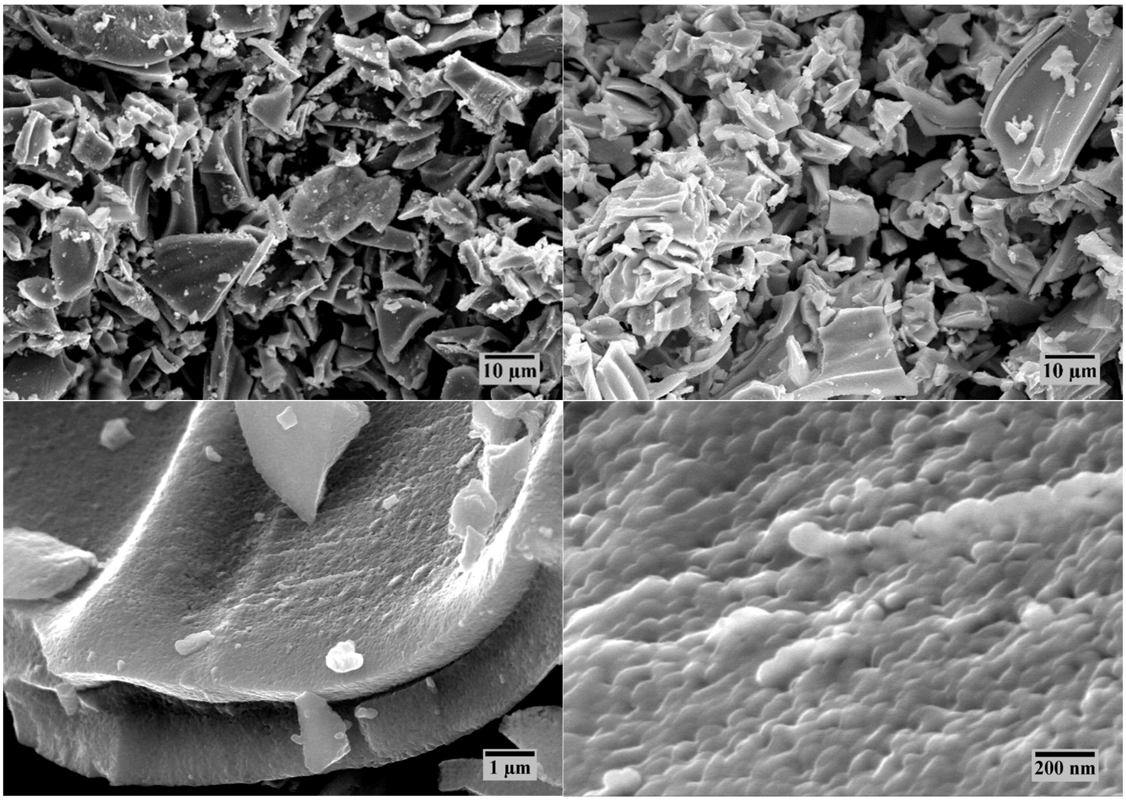

Figure 7.4 – Representative SEM images of all $RENbO_4$ synthesized powders.

Since a mixture of $RENbO_4$ phases was being produced, which was not desired, the heat treatment at 1400 °C was repeated. The results keep showing that even after a third heat treatment at this temperature, in air, a mixture of the tetragonal and monoclinic phases of $RENbO_4$ was present. Finally, to promote the grain growth, and thus the formation of only the monoclinic phase, the powders were pressed into pellets and the same heat treatment at 1400 °C was performed. As it will be shown in the next section, it was possible, by this way, to obtain the desired phase of monoclinic $RENbO_4$.

Therefore, Figure 7.5, Figure 7.6 and Figure 7.7 illustrate the synthesized fibres and pellets of $ErNbO_4$, $EuNbO_4$ and $SmNbO_4$, respectively.

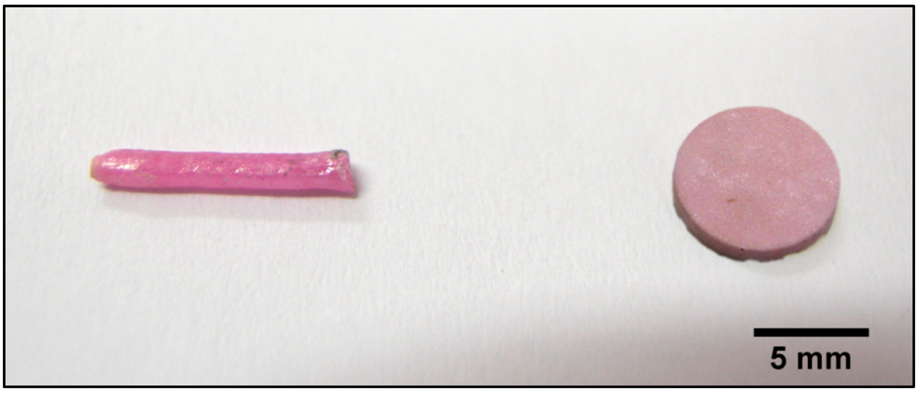

Figure 7.5 - Photograph of $ErNbO_4$ fibre (left) and pellet (right).

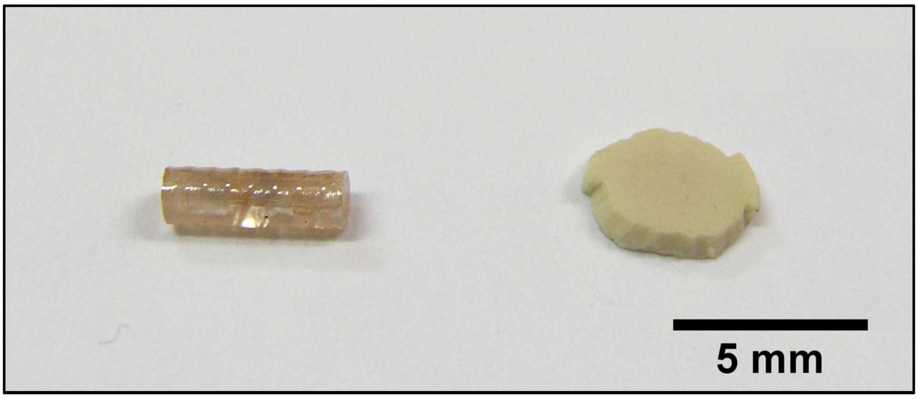

Figure 7.6 - Photograph of $EuNbO_4$ fibre (left) and pellet (right).

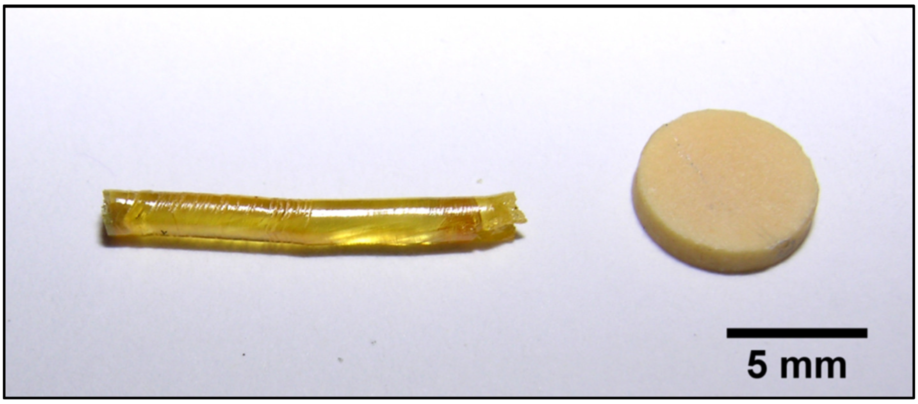

Figure 7.7 – Photograph of $SmNbO_4$ fibre (left) and pellet (right).

7.2 Results and Discussion

7.2.1 XRD

A small piece was cut from each of the RENbO$_4$ fibres and analysed by single-crystal XRD (SCXRD). The SCXRD data were collected on a CCD Bruker APEX II at 180 K (for the ErNbO$_4$ fibre) and on a CCD Bruker D8 Quest at 180 K (for the EuNbO$_4$ and SmNbO$_4$ fibres) using graphite monochromatized Mo K$_\alpha$ radiation ($\lambda \cong 0.71$ Å). The crystals were positioned at 35 mm (in the case of the ErNbO$_4$ fibre) and at 40 mm (in the case of the EuNbO$_4$ and SmNbO$_4$ fibres) from the CCD, and the spots were measured using 10 s counting time.

Figure 7.8 illustrates some of the acquired Laue patterns which suggest a single-crystalline nature of all the analysed specimens. The SCXRD data of the RENbO$_4$ fibres were assigned to the typical monoclinic structure of these materials. The calculated lattice parameters of the RENbO$_4$ fibres, as well as the assigned ICDD reference structure, are listed in Table 7.2.

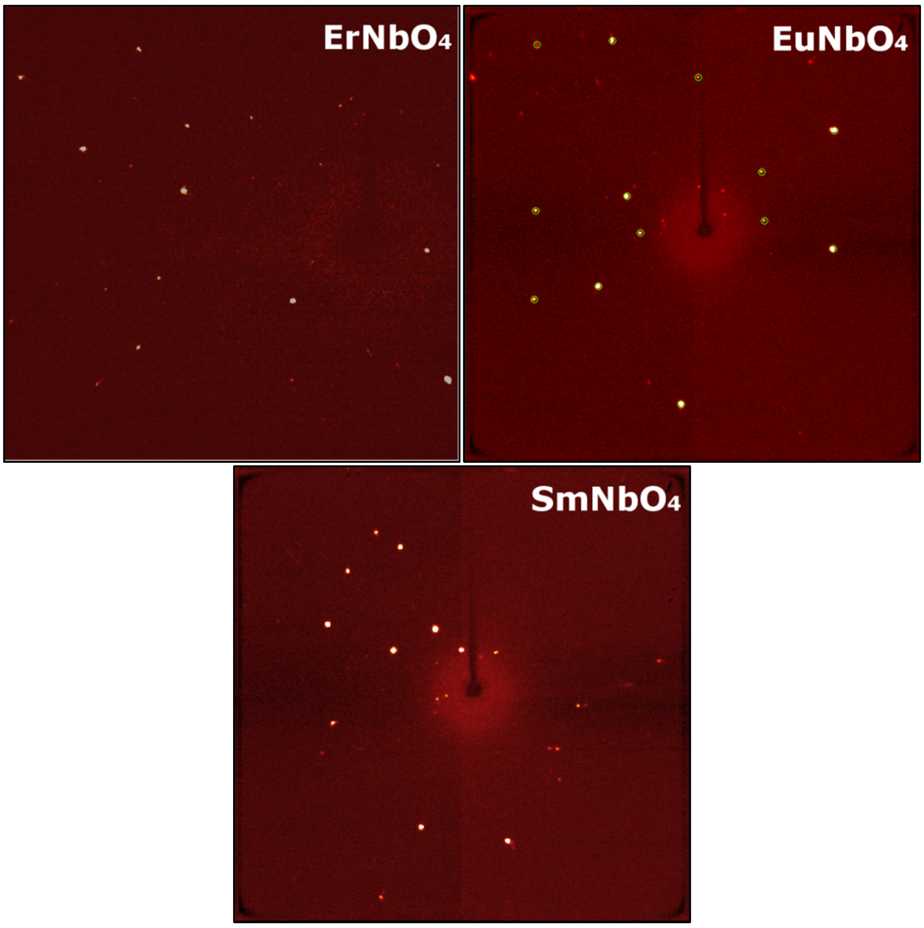

Figure 7.8 – Representative Laue patterns acquired of all the RENbO$_4$ fibres.

Table 7.2 – Single-crystal XRD data of the $RENbO_4$ fibres.

Fibre Specimen	Calculated Lattice Parameters	Space group	Assigned ICDD Ref.	
$ErNbO_4$	a = 6.93 Å b = 10.79 Å c = 5.07 Å α = γ = 90 ° β = 130.69 °	C_{2h}^6	04-005-5711	a = 7.0159 Å b = 10.907 Å c = 5.057 Å α = γ = 90 ° β = 131.425 °
$EuNbO_4$	a = 7.04 Å b = 11.23 Å c = 5.09 Å α = γ = 90 ° β = 132.05 °	C_{2h}^6	04-005-7367	a = 7.1223 Å b = 11.129 Å c = 5.112 Å α = γ = 90 ° β = 131.003 °
$SmNbO_4$	a = 7.00 Å b = 11.18 Å c = 5.10 Å α = γ = 90 ° β = 130.62 °	C_{2h}^6	04-006-2143	a = 7.1799 Å b = 11.2 Å c = 5.13 Å α = γ = 90 ° β = 130.943 °

Figure 7.9 shows the XRD spectra of all the $RENbO_4$ pellets. All the observed peaks matched extremely well with the ICDD reference data of monoclinic structure belonging to the C_{2h}^6 space group, which lattice parameters are enumerated in Table 7.3. Despite the fact that the diffraction patterns are very similar, it is possible to identify a shift in the position of the diffraction peaks as a function of the lanthanide ionic radius, diffracting for higher angles as the lattice parameters decrease (from $SmNbO_4$ to $ErNbO_4$).

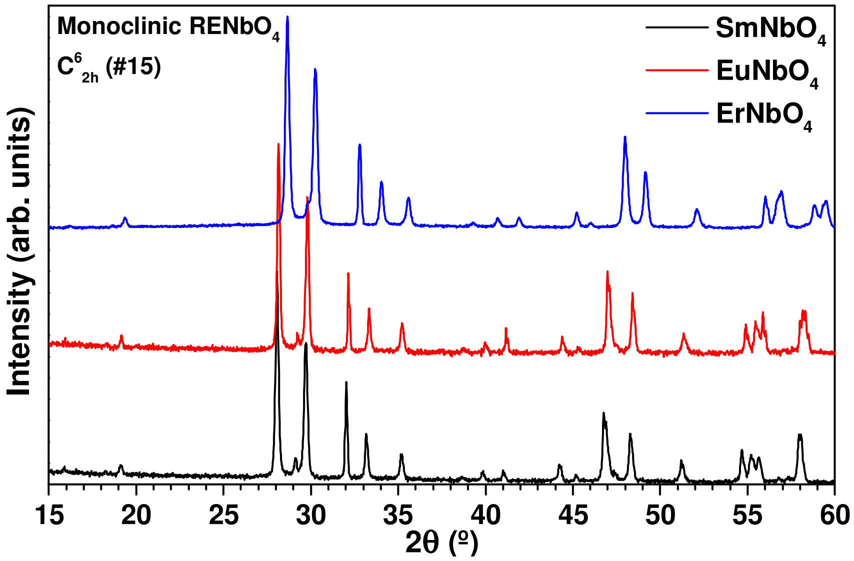

Figure 7.9 – XRD patterns for the $RENbO_4$ pellets.

Table 7.3 – Lattice parameters of the matched reference structure from the XRD analysis of the $RENbO_4$ pellets.

Pellet	Assigned ICDD Ref.		Space group
$ErNbO_4$	22-1095	a = 5.279 Å b = 10.91 Å c = 5.064 Å $\alpha = \gamma = 90^{o}$ $\beta = 94.53^{o}$	C_{2h}^{6}
$EuNbO_4$	22-1099	a = 5.393 Å b = 11.13 Å c = 5.112 Å $\alpha = \gamma = 90^{o}$ $\beta = 94.67^{o}$	C_{2h}^{6}
$SmNbO_4$	22-1303	a = 5.421 Å b = 11.17 Å c = 5.12 Å $\alpha = \gamma = 90^{o}$ $\beta = 94.70^{o}$	C_{2h}^{6}

With these XRD analyses it was possible to conclude that the $RENbO_4$ fibres and pellets crystallized in a monoclinic structure, which could be assigned to ICDD reference data. However, the calculated lattice parameters of the fibres do not exactly match the ICDD reference, which indicates deformation of the structure, likely originated during the growing process by non-optimized parameters such as speed, power or temperature gradients along the fibre. Additionally, it should be noted that the lattice parameters found in the $RENbO_4$ fibre specimens also differ from the lattice parameters of the pellets. Future work is necessary to clarify if the crystalline phase identified in the fibres can be considered to be a different polymorph of the $RENbO_4$, or simply a distorted lattice of the monoclinic structure.

7.2.2 Raman

Figure 7.10 shows the Raman spectra of the $RENbO_4$ fibres and pellets, acquired with a 325 nm laser excitation source.

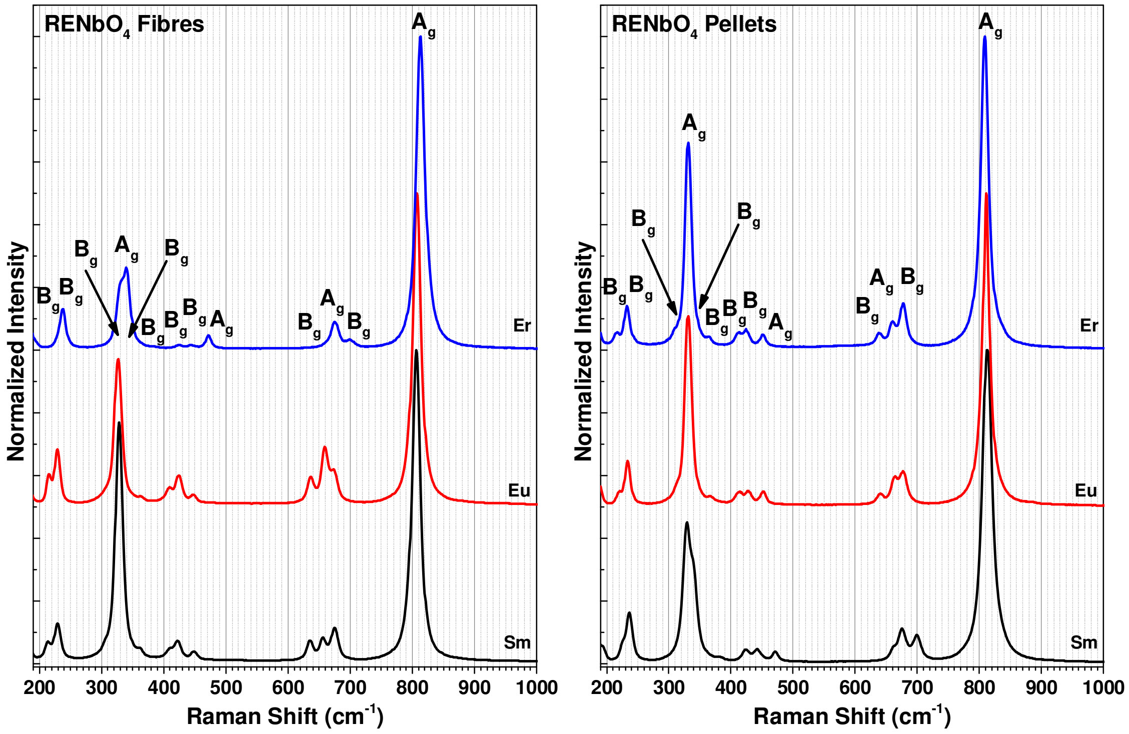

Figure 7.10 – Raman spectra of the RENbO4 fibres (at left) and pellets (at right) acquired with a 325 nm laser as excitation source.

A group theory analysis to the monoclinic structure of the RENbO4 with twelve atoms by unit cell, as described in section 1.4.3, reveals that the total vibrational modes at the centre of the Brillouin zone is defined by the irreducible representation $\Gamma = 8A_g \oplus 10B_g \oplus 8A_u \oplus 10B_u$, from which 18 $(8A_g \oplus 10B_g)$ are Raman active, according to the character table of the C_{2h} point group. However, it was not possible to detect all these Raman active vibrational modes. Siqueira *et al.* [178] were able to identify all the 18 modes for all the rare-earth orthoniobates with the same fergusonite-type structure. By comparison, the spectra illustrated in Figure 7.10 are extremely similar and almost all modes match well the reported energies for each RENbO4. However, 5 of the reported modes have energies below 200 cm^{-1}, a range of energies which was not possible to record due the available filters for the used wavelength to optically excite the samples. Longer wavelengths were available in the Raman spectrometer, with filters that could allow recording Raman shifts as low as 60 cm^{-1}, but the 325 nm excitation was the only one that could avoid superposition with luminescence emission from the samples due to transitions between the intra-4f levels of the trivalent rare-earth ions. Furthermore, there are two vibrational modes which in most cases are masked by the intense band between 330-340 cm^{-1}, both with B_g symmetries. Siqueira *et al.* [178] state that the vibrations with the lowest energies (less than 300 cm^{-1}) are related to the packing of the NbO4 units depending on the RE ion.

While the monoclinic structure can be described by NbO_6 octahedra, such polyhedra are distorted, i.e. there are Nb-O bonds that are considerably longer than others. Not knowing the strength of these longer bonds, can lead to an ambiguous description of the same structure, i.e. if such bonds are negligible one should consider the NbO_4 tetrahedra units, if not the NbO_6 octahedra should be considered instead. In the case of the scheelite-type structure of the $RENbO_4$, given the large distances between Nb and some of the O atoms, it becomes obvious that it should be described by NbO_4 tetrahedra.

The modes between ~400-500 cm^{-1} and ~600-700 cm^{-1} are assigned to anti-symmetric Nb-O vibrations, while the main modes at approximately 330 and 810 cm^{-1} are related to the symmetric Nb-O vibrations of the NbO_4 tetrahedra [262]. Siqueira *et al.* [178] observed that most bands shifted to higher wavenumbers as the ionic radius of the lanthanide ion increased. However, in the Raman spectra of the $RENbO_4$ fibres and pellets, shown in Figure 7.10, such trend was not clear. While energetic deviations of the modes were in fact observed for different samples, it is not possible to establish a direct relation with the ionic radius of the lanthanide ion. It is suggested that the deviation of these modes are due to a simultaneous contribution of the ionic radius and mass of the lanthanides, and also to the observed differences of the lattice parameters which are dependent on the RE element and to the growth/synthesis processes. Additionally it should be noted that, because the excitation source used for this Raman spectroscopy analysis is short (325 nm), the acquired spectra result from the interaction of the light with only the most superficial region of the samples, where is more likely to have structural deformations and defects, thus contributing to variations of the vibrational modes.

7.2.3 SEM

All the $RENbO_4$ samples were analysed by SEM in order to verify the existence, or not, of grain boundaries in the fibres and the morphology and grain sizes on the pellets. To do this, the fibres were impregnated in an epoxy so they could be mechanically polished without breaking, until the inner section was exposed. Regarding the pellets, small pieces were cut in order to acquire images of both the surface and the fracture. Figure 7.11, Figure 7.12 and Figure 7.13 respectively depict the SEM images of the $ErNbO_4$, $EuNbO_4$ and $SmNbO_4$ fibres and pellets.

It is possible to notice several cracks along the $ErNbO_4$ fibre, possibly due to structural tensions, which tend to be parallel between them. This might indicate that such cracks are produced along a certain lattice plane and kept well aligned along all the fibre, which is a strong evidence that the sample is single-crystalline. Additionally, the image of the fibre at the highest magnification shows small defects (only sporadically observed) that also tend to be aligned along the same directions. Such image also shows that no grain boundaries were observed, thus corroborating the single-crystalline nature of the fibre. The SEM image of the $ErNbO_4$ pellet revealed a dense ceramic with highly coalesced grains, with sizes between ~1 and 5 µm. Particles with rounded/spherical shape and also well faceted grains were observed.

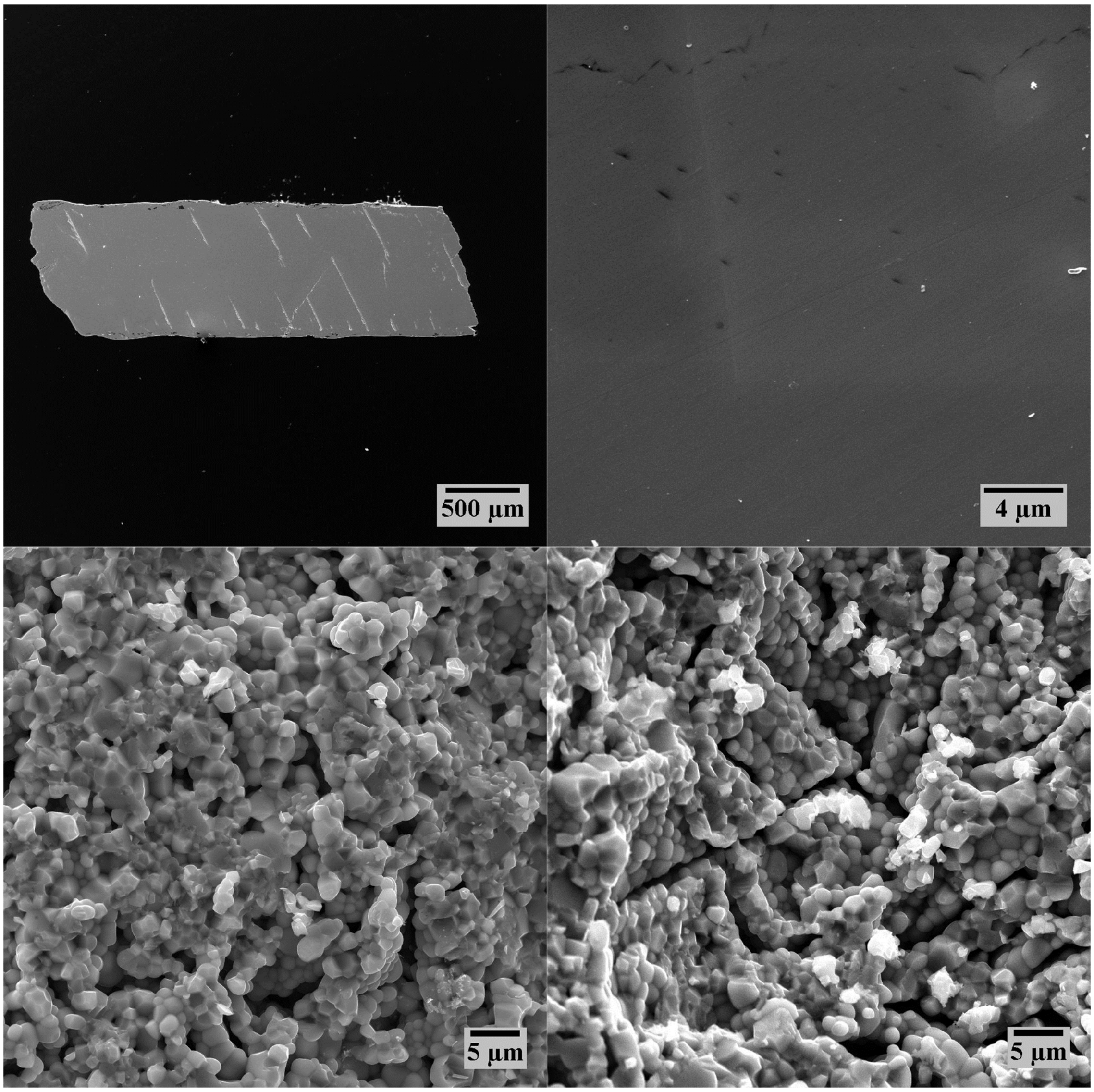

Figure 7.11 – SEM pictures of the $ErNbO_4$ fibre (on top) and pellet (on bottom).

Regarding the SEM of the $EuNbO_4$ fibre (Figure 7.12), it is possible to notice several cracks which are likely formed during the growth process due to temperature gradients and structural tensions. Nevertheless, it was not possible to identify any grain boundaries thus corroborating the single-crystalline nature of the fibre. The $EuNbO_4$ pellet, similarly to the $ErNbO_4$, shows a dense ceramic material with grain sizes, between ~2 and 10 µm.

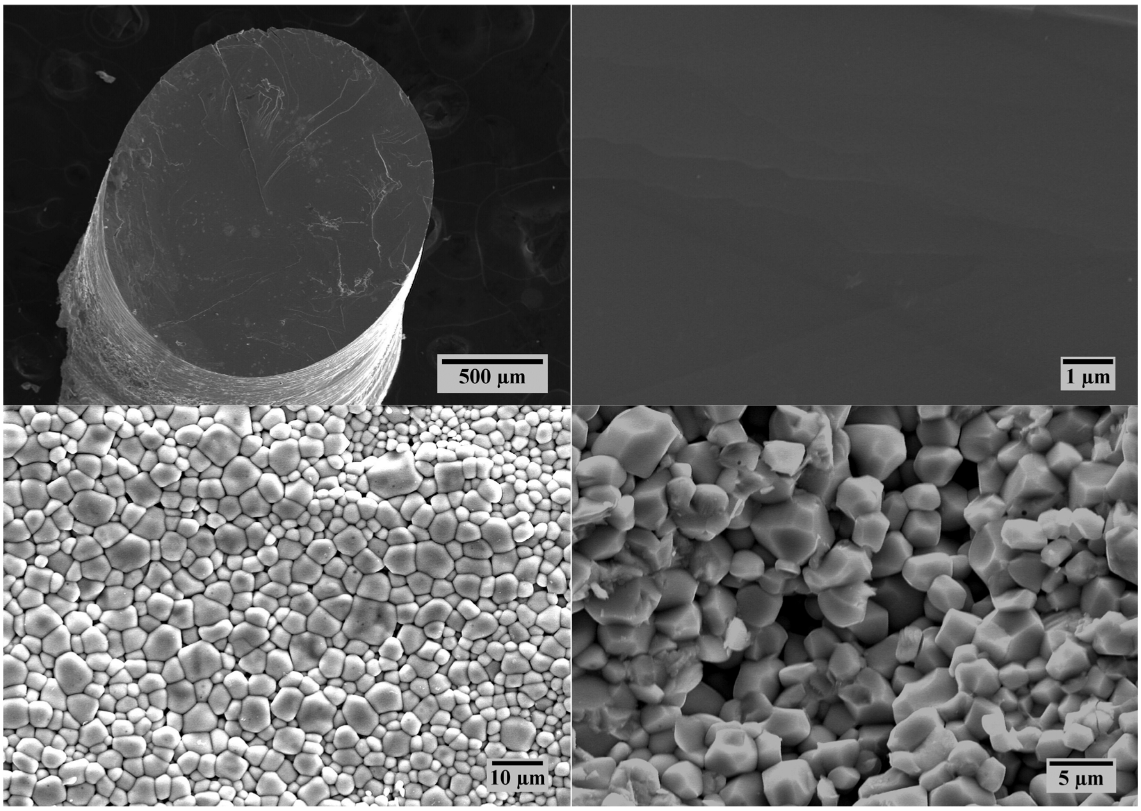

Figure 7.12 – SEM pictures of the $EuNbO_4$ fibre (on top) and pellet (on bottom).

Finally, the $SmNbO_4$ fibre also revealed some cracks which were created due to tensions during the growth process. While there are not as many as observed in the $ErNbO_4$ fibre, it is possible to observe at least 3 cracks aligned along the same direction, which can again imply a good orientation of the lattice planes along all the fibre. The observations of well oriented defects is better visible at higher magnifications, at which no grain boundaries were observed, suggesting again the single-crystalline nature of the fibre. Regarding the $SmNbO_4$ pellet, the same type of morphology (as in the other $RENbO_4$ pellets) was observed, with both rounded and faceted grains with sizes between 1 and 5 µm, highly coalesced.

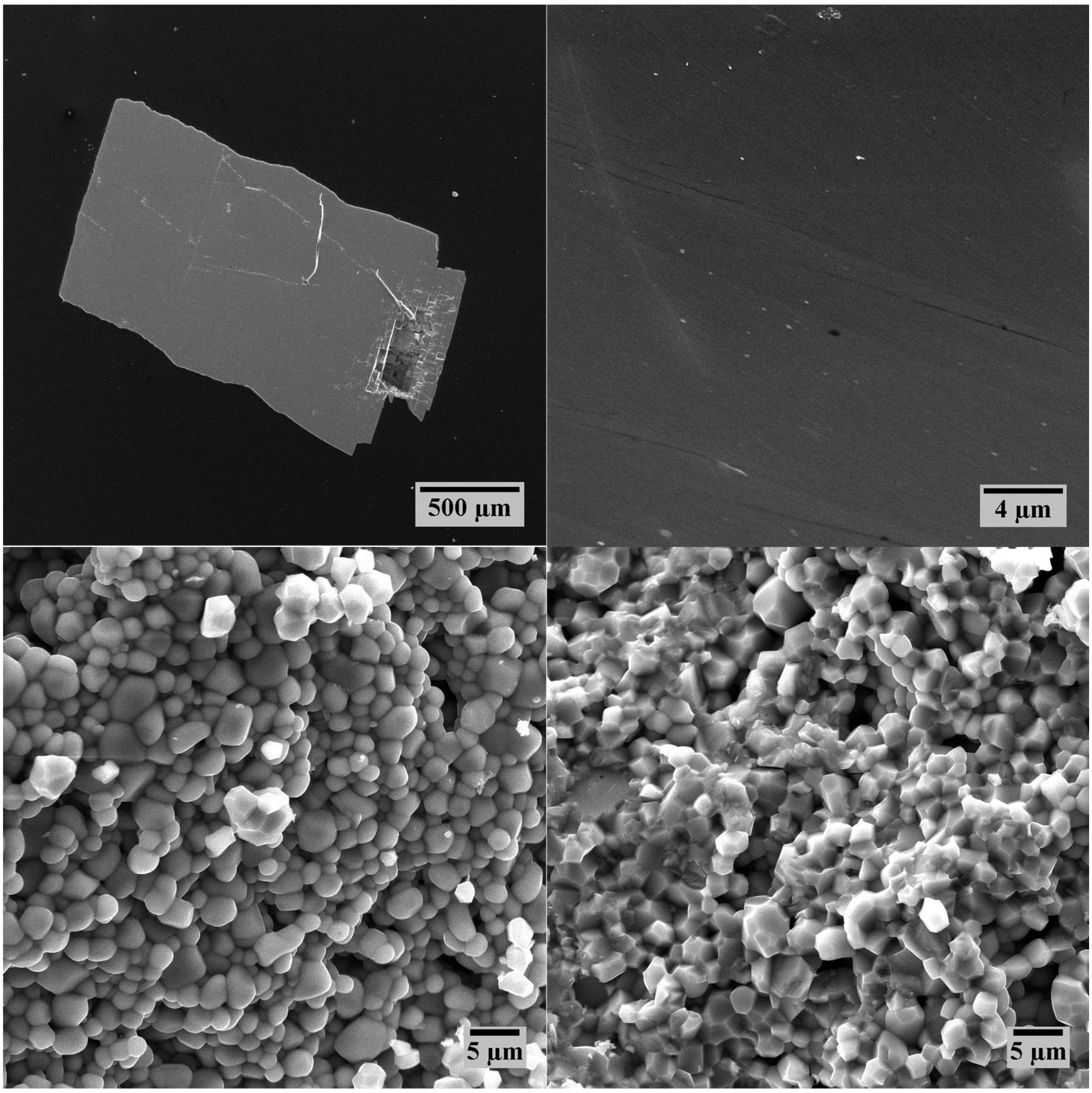

Figure 7.13 – SEM pictures of the $SmNbO_4$ fibre (on top) and pellet (on bottom).

7.2.4 Photoluminescence spectroscopy

7.2.4.1 $ErNbO_4$

Figure 7.14 shows the high resolution PL spectra, after being corrected to the optical response of the system, of the $ErNbO_4$ pellet excited with a He-Cd laser (325 nm), kept at 14 K with a cold finger of a closed cycle helium cryostat. Under these conditions, to naked eye, the sample emits strong red luminescence. Typical intra-4f^{11} transitions of the trivalent Er ion (Er^{3+}) were observed and assigned to the respective $^{2S+1}L_J$ electronic levels. Specifically, between 360 and 380 nm, a group of low intensity bands was assigned to the $^4G_{9/2}$ to the fundamental level $^4I_{15/2}$. Between 540 and 560 nm several narrow lines were assigned to the transitions between the $^4S_{3/2}$ to the $^4I_{15/2}$ multiplets. One of the most intense emission bands, between 650 and 680 nm, are due to the transitions from the $^4F_{9/2}$

to the $^4I_{15/2}$ levels. Weak but sharp emissions between 805 and 815 nm, assigned to the transitions from the $^2H_{9/2}$ to the $^4I_{9/2}$, were observed. Also, between 830 and 865 nm several sharp and intense emission lines were assigned to $^4S_{3/2}$ to the $^4I_{13/2}$.

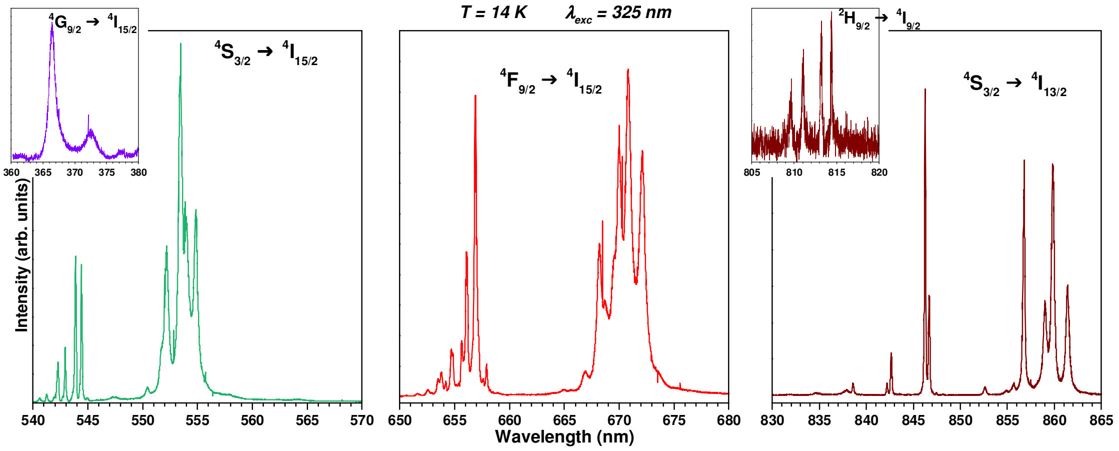

Figure 7.14 – High resolution PL spectra of the ErNbO$_4$ pellet at 14 K, excited with a 325 nm laser.

In the monoclinic structure of RENbO$_4$, the regular crystalline location of the RE ion (in this case the Er^{3+} ion) is a low symmetry site (C$_2$), and therefore it is expected a full splitting of the (2J+1)/2 of the $^{2S+1}L_J$ multiplets, each one being double degenerated since Er^{3+} is a Kramer's ion (half-integer J). Therefore, the $^4S_{3/2}$ and $^4I_{15/2}$ levels may split into a maximum of 2 and 8 Stark levels, respectively, thus being possible to observe 2×8 = 16 transitions between these levels, for each optical centre. However, analysing the luminescence spectrum between 540 and 560 nm ($^4S_{3/2}$ to $^4I_{15/2}$ transitions) at 14 K, shown in detail in Figure 7.15, it is possible to discern more than 16 lines (each one indicated with an arrow), which strongly suggests that there are at least 2 different optically active Er^{3+} sites in the lattice weakly coupled to the lattice vibrational modes. These results are consistent with what was reported by Zhang *et al.* [263] which has also observed more than 16 lines for this transitions, on ErNbO$_4$ powders.

Figure 7.16 shows the PL spectra of the ErNbO$_4$ pellet, excited with a He-Cd laser (325 nm), as a function of temperature from 14 K to RT, and also the variation of the integrated intensity of each group of transitions in inset. It is possible to observe an overall thermal quenching of the PL intensity but with slightly different rates. While the emissions coming from the $^4S_{3/2}$ level decrease at almost the same rate until they are almost undetectable at RT, the red emission from the $^4F_{9/2}$ to the $^4I_{15/2}$ ground state decreases more slowly, and is still visible at RT. None of the temperature dependent integrated intensities could be fitted to a simple non-radiative mechanism (as described by Eq. (2.24)), neither to a model considering two non-radiative mechanisms with different probabilities. This may be a consequence of the fact that the integrated intensities are calculated globally, i.e. not considering two or more centres with superimposed emissions.

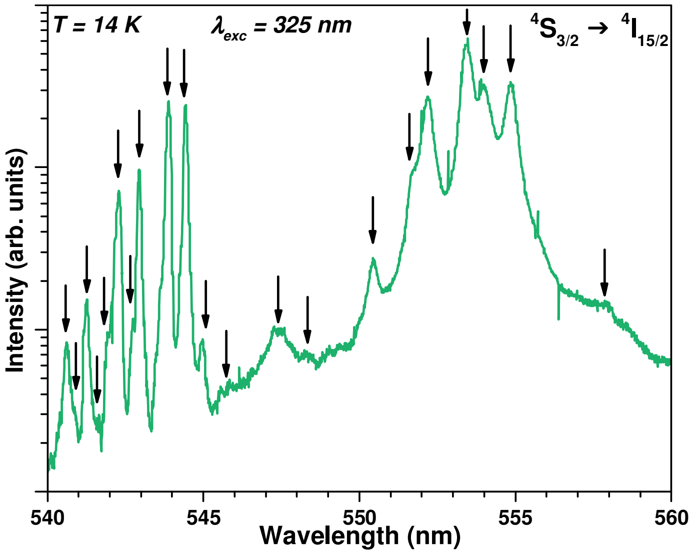

Figure 7.15 - Detail of the emission lines from the $^4S_{3/2}$ to $^4I_{15/2}$ transition of the $ErNbO_4$ pellet at 14 K excited with a 325 nm laser.

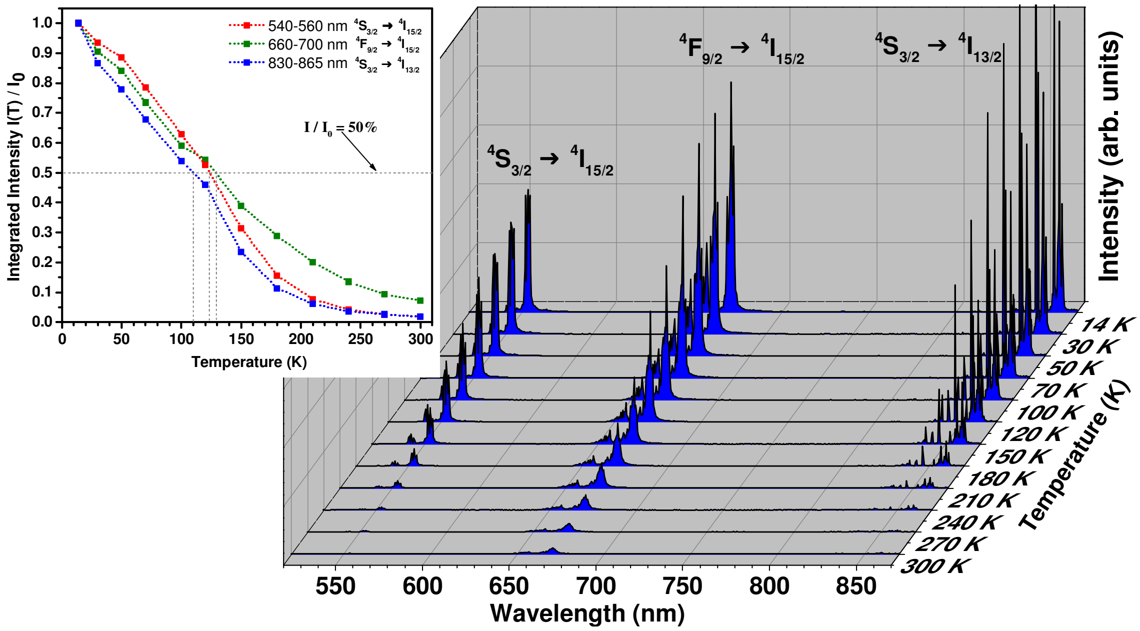

Figure 7.16 – PL spectra of the $ErNbO_4$ pellet at different temperatures excited with a 325 nm laser; integrated intensity of different transitions, as a function of temperature, in inset.

Figure 7.17 shows the PL spectra of the $ErNbO_4$ pellet at RT, using a 532 nm laser as excitation source, acquired with a Raman spectrometer. With this wavelength, the $^4S_{3/2}$ level is excited almost resonantly, and therefore transitions from this level to the $^4I_{15/2}$ (540-570 nm) and to the $^4I_{13/2}$ (830-870 nm) were observed. Additionally the $^4F_{9/2}$ to $^4I_{15/2}$ (620-680 nm), the $^2H_{9/2}$ to $^4I_{11/2}$ (690-710 nm) and the $^4I_{9/2}$ to $^4I_{15/2}$ (780-830 nm) transitions were assigned. In any of these cases the number of Stark lines surpassed the maximum number of transitions considering only one optically active Er^{3+} centre. The only exception was, once again, the $^4S_{3/2}$ to the $^4I_{15/2}$ emissions where it was possible to identify (even at RT) more than 16 lines. Additionally, while some of the observed emission bands are centred at very similar energies as in other oxide matrices, other bands of the same Er^{3+} transitions are significantly deviated in this material. Subsequently, a careful analysis of the assigned electronic transitions suggests the existence of overlapped Er^{3+} emitting centres with their manifold approximately 470 cm^{-1} apart, which is an uncommonly high value considering many different matrices doped with this ion, mainly due to the fact that the 4*f* electronic levels of the trivalent lanthanide ions are not very susceptible to the crystal field.

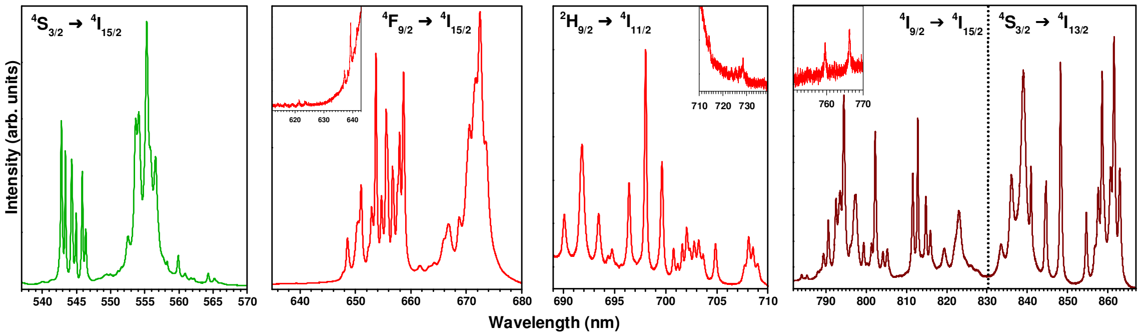

Figure 7.17 - PL spectra of the $ErNbO_4$ pellet at RT, excited with a 532 nm laser.

The same type of PL analysis at RT, performed in the Raman spectrometer, was done to the $ErNbO_4$ fibre, shown in Figure 7.18. It is possible to see that spectra of the fibre are very similar to the pellet, and also more than 16 lines were observed in the $^4S_{3/2}$ to the $^4I_{15/2}$ emissions.

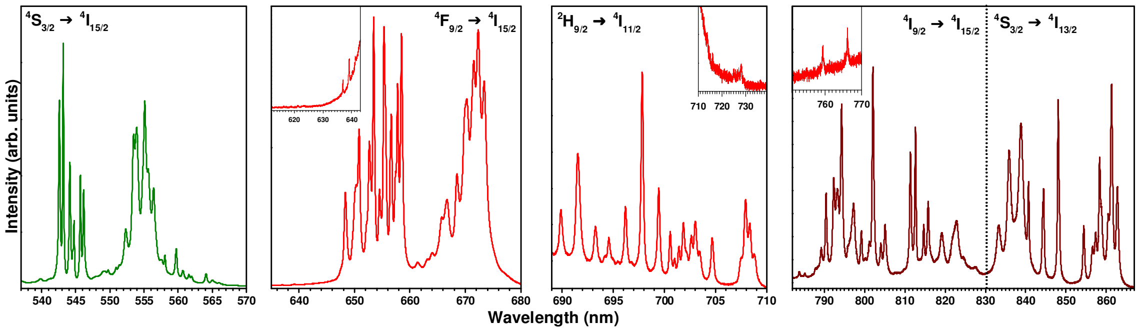

Figure 7.18 – PL spectra of the $ErNbO_4$ fibre at RT, excited with a 532 nm laser.

The energy levels diagram of the Er^{3+} free ion, and the intraionic electronic transitions that were observed in the monoclinic host and assigned when exciting with 325 nm, and when exciting with 532 nm, are schematically illustrated in Figure 7.22, where light grey lines represent the 470 cm^{-1} deviation for the respective level of the ion embedded in the crystalline matrix.

The infrared (IR) emission of the $ErNbO_4$ pellet was also analysed with a FTIR spectrometer, using a 488 nm laser as excitation source. The acquired spectra are shown in Figure 7.19, where it possible to observe several weak lines assigned to transitions from the $^4S_{3/2}$ to the $^4I_{J=\{13,11,9\}/2}$ manifolds, and extremely intense emissions between 975-1030 nm and also between 1530-1650 nm assigned to the transitions from the $^4I_{11/2}$ and $^4I_{13/2}$, respectively, to the fundamental state $^4I_{15/2}$.

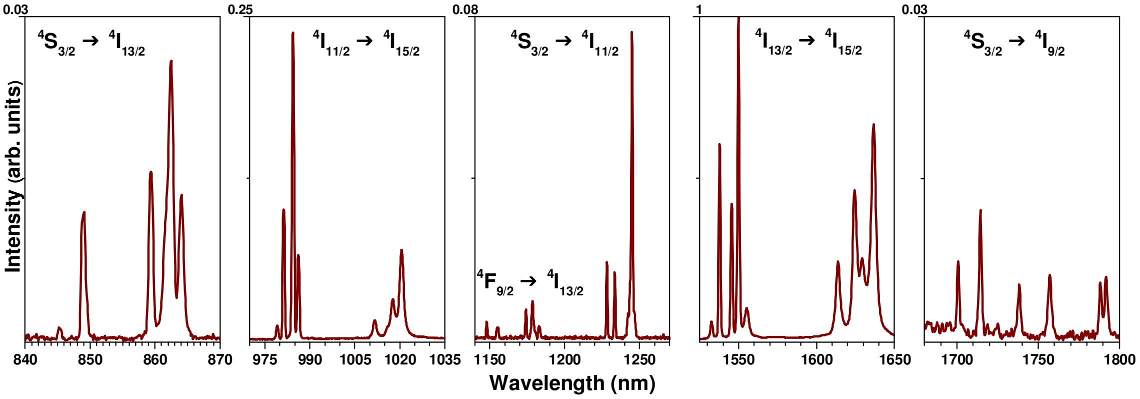

Figure 7.19 – IR PL spectra at RT of the $ErNbO_4$ pellet excited with a 488 nm laser.

Since the trivalent Er ion is known for having up-converting properties, PL studies exciting with a 980 nm laser line (resonant with the Er^{3+} absorption from the ground level $^4I_{15/2}$ to the $^4I_{11/2}$ level) were also performed to the $ErNbO_4$ pellet. At RT, no visible emission was observed with such IR excitation. However, cooling the pellet down to 14 K in the cold finger (of a closed cycle helium cryostat) revealed an intense red luminescence, which changed to yellow and to green depending on the excitation power. However, the colour was also dependent on the exposure time of the sample to the excitation source, even using low powers, which seemed to indicate a thermal effect, i.e. that the $ErNbO_4$ pellet was being heated with the exposure to IR laser light. Therefore, in order to increase the cooling power, the sample was cooled down to 5 K with a liquid He bath cryostat under high flux conditions. Figure 7.20 shows the PL spectra (in the visible range) of the $ErNbO_4$ pellet excited with different excitation powers of the 980 nm laser.

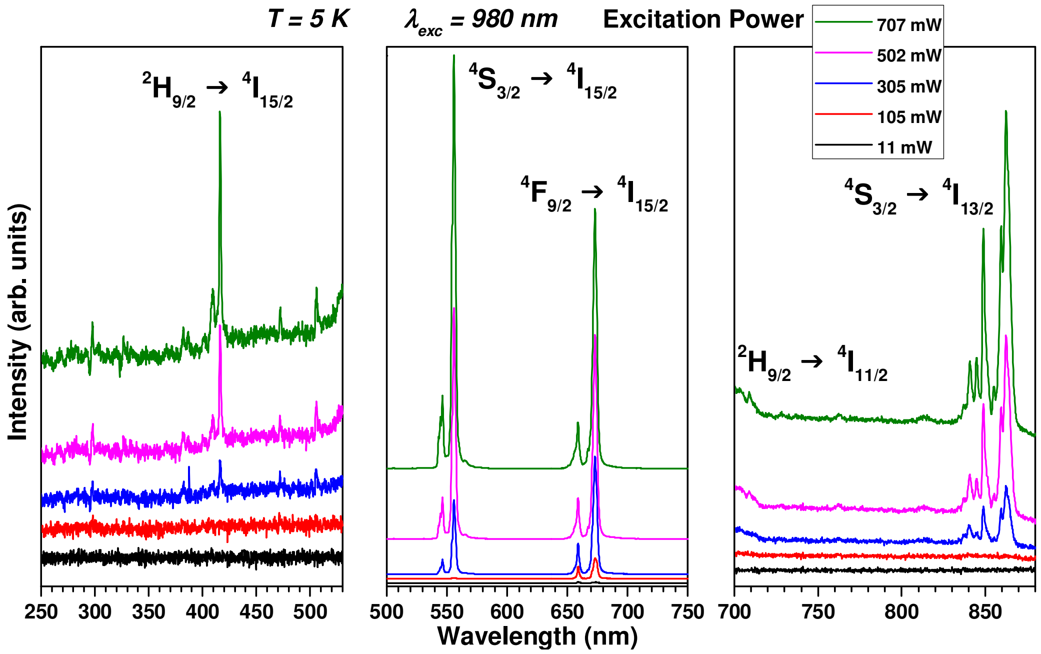

Figure 7.20 –PL spectra at 5 K of the $ErNbO_4$ for different excitation powers of a 980 nm laser

Two groups of intense emission bands were observed: in the green region, between 540-570 nm ($^4S_{3/2}$ to $^4I_{15/2}$), and in red region between 640-680 nm ($^4F_{9/2}$ to $^4I_{15/2}$). Additionally, at higher excitation powers, emissions from the $^2H_{9/2}$ level to the $^4I_{15/2}$ and to the $^4I_{11/2}$, and also from the $^4S_{3/2}$ to the $^4I_{13/2}$ were identified. With low excitation power, only the bands in the red region are observed. However, as the 980 nm laser power increases, the intensity of the $^4F_{9/2}$ to $^4I_{15/2}$ increases but also the emission in the green region starts to appear. With further power increase, the emission coming from the $^4S_{3/2}$ states increase at a faster rate than the bands from the $^4F_{9/2}$ levels, and therefore the sample changes colour from red, to yellow to green. As the $^4I_{13/2}$ level is populated due to the transition from the $^4S_{3/2}$ level (emission c.a. 850 nm), the emission coming from the $^2H_{9/2}$ starts to appear. Such state is probably populated through up-conversion from the

$^4I_{13/2}$ level, by absorbing ~555 nm photons. Figure 7.21 shows the study of the up-converting PL spectra, at 5 K, as a function of the 980 nm laser excitation power, and the CIE diagram illustrating the colour evolution from red, to yellow and finally to green. In such study, it becomes clear that the $^4F_{9/2}$ multiplet is suffering saturation effects at high excitation powers.

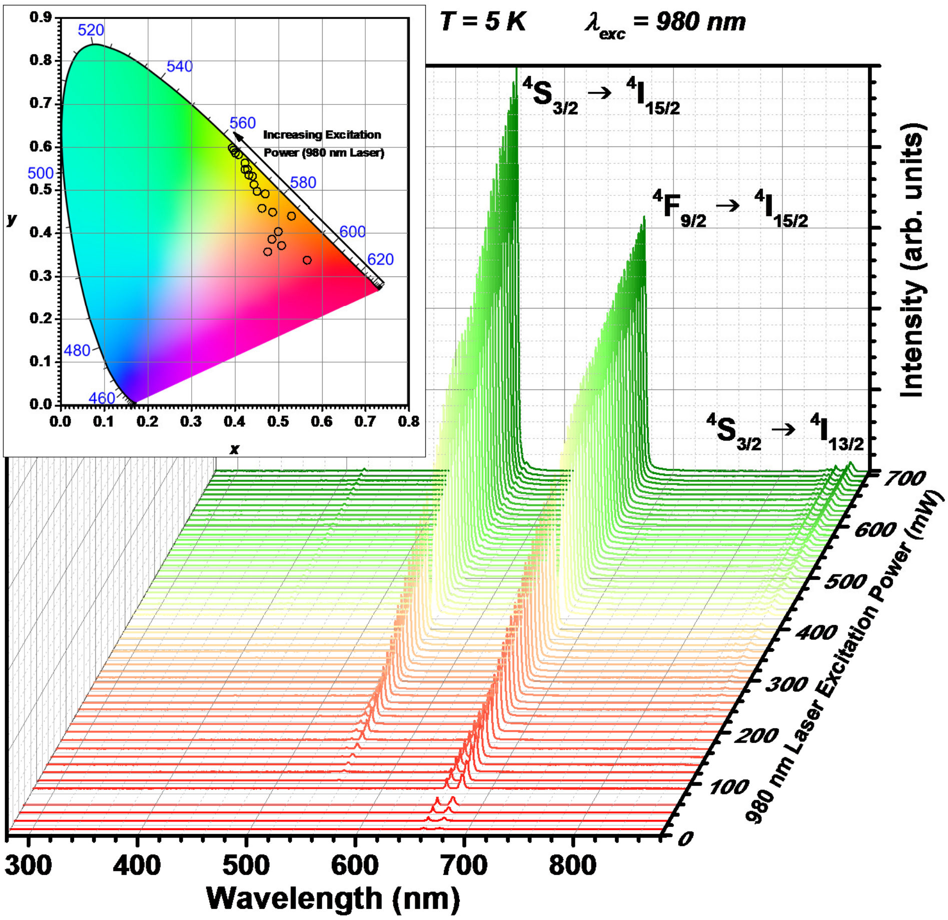

Figure 7.21 – PL spectra at 5 K of the $ErNbO_4$ as a function of the excitation power of a 980 nm laser; in inset, the CIE diagram with the corresponding colour coordinates.

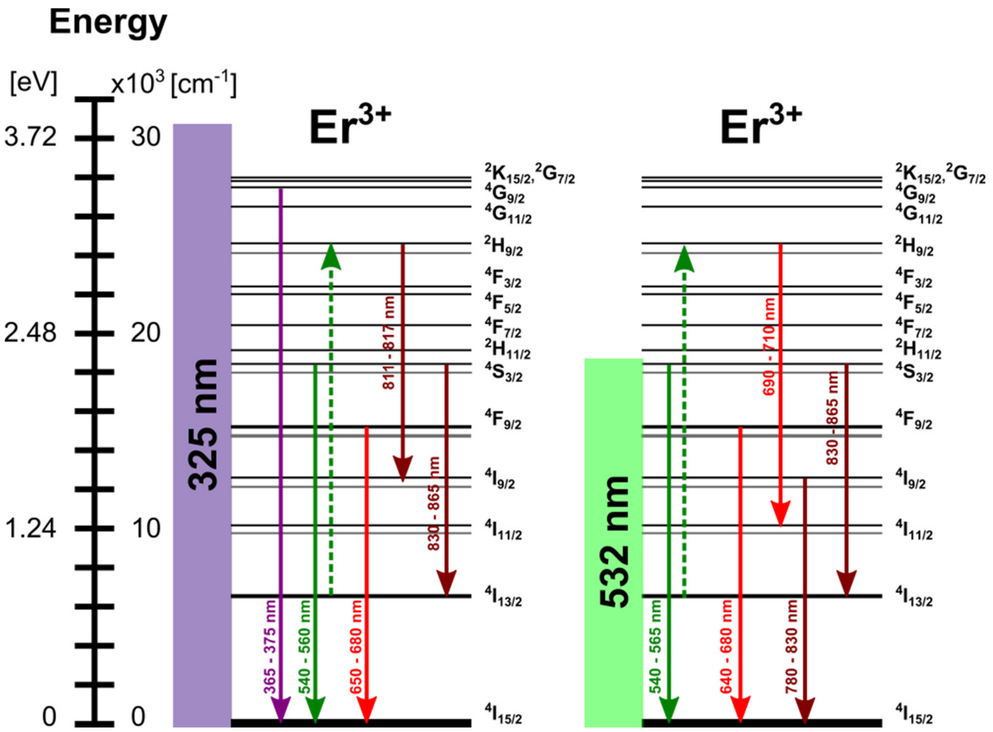
Energy
[eV]
x10^3 [cm^{-1}]
3.72
30
2.48
20
1.24
10
0
0
Er^{3+}
325 nm
$^2K_{15/2}$, $^2G_{7/2}$
$^4G_{9/2}$
$^4G_{11/2}$
$^2H_{9/2}$
$^4F_{3/2}$
$^4F_{5/2}$
$^4F_{7/2}$
$^2H_{11/2}$
$^4S_{3/2}$
$^4F_{9/2}$
$^4I_{9/2}$
$^4I_{11/2}$
$^4I_{13/2}$
$^4I_{15/2}$
365 - 375 nm
540 - 560 nm
650 - 680 nm
811 - 817 nm
830 - 865 nm
Er^{3+}
532 nm
540 - 565 nm
640 - 680 nm
690 - 710 nm
780 - 830 nm
830 - 865 nm

Figure 7.22 – Energy levels diagram of the free Er^{3+} ion and respective observed transitions observed in the ErNbO$_4$ samples, when excited with 325 nm (at left) and 532 nm (at right).

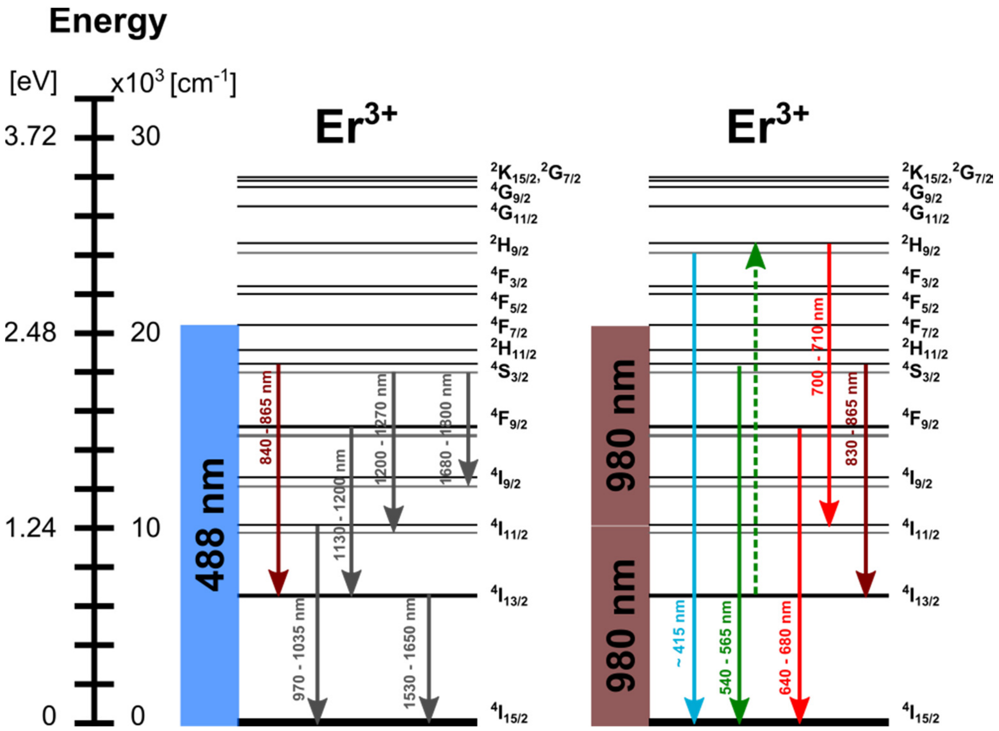
Energy
[eV]
x10^3 [cm^{-1}]
3.72
30
2.48
20
1.24
10
0
0
Er^{3+}
488 nm
$^2K_{15/2}$, $^2G_{7/2}$
$^4G_{9/2}$
$^4G_{11/2}$
$^2H_{9/2}$
$^4F_{3/2}$
$^4F_{5/2}$
$^4F_{7/2}$
$^2H_{11/2}$
$^4S_{3/2}$
$^4F_{9/2}$
$^4I_{9/2}$
$^4I_{11/2}$
$^4I_{13/2}$
$^4I_{15/2}$
840 - 865 nm
1130 - 1200 nm
1200 - 1270 nm
1680 - 1800 nm
970 - 1035 nm
1530 - 1650 nm
Er^{3+}
980 nm
980 nm
~ 415 nm
540 - 565 nm
640 - 680 nm
700 - 710 nm
830 - 865 nm

Figure 7.23 – Energy levels diagram of the free Er^{3+} ion and respective observed transitions observed in the ErNbO$_4$ samples, when excited with 488 nm (at left) and 980 nm (at right).

7.2.4.2 $EuNbO_4$

Figure 7.24 illustrates the high resolution PL spectrum at RT of the $EuNbO_4$ fibre, excited with a He-Cd laser (325 nm). Typical intra-$4f^6$ transitions of the trivalent Eu ion (Eu^{3+}), from to the $^5D_0$ to the $^7F_{J=\{0,1,2,3,4\}}$, but also from $^5D_1$ to the $^7F_{J=\{1,2\}}$ electronic levels, were observed producing a red/orange luminescence visible to naked eye.

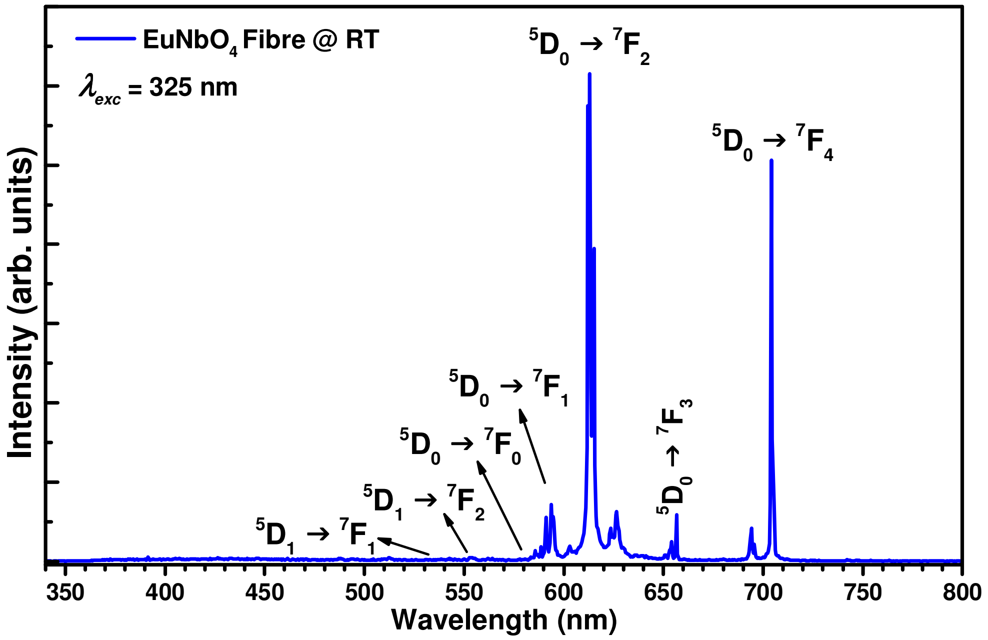

Figure 7.24 – PL spectrum of the $EuNbO_4$ fibre at RT, under 325 nm laser excitation.

It is possible to observe that the most intense emission lines are assigned to transitions from the $^5D_0$ electronic level. Therefore, in order to understand how such level can be preferentially populated, a PLE analysis was performed to the $EuNbO_4$ fibre at RT, using a Xe lamp as excitation source, monitoring the emission at 612 nm (the most intense line) assigned to a radiative transition from the $^5D_0$ to the $^7F_2$ level. The acquired PLE spectrum, with the observed excitation bands assigned to the respective intra-$4f^6$ transitions, is shown in Figure 7.25.

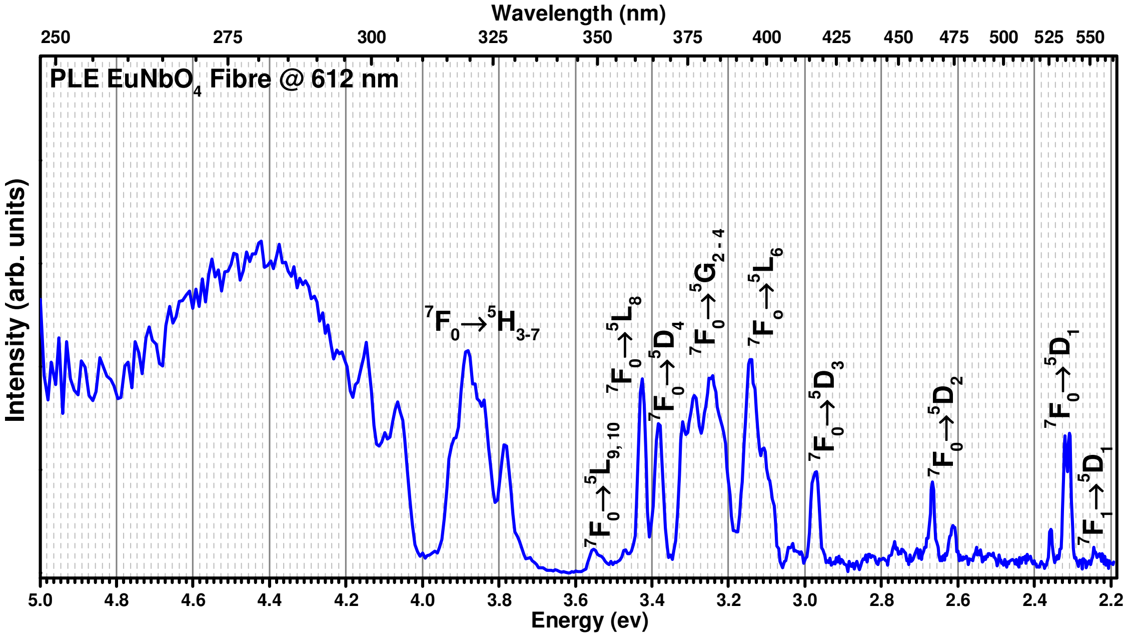

Figure 7.25 – PLE spectra at RT of the EuNbO$_4$ fibre, monitored at the 612 nm emission.

It is possible to identify, in the PLE spectrum, many of the high energy Eu^{3+} excited states that populate the $^5D_0$ level that gives rise to monitored emission. Therefore, the luminescence assigned to the $^5D_0$ to the ^7F_J transitions is preferentially excited *via* the broad excitation band, detected at high energies and centred at approximately 4.43 eV (~280 nm), as well as *via* the $^5D_{J=\{1,2,3,4\}}$, $^5L_{J=\{6,7,8,9,10\}}$, $^5G_{J=\{2,3,4\}}$ and $^5H_{J=\{3,4,5,6,7\}}$ multiplets. Large excitation bands, typically associated to charge transfer (CT) transitions [264,265], are commonly observed in many wide band gap oxide hosts, as in the case of the EuNbO$_4$ fibre. However, since two excitation lines are observed between 4.0 and 4.2 eV, superimposed with the edge of the band, it should not be excluded the hypothesis of the most energetic excited states of the Eu^{3+} being also contributing for such excitation band.

Figure 7.26 illustrates an electronic energy level diagram of the Eu^{3+} free ion, schematically showing the observed radiative transitions from the $^5D_0$ state, and also the excitation to the $^5H_3$ level through 325 nm radiation, which was used for the following PL studies.

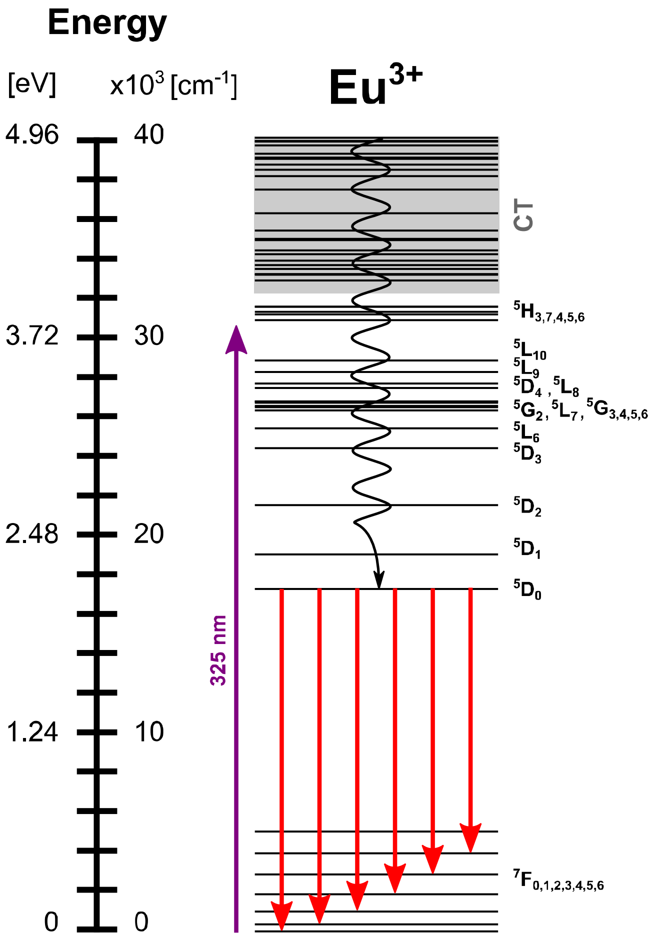

Figure 7.26 – Energy level diagram of the $4f^6$ electron configuration for the Eu^{3+} free ion with the observed radiative transitions of the ions embedded in the $EuNbO_4$ crystalline hosts.

Figure 7.27 shows the high resolution PL spectra of both the $EuNbO_4$ fibre and pellet at 14 K (excited with 325 nm) presenting very sharp and well resolved luminescence lines from each of the $^5D_0$ to the $^7F_{J=\{0,1,2,3,4\}}$ transitions. Despite its low intensity, it should be noted that the $^5D_0$ to the $^7F_0$ transition was observed, which confirms that (being a forbidden transition) the Eu^{3+} ions are in a low symmetry site, as predictable for a monoclinic structure. Therefore, a full splitting of the 2J+1 of the $^{2S+1}L_J$ multiplets is expected, i.e. a maximum of 1×3 = 3 ($^5D_0 \rightarrow {}^7F_1$), 1×5 = 5 ($^5D_0 \rightarrow {}^7F_2$), 1×3 = 7 ($^5D_0 \rightarrow {}^7F_3$) and 1×3 = 9 ($^5D_0 \rightarrow {}^7F_4$) Stark lines for each Eu^{3+} active optical centre. The black arrows in Figure 7.27 point to each different Stark line that was possible to identify (while some lines are very weak, in a logarithmic scale they are perfectly distinguished and were therefore also signalized). Counting the observed lines, it is clear that there is more than one optically active centre, which indicates that the Eu^{3+} ion is in more than one different site and/or crystalline environment. Actually, the fact that three lines were assigned to the $^5D_0 \rightarrow {}^7F_0$ transition indicates that there are at least three active optical centres.

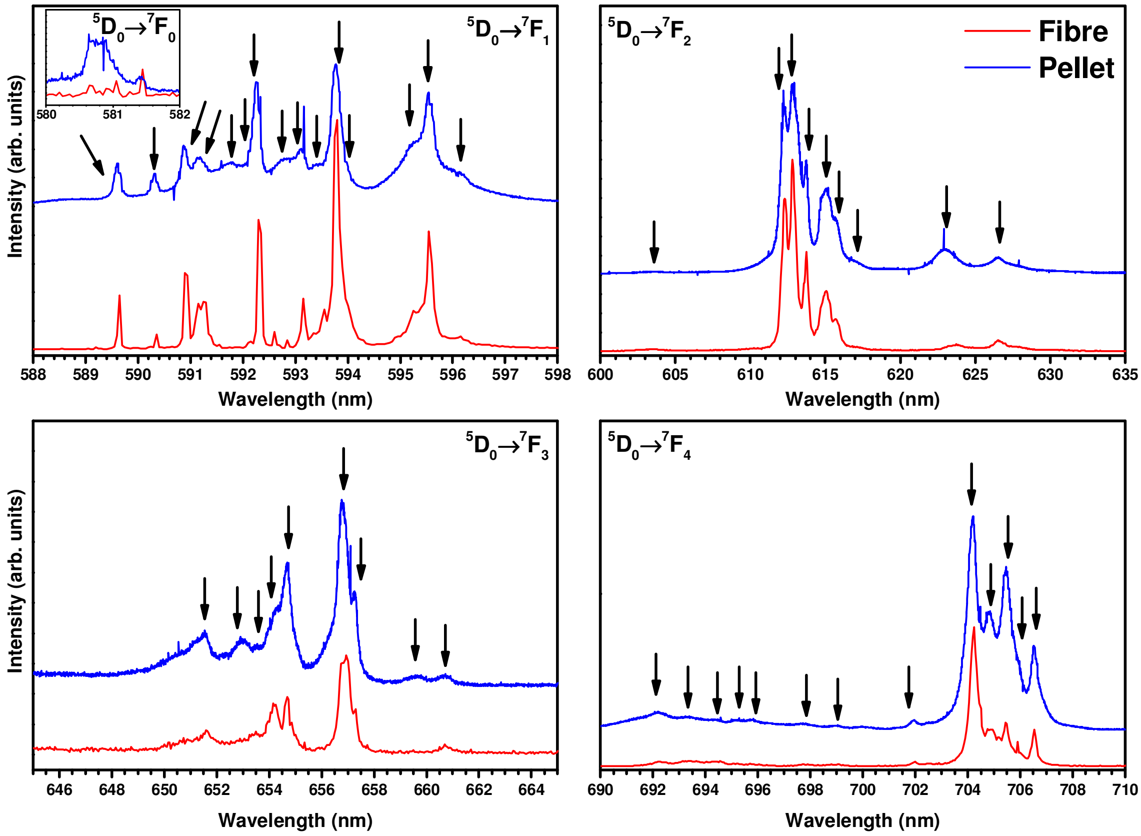

Figure 7.27 – High resolution PL spectra of the EuNbO$_4$ fibre and pellet (separated by an onset) at 14 K, under 325 nm laser excitation.

At 14 K the red luminescence of the EuNbO$_4$ samples, from the identified intra-4*f*^{6} transitions, was very intense, much more than at RT. Hence, a temperature dependent PL study was performed to both samples. Figure 7.28 shows the PL spectra of the EuNbO$_4$ pellet, under 325 nm excitation, at different temperatures, with the respective variation of the overall integrated intensity, determined from the $^5D_0$ state emissions, shown in inset. It is possible to see that there is strong thermal quenching of the luminescence, decreasing to almost 15 % of its intensity from 14 K to RT, but still perfectly perceived to naked eye.

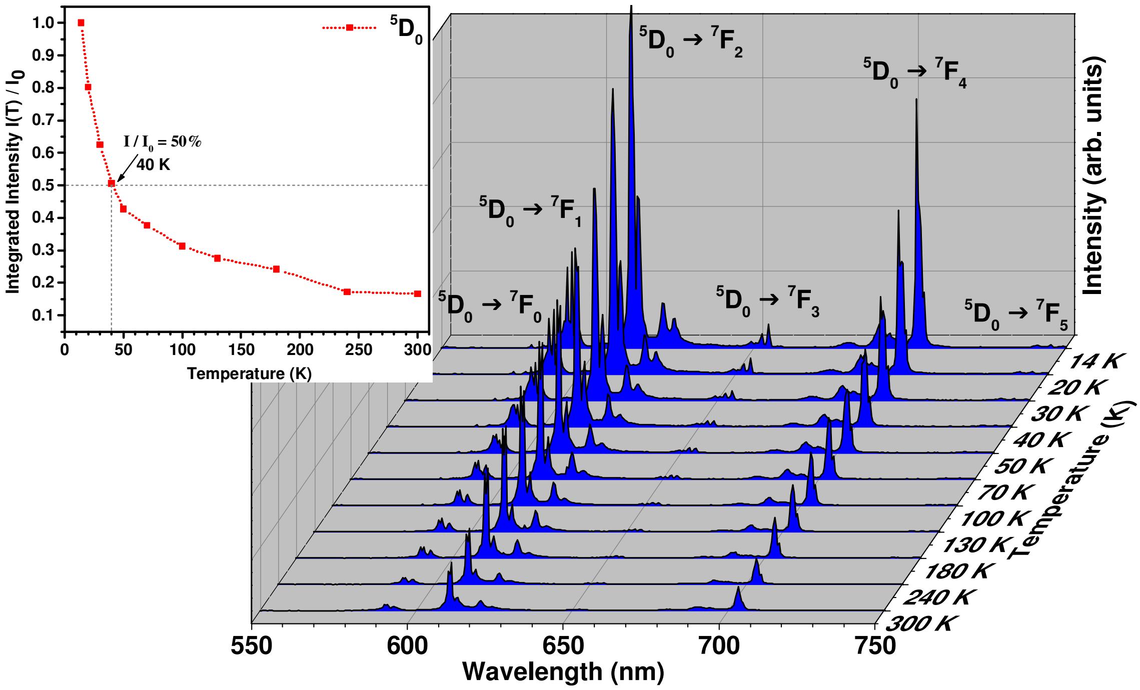

Figure 7.28 – Temperature dependent PL spectra of the EuNbO$_4$ pellet under 325 nm laser excitation; integrated intensity of the $^5D_0$ bands as a function of temperature (inset).

Figure 7.29 illustrates the high resolution temperature dependent PL spectra of the fibre optically excited with a 325 nm laser. The same behaviour of strong thermal quenching was also observed, as in the EuNbO$_4$ pellet. However, what is interesting to notice in this high resolution PL analysis is that many of the Stark lines observed at low temperature undergo a faster thermal quenching than others, being almost completely extinct at temperatures higher than 50 K. Therefore, in can be concluded that such Stark lines, signalized with black arrows in Figure 7.29, are thermally extinct faster than the others because they are due to a different optically active Eu^{3+} centre(s).

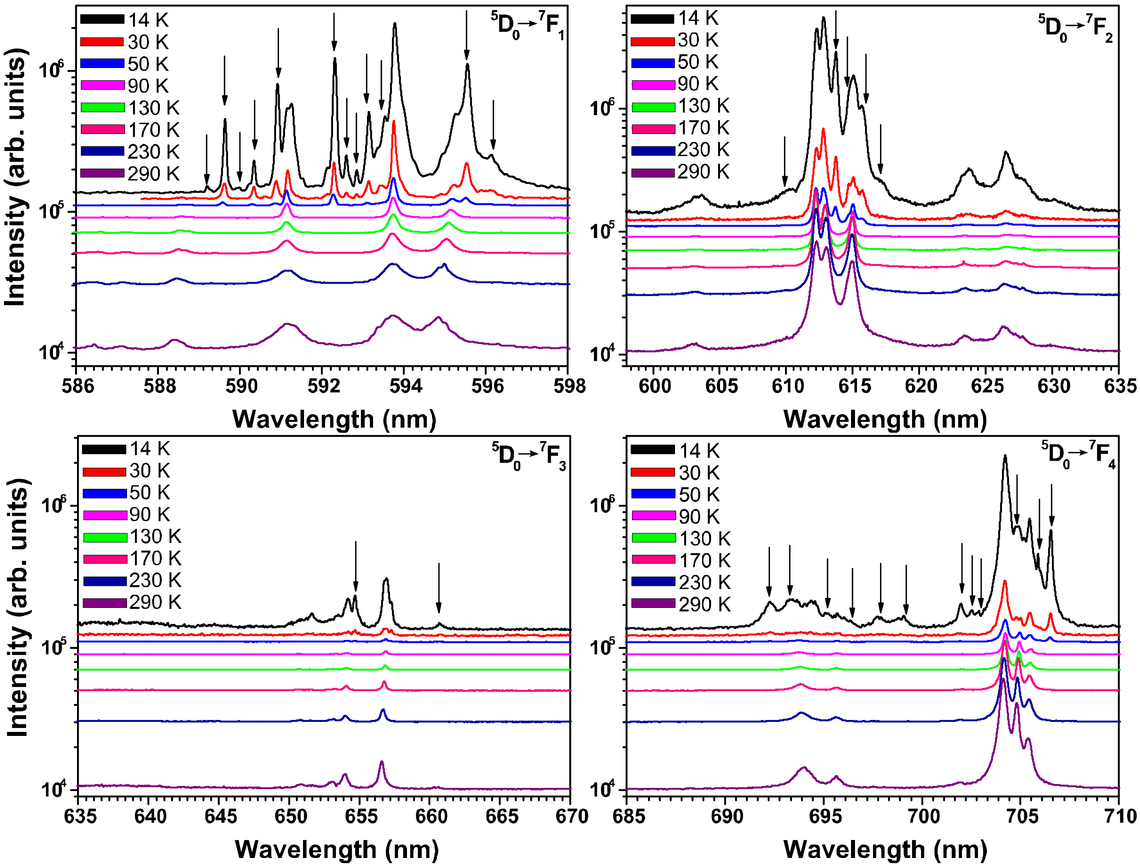

Figure 7.29 – High resolution temperature dependent PL spectra of the $EuNbO_4$ fibre under 325 nm laser excitation.

7.2.4.3 *$SmNbO_4$*

Under UV excitation (325 nm from a He-Cd laser), the $SmNbO_4$ pellet does not show detectable PL signal and therefore it was cooled in a closed cycle helium cryostat. Hence, Figure 7.30 illustrates the high resolution PL spectrum at 14 K of the $SmNbO_4$ pellet, under 325 nm optical excitation. It is possible to observe a red luminescence due to the typical intra-$4f^5$ transitions of the trivalent Sm ion (Sm^{3+}), from to the $^4G_{5/2}$ to the $^6H_{J=\{5,7,9,11\}/2}$ electronic levels.

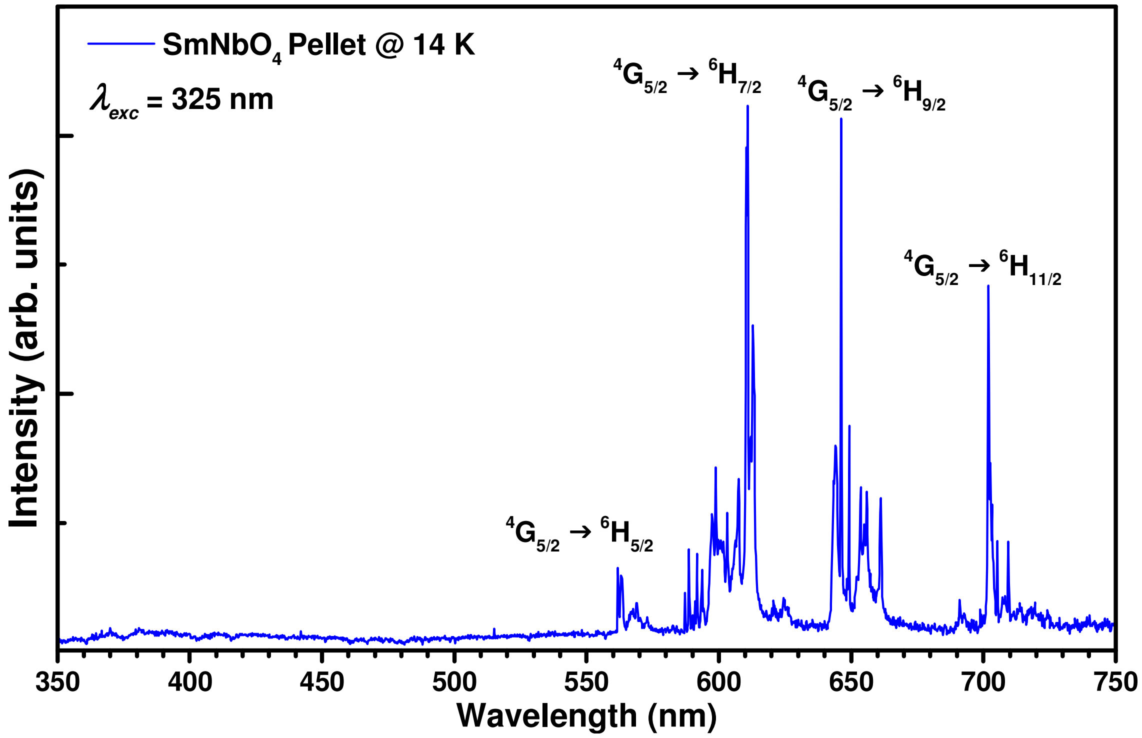

Figure 7.30 – PL spectrum of the $SmNbO_4$ pellet at 14 K, under 325 nm laser excitation.

In order to study how the $^4G_{5/2}$ electronic level, which gives rise to the observed emission lines, can be preferentially populated, both $SmNbO_4$ fibre and pellet were analysed by PLE at RT using a Xe lamp as excitation source, monitoring the emission at 647 nm, which corresponds to the $^4G_{5/2} \rightarrow {}^6H_{9/2}$ transition. The acquired spectra are shown in Figure 7.31.

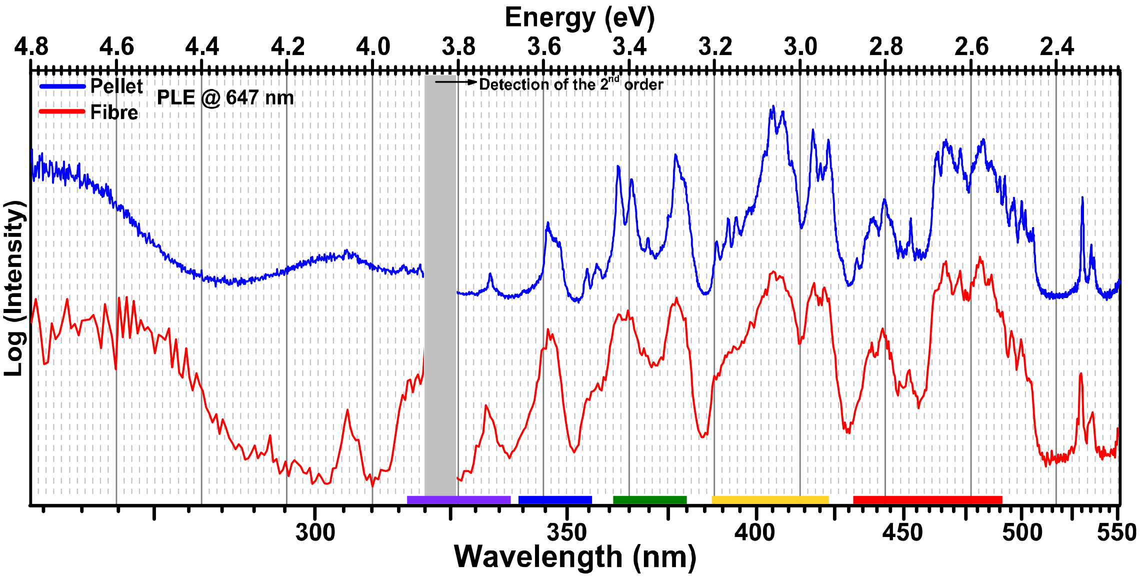

Figure 7.31 –PLE spectra at RT of the $SmNbO_4$ fibre and pellet, monitored at the 647 nm emission (colour bars refer to the electronic levels assignment in Figure 7.35).

It is possible to observe numerous sharp lines, some of them superimposed thus appearing as bands, which correspond the many 4*f*⁵ electronic levels of the trivalent Sm ion (Sm^{3+}). Therefore, the $^4G_{5/2}$ level can be populated by exciting basically all the upper states from the $^7F_{3/2}$ (2.34 eV ≅ 530 nm) to the $^4P_{5/2}$ (4.06 eV ≅ 305 nm). The assignment of such levels can be more easily visualized in the energy diagram of the Sm^{3+} ion illustrated in Figure 7.35. Additionally, the PLE spectra revealed a rising edge in the UV region that keeps nearly constant for higher excitation energies (at least up to 5.0 eV). Figure 7.32 shows in detail the excitation spectra, in the UV range of energies, of the $SmNbO_4$ fibre and pellet. It is possible to see that these edges start to rise at ~4.15 eV in the fibre and at ~4.35 eV in the pellet. These edges are probably related either to the band gap of the $SmNbO_4$ material, or to a charge transfer band, but there is insufficient information to affirm which case is it.

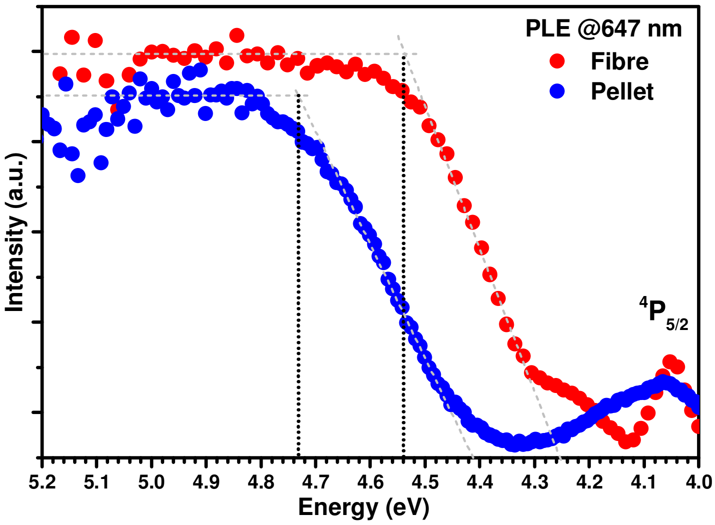

Figure 7.32 – Excitation edge, at high energies, of the $SmNbO_4$ fibre and pellet, from the PLE spectra monitored at the 647 nm emission.

PL spectra of the $SmNbO_4$ samples were acquired, using a Xe lamp to excite at 488 nm (one of the PLE maxima, corresponding to the $^4G_{7/2}$ level), illustrated in Figure 7.33. Additionally, a Raman spectrometer was used to record the luminescence of both $SmNbO_4$ samples exciting directly the $^7F_{3/2}$ level using a 532 nm laser. The spectra are shown in Figure 7.34.

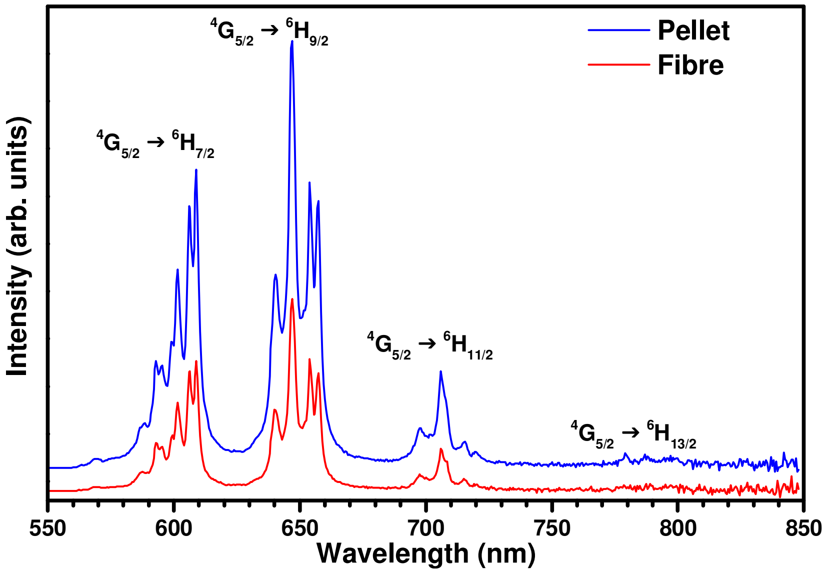

Figure 7.33 – PL spectra at RT of the SmNbO₄ samples excited with 480 nm from a Xe Lamp.

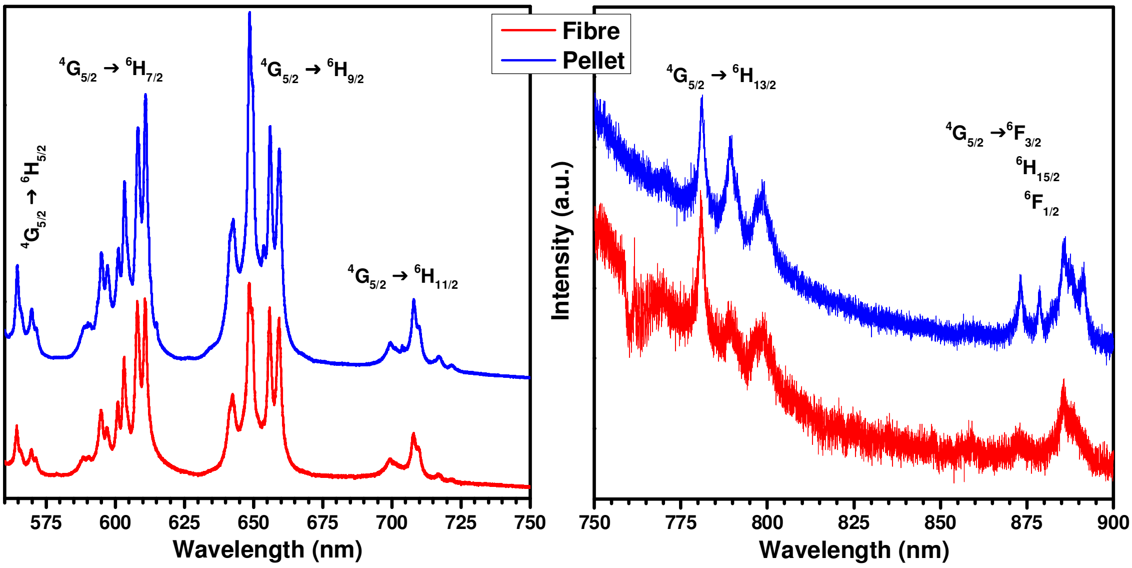

Figure 7.34 – PL spectra of the SmNbO₄ samples excited with a 532 nm laser at RT.

In Figure 7.33 and Figure 7.34, it is possible to observe typical red luminescence from intra-4f^5 transitions of the Sm^{3+}, more specifically from the $^4G_{5/2}$ level to the $^6H_{5/2}$, $^6H_{7/2}$, $^6H_{9/2}$, $^6H_{11/2}$ and $^6H_{13/2}$, showing sharp emission lines due to the splitting of the Stark levels. In the case of the spectra acquired in the Raman spectrometer (excited with 532 nm), it was even possible to detect luminescence between 870 and 900 nm assigned to the transitions from the $^4G_{5/2}$ to the $^6F_{3/2}$, $^6H_{15/2}$ and $^6F_{1/2}$ levels. In general, the intensity of the observed luminescence was very low in both $SmNbO_4$ samples at RT.

Many of the excited energy levels were excited resonantly with different wavelengths using the Xe lamp, but only the emissions from the $^4G_{5/2}$ level were observed (always with low intensity), and therefore it is suggested that the deexcitation from the upper levels only occur in a non-radiative way, as schematically illustrated in Figure 7.35.

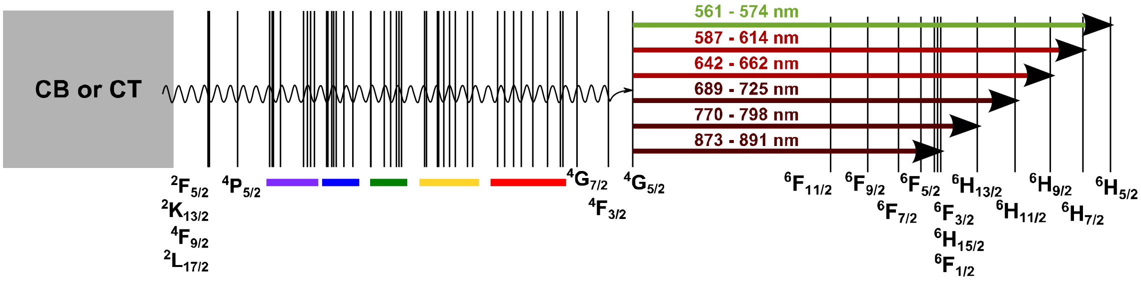
CB or CT
561 - 574 nm
587 - 614 nm
642 - 662 nm
689 - 725 nm
770 - 798 nm
873 - 891 nm
$^2F_{5/2}$
$^2K_{13/2}$
$^4F_{9/2}$
$^2L_{17/2}$
$^4P_{5/2}$
$^4G_{7/2}$
$^4F_{3/2}$
$^4G_{5/2}$
$^6F_{11/2}$
$^6F_{9/2}$
$^6F_{7/2}$
$^6F_{5/2}$
$^6F_{3/2}$
$^6H_{15/2}$
$^6F_{1/2}$
$^6H_{13/2}$
$^6H_{11/2}$
$^6H_{9/2}$
$^6H_{7/2}$
$^6H_{5/2}$

Figure 7.35 – Energy level diagram of the $4f^5$ electron configuration of Sm^{3+} with the observed radiative transitions observed in the $SmNbO_4$ samples.

The $SmNbO_4$ pellet was cooled down to 14 K with a cold finger of a closed cycle helium cryostat and, using a 325 nm laser and a high resolution spectrometer, the PL spectrum was recorded with step of 0.02 nm. Figure 7.36 illustrates in detail part of such PL spectrum, regarding the emission lines assigned to the $^4G_{5/2}$ to $^6H_{7/2}$ transition.

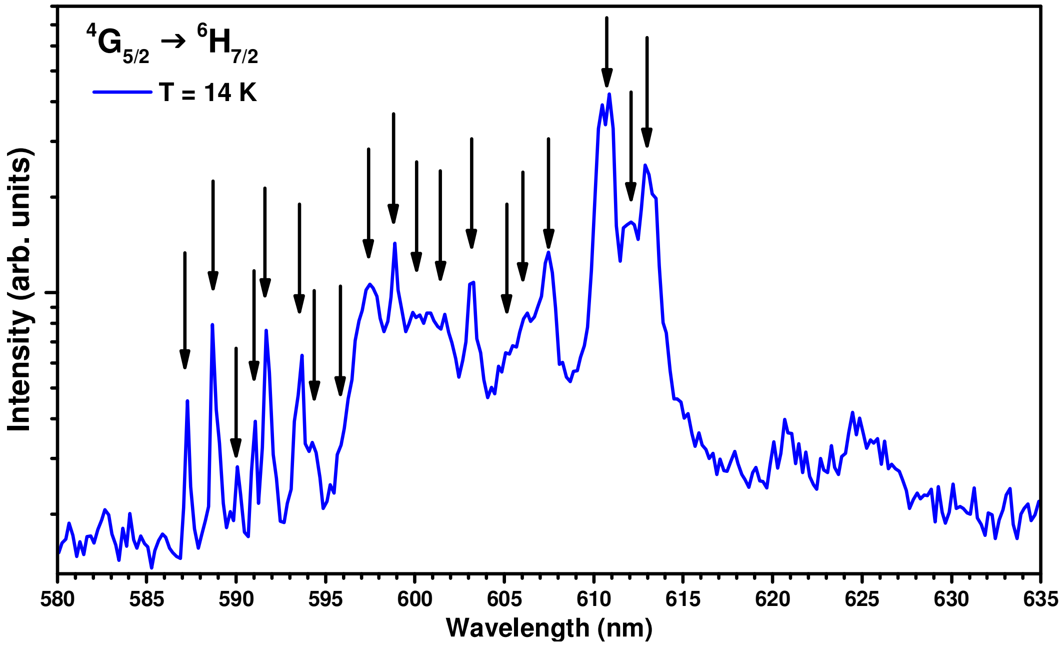

Figure 7.36 – High resolution PL spectra of the emission assigned to the $^4G_{5/2}$ to $^6H_{7/2}$ transition, from the $SmNbO_4$ pellet at 14 K under 325 nm laser excitation.

Sm^{3+} is a Kramer's ion, and therefore, assuming a low symmetry site, it is expected a full splitting of the (2J+1)/2 of the $^{2S+1}L_J$ multiplets. Hence, the $^4G_{5/2}$ and $^6H_{7/2}$ levels may split into a maximum of 3 and 4 Stark levels, respectively, thus being possible to observe 3×4 = 12 transitions between these levels, for each optical centre. While the spectra acquired at RT did not show more than such number of lines, in the spectrum at 14 K more than 12 Stark lines are clearly discerned thus indicating, once again, the existence of more than one optically active centre, which means that there are Sm^{3+} ions in more than one different site/environment.

A temperature dependent PL analysis was performed to the $SmNbO_4$ pellet from 14 K to RT, which is shown in Figure 7.37, also showing in inset the integrated intensity of the observed emission as a function of temperature. The red luminescence at 14 K was not very intense, but it was perfectly visible to naked eye. However, a strong thermal quenching was observed, and at 150 K the intensity of the emissions from the $^4G_{5/2}$ level was almost undetectable.

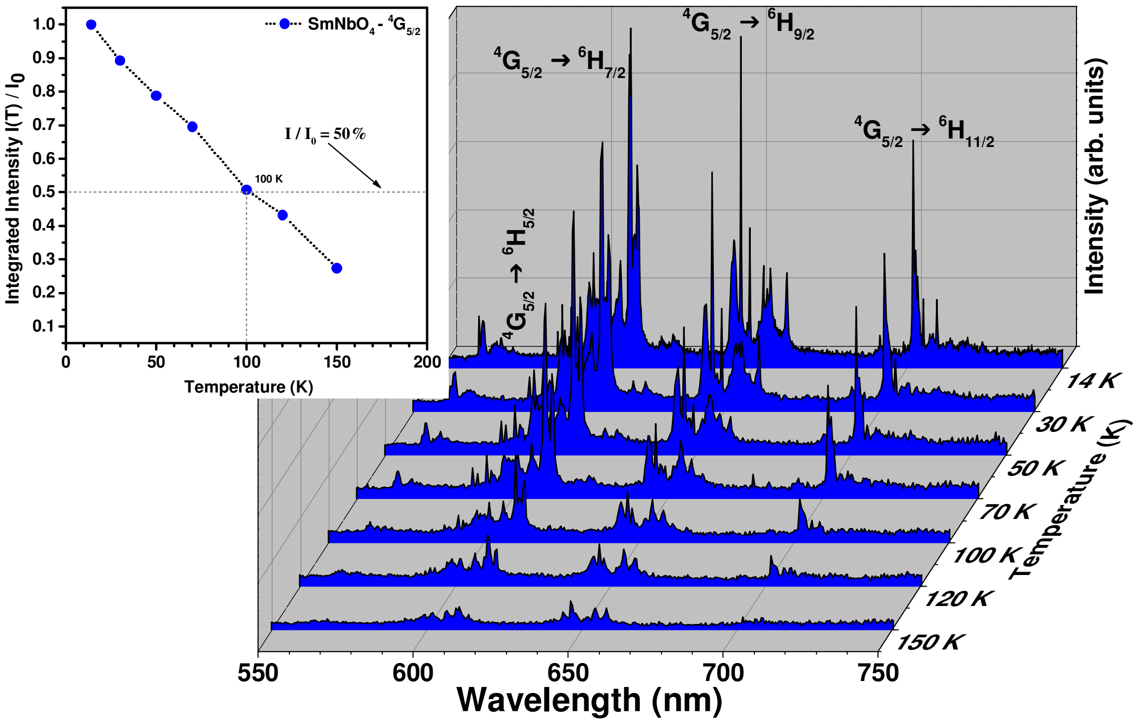

Figure 7.37 – Temperature dependent PL spectra of the $SmNbO_4$ pellet; in inset it is shown the integrated intensity of the $^5G_{5/2}$ emissions lines for the different temperatures.

7.2.5 *Electrical Properties*

Knowing that the rare-earth orthoniobates are reported for having mixed protonic, native ionic and electronic conductivity properties [181,266], preliminary electrical measurements at high temperatures were performed to the $RENbO_4$ samples. For that purpose, the pellets were placed between two platinum electrodes which were supported by an alumina structure so the sample could be kept in the middle of a tubular furnace. The measurements were performed using an Agilent 4294A precision impedance analyser in the Cp-Rp configuration, without dc bias and an ac signal with 500 mV of amplitude, from 100 Hz to 1 MHz. These first studies were done at air, without control of the pressure or humidity, from RT to 1000 ºC. The area and thickness of the pellets were measured beforehand and considered to be constant as a function of temperature.

Therefore, the total ac conductivity as a function of temperature, calculated from the impedance spectroscopy measurements of the $ErNbO_4$, $EuNbO_4$ and $SmNbO_4$ pellets are respectively shown in Figure 7.38, Figure 7.39 and Figure 7.40.

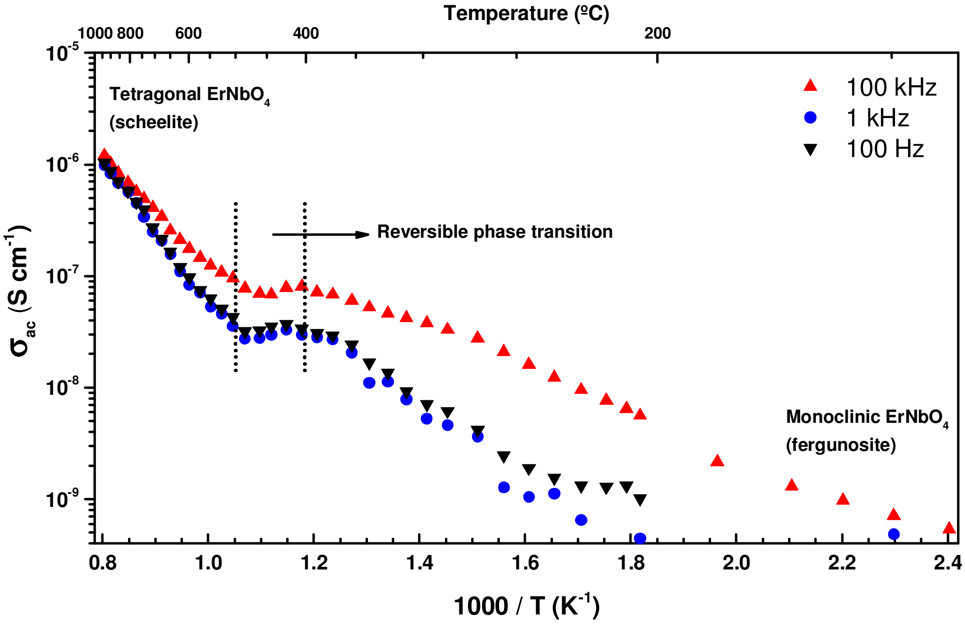

Figure 7.38 – Total ac conductivity of the $ErNbO_4$ pellet, measured at different frequencies, from RT to 1000 ºC in air.

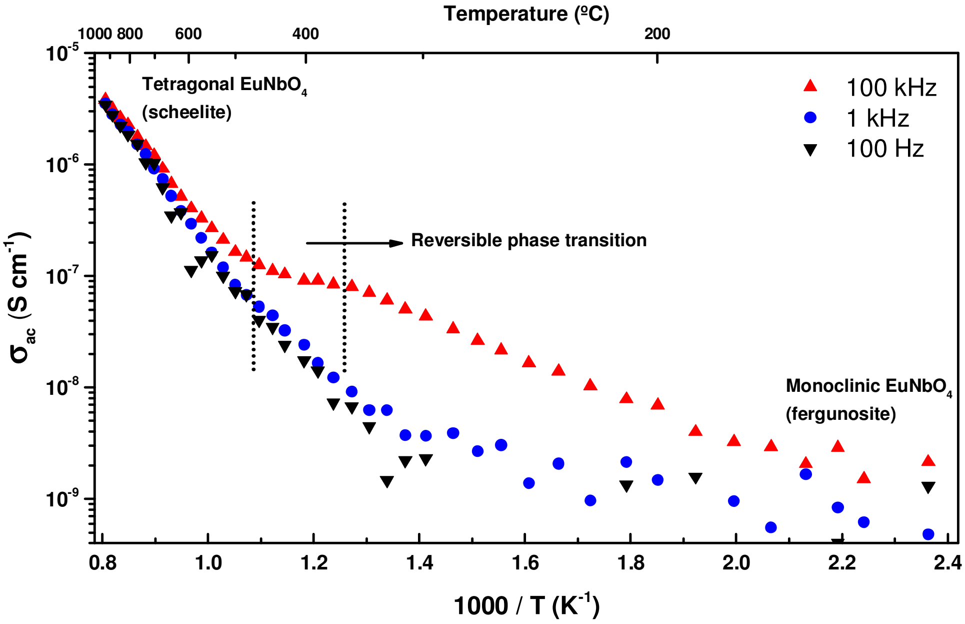

Figure 7.39 – Total ac conductivity of the EuNbO$_4$ pellet, measured at different frequencies, from RT to 1000 ºC in air.

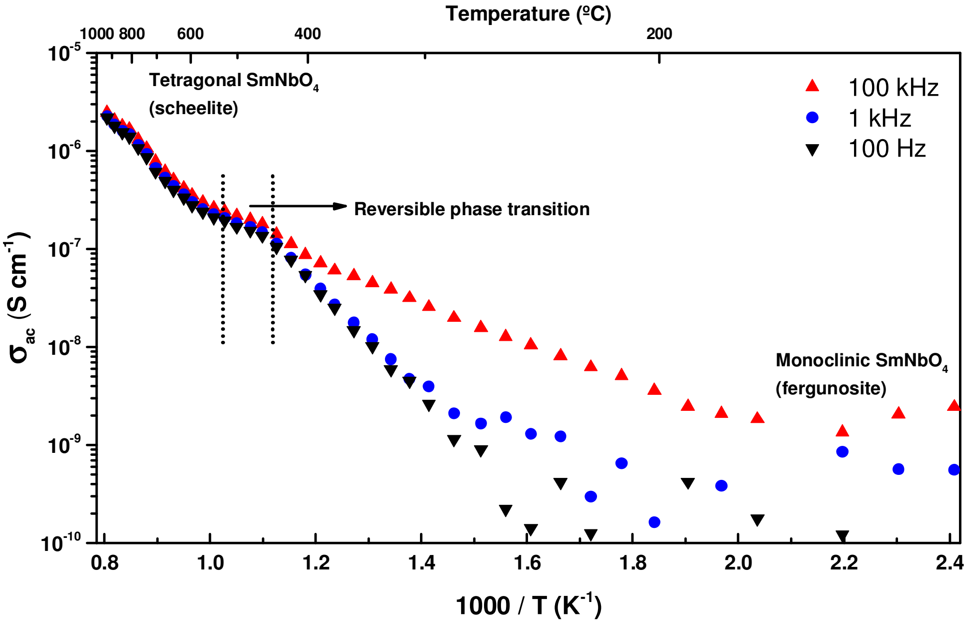

Figure 7.40 – Total ac conductivity of the SmNbO$_4$ pellet, measured at different frequencies, from RT to 1000 ºC in air.

It is possible to observe that the total ac conductivity in all the RENbO$_4$ samples increases with temperature in almost 5 orders of magnitude from ~10^{-10} to ~10^{-5} S/cm, at approximately the same rate except in a small range of temperatures between 400 and 600 ºC, depending on the RE ion. According with literature [181], it approximately matches the range at which the reversible phase transition from the monoclinic fergusonite-type structure (stable at RT) to the tetragonal scheelite-type structure (stable at high temperatures), occurs.

At low temperatures, before the phase transition to the scheelite-type structure, the conductivity at high frequencies (100 kHz) is clearly higher, and also seems to increase with temperature at a slower rate, than the conductivity at 100 Hz and 1 kHz. The dependency of the logarithm of the conductivity with the inverse of temperature is almost linear, which can suggest that only one conductivity mechanism is predominant. According with other works [181], the conductivity on these materials is almost pure protonic at temperatures below 800 °C. At high temperatures (after the phase transition) the conductivity at different frequencies converges to almost identical values increasing at the same rate with temperature in a very linear way. At such temperatures the electronic, and mainly native ionic conductivity, are likely predominant [181].

While further studies are necessary to clarify and quantify the contribution of different conductivity mechanisms, the observed behaviour of the analysed samples and values of the total ac conductivity as a function of temperature, are consistent with other reported works in rare-earth niobates and tantalates [181]. The protonic conductivity mechanism typically proposed for this type of materials, with a distorted perovskitic structure, relies on oxygen vacancies to which hydroxyl groups (OH^-) are bonded and conducted (Grotthuss mechanism) [267,268], as illustrated in Figure 7.41. Therefore, in order to promote the creation of oxygen vacancies in these materials, it is common to partially substitute the RE with other ions with different electronic valence like Ca [181]. However, in the case of the stoichiometric $RENbO_4$ samples, analysed in this work, the oxygen vacancies probably have an intrinsic nature due to defects originated during the synthesis process.

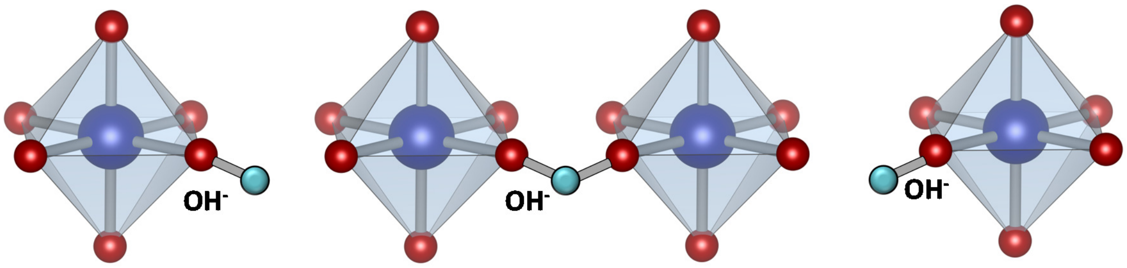

Figure 7.41 – Schematic illustration of the Grotthuss mechanism for protonic conduction through oxygen vacancies (adapted from [268]).

The relative dielectric constant as a function of temperature was also calculated from the impedance spectroscopy measurements of the $ErNbO_4$, $EuNbO_4$ and $SmNbO_4$ pellets, and the results are respectively shown in Figure 7.42, Figure 7.43 and Figure 7.44.

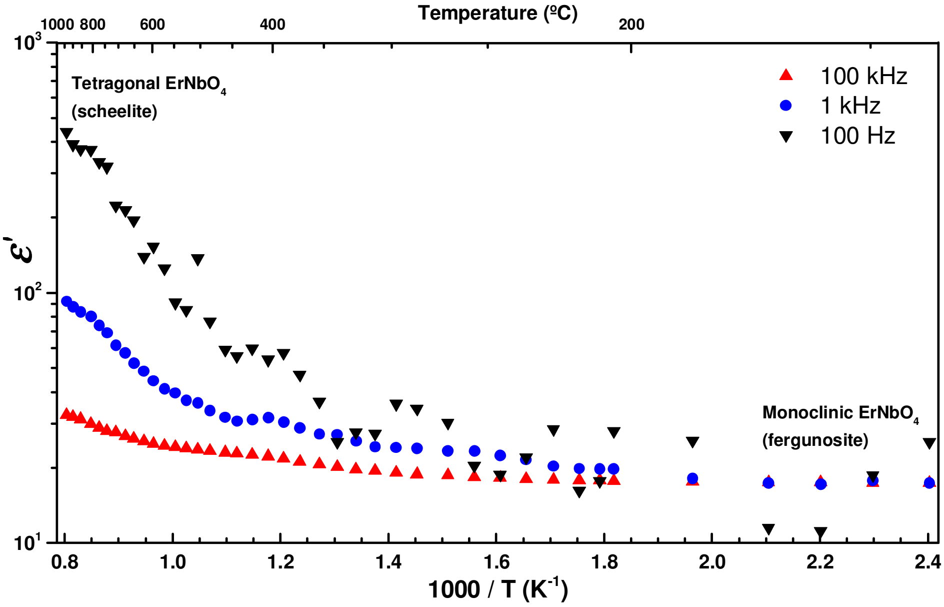

Figure 7.42 – Relative dielectric constant of the $ErNbO_4$ pellet, measured at different frequencies, from RT to 1000 ºC in air.

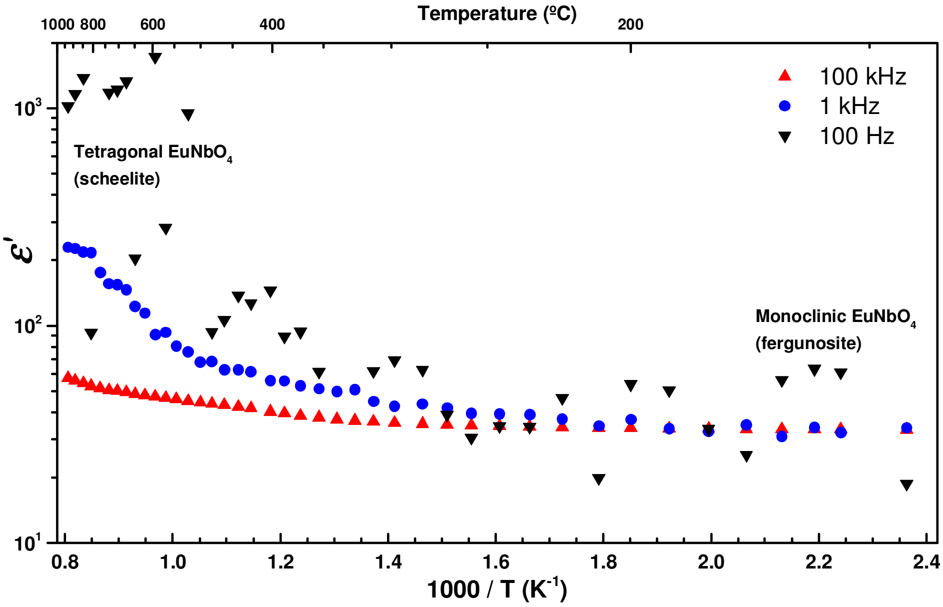

Figure 7.43 – Relative dielectric constant of the $EuNbO_4$ pellet, measured at different frequencies, from RT to 1000 ºC in air.

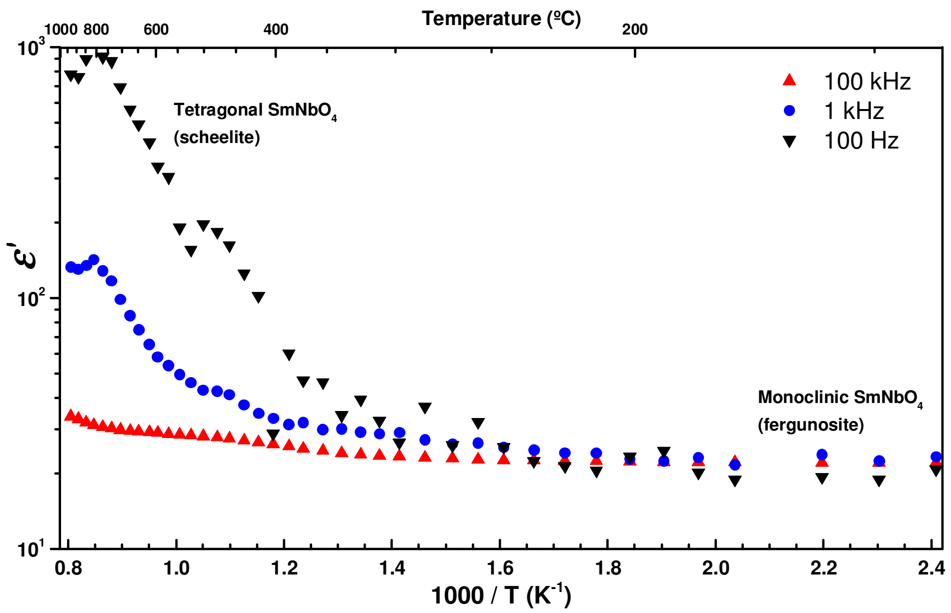

Figure 7.44 – Relative dielectric constant of the $SmNbO_4$ pellet, measured at different frequencies, from RT to 1000 ºC in air.

It can be observed that the relative dielectric constant follows a general trend for all the $RENbO_4$ samples, increasing with temperature from RT to 1000 ºC. At RT, the *ε'* of the $ErNbO_4$, $EuNbO_4$, $SmNbO_4$ pellets is respectively 56, 52 and 30 at 100 Hz, decreasing with the increase of frequency to 19, 33 and 22 at 100 kHz. While the phase change from monoclinic to tetragonal is not as evident in these dielectric constant results, as it is in the total conductivity, it is possible to see that from RT up to approximately 400 ºC the *ε'* increases only slightly, increasing at a faster rate for higher temperatures. At the highest temperatures (c.a. 1000 ºC) the *ε'* of the $ErNbO_4$, $EuNbO_4$, $SmNbO_4$ pellets for a frequency of 100 Hz is respectively 439, 1025 and 780 (more than an order of magnitude higher than at RT), but only 33, 57 and 34 at 100 kHz (less than the double comparing with RT). It is known that orientational polarization type shows high dependence with temperature, while ionic polarization type shows weak temperature dependence [231]. However, at very high temperatures the mobility of ions and molecules increase and thus the polarization is significantly facilitated. Additionally, the electron polarization is characterized by a rapid response to electric field variations, i.e. it has a weak frequency dependency [231], which is not observed in the $RENbO_4$ samples at high temperatures. Therefore, these results suggest that the dielectric behaviour of the $RENbO_4$ samples above 400 ºC is dominated by ionic polarization. The fact that these materials show a dielectric permittivity which is almost constant at high frequencies in a wide range of temperatures from 400 ºC to RT, but also down to 100 K, as reported by Graça *et al.* [184], may be technologically interesting for applications where assuring a stable operation under conditions of variable temperature is required.

7.2.6 A note on oxygen vacancies

During the study of the physical properties of the $RENbO_4$ samples, there were some observations that are noteworthy. After the synthesis, the $ErNbO_4$, $EuNbO_4$ and $SmNbO_4$ pellets, had a very uniform and homogeneous colour (pink, white and yellow respectively). However, after being subjected to some characterization techniques, such as Raman and PL spectroscopies, or electrical characterization at high temperatures, the samples tended to become darker and with an inhomogeneous look. Figure 7.45 illustrates the $ErNbO_4$ pellet right after being synthesized (at left) and after being analysed by Raman and PL spectroscopy.

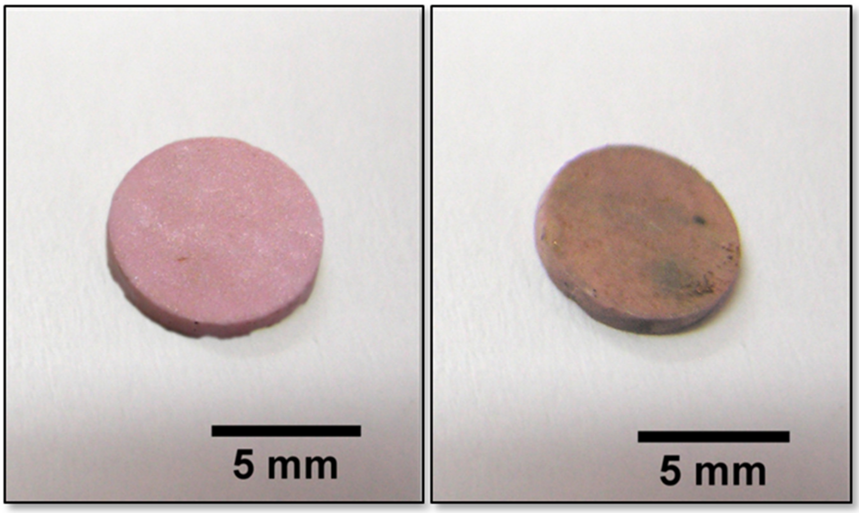

Figure 7.45 – Pictures of the $ErNbO_4$ pellet before (at left) and after (at right) laser irradiation.

Such effect was also observed in the other $RENbO_4$ pellets after being irradiated with a laser. Additionally, after an experiment (not shown) of electrical measurements at high temperature (up to 1200 °C), performed in an atmosphere with 5 % of H_2 and 95 % of N_2, the pellets became very dark. However, after being heat treated in air at 1400 °C all the samples recovered the original look and colour. A similar behaviour was also observed with the $EuNbO_4$ fibre which was transparent and colourless after being grown and became darker, with a brownish colour after being irradiated with a 325 nm laser during PL spectroscopy measurements (Figure 7.46). Similarly, in this case the fibre could recover the colourless look after being heat treated in air at 1400 °C. It is possible that heat treatments at lower temperatures could lead to the same result, but such study was not performed.

This type of photochromic behaviour is very likely due to the formation of oxygen vacancies, similarly to what is observed in other matrices [76,269], which are filled back again with O atoms when heat treated in air. Such observations were never reported for $RENbO_4$, but reveal the intrinsic nature and the ability of these materials to accommodate oxygen vacancies, similarly to what is observed in niobium oxides [76,269]. It is suggested that the NbO_6 octahedra (or NbO_4 tetrahedra, depending on the considered length of the Nb-O bonds), and the way they are linked between them, may also play an important role in this property. Furthermore, the existence of regions with oxygen vacancies, and therefore structural deformation and defects, along the crystalline structure of the samples, may justify the existence of at least two different RE^{3+} optically active centres observed in the PL spectroscopy measurements.

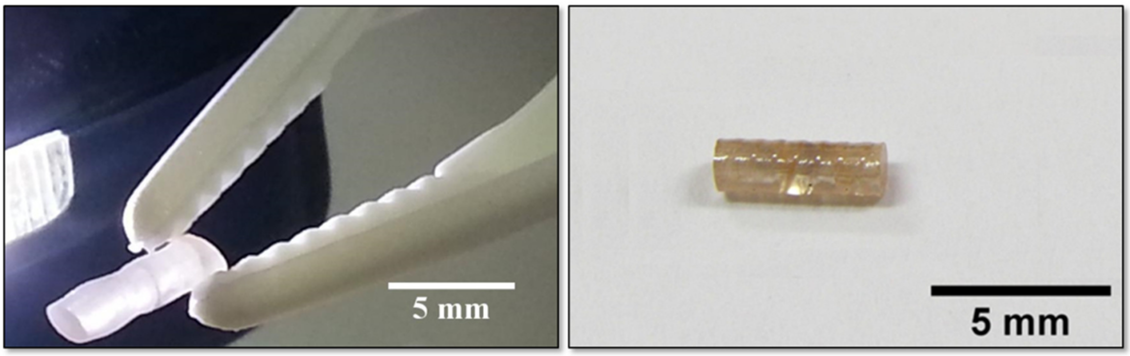

Figure 7.46 – Pictures of the $EuNbO_4$ fibre before (at left) and after (at right) laser irradiation.

7.3 Summary

In this chapter, it was intended to make a preliminary and explorative study of the physical properties of rare-earth orthoniobates. Hence, $ErNbO_4$, $EuNbO_4$ and $SmNbO_4$ fibres grown by the LFZ, and powders synthesized by the Pechini method, were prepared. The earliest analysis to the powders revealed the existence of the typical monoclinic phase (stable at RT) mixed with a metastable tetragonal phase which is probably stabilized due to grain size effects. Therefore, the powders were pressed into pellets and sintered at 1400 °C in order to increase the grain size and stabilize only the monoclinic phase.

These $RENbO_4$ fibres were characterized by SCXRD, revealing a very intense signal and well defined pattern (typical of a single-crystal), assigned to a referenced monoclinic structure but with slightly different lattice parameters, which are probably caused by tensions created during the growth process. Furthermore, the Raman spectra confirmed the existence of only the characteristic modes of such monoclinic structure. The SEM analysis of all three $RENbO_4$ revealed clear signs of single-crystalline samples, i.e. without grain boundaries and with some well oriented cracks along the fibres.

Regarding the $RENbO_4$ pellets, the acquired XRD patterns were very well defined and intense, and matched extremely well with the reference patterns of the typical monoclinic structure of these materials. The Raman spectroscopy also confirmed the characteristic vibrational modes of this structure. The SEM images of the pellets have shown highly coalesced grains, with two different types of morphologies (rounded and faceted), and with sizes ranging from 1 to 10 μm.

Photoluminescence studies were performed to all $RENbO_4$ samples, at different temperatures and with different excitation wavelengths. Typical intra-4*f* transitions of the trivalent rare-earth ions Er^{3+}, Eu^{3+} and Sm^{3+} were observed and assigned accordingly.

Particularly, the $ErNbO_4$ revealed intense green and red emission at 14 K when excited with 325 nm, undergoing a strong thermal quenching as the temperature increases up to RT. Also, when excited with 980 nm at cryogenic temperatures, the $ErNbO_4$ sample has shown very intense up-converting luminescence varying from red, to yellow to green, depending on the excitation power, by changing the relative intensity of the green and the red emission bands. Furthermore, it was interesting to observe that this sample quickly increased its temperature when excited with the IR laser, even at low powers, which would also lead to a variation of the relative intensities of the emission bands. The $EuNbO_4$ pellet also revealed the typical red/orange emission of this lanthanide ion (from the $^5D_0$ electronic state), when excited with a 325 nm laser, suffering a strong thermal quenching from 14 K to RT. Similarly, the $SmNbO_4$ pellet has shown a red emission at 14 K, as a result of the transitions coming from the $^4G_{5/2}$ level, when excited with 325 nm, and also at RT when excited with other wavelengths resonant with excited states of the ion (488 or 532 nm). Although the monoclinic structure of the $RENbO_4$ is described by having a RE atom in only one type of symmetry, in all the studied samples it was found that there are at least 3 different sites/environments of the respective trivalent lanthanide ion.

Impedance spectroscopy analysis was performed in air RT to 1000 ^{o}C, for all the $RENbO_4$ pellets, in order to verify the existence of reported protonic conductivity for this type of materials. Generally, all the samples revealed an increase of the total conductivity with temperature in almost 5 orders of magnitude, in concordance with similar works reported in literature. It was possible to observe, approximately between 400 and 600 ºC, a behaviour that was associated to the reversible phase transition from the monoclinic to the tetragonal crystalline structure of the $RENbO_4$ materials. The conductivity behaviour measured before the phase transition is associated to protonic conductivity, which in literature is commonly explained by the existence of oxygen vacancies through which OH^- molecules are transported. The dielectric permittivity measurements corroborated these results, showing typical ionic polarization dependency with temperature and frequency.

In fact, photochromic properties were observed in all samples after being irradiated with laser light, producing darkening of the colour. Such phenomenon was found to be reversible after heat treating the samples in air at high temperature, and therefore it was associated to the production of oxygen vacancies. It is suggested that the $RENbO_4$ materials can easily produce this type of defects, similarly to what happens in niobium oxides. The existence of such oxygen vacancies can explain the different environments of the RE optically active centres observed by PL spectroscopy.

Chapter 8

Final overview, conclusions and future work

8. Final overview, conclusions and future work

In this work, several fundamental characterization studies were presented, mostly in niobium oxides, but also on rare-earth orthoniobates. One of the main objectives in working with these materials was the opportunity to develop a new family of solid electrolytic capacitors based on niobium oxides, as an alternative to the current technology based on tantalum. Niobium oxides are reported to have higher dielectric constant and also higher ignition energy than tantalum oxide which, allied to the much lower price, represents an interesting technological asset. Additionally, niobium and tantalum are, from the chemical point of view, very similar which may facilitate the adaptation of an existing industrial production line of tantalum based capacitors.

The available literature on niobium oxides reveals that this is a complex metal oxide system, with many phases and polymorphs, and many works reporting contradictory or inconsistent information. Therefore, it should be emphasized that the review of the physical properties and state of art of niobium oxides, performed in the first chapter, is an important and solid groundwork for future research on these materials. Moreover, it was shown that this metal oxide system can lead to many different and interesting properties, making it a very versatile group of materials (but difficult to work with). More specifically, stoichiometry problems are one of the most common complications in niobium oxides and in many different niobates, where NbO_6 octahedra are typically the basic structural units.

Regarding the evolution of the research on niobium-based capacitors and the current state of the art, it was found that using niobium monoxide (instead of metallic Nb) as the anode of the capacitors would bring several advantages, mainly regarding the commonly reported problems with oxygen diffusion from the dielectric layer to the anode. Therefore, NbO was the starting material for many of the characterizations made during this work.

Hence, as described in chapter 4, NbO powders (that would be later used for the production of niobium capacitors), were pressed into pellets and heat treated in air at different temperatures. These samples were characterized by XRD and Raman spectroscopy revealing the presence of different niobium pentoxide polymorphs: the tetragonal phase T- Nb_2O_5, the monoclinic B- Nb_2O_5 and H- Nb_2O_5 phases. PL analysis has shown a broad and emission centre c.a. 2.25 eV in all samples, except for those treated at 900 ºC where the band was blue shifted. The temperature dependent PL analysis suggests the existence of two overlapped emitting centres. Impedance spectroscopy analyses performed to the sintered NbO pellets have shown a dielectric constant of ~25, at high frequencies, for the samples treated at 800 and 900 ºC, rising to ~55 for the samples treated at 1100 ºC (with the H-Nb_2O_5 polymorph). Additionally, the NbO pellets treated at 300 ºC, which had shown the existence of the crystalline phase of NbO (in XRD) and also traces of amorphous Nb_2O_5 (by Raman spectroscopy), revealed an extraordinary high dielectric constant (around 1100 at low frequencies and ~200 at high frequencies).

The observed dielectric behaviour registered in the NbO pellet treated at 300 ºC raised many questions, and therefore an *in-situ* XRD analysis as a function of temperature (from RT to 1100 ºC) was performed to NbO pressed anodes, as shown in chapter 5. It was observed that between 300 and 500 ºC the crystalline phase disappears giving rise to an amorphous phase before it starts to crystallize into the T-Nb_2O_5 phase for higher temperatures. *In-situ* Raman spectroscopy, performed in this range of temperatures has shown that the formed amorphous phase is a niobium pentoxide. This process is accompanied by a variation in a wide range of colours, which was concluded to be a consequence of optical interference caused by the formation of NbO/Nb_2O_5 core-shell structures, as demonstrated by SEM and *in-situ* reflectance spectroscopy. These observations justify the high capacitance values measured in the NbO pellets heat treated at 300 ºC, since a thin layer of dielectric (amorphous Nb_2O_5) is created by thermal oxidation.

With these important aspects in mind, the production of solid electrolytic capacitors based on niobium oxides, was therefore carried on in chapter 6. NbO powders were pressed, testing different densities, into the capacitor anodes, before being sintered in vacuum. XRD analysis revealed an undesired formation of a small amount of NbO_2 after sintering. Afterwards, the anodes were anodized using different forming voltages to create the dielectric layer of amorphous Nb_2O_5 around the NbO grains. In most cases, high values of capacitances were measured. By comparing the measured dielectric thicknesses from SEM analysis, and the electrical properties, it was suggested that an oxygen deficient niobium pentoxide must be formed in a non-controlled way, possibly related to the current used during the anodization, which depending on the magnitude can promote the oxygen diffusion from the dielectric into the anode. After testing the tempering process in air and in vacuum, at different temperatures, and measuring the electrical properties, it was concluded that tempering in vacuum produced the best results, since it increases the capacitance (which can be corrected afterwards by a re-forming process). Finally, the impregnation of MnO_2 (the cathode layer) was tested using two different pyrolysis temperatures (230 and 270 ^oC). While in both cases a good and homogeneous coverage of the niobium oxides grains was observed, at 270 ^oC mushroom shaped manganese oxide structures were produced at the surface of the anodes, which are undesirable because it may compromise the impregnation and adhesion of the conductive layers on the last stages of the production process. It is suggested that further tests should exist in order to achieve a final prototype of a niobium oxide based capacitor. Furthermore, it is also suggested the use of polypyrrole as the cathode layer, since it can offer significant advantages comparing to the MnO_2. Overall, niobium oxides seem to be suitable for the production of solid electrolytic capacitors. In fact niobium oxide based capacitors, produced by AVX, can be found in the market with maximum rated voltages of 10 V [243]. However, the development of capacitors operating at higher voltages may be limited by oxygen diffusion from the dielectric layer (Nb_2O_5) to the anode (NbO), which would lead to an increase of the conductivity and consequent failure of the capacitor.

However, besides the capacitors, niobium oxides have been showing also great potentiality in other technological applications that are worth to proceed with studies, most of them based on one important question that can lead to very different properties: oxygen vacancies.

This is the case of the reported photochromic properties of niobium oxides [269] and the synthesis of $Nb_{12}O_{29}$ thin films to be used as a transparent conductive oxide (TCO) [152]. Also, it should be emphasized one of the most interesting and hot topics to which niobium oxides are candidates: the memristors. In the case of niobium oxides, what may be a problem for the application in the solid electrolytic capacitors, i.e. the oxygen diffusion and variation of conductivity, can be the key factor to achieve a fully operational memristor. There are some, but still few, works that have been reported regarding resistive switching in niobium oxides (and other metal oxides) [38,131–143,270–273], and it seems clear that following this research topic is a great research opportunity. The synthesis of niobium oxides thin films and its electrical characterization is encouraged for future work. While the most common experimental techniques used to characterize memristive properties are based on cyclic voltammetry [273–276], i.e. recording hysteretic current-voltage profiles, Messerschmitt *et al.* [273] have done an interesting work showing that chronoamperometry and also bias-dependent resistive measurements can be powerful methods to understand the defect kinetics that give rise to the resistive switching behaviour.

The fact that $Nb_{12}O_{29}$ can be a TCO, can enable its application as an interface layer in OLEDs to facilitate the charge injection and extraction to and from the device [277,278]. Also in this context and inspired in reported works [108] regarding dye-sensitized solar cells using mesoporous Nb_2O_5 tubular structures as an alternative to TiO_2, it would be interesting to try using $Nb_{12}O_{29}$ instead (transparent and conductive) by performing a thermal treatment in a reducing atmosphere to the Nb_2O_5 mesoporous structure.

Therefore, future studies on niobium oxides focused in understanding and controlling the phase transformations, oxidations and oxygen vacancies are crucial to take advantage of the broad range of properties. It is suggested, for instance, that an *in-situ* Raman spectroscopy analysis (from RT to 1200 ^{o}C) should be performed to niobium oxides in different oxidizing and reducing atmospheres. Such experiment might help to understand the role of the oxygen vacancies on the vibrational modes of niobium oxides, thus allowing a better control of the stoichiometry of these materials. There is still much work to be done on these materials, not only on fundamental characterization, but also related with the synthesis of thin films and micro and nanostructures.

The research and development of different types of niobates, particularly alkali niobates, is often limited by the difficulties on the synthesis and phase stability. Many of such problems are related to niobium oxygen system and therefore it is believed that the fundamental characterizations of the niobium oxides presented and discussed in this work are an important contribution to better understand such niobates.

A preliminary study on rare-earth orthoniobates is presented in chapter 7. These materials have been reported for their interesting optical and electrical properties, and therefore $ErNbO_4$, $EuNbO_4$ and $SmNbO_4$ samples were synthesized. Hence, millimetric sized fibres were grown by LFZ, while powders were prepared by the Pechini method. In order to avoid metastable phases, the powders were pressed into pellets and heat treated at 1400 ^{o}C. The SCXRD analysis revealed that the $RENbO_4$ fibres had a single-crystalline nature (also suggested by SEM, where no grain boundaries were found), with measured lattice parameters slightly different from the reference data, possibly due to stress caused during the growth. The XRD analyses of $RENbO_4$ pellets have shown that only the expected monoclinic phase, typical from these materials, was detected.

PL studies revealed typical intra-4*f* transitions of the corresponding RE ion in all samples. With 980 nm photon excitation, at low temperatures, the $ErNbO_4$ pellet has shown strong red and green Er^{3+} emission bands, which absolute and relative intensities depend on the excitation power. It was also verified that even with low excitation power the temperature of the sample would increase resulting in different relative intensities of the red and green luminescence bands. PL and PLE studies were performed to $EuNbO_4$ samples, revealing an intense red luminescence which could be excited through many of the ladder-like excited states of Eu^{3+}. $SmNbO_4$ pellet has shown a low intensity red luminescence which could also be optically activated by almost all of the Sm^{3+} electronic levels. At low temperatures, all the $RENbO_4$ have shown more Stark lines than the maximum allowed number for one optically active centre, thus indicating that the RE ions are in more than one type of lattice site and/or environment. Temperature dependent PL studies have shown that all the $RENbO_4$ samples undergo a strong thermal quenching from 14 K to RT. Additionally, in the case of the $EuNbO_4$ fibre it was possible to verify that some Stark lines would suffer a faster thermal quenching than others, confirming the existence of multiple optically active centres.

An increase of the electrical conductivity, in almost 5 orders of magnitude, was observed for all the $RENbO_4$, from RT to 1000 ^{o}C, in concordance with similar works reported in literature. The observed behaviour is typically associated to protonic conductivity (predominant at temperature below 700 ^{o}C) by the hopping of OH^- groups through oxygen vacancies. In future works, the presence and role of such hydrogen bonded complex can be investigated through absorption spectroscopy in the IR region, and also by electron paramagnetic resonance (EPR). Photochromic properties were observed in all samples and were associated to the production of oxygen vacancies after being irradiated with laser light. Such phenomenon was found to be reversible after heat treating in air. The existence of such oxygen vacancies can explain the different environments of the RE optically active centres observed by PL spectroscopy.

PLE and lifetime measurements on $RENbO_4$ samples would definitely be essential to better understand the optical properties of these materials and confirm the existence of different active optical centres. PL studies at higher temperatures, before and after phase transition, could also be interesting. The conductivity measurements at high temperatures of $RENbO_4$ should be further studied using different atmospheres so it is possible to quantify the contributions of electronic, protonic and ionic conductivities, and understand how they are influenced and how can they be controlled by the processing techniques and parameters.

From a technological application point of view, the $ErNbO_4$ can be a particularly interesting material for the production of nanothermometers and photo-thermal medical therapy [279–282]. This can be achieved by the synthesis and bio-functionalization of

$ErNbO_4$ nanoparticles which would bond to cancer cells. Because it was observed that the $ErNbO_4$ was easily heated under 980 nm radiation, with an up-converting luminescence which spectrum is dependent on the temperature, $ErNbO_4$ nanoparticles could simultaneously perform therapy (through heat) and bio-imaging (through the visible luminescence), but also act as a nanothermometer (based on red/green intensity ratio of the intraionic transitions). For such application be viable, the up-converting luminescence should be detectable at RT and not only at cryogenic temperatures, and therefore more studies regarding the synthesis and eventually doping of the $ErNbO_4$ should take place in order to optimize the intensity of the PL intensity. Moreover, additional studies on the nanoparticles toxicity should be envisaged.

References

References

[1] Rose H 1844 Ueber die Zusammensetzung der Tantalite und ein im Tantalite von Baiern enthaltenes neues Metall *Annalen der Physik* **139** 317–41

[2] Rose H 1845 On two new metals, pelopium and niobium, discovered in the bavarian tantalites *Philosophical Magazine Series 3* **26** 179–81

[3] Hermann R 1847 Untersuchungen über das Ilmenium *Journal für Praktische Chemie* **40** 457–80

[4] Kobell F V 1860 Ueber eine eigenthümliche Säure, Diansäure, in der Gruppe der Tantal- und Niob- verbindungen *Journal für Praktische Chemie* **79** 291–303

[5] De Marignac J C G 1866 *Recherches sur les combinaisons du niobium* (Genève: The Swiss National Library)

[6] De Marignac J C G 1866 *Recherches sur les combinaisons du tantale* (Genéve: The Swiss National Library)

[7] Rayner-Canham G and Zheng Z 2008 Naming elements after scientists: an account of a controversy *Foundations of Chemistry* **10** 13–8

[8] British Geological Survey (BGS). Niobium - Tantalum. http://www.bgs.ac.uk/downloads/start.cfm?id=2033 (access April 23, 2014)

[9] Luisa Moreno, Jacob Securities Inc. Rare Metals Report on Tantalum & Niobium by Jacob Securities (July 19, 2011)

[10] Tantalum-Niobium International Study Center. Tantalum - Raw Materials and Processing http://tanb.org/tantalum (access April 23, 2014)

[11] Tantalum-Niobium International Study Center. Niobium - Raw Materials and Processing http://tanb.org/niobium(access April 23, 2014)

[12] Ayanda O S and Adekola F A 2011 A Review of Niobium-Tantalum Separation in Hydrometallurgy *Journal of Minerals and Materials Characterization and Engineering* **10** 245

[13] Austrian Mint. 2012. 25 Euro Silver Niobium Coins. www.muenzeoesterreich.at (access September 3, 2012)

[14] Wolfram Alpha LLC. 2014. Wolfram|Alpha. www.wolframalpha.com/input/?i=niobium%20and%20tantalum%20price%20over%20time (access April 23, 2014).

[15] Ross Sidney D 1962 Electrolytic capacitor. Patent US3067367 A

[16] Schwartz N, Gresh M and Karlik S 1961 Niobium Solid Electrolytic Capacitors *J. Electrochem. Soc.* **108** 750–8

[17] Shtasel A and Knight H T 1961 An Investigation of Columbium as an Electrolytic Capacitor Metal *J. Electrochem. Soc.* **108** 343–7

[18] Kathirgamanathan P and Ravichandran S 1995 Conducting polymer cathodes for high-frequency operable electrolytic niobium capacitors *Synthetic Metals* **74** 165–70

[19] Pozdeev Y 1998 Reliability comparison of tantalum and niobium solid electrolytic capacitors *Quality and Reliability Engineering International* **14** 79–82

[20] Fife J A, Liu J J and Steele R W 2000 Niobium powders and niobium electrolytic capacitors. US Patent 6165623

[21] Fife J A 2000 Nitrided niobium powders and niobium electrolytic capacitors. US Patent 6051044

[22] Kumagai N, Koishikawa Y, Komaba S and Koshiba N 1999 Thermodynamics and Kinetics of Lithium Intercalation into Nb2O5 Electrodes for a 2 V Rechargeable Lithium Battery *J. Electrochem. Soc.* **146** 3203–10

[23] De Holanda J N F, Strecker K, Pinatti D G and Gomes U U 1999 Study on sintered anodes of Nb-Ta-Al aluminothermic alloys *Int. J. Refract. Met. H.* **17** 253–7

[24] Holanda J N F, Gomes U U and Strecker K 1999 Characterization of Prealloyed Nb-Ta-Al Powders for Capacitors *Materials Characterization* **43** 235–42

[25] Qiu Y, Smyth D and Kimmel J 2002 The stabilization of niobium-based solid electrolyte capacitors *Act. Passive Electron. Compon.* **25** 201–9

[26] Fife J A 2003 Method of making a capacitor anode of a pellet of niobium oxide. Patent US6527937 B2

[27] Fife J A 2003 Methods to make capacitors containing a partially reduced niobium metal oxide. Patent US6592740 B2

[28] Fonville T J, Higgins B J, Motchenbacher C A and Robison J W 2007 Production of high-purity niobium monoxide and capacitor production therefrom. Patent US7157073 B2

[29] Freeman Y, Lessner P M, Poltorak J and Hahn R S 2008 NbO Capacitors With Improved Performance And Higher Working Voltages. Patent US20080254269 A1

[30] Karnik T 2009 Ceramic Powder For Use In Forming An Anode Of An Electrolytic Capacitor

[31] Störmer H, Weber A, Fischer V, Ivers-Tiffée E and Gerthsen D 2009 Anodically formed oxide films on niobium: Microstructural and electrical properties *J. Eur. Ceram. Soc.* **29** 1743–53

[32] Jones B A, McCracken C, Fife J, Margerison I and Karnik T 2010 Powder modification in the manufacture of solid state capacitor anodes. US Patent 7824452

[33] Le Viet A, Reddy M V, Jose R, Chowdari B V R and Ramakrishna S 2011 Electrochemical properties of bare and Ta-substituted Nb2O5 nanostructures *Electrochimica Acta* **56** 1518–28

[34] Zednicek T, Zednicek S and Sita Z 2002 Niobium Oxide Technology Roadmap *AVX Corporation*

[35] Tauseef Tanvir M, Aoki Y and Habazaki H 2009 Formation of porous niobium films by oblique angle deposition: Influence of substrate morphology *Thin Solid Films* **517** 6711–6

[36] Brauer G 1941 Die Oxyde des Niobs *Zeitschrift für anorganische und allgemeine Chemie* **248** 1–31

[37] Ling H W and Kolski T L 1962 Niobium Solid Electrolyte Capacitors *J. Electrochem. Soc.* **109** 69–70

[38] Hiatt W R and Hickmott T W 1965 Bistable switching in niobium oxide diodes *Applied Physics Letters* **6** 106

[39] Cox B and Johnston T 1963 The Oxidation and Corrosion of Niobium (Columbium) *Trans. AIME* **227**

[40] Gatehouse B M and Wadsley A D 1964 The crystal structure of the high temperature form of niobium pentoxide *Acta Cryst* **17** 1545–54

[41] Bowman A L, Wallace T C, Yarnell J L and Wenzel R G 1966 The crystal structure of niobium monoxide *Acta Cryst* **21** 843–843

[42] Schäfer H, Gruehn R and Schulte F 1966 The Modifications of Niobium Pentoxide *Angewandte Chemie International Edition in English* **5** 40–52

[43] Fromm E 1968 Thermodynamische beschreibung der festen lösung von kohlenstoff, stickstoff und sauerstoff in niob und tantal *Journal of the Less Common Metals* **14** 113–25

[44] Allpress J G, Sanders J V and Wadsley A D 1968 Electron microscopy of high-temperature Nb2O5 and related phases *physica status solidi (b)* **25** 541–50

[45] Pollard Jr E R 1968 *Electronic properties of niobium monoxide* (Massachusetts Institute of Technology)

[46] Bach D 2009 *EELS investigations of stoichiometric niobium oxides and niobium-based capacitors* (Karlsruhe: Universität Karlsruhe, Fakultät für Physik)

[47] Bach D, Störmer H, Schneider R, Gerthsen D and Verbeeck J 2006 EELS Investigations of Different Niobium Oxide Phases *Microscopy and Microanalysis* **12** 416–23

[48] Bach D, Störmer H, Schneider R and Gerthsen D 2007 Quantitative EELS Analysis of Niobium Oxides *MAM* **13**

[49] Bach D, Störmer H, Schneider R, Gerthsen D and Sigle W 2007 EELS Investigations of Reference Niobium Oxides and Anodically Grown Niobium Oxide Layers *Microscopy and Microanalysis* **13** 1274–5

[50] Bach D, Schneider R, Gerthsen D, Verbeeck J and Sigle W 2009 EELS of Niobium and Stoichiometric Niobium-Oxide Phases—Part I: Plasmon and Near-Edges Fine Structure *Microsc Microanal* **15** 505

[51] Bach D, Schneider R and Gerthsen D 2009 EELS of Niobium and Stoichiometric Niobium-Oxide Phases—Part II: Quantification *Microsc Microanal* **15** 524

[52] Elliott R P 1960 Columbium-oxygen system *Trans. Am. Soc. Met.* **52** 990–1014

[53] Massalski T B and International A S M 1990 *Binary Alloy Phase Diagrams* ed H Okamoto (Materials Park, Ohio: Asm Intl)

[54] Shamrai V F, Blagoveshchenski Y V, Gordeev A S, Mitin A V and Drobinova I A 2007 Structural states and electrical conductivity of oxidized niobium nanopowders *Russ. Metall.* **2007** 322–6

[55] Delheusy M, Stierle A, Kasper N, Kurta R P, Vlad A, Dosch H, Antoine C, Resta A, Lundgren E and Andersen J 2008 X-ray investigation of subsurface interstitial oxygen at Nb/oxide interfaces *Applied Physics Letters* **92** 101911

[56] Kurmaev E Z, Moewes A, Bureev O G, Nekrasov I A, Cherkashenko V M, Korotin M A and Ederer D L 2002 Electronic structure of niobium oxides *Journal of Alloys and Compounds* **347** 213–8

[57] Hulm J K, Jones C K, Hein R A and Gibson J W 1972 Superconductivity in the TiO and NbO systems *Journal of Low Temperature Physics* **7** 291–307

[58] Karnik T 2010 Doped ceramic powder for use in forming capacitor anodes. Patent US 7760487 B2

[59] Vezzoli G C 1982 Electrical properties of NbO2 and Nb2O5 at elevated temperature in air and flowing argon *Phys. Rev. B* **26** 3954

[60] Passier F, Wouters Y, Galerie A and Caillet M 2001 Thermal Oxidation of Metallic Niobium by Water Vapor *Oxid. Met.* **55** 153–63

[61] Terao N 1963 Structures des Oxydes de Niobium *Jpn. J. Appl. Phys.* **2** 156–74

[62] Cheetham A K and Rao C N R 1976 A neutron diffraction study of niobium dioxide *Acta Crystallogr B Struct Crystallogr Cryst Chem* **32** 1579–80

[63] Zhao Y, Zhang Z and Lin Y 2004 Optical and dielectric properties of a nanostructured NbO2 thin film prepared by thermal oxidation *J. Phys. D: Appl. Phys.* **37** 3392–5

[64] Rimai D S and Sladek R J 1978 Pressure dependences of the elastic constants of semiconducting NbO_{2} at 296 K *Phys. Rev. B* **18** 2807

[65] Gervais F and Kress W 1985 Lattice dynamics of oxides with rutile structure and instabilities at the metal-semiconductor phase transitions of NbO2 and VO2 *Phys. Rev. B* **31** 4809

[66] Helali S, Abdelghani A, Hafaiedh I, Martelet C, Prodromidis M I, Albanis T and Jaffrezic-Renault N 2008 Functionalization of niobium electrodes for the construction of impedimetric biosensors *Materials Science and Engineering: C* **28** 826–30

[67] Lee S, Yoon H, Yoon I and Kim B 2012 Single Crystalline NbO2 Nanowire Synthesis by Chemical Vapor Transport Method *Bull. Korean Chem. Soc* **33** 839

[68] Sasaki K and Maier J 2000 Re-analysis of defect equilibria and transport parameters in Y2O3-stabilized ZrO2 using EPR and optical relaxation *Solid State Ionics* **134** 303–21

[69] Reznichenko L A, Akhnazarova V V, Shilkina L A, Razumovskaya O N and Dudkina S I 2009 Invar effect in n-Nb2O5, αht-Nb2O5, and L-Nb2O5 *Crystallogr. Rep.* **54** 483–91

[70] Valencia-Balvín C, Pérez-Walton S, Dalpian G M and Osorio-Guillén J M 2014 First-principles equation of state and phase stability of niobium pentoxide *Computational Materials Science* **81** 133–40

[71] Soares M R N, Leite S, Nico C, Peres M, Fernandes A J S, Graça M P F, Matos M, Monteiro R, Monteiro T and Costa F M 2011 Effect of processing method on physical properties of Nb2O5 *J. Eur. Ceram. Soc.* **31** 501–6

[72] Nico C, Soares M R N, Rodrigues J, Matos M, Monteiro R, Graça M P F, Valente M A, Costa F M and Monteiro T 2011 Sintered NbO Powders for Electronic Device Applications *J. Phys. Chem. C* **115** 4879–86

[73] Graça M P F, Meireles A, Nico C and Valente M A 2013 Nb2O5 nanosize powders prepared by sol–gel – Structure, morphology and dielectric properties *Journal of Alloys and Compounds* **553** 177–82

[74] Viet A L, Reddy M V, Jose R, Chowdari B V R and Ramakrishna S 2010 Nanostructured Nb2O5 Polymorphs by Electrospinning for Rechargeable Lithium Batteries *J. Phys. Chem. C* **114** 664–71

[75] Le Viet A, Jose R, Reddy M V, Chowdari B V R and Ramakrishna S 2010 Nb2O5 Photoelectrodes for Dye-Sensitized Solar Cells: Choice of the Polymorph *J. Phys. Chem. C* **114** 21795–800

[76] Brayner R and Bozon-Verduraz F 2003 Niobium pentoxide prepared by soft chemical routes: morphology, structure, defects and quantum size effect *Phys. Chem. Chem. Phys.* **5** 1457–66

[77] Gruehn R 1966 Eine weitere neue Modifikation des niobpentoxids *Journal of the Less Common Metals* **11** 119–26

[78] Hibst H and Gruehn R 1978 Weitere neue Nb2O5-Modifikationen, metastabile Oxidationsprodukte von NbOx-Phasen (2, 4 *Zeitschrift für anorganische und allgemeine Chemie* **442** 49–78

[79] Meyer B and Gruehn R 1982 Investigation of Metastable Niobium Oxides by Transmission Electron Microscopy1 *Comments on Inorganic Chemistry* **1** 361–77

[80] Stoneham A M and Durham P J 1973 The ordering of crystallographic shear planes: Theory of regular arrays *Journal of Physics and Chemistry of Solids* **34** 2127–35

[81] Mrowec S 1978 On the defect structure in nonstoichiometric metal oxides *Ceramurgia International* **4** 47–58

[82] Anderson J S, Browne J M, Cheetham A K, Dreele R V, Hutchison J L, Lincoln F J, Bevan D J M and Straehle J 1973 Point Defects and Extended Defects in Niobium Oxides *Nature* **243** 81–3

[83] Iijima S, Kimura S and Goto M 1974 High-resolution microscopy of nonstoichiometric $Nb_{22}O_{54}$ crystals: point defects and structural defects *Acta Crystallographica Section A* **30** 251–7

[84] Iijima S, Kimura S and Goto M 1973 Direct observation of point defects in $Nb_{12}O_{29}$ by high-resolution electron microscopy *Acta Crystallographica Section A* **29** 632–6

[85] Dhawan S, Dhawan T and Vedeshwar A G 2014 Growth of Nb2O5 quantum dots by physical vapor deposition *Materials Letters* **126** 32–5

[86] Tamura S 1972 High-pressure phase research on Nb2O5 *J Mater Sci* **7** 298–302

[87] Madelung O, Rössler U and Schulz M 2000 *Non-Tetrahedrally Bonded Binary Compounds II* vol 41D (Berlin/Heidelberg: Springer-Verlag)

[88] Zibrov I P, Filonenko V P, Werner P-E, Marinder B-O and Sundberg M 1998 A New High-Pressure Modification of Nb2O5 *Journal of Solid State Chemistry* **141** 205–11

[89] Jehng J M and Wachs I E 1991 Structural chemistry and Raman spectra of niobium oxides *Chem. Mat.* **3** 100–7

[90] Nowak I and Ziolek M 1999 Niobium Compounds: Preparation, Characterization, and Application in Heterogeneous Catalysis *Chemical Reviews* **99** 3603–24

[91] Sá A I de, Rangel C M and Skeldon P 2006 Semiconductive Properties of Anodic Niobium Oxides *Port. Electrochim. Acta* **24** 305–11

[92] De Filho D A B, Franco D W, Filho P P A and Alves O L 1998 Niobia films: surface morphology, surface analysis, photoelectrochemical properties and crystallization process *Journal of Materials Science* **33** 2607–16

[93] Schultze J W and Lohrengel M M 2000 Stability, reactivity and breakdown of passive films. Problems of recent and future research *Electrochimica Acta* **45** 2499–513

[94] Fischer V, Stormer H, Gerthsen D, Stenzel M, Zillgen H and Ivers-Tiffee E 2003 Niobium as new material for electrolyte capacitors with nanoscale dielectric oxide layers *Proceedings of the 7th International Conference on Properties and Applications of Dielectric Materials (ICPADM 2003)* (Nagoya (Japan)) pp 1134–7 vol.3

[95] Cavigliasso G E, Esplandiu M J and Macagno V A 1998 Influence of the forming electrolyte on the electrical properties of tantalum and niobium oxide films: an EIS comparative study *Journal of applied electrochemistry* **28** 1213–9

[96] Macek M and Orel B 1998 Electrochromism of sol-gel derived niobium oxide films *Solar Energy Materials and Solar Cells* **54** 121–30

[97] Schäfer H, Bergner D and Gruehn R 1969 Beiträge zur Chemie der Elemente Niob und Tantal. LXXI. Die thermodynamische Stabilität der sieben zwischen 2,00 und 2,50 O/Nb existierenden Phasen *Z. anorg. allg. Chem.* **365** 31–50

[98] Zednicek T and Vrana B Tantalum and Niobium technology roadmap *AVX Corporation*

[99] Kukli K, Ritala M and Leskelä M 2001 Development of Dielectric Properties of Niobium Oxide, Tantalum Oxide, and Aluminum Oxide Based Nanolayered Materials *J. Electrochem. Soc.* **148** F35–41

[100] Aegerter M A 2001 Sol–gel niobium pentoxide: A promising material for electrochromic coatings, batteries, nanocrystalline solar cells and catalysis *Solar energy materials and solar cells* **68** 401–22

[101] Maruyama T and Arai S 1993 Electrochromic properties of niobium oxide thin films prepared by radio-frequency magnetron sputtering method *Applied physics letters* **63** 869–70

[102] Özer N, Rubin M D and Lampert C M 1996 Optical and electrochemical characteristics of niobium oxide films prepared by sol-gel process and magnetron sputtering A comparison *Solar Energy Materials and Solar Cells* **40** 285–96

[103] Pawlicka A, Atik M and Aegerter M A 1997 Synthesis of multicolor Nb2O5 coatings for electrochromic devices *Thin Solid Films* **301** 236–41

[104] Costa E D, Avellaneda C O and Pawlicka A 2001 Alternative Nb2O5-TiO2 thin films for electrochromic devices *Journal of Materials Science* **36** 1407–10

[105] Huang Y, Zhang Y and Hu X 2003 Structural, morphological and electrochromic properties of Nb2O5 films deposited by reactive sputtering *Solar Energy Materials and Solar Cells* **77** 155–62

[106] Pehlivan E, Tepehan F Z and Tepehan G G 2003 Comparison of optical, structural and electrochromic properties of undoped and WO3-doped Nb2O5 thin films *Solid State Ionics* **165** 105–10

[107] Romero R, Dalchiele E A, Martín F, Leinen D and Ramos-Barrado J R 2009 Electrochromic behaviour of Nb2O5 thin films with different morphologies obtained by spray pyrolysis *Solar Energy Materials and Solar Cells* **93** 222–9

[108] Abdul Rani R, Zoolfakar A S, Subbiah J, Ou J Z and Kalantar-zadeh K Highly ordered anodized Nb2O5 nanochannels for dye-sensitized solar cells *Electrochemistry Communications*

[109] Barea E, Xu X, González-Pedro V, Ripollés-Sanchis T, Fabregat-Santiago F and Bisquert J 2011 Origin of efficiency enhancement in Nb2O5 coated titanium dioxide nanorod based dye sensitized solar cells *Energy Environ. Sci.* **4** 3414–9

[110] Tanabe K 2003 Catalytic application of niobium compounds *Catalysis Today* **78** 65–77

[111] Fan M-Q, Sun L-X, Zhang Y, Xu F, Zhang J and Chu H 2008 The catalytic effect of additive Nb2O5 on the reversible hydrogen storage performances of LiBH4–MgH2 composite *International Journal of Hydrogen Energy* **33** 74–80

[112] Kurioka N, Watanabe D, Haneda M, Shimanouchi T, Mizushima T, Kakuta N, Ueno A, Hanaoka T and Sugi Y 1993 Preparation of niobium oxide films as a humidity sensor *Catalysis Today* **16** 495–501

[113] Choi J, Lim J H, Rho S, Jahng D, Lee J and Kim K J 2008 Nanoporous niobium oxide for label-free detection of DNA hybridization events *Talanta* **74** 1056–9

[114] Eisenbarth E, Velten D, Müller M, Thull R and Breme J 2006 Nanostructured niobium oxide coatings influence osteoblast adhesion *Journal of Biomedical Materials Research Part A* **79** 166–75

[115] Velten D, Eisenbarth E, Schanne N and Breme J 2004 Biocompatible Nb2O5 thin films prepared by means of the sol–gel process *Journal of Materials Science: Materials in Medicine* **15** 457–61

[116] Ramírez G, Rodil S E, Arzate H, Muhl S and Olaya J J 2011 Niobium based coatings for dental implants *Applied Surface Science* **257** 2555–9

[117] Cardinal T, Fargin E, Le Flem G and Leboiteux S 1997 Correlations between structural properties of Nb2O5-NaPO3-Na2B4O7 glasses and non-linear optical activities *Journal of non-crystalline solids* **222** 228–34

[118] Praveena R, Venkatramu V, Babu P and Jayasankar C K 2008 Fluorescence spectroscopy of Sm3+ ions in P2O5-PbO-Nb2O5 glasses *Physica. B, Condensed matter* **403** 3527–34

[119] Sanghi S, Rani S, Agarwal A and Bhatnagar V 2010 Influence of Nb2O5 on the structure, optical and electrical properties of alkaline borate glasses *Materials Chemistry and Physics* **120** 381–6

[120] Graça M P F, Valente M A and Ferreira Da Silva M G 2006 The electric behavior of a lithium-niobate-phosphate glass and glass-ceramics *J Mater Sci* **41** 1137–44

[121] Lin H, Jiang S, Wu J, Song F, Peyghambarian N and Pun E Y B 2003 Er3+ doped Na2O–Nb2O5–TeO2 glasses for optical waveguide laser and amplifier *Journal of Physics D: Applied Physics* **36** 812

[122] Aquino F T, Ferrari J L, Ribeiro S J L, Ferrier A, Goldner P and Goncalves R R 2013 Broadband NIR emission in novel sol–gel Er^{3+}-doped SiO_2–Nb_2 O_5 glass ceramic planar waveguides for photonic applications *Optical Materials* **35** 387–96

[123] Eckert J, Reichert K, Schnitter C and Seyeda H Processing of columbite-tantalite ores and concentrates for niobium and niobium compounds in electronic applications

[124] Chua L O 1971 Memristor-The missing circuit element *IEEE Transactions on Circuit Theory* **18** 507–19

[125] Strukov D B, Snider G S, Stewart D R and Williams R S 2008 The missing memristor found *Nature* **453** 80–3

[126] Yang J J, Strukov D B and Stewart D R 2013 Memristive devices for computing *Nat Nano* **8** 13–24

[127] Jo S H, Chang T, Ebong I, Bhadviya B B, Mazumder P and Lu W 2010 Nanoscale Memristor Device as Synapse in Neuromorphic Systems *Nano Lett.* **10** 1297–301

[128] Liu X, Sadaf S M, Son M, Park J, Shin J, Lee W, Seo K, Lee D and Hwang H 2012 Co-Occurrence of Threshold Switching and Memory Switching in Cells for Crosspoint Memory Applications *Electron Device Letters, IEEE* **33** 236–8

[129] Linn E, Rosezin R, Kügeler C and Waser R 2010 Complementary resistive switches for passive nanocrossbar memories *Nature materials* **9** 403–6

[130] Rosezin R, Linn E, Nielen L, Kugeler C, Bruchhaus R and Waser R 2011 Integrated complementary resistive switches for passive high-density nanocrossbar arrays *Electron Device Letters, IEEE* **32** 191–3

[131] Sawa A 2008 Resistive switching in transition metal oxides *Materials Today* **11** 28–36

[132] Yang J J, Zhang M-X, Strachan J P, Miao F, Pickett M D, Kelley R D, Medeiros-Ribeiro G and Williams R S 2010 High switching endurance in TaOx memristive devices *Applied Physics Letters* **97** 232102

[133] Lee M-J, Lee C B, Lee D, Lee S R, Chang M, Hur J H, Kim Y-B, Kim C-J, Seo D H and Seo S 2011 A fast, high-endurance and scalable non-volatile memory device made from asymmetric Ta2O5- x/TaO2- x bilayer structures *Nature materials* **10** 625–30

[134] Chen Y-S, Lee H-Y, Chen P-S, Chen W-S, Tsai K-H, Gu P-Y, Wu T-Y, Tsai C-H, Rahaman S Z and Lin Y-D 2014 Novel Defects-Trapping TaOX/HfOX RRAM With Reliable Self-Compliance, High Nonlinearity, and Ultra-Low Current

[135] Liu X, Sadaf S M, Park S, Kim S, Cha E, Lee D, Jung G-Y and Hwang H 2013 Complementary Resistive Switching in Niobium Oxide-Based Resistive Memory Devices *Electron Device Letters, IEEE* **34** 235–7

[136] Grishin A M, Velichko A A and Jalalian A 2013 Nb2O5 nanofiber memristor *Applied Physics Letters* **103** 053111

[137] Sadaf S M, Liu X, Son M, Park S, Choudhury S H, Cha E, Siddik M, Shin J and Hwang H 2012 Highly uniform and reliable resistance switching properties in bilayer WOx/NbOx RRAM devices *physica status solidi (a)* **209** 1179–83

[138] Kundozerova T V, Grishin A M, Stefanovich G B and Velichko A A 2012 Anodic Nb2O5 Nonvolatile RRAM *IEEE Transactions on Electron Devices* **59** 1144–8

[139] Liu X, Sadaf S M, Son M, Shin J, Park J, Lee J, Park S and Hwang H 2011 Diode-less bilayer oxide (WOx–NbOx) device for cross-point resistive memory applications *Nanotechnology* **22** 475702

[140] Jo Y, Sim H, Hwang H, Ahn K and Jung M-H 2010 Reverse resistance switching in polycrystalline Nb2O5 films *Thin Solid Films* **518** 5676–8

[141] Hyunjun Sim, Dooho Choi, Dongsoo Lee, Sunae Seo, Myong-Jae Lee, In-Kyeong Yoo and Hyunsang Hwang 2005 Resistance-switching Characteristics of polycrystalline Nb2O5 for nonvolatile memory application *IEEE Electron Device Letters* **26** 292–4

[142] Mitin A, Shamray V and Gordeev A 2009 Effects of resistance switching in niobium oxides: Metastable nanochannels *Bulletin of the Russian Academy of Sciences: Physics* **73** 125–8

[143] Baek H, Lee C, Choi J and Cho J 2013 Nonvolatile Memory Devices Prepared from Sol–Gel Derived Niobium Pentoxide Films *Langmuir* **29** 380–6

[144] Rani R A, Zoolfakar A S, O'Mullane A P, Austin M W and Kalantar-Zadeh K 2014 Thin films and nanostructures of niobium pentoxide: fundamental properties, synthesis methods and applications *J. Mater. Chem. A* **2** 15683

[145] Roberts M W, Thomas J M, Anderson J S and Tilley R J D 2007 Crystallographic shear and non-stoicheiometry *Surface and Defect Properties of Solids: Volume 3*

[146] Iijima S 1973 Direct observation of lattice defects in *H* -Nb_2O_5 by high resolution electron microscopy *Acta Crystallographica Section A* **29** 18–24

[147] Niebuhr J 1966 Die niederen Oxide des Niobs *Journal of the Less Common Metals* **11** 191–203

[148] Kimura S 1973 Phase equilibria in the system NbO2 - Nb2O5: Phase relations at 1300 and 1400° C and related thermodynamic treatment *Journal of Solid State Chemistry* **6** 438–49

[149] Marucco J F 1974 Thermodynamic study of the system NbO2-Nb2O5 at high temperature *Journal of Solid State Chemistry* **10** 211–8

[150] Marucco J F 1979 Electrical resistance and defect structure of stable and metastable phases of the system Nb12O29–Nb2O5 between 800 and 1100 °C *The Journal of Chemical Physics* **70** 649–54

[151] McQueen T, Xu Q, Andersen E N, Zandbergen H W and Cava R J 2007 Structures of the reduced niobium oxides Nb12O29 and Nb22O54 *Journal of Solid State Chemistry* **180** 2864–70

[152] Ohsawa T, Okubo J, Suzuki T, Kumigashira H, Oshima M and Hitosugi T 2011 An n-type transparent conducting oxide: Nb12O29 *The Journal of Physical Chemistry C* **115** 16625–9

[153] Waldron J E L, Green M A and Neumann D A 2004 Structure and electronic properties of monoclinic Nb12O29 *Journal of Physics and Chemistry of Solids* **65** 79–86

[154] Cava R J, Batlogg B, Krajewski J J, Gammel P, Poulsen H F, Peck W F and Rupp L W 1991 Antiferromagnetism and metallic conductivity in Nb12O29 *Nature* **350** 598–600

[155] Waldron J E L, Green M A and Neumann D A 2001 Charge and Spin Ordering in Monoclinic Nb12O29 *Journal of the American Chemical Society* **123** 5833–4

[156] Xu J, Jarlborg T and Freeman A 1989 Self-consistent band structure of the rutile dioxides NbO2, RuO2, and IrO2 *Phys. Rev., B Condens. Matter* **40** 7939–47

[157] Ikeya T and Senna M 1988 Change in the structure of niobium pentoxide due to mechanical and thermal treatments *J. Non-Cryst. Solids* **105** 243–50

[158] McConnell A A, Aderson J S and Rao C N R 1976 Raman spectra of niobium oxides *Spectrochim. Acta Mol. Spectros.* **32** 1067–76

[159] Huang B X, Wang K, Church J S and Li Y-S 1999 Characterization of oxides on niobium by raman and infrared spectroscopy *Electrochim. Acta* **44** 2571–7

[160] Balachandran U and Eror N G 1982 Raman spectrum of the high temperature form of Nb2O5 *J Mater Sci Lett* **1** 374–6

[161] Manzo M, Laurell F, Pasiskevicius V and Gallo K 2013 Lithium Niobate: The Silicon of Photonics! *Nano-Optics for Enhancing Light-Matter Interactions on a Molecular Scale* NATO Science for Peace and Security Series B: Physics and Biophysics ed B D Bartolo and J Collins (Springer Netherlands) pp 421–2

[162] Wang K and Li J-F 2012 (K, Na)NbO3-based lead-free piezoceramics: Phase transition, sintering and property enhancement *J Adv Ceram* **1** 24–37

[163] Thierfelder C, Sanna S, Schindlmayr A and Schmidt W G 2010 Do we know the band gap of lithium niobate? *physica status solidi (c)* **7** 362–5

[164] Rachel, Dutto F and Radenovic A 2011 Niobates Nanowires: Synthesis, Characterization and Applications *Nanowires - Implementations and Applications* ed A Hashim (InTech)

[165] Graça M P F, Valente M A, Peres M, Cruz A, Soares M J, Neves A J, Monteiro T, Alves L C and Alves E 2007 Structural and optical properties of Er3+ ion in sol–gel grown LiNbO3 *J. Phys.: Condens. Matter* **19** 016213

[166] Nico C, Graça M P F, Monteiro T and Valente M A 2011 Lithium niobosilicate glass doped with samarium: Dielectric and optical analysis *physica status solidi (a)* **208** 2288–92

[167] Fang J, Wang X, Tian Z, Zhong C, Li L and Zuo R 2010 Two-Step Sintering: An Approach to Broaden the Sintering Temperature Range of Alkaline Niobate-Based Lead-Free Piezoceramics *Journal of the American Ceramic Society* **93** 3552–5

[168] Kuznetsova E, Reznichenko L, Razumovskaya O and Shilkina L 2001 The polymorphism of niobium pentoxide and the properties of alkali metal niobates for ferroelectric piezoceramics *Technical Physics Letters* **27** 189–92

[169] Hreščak J, Bencan A, Rojac T and Malič B 2013 The influence of different niobium pentoxide precursors on the solid-state synthesis of potassium sodium niobate *Journal of the European Ceramic Society* **33** 3065–75

[170] Yan C, Nikolova L, Dadvand A, Harnagea C, Sarkissian A, Perepichka D F, Xue D and Rosei F 2010 Multiple NaNbO3/Nb2O5 Heterostructure Nanotubes: A New Class of Ferroelectric/Semiconductor Nanomaterials *Adv. Mater.* **22** 1741–5

[171] Pullar R C 2009 The Synthesis, Properties, and Applications of Columbite Niobates (M2+Nb2O6): A Critical Review *Journal of the American Ceramic Society* **92** 563–77

[172] Qin L, Wei D, Huang Y, Kim S I, Yu Y M and Seo H J 2013 Triple-Layered Perovskite Niobates CaRNb3O10 (R = La, Sm, Eu, Gd, Dy, Er, Yb, or Y): New Self-Activated Oxides *Inorg. Chem.* **52** 10407–13

[173] Rooksby H P, White E A D and Langston S A 1965 Perovskite-Type Rare-Earth Niobates and Tantalates *Journal of the American Ceramic Society* **48** 447–9

[174] Rooksby H P and White E A D 1964 Rare-Earth Niobates and Tantalates of Defect Fluorite-and Weberite-Type Structures *Journal of the American Ceramic Society* **47** 94–6

[175] Rooksby H P and White E A D 1963 The structures of 1: 1 compounds of rare earth oxides with niobia and tantala *Acta Crystallographica* **16** 888–90

[176] Cashion J D, Cooke A H, Leask M J M, Thorp T L and Wells M R 1968 Crystal growth and magnetic susceptibility of some rare-earth compounds *J Mater Sci* **3** 402–7

[177] Garton G and Wanklyn B M 1968 Crystal growth and magnetic susceptibility of some rare-earth compounds *J Mater Sci* **3** 395–401

[178] Siqueira K P F, Moreira R L and Dias A 2010 Synthesis and Crystal Structure of Lanthanide Orthoniobates Studied by Vibrational Spectroscopy *Chem. Mat.* **22** 2668–74

[179] Kim D-W, Kwon D-K, Yoon S H and Hong K S 2006 Microwave Dielectric Properties of Rare-Earth Ortho-Niobates with Ferroelasticity *J American Ceramic Society* **89** 3861–4

[180] Siqueira K P F, Carvalho G B and Dias A 2011 Influence of the processing conditions and chemical environment on the crystal structures and phonon modes of lanthanide orthotantalates *Dalton Trans.* **40** 9454–60

[181] Haugsrud R and Norby T 2006 Proton conduction in rare-earth ortho-niobates and ortho-tantalates *Nature Materials* **5** 193–6

[182] Nyman M, Rodriguez M A, Rohwer L E S, Martin J E, Waller M and Osterloh F E 2009 Unique LaTaO4 Polymorph for Multiple Energy Applications *Chem. Mater.* **21** 4731–7

[183] Octaviano E S, Reyes Ardila D, Andrade L H C, Siu Li M and Andreeta J P 2004 Growth and evaluation of lanthanoids orthoniobates single crystals processed by a miniature pedestal growth technique *Cryst. Res. Technol.* **39** 859–63

[184] Graça M P F, Peixoto M, Ferreira N, Rodrigues J, Nico C, Costa F and Monteiro T 2013 Optical and dielectric behaviour of EuNbO4 crystals *Journal of Materials Chemistry C* **1** 2913–9

[185] Xiao X and Yan B 2005 Synthesis and luminescent properties of novel RENbO4:Ln3+ (RE = Y, Gd, Lu; Ln = Eu, Tb) micro-crystalline phosphors *Journal of Non-Crystalline Solids* **351** 3634–9

[186] Nyman M D and Rohwer L E S 2013 Rare-earth tantalates and niobates suitable for use as nanophosphors

[187] Kato K, Toyoura K, Nakamura A and Matsunaga K 2013 First-principles analysis on proton diffusivity in La_3NbO_7 *Solid State Ionics* **262** 472–5

[188] Ivanova M, Ricote S, Meulenberg W A, Haugsrud R and Ziegner M 2012 Effects of A-and B-site (co-) acceptor doping on the structure and proton conductivity of $LaNbO_4$ *Solid State Ionics* **213** 45–52

[189] Kepaptsoglou D-M, Hadidi K, Løvvik O-M, Magraso A, Norby T, Gunnaes A E, Olsen A and Ramasse Q M 2012 Interfacial Charge Transfer and Chemical Bonding in a Ni–LaNbO4 Cermet for Proton-Conducting Solid-Oxide Fuel Cell Anodes *Chemistry of Materials* **24** 4152–9

[190] Amsif M, Marrero-López D, Ruiz-Morales J C, Savvin S and Núñez P 2012 Low temperature sintering of $LaNbO_4$ proton conductors from freeze-dried precursors *Journal of the European Ceramic Society* **32** 1235–44

[191] Mather G C, Fisher C A J and Islam M S 2010 Defects, Dopants, and Protons in LaNbO4 *Chem. Mater.* **22** 5912–7

[192] Tolchard J R, Lein H L and Grande T 2009 Chemical compatibility of proton conducting LaNbO4 electrolyte with potential oxide cathodes *Journal of the European Ceramic Society* **29** 2823–30

[193] Reijers R and Haije W 2008 Literature review on high temperature proton conducting materials *Energy research Centre of the Netherlands*

[194] Mokkelbost T, Kaus I, Haugsrud R, Norby T, Grande T and Einarsrud M-A 2008 High-Temperature Proton-Conducting Lanthanum Ortho-Niobate-Based Materials. Part II: Sintering Properties and Solubility of Alkaline Earth Oxides *Journal of the American Ceramic Society* **91** 879–86

[195] Mokkelbost T, Andersen Ø, Strøm R A, Wiik K, Grande T and Einarsrud M-A 2007 High-Temperature Proton-Conducting LaNbO4-Based Materials: Powder Synthesis by Spray Pyrolysis *Journal of the American Ceramic Society* **90** 3395–400

[196] Baughman R H, Stafström S, Cui C and Dantas S O 1998 Materials with negative compressibilities in one or more dimensions *Science* **279** 1522–4

[197] Smart L E and Moore E A 2005 *Solid State Chemistry: An Introduction, Third Edition* (CRC Press)

[198] West A R 1985 *Solid State Chemistry and Its Applications* (John Wiley & Sons)

[199] Callister W D and Rethwisch D G 2010 *Materials Science and Engineering: An Introduction* (John Wiley & Sons)

[200] Brinker C J and Scherer G W 1990 *Sol-gel Science: The Physics and Chemistry of Sol-gel Processing* (Gulf Professional Publishing)

[201] Attia Y A 1994 *Sol-Gel Processing and Applications* (Boston, MA: Springer US : Imprint: Springer)

[202] Sakka S 2008 *Handbook of Sol-Gel Science and Technology: Processing, Characterization and Applications, V. I - Sol-Gel Processing/Hiromitsu Kozuka, Editor, V. II - ... Sol-Gel Technology/Sumio Sakka, Editor (v. 1)* (Springer)

[203] Rao C N R 1997 *New Directions in Solid State Chemistry* (Cambridge University Press)

[204] Pechini M P 1967 *Method of preparing lead and alkaline earth titanates and niobates and coating method using the same to form a capacitor US Patent# 3.330. 697*

[205] Valente M A, Silva C C, Sombra A S B and Graça M P F 2010 Dielectric spectroscopy of LiNbO3 and TmNbO4 nanocrystals embedded in a SiO2 glass matrix *J. Non-Cryst. Solids* **356** 800–4

[206] Graça M, Ferreira da Silva M and Valente M 2007 Preparation, structure, morphology, and dc and ac conductivity of the 88SiO2-6Li2O-6Nb2O5 (% mole) sol-gel derived glass-ceramics *Journal of Sol-Gel Science and Technology* **42** 1–8

[207] Schropp R E I and Zeman M 1998 *Amorphous and Microcrystalline Silicon Solar Cells: Modeling, Materials and Device Technology* vol 5 (Springer)

[208] Chang W S C 2002 *RF Photonic Technology in Optical Fiber Links* (Cambridge University Press)

[209] Carter C B and Norton M G 2007 *Ceramic Materials: Science and Engineering* (Springer)

[210] Rudolph P and Fukuda T 1999 Fiber crystal growth from the melt *Crystal Research and Technology* **34** 3–40

[211] Koohpayeh S M, Fort D and Abell J S 2008 The optical floating zone technique: A review of experimental procedures with special reference to oxides *Progress in Crystal Growth and Characterization of Materials* **54** 121–37

[212] Soares M R, Rodrigues J, Santos N F, Nico C, Carvalho R G, Fernandes A J S, Graça M P, Rino L, Soares M J, Neves A J, Costa F M and Monteiro T 2013 Prospects on laser processed wide band gap oxides optical materials *Proc. SPIE 8626* Oxide-based Materials and Devices IV vol 8626, ed F H Teherani, D C Look and D J Rogers (Oxide-based Materials and Devices IV) pp 862607–01 – 15

[213] Jenkins R and Snyder R L 1996 *Introduction to X-ray powder diffractometry* (New York: Wiley)

[214] Cheetham A K and Day P 1987 *Solid State Chemistry: Techniques* (Clarendon Press)

[215] Scherrer P 1918 Bestimmung der Grösse und der inneren Struktur von Kolloidteilchen mittels Röntgenstrahlen *Nachrichten von der Gesellschaft der Wissenschaften zu Göttingen, mathematisch-physikalische Klasse* **1918** 98–100

[216] Langford J I and Wilson A J C 1978 Scherrer after sixty years: A survey and some new results in the determination of crystallite size *Journal of Applied Crystallography* **11** 102–13

[217] Scardi P, Leoni M and Delhez R 2004 Line broadening analysis using integral breadth methods: a critical review *Journal of Applied Crystallography* **37** 381–90

[218] Rietveld H 1969 A profile refinement method for nuclear and magnetic structures *Journal of applied Crystallography* **2** 65–71

[219] Egerton R 2005 *Physical Principles of Electron Microscopy - An Introduction to TEM, SEM, and AEM* (Springer)

[220] Williams D B and Carter C B 2009 *Transmission Electron Microscopy: A Textbook for Materials Science* (New York: Springer)

[221] Salh R 2011 Silicon Nanocluster in Silicon Dioxide: Cathodoluminescence, Energy Dispersive X-Ray Analysis and Infrared Spectroscopy Studies *Crystalline Silicon - Properties and Uses* ed S Basu (InTech)

[222] Steff 2010 Schema MEB (en) *en.wikipedia.org/wiki/ File:Schema_MEB_(en).svg*

[223] Ferraro J R 2003 *Introductory Raman Spectroscopy* (Academic Press)

[224] YU P and Cardona M 2010 *Fundamentals of Semiconductors: Physics and Materials Properties* (Springer Berlin Heidelberg)

[225] Venkateswarlu K 1941 Relative intensities of stokes and anti-stokes Raman lines in crystals *Proc. Indian Acad. Sci. (Math. Sci.)* **13** 64–7

[226] Solé J 2005 *An Introduction to the Optical Spectroscopy of Inorganic Solids* (John Wiley and Sons)

[227] Blasse G and Grabmaier B C 1994 *Luminescent materials* vol 44 (Springer-Verlag Berlin)

[228] Livingston J D 1999 *Electronic properties of engineering materials* (New York: Wiley)

[229] Macdonald J R 1987 *Impedance Spectroscopy: Emphasizing Solid Materials and Analysis* (John Wiley & Sons, New York)

[230] Mendiratta S K 1984 *Introdução ao electromagnetismo* (Lisboa: Fundação Calouste Gulbenkian)

[231] Feldman Y, Puzenko A and Ryabov Y 2006 Dielectic Relaxation Phenomena in Complex Materials *Advances in chemical physics* **133** 1

[232] Lambert B 2010 Dielectric responses.svg *en.wikipedia.org/wiki/ File:Dielectric_responses.svg*

[233] Gill J *Basic Tantalum Capacitor Technology* (Paignton, England: AVX Ldt., Tantalum Division)

[234] Anon 2012 *KEMET Tantalum Capacitor Manufacturing* (Youtube)

[235] Ho J, Jow T R and Boggs S 2010 Historical introduction to capacitor technology *IEEE Electrical Insulation Magazine* **26** 20–5

[236] Alapatt G 2010 *Investigating pre-breakdown currents in polymer tantalum capacitors* (Clemson University)

[237] Vernitskaya T V and Efimov O N 1997 Polypyrrole: a conducting polymer; its synthesis, properties and applications *Russ. Chem. Rev.* **66** 443

[238] Conway B E 1999 *Electrochemical Supercapacitors: Scientific Fundamentals and Technological Applications* (Boston, MA: Springer US)

[239] KEMET Introduction to Capacitor Technologies - What is a Capacitor? http://www.kemet.com/Lists/TechnicalArticles/Attachments/6/What%20is%20a%20Capacitor.pdf (access April 24, 2014)

[240] Elcap 2014 Fixed-capacitors-overview *"Fixed-capacitors-overview" commons.wikimedia.org/wiki/ File:Fixed-capacitors-overview.png*

[241] Elcap Kondensatoren-Kap-Versus-Spg-English *"Kondensatoren-Kap-Versus-Spg-English" commons.wikimedia.org/wiki/ File:Kondensatoren-Kap-Versus-Spg-English.svg*

[242] Kötz R and Carlen M 2000 Principles and applications of electrochemical capacitors *Electrochimica Acta* **45** 2483–98

[243] AVX Tantalum and Niobium Oxide Capacitors (Version 14.11)

[244] Doty Arnold S 1964 Method of producing porous sintered tantalum anodes. Patent US3144328 A

[245] Fresia E J 1990 Solid tantalum capacitor process. Patent CA1275712 C

[246] Henley V F 2013 *Anodic Oxidation of Aluminium and Its Alloys: The Pergamon Materials Engineering Practice Series* (Elsevier)

[247] Lee W and Park S-J 2014 Porous Anodic Aluminum Oxide: Anodization and Templated Synthesis of Functional Nanostructures *Chem. Rev.* **114** 7487–556

[248] Haas H, Hagymasi M, Brumm H and Schnitter C 2014 Method for producing electrolytic capacitors from valve metal powders. Patent US20140185190 A1

[249] A H, J P and J S 1974 Method of forming a solid tantalum capacitor. Patent US3850764 A

[250] Lim J H and Choi J 2009 Formation of niobium oxide nanowires by thermal oxidation *J. Ind. Eng. Chem.* **15** 860–4

[251] Braga V S, Garcia F A C, Dias J A and Dias S C L 2007 Copper oxide and niobium pentoxide supported on silica-alumina: Synthesis, characterization, and application on diesel soot oxidation *J. Catal.* **247** 68–77

[252] Momma K and Izumi F 2011 VESTA 3 for three-dimensional visualization of crystal, volumetric and morphology data *Journal of Applied Crystallography* **44** 1272–6

[253] Reshchikov M A, Morkoē H, Nemeth B, Nause J, Xie J, Hertog B and Osinsky A 2007 Luminescence properties of defects in ZnO *Physica B* **401** 358–61

[254] Barros Filho D D ., Abreu Filho P P, Werner U and Aegerter M A 1997 Photoelectrochemical properties of sol-gel Nb2O5 films *J. Sol-Gel Sci. Technol.* **8** 735–42

[255] Henn F, Vanderschueren J, Giuntini J C and Zanchetta J V 1999 Cooperative or noncooperative dielectric relaxation in ionic solids: A discriminating experimental approach *J. Appl. Phys.* **85** 2821

[256] Jonscher A K 1983 *Dielectric relaxation in solids* (Chelsea Dielectrics Press)

[257] Nico C, Rino L, Matos M, Monteiro R, Costa F M, Monteiro T and Graça M P F NbO/Nb2O5 core–shells by thermal oxidation *J. Eur. Ceram. Soc.*

[258] KEMET 2014 *Tantalum Surface Mount Capacitors, Standard Tantalum*

[259] Fontalvo G A, Terziyska V and Mitterer C 2007 High-temperature tribological behaviour of sputtered NbNx thin films *Surface and Coatings Technology* **202** 1017–22

[260] Peixoto M 2012 *Preparação e caracterização física do ortoniobato de európio* (Aveiro: Universidade de Aveiro)

[261] Mather S A and Davies P K 1995 Nonequilibrium Phase Formation in Oxides Prepared at Low Temperature: Fergusonite-Related Phases *Journal of the American Ceramic Society* **78** 2737–45

[262] Blasse G 1973 Vibrational spectra of yttrium niobate and tantalate *J. Solid State Chem.* **7** 169–71

[263] Zhang D-L, Wang Y-F, Pun E Y ., Yu Y-Z, Chen C-H and Yao J-Q 2004 Absorption and emission of ErNbO4 powder *Optical Materials* **25** 379–92

[264] Blasse G, Gschnneidner Jr K A and Eyring L 1979 *Handbook on the Physics and Chemistry of Rare Earths, vol. 4* (North Holland, Amsterdam)

[265] Soares M R N, Nico C, Peres M, Ferreira N, Fernandes A J S, Monteiro T and Costa F M 2011 Structural and optical properties of europium doped zirconia single crystals fibers grown by laser floating zone *J. Appl. Phys.* **109** 013516

[266] Packer R J, Tsipis E V, Munnings C N, Kharton V V, Skinner S J and Frade J R 2006 Diffusion and conductivity properties of cerium niobate *Solid State Ionics* **177** 2059–64

[267] Kreuer K D 1999 Aspects of the formation and mobility of protonic charge carriers and the stability of perovskite-type oxides *Solid State Ionics* **125** 285–302

[268] Souza E C C de and Muccillo R 2010 Properties and applications of perovskite proton conductors *Materials Research* **13** 385–94

[269] Pan L, Wang Y, Wang X, Qu H, Zhao J, Li Y and Gavrilyuk A 2014 Hydrogen photochromism in Nb2O5 powders *Physical Chemistry Chemical Physics*

[270] Joshua Yang J, Miao F, Pickett M D, Ohlberg D A A, Stewart D R, Lau C N and Williams R S 2009 The mechanism of electroforming of metal oxide memristive switches *Nanotechnology* **20** 215201

[271] Park S-J, Lee J-P, Jang J S, Rhu H, Yu H, You B Y, Kim C S, Kim K J, Cho Y J, Baik S and Lee W 2013 In situ control of oxygen vacancies in TiO2 by atomic layer deposition for resistive switching devices *Nanotechnology* **24** 295202

[272] Waser R and Aono M 2007 Nanoionics-based resistive switching memories *Nature materials* **6** 833–40

[273] Messerschmitt F, Kubicek M, Schweiger S and Rupp J L M 2014 Memristor Kinetics and Diffusion Characteristics for Mixed Anionic-Electronic SrTiO3-δ Bits: The Memristor-Based Cottrell Analysis Connecting Material to Device Performance *Adv. Funct. Mater.* **24** 7448–60

[274] Valov I 2014 Redox-Based Resistive Switching Memories (ReRAMs): Electrochemical Systems at the Atomic Scale *CHEMELECTROCHEM* **1** 26–36

[275] Lee S, Na H, Kim J, Moon J and Sohn H 2011 Anion-Migration-Induced Bipolar Resistance Switching in Electrochemically Deposited TiO x Films *J. Electrochem. Soc.* **158** H88–92

[276] Waser R, Dittmann R, Staikov G and Szot K 2009 Redox-Based Resistive Switching Memories–Nanoionic Mechanisms, Prospects, and Challenges *Advanced Materials* **21** 2632–63

[277] Hamwi S, Meyer J, Kröger M, Winkler T, Witte M, Riedl T, Kahn A and Kowalsky W 2010 The Role of Transition Metal Oxides in Charge-Generation Layers for Stacked Organic Light-Emitting Diodes *Adv. Funct. Mater.* **20** 1762–6

[278] Liang J, Zu F-S, Ding L, Xu M-F, Shi X-B, Wang Z-K and Liao L-S 2014 Aqueous solution-processed MoO3 thick films as hole injection and short-circuit barrier layer in large-area organic light-emitting devices *Appl. Phys. Express* **7** 111601

[279] Vetrone F, Naccache R, Zamarrón A, Juarranz de la Fuente A, Sanz-Rodríguez F, Martinez Maestro L, Martín Rodriguez E, Jaque D, García Solé J and Capobianco J A 2010 Temperature Sensing Using Fluorescent Nanothermometers *ACS Nano* **4** 3254–8

[280] Brites C D S, Lima P P, Silva N J O, Millán A, Amaral V S, Palacio F and Carlos L D 2012 Thermometry at the nanoscale *Nanoscale* **4** 4799–829

[281] Brites C D S, Lima P P, Silva N J O, Millán A, Amaral V S, Palacio F and Carlos L D 2013 Ratiometric highly sensitive luminescent nanothermometers working in the room temperature range. Applications to heat propagation in nanofluids *Nanoscale* **5** 7572–80

[282] Brites C D S, Lima P P, Silva N J O, Millán A, Amaral V S, Palacio F and Carlos L D 2011 Lanthanide-based luminescent molecular thermometers *New J. Chem.* **35** 1177–83